BEHAVIOUR OF COHESIVE SOILS UNDER UPLIFT FORCES

by

John R. Davie, B.Sc., M.E.

A Thesis submitted for the Degree of

Doctor of Philosophy

Department of Civil Engineering

University of Glasgow

July, 1973

CONTENTS

TABLES AND FIGURES.

All tables and figures are placed in order at the end of the chapters and appendices to which they refer, except Tables 4.1 and E.1 which are incorporated in the text.

FLOW CHART

The flow chart of the finite element analysis is placed inside the back cover.

ACKNOWLEDGMENTS

The laboratory work for this investigation was carried out in the Civil Engineering Laboratories at the University of Glasgow.

The author wishes to express his sincere thanks to Professor H.B. Sutherland, Cormack Professor of Civil Engineering at the University of Glasgow, for his encouragement and advice throughout the course of the investigation.

Thanks are extended to Dr. I.M. Smith of the Department of Civil Engineering at the University of Manchester for providing the basis of the finite element program used in the investigation. Thanks are also extended to colleagues in the Department of Civil Engineering at the University of Glasgow for many useful discussions and suggestions during the course of the work, and to members of staff of the Computing Service at the University of Glasgow for their friendly and efficient service.

The author wishes to thank the laboratory staff in the Department of Civil Engineering at the University of Glasgow for manufacturing much of the non-standard equipment used in the laboratory tests. In particular, thanks are due to Mr. W. Nisbet for his valuable assistance in preparing soil samples and to Mr. D. Wood for processing the photographs. I wish to thank Mrs. J.F. Park for typing this thesis.

Finally, I wish to thank my wife, Pamela, for her encouragement over the period of this work and for her assistance in typing this thesis.

NOTATION

General Notation

a	dimensional factor, Matsuo (1967)
b	dimensional factor, Matsuo (1967)
B	diameter of anchor plate
B_c	diameter of soil container
B_o	diameter of anchor shaft
B_2	dimension in Matsuo's (1967) Theory
c	cohesion of soil
c_a	adhesion between soil and anchor plate
c'	vertical component of cohesive force acting on conical wedge, Ali (1968)
C_{1-4}	expressions in Vesic's (1963 and 1965) Shallow Anchor Theory
d_a	vertical displacement of anchor plate
$d_{a(max)}$	vertical displacement of anchor plate at ultimate uplift resistance
d_s	vertical displacement of soil surface above centre of anchor plate
D	depth of placement of anchor plate
D_1	dimension in Matsuo's (1967) Theory
D_2	dimension in Matsuo's (1967) Theory
E	modulus of elasticity (Young's modulus)
F	vertical component of limiting frictional force, Earth Pressure Theory
F_c, F_q	Vesic's (1963 and 1965) breakthrough cavity factors
F_{1-3}	factors in Balla's (1961) Theory
F_{1-4}	anchor loads in shallow anchor model tests
$\bar{F}$	uplift resistance factor
$\bar{F}_c, \bar{F}_q$	Vesic's (1963 and 1965) cavity expansion factors
$\bar{F}_u$	ultimate uplift resistance factor
F'_{1-7}	factors in Matsuo's (1967) Theory
g	acceleration due to gravity

G_o	weight of anchor
G_{1-7}	weights of various volumes of soil
H	depth of local shear, Meyerhof and Adams (1968)
I_r	rigidity index, Vesic (1963 and 1965)
K	coefficient of earth pressure, Earth Pressure Theory
K_o	coefficient of earth pressure at rest
K_p	coefficient of passive earth pressure
K_{pv}	coefficient in Meyerhof and Adams's (1968) Theory
K_u	coefficient in Meyerhof and Adams's (1968) Theory
K_1, K_2'	factors in Matsuo's (1967) Theory
L	length
m	coefficient in Meyerhof and Adams's (1968) Theory
m_v	coefficient of volume compressibility due to consolidation
M	mass
$M_{1,2}$	moments due to structural stiffness of soil
n	coefficient in Mariupol'skii's (1965) Theory
N	factor from Brinch Hansen (1953)
N_{cqr}, N_u	ultimate bearing capacity factors, Meyerhof (1951)
p	uplift resistance pressure
p_s	superimposed surface loading
p_u	ultimate uplift resistance pressure
p_{uc}	ultimate cavity pressure, Vesic (1963 and 1965)
p_i	cavity pressure, Vesic (1963 and 1965)
P_p	factor for uplift resistance force, Mariupol'skii (1965)
P_{1-4}	denote yielded zones predicted by finite element analysis
P'_{1-3}	denote yielded zones in shallow anchor model tests
q	overburden pressure
Q	total cohesive force over failure surface, Mariupol'skii (1965)

r	distance, radius, cylindrical co-ordinate
R	ultimate uplift resistance force
R_i	initial radius of cavity, Vesic (1963 and 1965)
R_p	radius of the plastic zone, Vesic (1963 and 1965)
R_u	ultimate radius of cavity, Vesic (1963 and 1965)
S	shape factor, Meyerhof and Adams (1968)
S'	amount of anchor displacement, Mariupol'skii (1965)
t	tensile strength of soil
t	thickness of anchor plate
T	time
T	tensile region near soil surface in shallow anchor case
T	factor from Brinch Hansen (1953)
T_v	vertical component of shearing, Balla (1961)
T_v'	vertical component of resultant shearing, Matsuo (1967)
u_p	radial movement of elastic-plastic boundary, Vesic (1963 and 1965)
V_o	volume of anchor
V_{1-5}	various volumes of soil
w	diameter of surface bulge
x_o, y_o	co-ordinates of centre of logarithmic spiral, Matsuo (1967)
X	denotes region of soil yielded in tension
z	cylindrical co-ordinate
α	Earth Cone angle
α	apex angle of cone, Mariupol'skii (1965)
α	angle in Vesic's (1963 and 1965) Theory
α_o	angle in Balla's (1961) Theory
γ	density of soil
γ_{rz}	shear strain in $r-z$ plane

δ	Earth Pressure friction angle
δ_{1-4}	displacements of anchor
δ'_{1-3}	displacements of anchor
Δ	average volume strain in plastic zone, Vesic (1963 and 1965)
$\epsilon_r, \epsilon_z, \epsilon_\theta$	normal strains in r , z and θ directions
θ	angle of major principal stress to the horizontal
θ	angle, Matsuo (1967)
λ	coefficient of anchor dimensions, Balla (1961)
ν	Poisson's ratio
ρ	radius of logarithmic spiral, Matsuo (1967)
ρ_o	original radius of logarithmic spiral, Matsuo (1967)
$\sigma_r, \sigma_z, \sigma_\theta$	normal stresses in r , z and θ directions
τ_{rz}	shear stress in $r-z$ plane
τ_{max}	maximum shear stress
ω	function of inverse of soil compressibility, Mariupol'skii (1965)

Finite Element Method Notation

A_e	area of element
$[B]$	strain-displacement matrix
$\{BK\}$	structural stiffness vector
d	depth from top surface of mesh to centre of element
$[D]$	stress-strain matrix, elastic
$[DPL]$	stress-strain matrix, plastic
$\{F\}$	force vector
FAC	factor used with plastic stress-strain matrix
$[J]$	Jacobian transformation matrix
$[KM]$	element stiffness matrix
$[N]$	shape and displacement function matrices
$\{P\}$	balancing nodal force vector
$[PL]$	reduced plastic stress-strain matrix
r,z,θ	cylindrical co-ordinate system
r',z',θ'	local cylindrical co-ordinate system
R	load adjustment factor
u,v	displacements related to cylindrical co-ordinate system
w	half-band width of matrix
$\{\delta\}$	nodal displacement vector
$\{\epsilon\}$	strain vector
θ	angle of major principal stress to the horizontal
$\{\sigma\}$	stress vector
σ_0	original stress in "initial stress" procedure
σ'	elastic stress in "initial stress" procedure
σ''	"initial stress" in "initial stress" procedure
$\bar{\sigma}$	Von Mises stress in element
$\bar{\sigma}_{max}$	Von Mises stress in "critical" element after first load increment

σ_1, σ_{maj}	major principal stress
σ_3, σ_{min}	minor principal stress
$\bar{\sigma}_y$	Von Mises yield stress
τ_{max}	maximum shear stress in element

SUMMARY

This thesis is concerned with various aspects of the behaviour of purely cohesive soils under uplift forces. Previous authors have predicted theoretically the ultimate uplift resistance of soils possessing both cohesion and internal friction by assuming various shapes of rupture surfaces above an anchor and calculating the shearing stresses over these surfaces. For very deep anchors in which surface effects had disappeared, the problem was treated as that of a deep foundation. The various theories have been reduced to dimensionless terms by the author and are compared and discussed for purely cohesive soils.

A dimensional analysis of the problem is presented and the importance of the various factors is discussed. The effect of using the same soil in uplift model testing as in the prototype is discussed with reference to Vesic's (1963 and 1965) theories. Limiting values of prototype anchor dimensions and soil properties which can be modelled with complete dimensional similarity are presented in dimensionless terms.

Apparatus was constructed to enable both model pushout and pullout tests to be performed using either load-controlled or displacement-controlled loading. The load on the anchor, the displacement of the anchor and the surface displacement of the clay sample were measured electronically. This apparatus was modified to enable the sample to be split open after the test to examine deformations and cracking patterns in the soil. Uplift resistance tests were carried out on two types of very soft clays, namely mixtures of bentonite and glycerine and a mixture of silty clay from the Grangemouth area and Fayles Blue clay. The uplift samples were compacted by hand.

The results of the model uplift tests indicated three categories of anchor depth to breadth ratios, namely shallow anchor ratios, intermediate depth of anchor ratios and deep anchor ratios. A mechanism

of general type failure which comprised a combination of shear and tensile failure and tensile cracking of the soil was proposed for the shallow anchor ratios. A local type of failure was observed to occur at the deep anchor ratios while a combination of local and general type failure occurred at the intermediate depth ratios. The mechanism of ultimate failure in tests with a suction effect below the anchor plate was different from that without the suction effect. No significant difference was found between the results of pullout and pushout tests. Creep in the bentonite and glycerine samples was observed in the load-controlled tests.

The values of ultimate uplift resistance obtained from the shallow anchor model tests ranged from fifty per cent to sixty-five per cent of those predicted by Vesic's theory. The values predicted by Vesic's theory in the deep anchor range agreed approximately with the model tests. The results from model tests by previous authors were found to be in generally poor agreement with each other and with the results from model tests by the author.

A finite element analysis of the problem was developed to investigate primarily the magnitude and direction of the various stresses acting in the soil during uplift resistance tests. The analysis was an axi-symmetric, elastic-plastic iterative procedure which employed Von Mises yielding criterion. Three basic meshes using rectangular isoparametric elements were used to simulate shallow, intermediate and deep anchor cases, the anchor being assumed rigid at all times. Each mesh comprised approximately two hundred elements. The finite element analysis could only predict a general type of failure, regardless of the depth of the anchor, could only be used accurately at small element strains, and employed a linear elastic non-strain hardening plastic stress-strain curve as an approximation to an actual soil stress-strain curve. Within these limitations, the analysis predicted the order of plastic yielding of the elements in

the mesh, the magnitude and direction of all stresses in the elements, the nodal displacements of each element and the relationship between anchor displacement and uplift resistance.

CHAPTER ONE

INTRODUCTION

1.1. General Introduction

In recent years considerable progress has been achieved in developing methods for calculating the bearing capacity of soils and predicting the deformations associated with different types of foundations and soils. However, research into the less usual problem of the uplift resistance capacity of soils has been more limited. At present there exists no generally accepted theory of soil uplift resistance which is used in practical design.

The uplift resistance problem may be demonstrated by considering the foundation of a high structure subjected to strong wind forces (Fig. 1.1.). This structure could be an electricity pylon, a radio or television mast or any structure which must resist an overturning load. The tensile forces in the structure, caused by the eccentricity of the loading, may be considerable at the corner posts. The dimensions of the footings to which these posts are anchored must be chosen to enable the soil surrounding the footings to resist this level of pull-out force. There must therefore be an understanding of the mechanism which causes ultimate failure.

Often in foundation engineering, the limiting design criterion is the foundation movement. The allowable amount of movement which is caused by a load is frequently well below that required to cause ultimate failure. For high masts, the upward movement of footings below the corner posts will tend to increase the eccentricity of the loading, consequently increasing the pull-out load. Predictions of the movement of these footings as well as predictions of the ultimate uplift resistance of the soil are therefore important.

Another form of the uplift resistance problem also exists. At

Sizewell Nuclear Power Station vertical shafts were raised from the cooling water tunnels below the sea bed by jacking the closed ends of the shafts up through the soil to sea bed level. In this type of operation the uplift forces experienced by the soil during jacking are of a similar nature to those above a high mast footing resisting pull-out.

In mast foundations, a large factor of safety is normally incorporated in the footing design and this may disguise any inaccurate estimate of ultimate uplift resistance. However, the final level of loading applied to the jack in shaft-raising operations will be the ultimate uplift resistance of the soil. An accurate assessment of this ultimate uplift resistance in these situations will be required to ensure the most economical use of equipment.

This thesis is concerned with the investigation of the uplift resistance problem in purely cohesive soils. It is considered that a better understanding of the important variables in the problem will assist engineers in the future design of uplift resisting foundations in these soils.

1.2. Scope of Thesis

From the previous literature, a review of uplift resistance theories for soils possessing both friction and cohesion is presented. These theories are compared and discussed with particular reference to purely cohesive soils. The results of the better documented uplift resistance laboratory tests in purely cohesive soils are presented and compared.

In order to examine and assess the factors most relevant to the problem, a dimensional analysis is included. By placing the variables in dimensionless groups, an assessment was made of the model scaling effect.

Model uplift resistance tests, using rigid anchor plates, were performed in the laboratory to examine (i) the load-displacement characteristics of purely cohesive soils up to ultimate load and (ii) the failure mechanism at this load. The resulting surface and internal deformations and cracking of the soil were investigated.

Because of the complex nature of the stress and deformation aspects of the problem, a finite element analysis was developed to examine primarily the distribution, magnitude and direction of stresses in the soil during uplift resistance tests. In both the laboratory model tests and the finite element analysis, the important factors demonstrated by the dimensional analysis were varied.

Finally, the results from the laboratory model tests and from the finite element analysis are discussed and conclusions drawn.

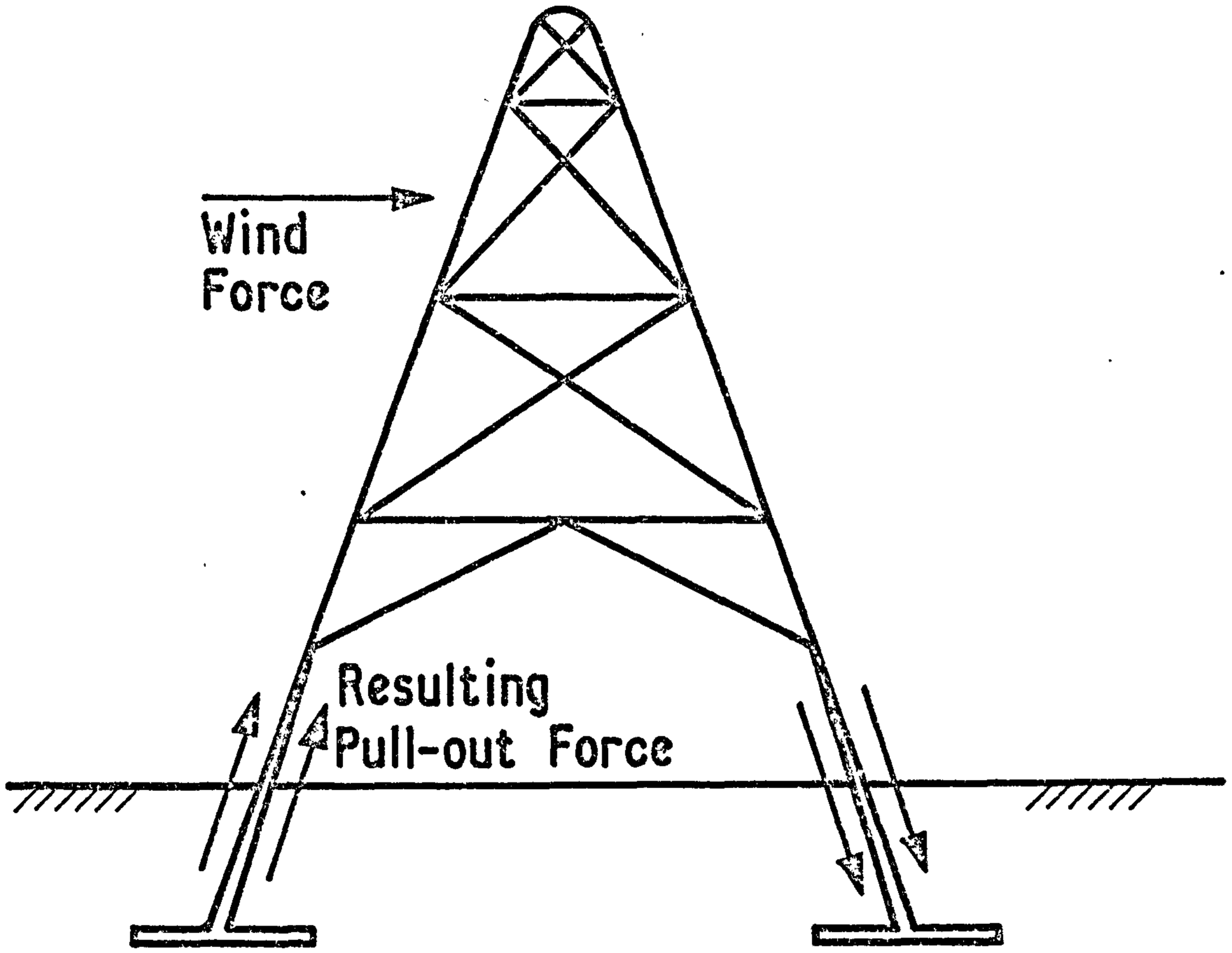

FIG. 1.1 TENSILE FORCES ON FOOTINGS

CHAPTER TWO

REVIEW OF LITERATURE

2.1. Introduction

Over the past fifteen years, various authors have proposed theoretical solutions to the uplift resistance problem. Most of the theories have been derived for soils possessing both friction and cohesion. Some have been developed for anchors at all depths, some for shallow anchors only and some for deep anchors only.

A shallow anchor may be defined as one above which the slip failure surface in the soil reaches to ground level at ultimate load. A more general definition, which is more suitable for purely cohesive soils, is that a shallow anchor is one in which the effect of the ground surface above the anchor plays a major part in the behaviour of the soil under uplift pressure. In the existing shallow anchor theories the shape of the slip failure surface is an assumed shape, and in most cases the ultimate uplift force is calculated by considering the stresses acting over this surface. No movement of the anchor is assumed before ultimate failure occurs.

A deep anchor may be defined as one whose ultimate load is not affected by the ground surface boundary. None of the deep anchor theories assume a slip failure surface extending from the anchor to ground level.

In the following sections on existing shallow and deep anchor theories, the derivations of the ultimate uplift force for round anchors only will be considered. In the sections which summarise and discuss the existing theories, soils possessing both friction and cohesion will be considered, but the results of the theories will be compared for purely cohesive soils only.

2.2. Summary of Shallow Anchor Theories

A. Traditional Approaches

Earth Cone Theory (Fig. 2.1.). The ultimate uplift load is taken to be equal to the dead-weight of the anchor plus the weight of soil contained in the truncated cone (with apex angle 2α) which this method assumes will be formed above the anchor slab when failure occurs:

$$R = G_o + \gamma_g (V_1 - V_o) \qquad \cdots\cdots (2.1)$$

For a round slab, the volume of earth in the truncated cone is:

$$V_1 = \frac{\pi D}{4}\left(B^2 + 2BD\tan\alpha + \frac{4}{3} D^2 \tan^2\alpha \right) \qquad \cdots (2.2)$$

The earth-load angle α varies, depending on the type of soil and the shape of the foundation and can only be found approximately by estimation.

Earth Pressure Theory (Fig. 2.2.). The ultimate uplift load is taken to be equal to the dead-weight of the anchor, plus the weight of the soil contained in the cylinder above the anchor (and with diameter equal to the anchor) plus the vertical component of the limiting frictional force on the surface of this cylinder, (assumed to be the slip failure surface). The lateral earth pressure is found using the value of the earth pressure coefficient at rest, K_o:

$$R = G_o + \gamma_g (V_2 - V_o) + F \qquad \cdots\cdots (2.3)$$

where the cylindrical volume of soil is:

$$V_2 = \pi/4 \,(B^2 D) \qquad \cdots\cdots (2.4)$$

and the vertical component of the limiting frictional force is:

$$F = \pi/2 \,(K_o \gamma_g B D^2 \tan\delta) \qquad \cdots\cdots (2.5)$$

Shearing Stress Theory (Fig. 2.2.). This is similar to the Earth Pressure theory except that the term representing the vertical component of limiting frictional force on the assumed cylindrical slip failure surface is replaced by a term which represents the shear force acting on this surface:

$$R = G_o + \gamma_g (V_2 - V_o) + T \qquad \cdots\cdots (2.6)$$

where the shear force on the cylindrical slip failure surface is:

$$T = \pi c B D + \pi/2 (K \gamma_g B D^2 \tan \phi) \qquad \ldots\ldots (2.7)$$

B. Balla's (1961) Theory (Fig. 2.3.)

Balla assumes that the slip failure surface is part of a circular arc, tangential to the edge of the anchor slab, whose centre is on the same horizontal plane as the top of the slab. He derives an expression for the ultimate uplift load for a round anchor, but, owing to a lack of satisfactory theory for the axially-symmetric stress state, he assumes a plane stress state. Kotter's equation is employed to find the shear resistance along the circular arc and to show that the angle at which the arc cuts the surface is:

$$\alpha_o = \pi/4 - \phi/2 \qquad \ldots\ldots\ldots (2.8)$$

Balla derives the ultimate uplift resistance:

$$R = G_1 + G_2 + T_v \qquad \ldots\ldots\ldots (2.9)$$

where G_1 = the weight of the breaking-out soil solid of revolution (including the anchor shaft taken as soil)

$$= (D-t)^3 \gamma_g F_1 \qquad \ldots\ldots\ldots (2.10)$$

where F_1 is a factor depending on ϕ and λ, a coefficient characteristic of the anchor's dimensions.

G_2 = the difference in weight between the anchor material and the soil for the volume of the anchor shaft,

T_v = the vertical component of shearing over the slip failure surface

$$= (D-t)^3 \gamma_g \left[\left(c/\gamma_g (D-t) \right) F_2 + F_3 \right] \qquad \ldots\ldots (2.11)$$

where F_2 and F_3 are factors depending on ϕ and λ.

C. Mariupol'skii's Theory (Fig. 2.4.).

Mariupol'skii considers the ultimate uplift load to be equal to the deadweight of the anchor, plus the weight of the breaking-out solid of revolution of soil above the anchor, plus the cohesive

and friction forces over the surface of this solid. He proposes that after the friction forces along the vertical cylindrical surfaces around the anchor have been increased to a maximum, failure occurs in tension along the curved generatrix formed at the base of these vertical cylinders (ol Fig. 2.4.), and the soil within these cylinders separates from the surrounding mass. He derives the ultimate uplift resistance:

$$R = G_o + G_3 + \gamma_g V_3 + Q \qquad \cdots\cdots (2.12)$$

where V_3 = the volume of the breaking-out soil solid of revolution,

G_3 = the weight of the circular earth column above the anchor,

Q = the total "cohesive" force over the failure surface

$$= \pi B\left[cD + \tan\phi\left(K\gamma_g \tfrac{D^2}{2} + \int_0^D \sigma_r\, dz\right)\right] - \gamma_g V_3 \qquad \cdots (2.13)$$

where σ_r designates the additional radial stresses created in a cylindrical section of diameter B by pressing the anchor slabs on to the overlying earth column. σ_r is determined from equations of equilibrium. Failure in tension is assumed when $\tau_{rz} = \sigma_r \tan\phi$

A complex exponential expression is obtained for σ_r . From this, Mariupol'skii obtains a workable expression for ultimate uplift resistance load:

$$R = G_o + \tfrac{\pi}{4}(B^2 - B_o^2)\left[\frac{\gamma_g D\left\{1 - \left(\tfrac{B_o}{B}\right)^2 + 2K_o\left(\tfrac{D}{B}\right)\tan\phi\right\} + 4c\,\tfrac{D}{B}}{1 - \left(\tfrac{B_o}{B}\right)^2 - 2n\,\tfrac{D}{B}}\right] \qquad (2.14)$$

where n is a function of ϕ and is derived from laboratory tests.

D. Vesic's (1963 & 1965) Theory (Fig. 2.5.)

Vesic's solution to the uplift resistance problem is an adaptation of his expanding sphere theorem, in which he considers the effect on the soil of an explosive charge placed at moderate depth beneath the ground surface. His basic assumption is that the spherical cavity expands, and at a limiting pressure a slip failure surface forms above the cavity, causing yielding. The ultimate uplift resistance is thus derived in terms of the limiting pressure inside the spherical cavity. Vesic's assumed slip failure surface is similar to that assumed by

Balla, with a circular arc tangential to the expanded cavity meeting the soil surface at an angle of $\pi/4 - \phi/2$. An equation of vertical equilibrium, using expressions derived for the two-dimensional case by Brinch Hansen (1953) yields:

$$R = G_4 + G_5 + T\cos\alpha - N\sin\alpha \qquad \cdots\cdots (2.15)$$

where T and N were taken by Vesic from Brinch Hansen and are functions of ϕ and α. G_4, G_5 and α are shown in Fig. 2.5. The ultimate uplift resistance load is equated to the limiting cavity pressure at yield:

$$p_i = cF_c + \gamma_g D F_q \qquad \cdots\cdots (2.16)$$

where: $$F_q = 1{\cdot}0 + B/3D + 2C_1 D/B + 4C_2 (D/B)^2 \qquad \cdots\cdots (2.17)$$

and: $$F_c = 2C_3 D/B + 4C_4 (D/B)^2 \qquad \cdots\cdots (2.18)$$

C_{1-4} are expressions in ϕ and α. When $\phi = 0$, F_c and F_q reduce to relatively simple terms. Esquivel-Diaz (1967) adjusted the limiting cavity pressure for breakthrough to the uplift resistance of soil above anchors. Instead of a hollow cavity he assumed a hemisphere filled with soil which exerted a pressure on the anchor slab of $\gamma_g \frac{B}{3}$.

The ultimate uplift resistance was then:

$$R = \pi B^2/4 \left[c F_c + \gamma_g D F_q + \gamma_g B/3\right] \qquad \cdots\cdots (2.19)$$

E. Matsuo's (1967) Theory (Fig. 2.6.)

Matsuo assumes failure to occur along a logarithmic spiral slip failure surface with equation:

$$\rho = \rho_o e^{\theta \tan\phi} \qquad \cdots\cdots (2.20)$$

which is tangential to (at A in Fig.2.6.) a plane slip failure surface which meets the ground surface at an angle $\pi/4 - \phi/2$. The critical sliding surface is the one which results in the minimum pressure on the anchor. This pressure is found by taking moments about O_1.

Matsuo derives the ultimate uplift resistance load:

$$R = G_o + \gamma_g V_4 + T_v' \qquad \cdots\cdots (2.21)$$

where V_4 = the volume of soil in the breaking-out solid of revolution,

and T_v' = the vertical component of the resultant shearing resistance acting on the slip failure surface.

The ultimate shearing resistance is found by deriving a differential equation equivalent to Kotter's, but with a different co-ordinate system and is the resultant of both shearing forces and normal forces on the slip failure surface. (Balla considers only the shearing forces which act along the slip failure surface). From tests in clays, Matsuo found that the angle θ_o varied between 35 and 45 degrees and he assumed it to be 40 degrees for ease of calculation. He also observed from his shallow anchor tests in clays that ultimate uplift resistance was mobilised when tension cracks in the clay, extending downwards from the ground surface, reached the slip failure surface. He adjusted the volume V_4 in his calculations to allow for this. The eventual value derived for the ultimate uplift resistance load in soils possessing both cohesion and friction was:

$$R = G_o + \gamma g (B_2^3 K_1 - V_5) + c B_2 K_2' \quad \cdots\cdots (2.22)$$

where V_5 = the volume of the foundation below the ground surface,

$$K_1 = \pi [(a-1)(a^2 F_1' + a F_2' + ab F_3' + b F_4' + F_5') + b] \quad (2.23)$$

$$K_2' = \pi (a-1)(a F_6' + F_7') \quad \cdots\cdots (2.24)$$

$$a = x_o / B_2 \quad \cdots\cdots (2.25)$$

$$b = D_2 / B_2 \quad \cdots\cdots (2.26)$$

F_{1-7} are factors depending on θ_o and ϕ . x_o, B_2 and D_2 are shown in Fig. 2.6.

F. Meyerhof and Adams's (1968) Theory (Fig. 2.7.)

Meyerhof and Adams have developed an approximate general theory of uplift resistance in soil based on theoretical considerations and experimental observations. They propose a curved slip failure surface with the cohesive force and friction force at failure having assumed average inclinations with the vertical. However, because of the absence of a rigorous theory to predict the stresses on the curved rupture surface, Meyerhof and Adams proceed by assuming a vertical slip failure surface, as in the Shearing Theory (2.2.A). From the results of

trial calculations they assume:

$$\delta' = 2\phi/3 \qquad \cdots\cdots\cdots\cdots \quad (2.27)$$

where δ' is the inclination of the total passive earth pressure to the horizontal. For a circular anchor, Meyerhof and Adams derive the ultimate uplift resistance load:

$$R = G_o + G_6 + \pi c B D + \pi/2 \, S \gamma_g B D^2 K_u \tan\phi \quad \cdots \quad (2.28)$$

where G_6 is the weight of the soil in the breaking-out cylinder,

$$K_u = K_{pv} \tan\phi \qquad \cdots\cdots\cdots\cdots \quad (2.29)$$

where K_{pv} is the vertical component of the coefficient of passive earth pressure K_p and,

$$K_{pv} = K_p \tan\delta' \qquad \cdots\cdots\cdots\cdots \quad (2.30)$$

S is the shape factor governing the value of the passive earth pressure on a convex cylindrical wall:

$$S = 1 + m\, D/B \qquad \cdots\cdots\cdots\cdots \quad (2.31)$$

where m is a coefficient depending on ϕ .

2.3. Summary of Deep Anchor Theories.

A. Mariupol'skii's (1965) Theory (Fig. 2.8.)

Mariupol'skii proposes that when deep anchors reach the maximum or limiting uplift resistance load, a conical wedge, which has been formed immediately above the anchor, forces the soil above it apart and to the sides, allowing the anchor to move upwards under constant load. He found from tests that the apex angle 2α of the cone was approximately 90 degrees. Mariupol'skii derives an equation relating approximately the work done in withdrawing the circular anchor a height S' to the work done in expanding a cylindrical cavity of height S' from its original diameter B_o to B (Fig. 2.8.). He takes into account the "useless" work expended to overcome friction between the surface of the conical wedge and the soil which surrounds it,

and obtains:

$$R = G_o + P_p \qquad \ldots\ldots\ldots\ldots \quad (2.32)$$

where $$P_p = \frac{\sigma_r \pi (B^2 - B_o^2)}{4(1 - 0.5 \tan\phi)} \qquad \ldots\ldots\ldots \quad (2.33)$$

and σ_r is the radial pressure. He assumes that the soil is in plastic equilibrium within a certain radius and in elastic equilibrium beyond this radius. Mariupol'skii finds the value of the radius of the elasto-plastic boundary and the radial stresses on the boundary in terms of γ_g , ϕ , c , B and m_v (the coefficient of volume compressibility due to consolidation). Because of its size and complexity this expression is not included here.

B. Vesic's (1963 & 1965) Theory (Fig. 2.9.)

Vesic bases his solution for a deep circular anchor on the amount of pressure required to expand a point charge within an infinite, homogeneous, isotropic mass of soil. The point charge expands, forming an expanding spherical cavity, expanding to radius R_u (Fig. 2.9.). Around this cavity a compressible plastic zone is formed which compresses and displaces the elastic zone outside the plastic zone such that the volume increase at the limit of the plastic zone is equal to the volume increase of the original cavity. The radial stress at any point in the plastic zone is obtained by solving the differential equations of equilibrium and the equations for the conditions of rupture to obtain an expression for the radial stress σ_r at any radius r in terms of r , R_u , c , ϕ and the ultimate cavity pressure p_{uc} . The volume change of the cavity is equated to the volume change of the elastic plus plastic zones in an expression involving u_p , the radial movement at the elastic-plastic boundary (Fig. 2.9.). This expression is combined with the equation for radial stress at the boundary of the plastic zone, giving a relationship between the expanded cavity radius R_u and the radius of the plastic zone R_p in terms of the soil parameters E , ν , c , ϕ , q , (the effective

overburden pressure), Δ (the plastic volume change), and p_{uc}. Vesic uses the equilibrium of stress conditions at the plastic boundary to obtain, from his relationship between R_u and R_p, an expression for the ultimate cavity pressure:

$$p_{uc} = c\bar{F}_c + q\bar{F}_q \quad \cdots\cdots\cdots\cdots \quad (2.34)$$

where $$\bar{F}_q = \frac{3(1+\sin\phi)}{3-\sin\phi}\left[\frac{I_r}{(2(1+\frac{I_r\Delta}{2}))}\right]^{\frac{4\sin\phi}{3(1+\sin\phi)}} \quad \cdots \quad (2.35)$$

and $$\bar{F}_c = (\bar{F}_q - 1)\cot\phi \quad \cdots\cdots\cdots\cdots \quad (2.36)$$

$$I_r = \frac{E}{(1+\nu)(c+q\tan\phi)} \quad \cdots\cdots\cdots\cdots \quad (2.37)$$

and is called the soil rigidity index, being the ratio of the soil rigidity to its initial shear strength. When $\phi = 0$, $\bar{F}_q$ becomes equal to unity.

Ali (1968) adjusted the limiting cavity pressure to the ultimate uplift pressure above a deep anchor and assumed:

$$R = \frac{\pi B^2}{4} p_{uc} + c' \quad \cdots\cdots\cdots\cdots \quad (2.38)$$

where c' is the vertical component of the cohesive force acting along the surface of the conical wedge of soil which Ali assumed to be formed above the anchor.

$$c' = \frac{\pi B^2 c}{4} \quad \cdots\cdots\cdots\cdots \quad (2.39)$$

and $$R = \frac{\pi B^2}{4}\left[c(\bar{F}_c + 1) + q\bar{F}_q\right] \quad \cdots\cdots\cdots \quad (2.40)$$

C. Meyerhof and Adams's (1968) Theory (Fig. 2.7.)

For the case of a deep anchor, Meyerhof and Adams assume that the slip failure surface does not extend to the surface (Fig. 2.7.). The extent of local shear failure is included in the analysis by limiting the vertical height H of the slip failure surface and utilising the surcharge pressure above the level of the failure surface. From experimental observations, they predict the value of H as a function of ϕ and B. For deep circular anchors, the ultimate uplift resistance load is:

$$R = G_o + G_7 + \pi c B H + \pi/2 \, S \, \gamma_g \, B (2D-H) H K_u \tan\phi \quad \cdots (2.41)$$

where G_7 is the weight of the soil above the footing. Meyerhof and Adams argue that at a certain depth there will be a limiting value of R, equal to that given by the bearing capacity of the footing under downward load. Thus, for purely cohesive soils, the ultimate uplift resistance load becomes:

$$R = G_o + G_7 + \frac{\pi B^2 c N_u}{4} \quad \cdots\cdots\cdots\cdots (2.42)$$

The limiting value of N_u is taken as the theoretical bearing capacity coefficient N_{cqr} as defined by Meyerhof (1951) in an earlier paper. For a rough anchor at a D/B value of greater than 1.7 in a perfectly rigid soil, Meyerhof calculated that $N_{cqr} = 9.34$. By using the equation for the limiting internal pressure in a sphere, derived by Bishop, Hill and Mott (1945), Meyerhof calculated that the N_{cqr} value for a highly compressible material would be reduced to approximately 7.0.

2.4. Uni-axial Finite Element Analysis by Ashbee (1969).

For his finite element analysis, Ashbee adopts a uni-axial model which is defined as one where all movements and forces in the soil are in a direction parallel to the direction of the shaft movement. Therefore, the model assumes that there are no radial movements or forces in the soil. Since soils possessing friction experience an increase in shear strength in the vertical plane when there is an increase in radial pressure, the uni-axial model cannot be correctly applied to them. Similarly problems involving the non-vertical plastic flow of material cannot use this model.

The soil structure is divided into an equivalent link network, clearly differentiating between the effects of compression and tension and shear. Ashbee assumes a linear elastic non-strain hardening plastic soil stress-strain relationship with different elastic moduli for

tension and compression, and degradation of shear strength to a residual value after the maximum shear strength has been reached. An examination by Ashbee of the load-deflection relationship for a shafted anchor being pulled out of the soil showed that the yield points at the various parts of the soil network occurred at different load levels, e.g. at peak load only 20% of the possible soil pressures on some parts of the anchor slab were being utilised and almost half of the shaft-interface elements were in residual shear.

2.5. Discussion and Comparisons of Foregoing Procedures.

A. Introduction

For each shallow and deep anchor theory presented in sections 2.2 and 2.3, a corresponding expression for ultimate uplift resistance load was included. In the shallow anchor theories, this load was a function of the cohesion of the soil C , the internal angle of friction of the soil ϕ , the unit weight of the soil γ_g , the diameter of the anchor and its depth of placement. In the deep anchor theories, the elastic modulus E , the Poisson's ratio ν , the plastic volume change Δ and the compressibility m_v of the soil were also shown to affect the ultimate uplift resistance.

A direct comparison of the theories expressed in terms of the ultimate resistance load is complicated by the fact that in different theories, parameters such as soil cohesion and unit weight have varying importance in their effect on the ultimate uplift resistance. It is therefore difficult to decide the values of cohesion and unit weight which should be chosen for comparative purposes. This difficulty is overcome if the uplift resistance is expressed in dimensionless terms as a function of c , ϕ , γ_g etc. Chapter 3 presents a complete dimensional analysis of the problem, and demonstrates that for all the existing shallow anchor theories, the ultimate uplift resistance

can be expressed as the dimensionless ratio $P_u/\gamma_g D$. Soil cohesion can be expressed in a similar dimensionless group $c/\gamma_g D$ and the depth and breadth of the anchor related by the ratio D/B. The internal angle of friction ϕ is a dimensionless parameter. Table 2.1 gives equations of $P_u/\gamma_g D$ for the existing shallow anchor theories for soils possessing both friction and cohesion. Since the present investigation is concerned primarily with purely cohesive soils, equations for $P_u/\gamma_g D$ for soils where $\phi = 0$ are included.

In the existing deep anchor theories, the additional parameters taken into account in ultimate uplift resistance calculations can also be considered dimensionally. In Vesic's deep anchor theory, the rigidity index I_r is a dimensionless group. The plastic volume change expression Δ is a ratio in terms of the original volume and is dimensionless. In Mariupol'skii's deep anchor theory, the soil compressibility is expressed as a dimensionless group ω, a function of the inverse of compressibility. Meyerhof and Adams use the dimensionless uplift coefficient N_u in their deep anchor theory. Table 2.2 gives equations of $P_u/\gamma_g D$ for deep anchor theories for soils possessing both friction and cohesion and also for purely cohesive soils.

In order to obtain a general comparison between the various existing theories (both shallow and deep), the radius of the anchor shaft and the thickness of the slab are assumed to be negligibly small.

B. Discussion of Existing Shallow Anchor Theories

For soils possessing cohesion and friction. The Earth Cone Theory (2.2.A) may be discounted since it has no basis in soil mechanics theory, taking account of neither soil cohesion nor internal friction. The Earth Pressure Theory (2.2.A) is based on the earth pressure theory of soil mechanics, but, like the Earth Cone Theory, ignores both soil cohesion and internal friction.

The Shearing Theory (2.2.A) includes both cohesion and friction.

The main weakness of this theory with respect to soils which possess internal friction is the simplifying assumption of a vertical slip failure surface. The shear strength of a soil possessing internal friction increases with increasing normal stress (according to the Coulomb-Mohr equation). It may therefore be expected that the soil outside the region immediately above the anchor would possess less shear strength, thereby encouraging the formation of a non-vertical slip failure surface.

Balla (2.2.B.) was the first to select a curved slip failure surface and to analyse the shear stresses developed over it. However, the numerical values of the factors F_2 and F_3 in his paper appear to be incorrect, according to Vesic (1969). He also uses the vertical component of the shearing stress only and takes no account of the normal stresses which act on the slip failure surface. It has been shown by Sutherland (1965) that the slip failure surfaces calculated from Balla's proposals for very loose sand and very dense sand differ only fractionally, giving similar uplift resistance values.

Mariupol'skii (2.2.C) adopts an unconventional approach to the problem. He argues that, as the anchor moves upwards and compresses the soil, the frictional forces in the vertical cylinders of soil around the anchor increase and failure occurs in tension over a surface below this soil. Forms of the Earth Pressure Theory (2.2.A) and the Shearing Theory (2.2.A) are used to calculate the shear forces developed in the cylinders. However, the assumption that separation in tension occurs when the shear force equals $\sigma_r \tan \phi$ seems to be arbitrarily founded. The parameter n in Mariupol'skii's equation for ultimate uplift resistance appears to have been derived from experimental results. This reduces the theoretical value of the procedure.

Vesic's expanding sphere theory (2.2.D) assumes a circular slip failure surface similar to that assumed by Balla, but takes into account both the normal and shear components of stress on the slip

failure surface. The adaptation of the expanding cavity theory by Esquivel-Diaz (1967) to that of the pullcut problem by adding the pressure due to the weight of soil contained in the hemi-spherical cavity above the anchor cannot be applied accurately to problems with anchor depth to breadth ratios ($^{D}/_{B}$) of less than 0.5.

Matsuo (2.2.E), like Vesic, includes the normal stresses on the slip failure surface in his calculation of ultimate uplift resistance. Like Balla and Vesic, he encountered difficulties in trying to extend Kotter's equation, derived for the two-dimensional case, to the three dimensional case of axial symmetry. He was forced to extend his plane strain assumptions of stress distribution and slip failure surface shape to the circular anchor case.

Meyerhof and Adams (2.2.F) initially assume a curved slip failure surface. However, recognising the difficulty found by previous authors of analysing stresses on a curved surface in three dimensions, they finally assume the slip failure surface to be a cylinder (with diameter equal to the anchor), and introduce into the calculation certain factors which were derived from experimental observations. Their expression for ultimate uplift resistance is therefore partly theoretical and partly empirical.

Discussion of Existing Shallow Anchor Theories for Purely Cohesive Soils. When internal friction is removed from the calculation of ultimate uplift resistance, many of the shallow anchor theories are considerably simplified.

The Shearing theory, Mariupol'skii's theory and Meyerhof and Adams's theory all reduce to the same expression. In the latter two theories, the important assumptions which differentiated them were made only for materials possessing internal friction and do not affect the calculation for purely cohesive soils. These three theories will be referred to as the Shearing theory when dealing with purely cohesive

soils.

When $\phi = 0$, the logarithmic spiral section of the slip failure surface (eq.2.20) assumed by Matsuo becomes circular. However, whereas both Balla and Vesic assume that the circular slip failure surface extends to ground level, Matsuo bases his theory on the assumption that the circular slip failure surface becomes a plane slip failure surface before reaching this level (Fig.2.6.).

C. Comparison of Existing Shallow Anchor Theories for Purely Cohesive Soils

Fig. 2.10 shows the shallow anchor theories (excluding the Earth Cone and Earth Pressure theories) drawn on a dimensionless graph of $P_u/\gamma_g D$ v D/B for two typical values of $c/\gamma_g D$. (Chapter 3 discusses typical values of $c/\gamma_g D$ for prototype and model anchors and soils). The internal angle of friction is not included since only purely cohesive soils are being considered. These theories give well-conditioned curves for $P_u/\gamma_g D$ v D/B for fixed values of $c/\gamma_g D$. The value of $P_u/\gamma_g D$ must be treated in the limit as $D/B \to 0$ since when $D/B = 0$ then $D = 0$, and $P_u/\gamma_g D$ becomes meaningless. Only the Shearing theory gives a linear plot of $P_u/\gamma_g D$ v D/B. The other theories give concave upwards curves, because of the non-linear relationship between depth and ultimate uplift resistance inherent in the assumption of a curved slip failure surface. However, the values of $P_u/\gamma_g D$ for all of the theories are linearly related to the values of $c/\gamma_g D$ for a constant D/B value (Fig. 2.11), since the form of all of the theories considered is:

$$P_u/\gamma_g D = X + (c/\gamma_g D)\, Y \qquad \cdots\cdots \quad (2.43)$$

where X and Y are constants for fixed D/B values.

Fig. 2.10 illustrates that Balla's theory gives considerably higher values for $P_u/\gamma_g D$ than the other theories, whose values are in relatively good agreement. These higher values appear to be due to his failure to include the normal reaction forces along the slip

failure surface and his incorrect values for factor F_2 . The small difference between Vesic's and Matsuo's values of $p_u/\gamma_g D$ result from their slightly different assumptions of slip failure surface. As D/B increases, these values of $p_u/\gamma_g D$ start to diverge from those predicted by the Shearing theory. However, as will be seen from the discussion of deep anchor procedures and from experimental results obtained by the author (chapters 4 and 5), values of D/B above approximately 2.0 cannot be considered to be strictly in the shallow range.

D. Discussion of Existing Deep Anchor Theories and Ashbee's Finite Element Analysis

Mariupol'skii (2.3.A) equates the work involved in lifting a deep anchor by a certain amount to the work required to move the soil enough to enable the anchor to pass through. His assumptions of equilibrium and the continuity of the elastic and plastic states on the elastic-plastic boundary enable him to derive expressions for the radial stress on that boundary and eventually to calculate the ultimate uplift resistance of the soil. However, his method for obtaining these expressions is not clearly demonstrated and he appears to include in them parameters not previously mentioned in his paper. One of these parameters is the volume compressibility of the soil. No explanation for the inclusion of this parameter is given, although the assumed lateral expansion of the soil must depend to an extent on this compressibility. The volume compressibility factor implies consideration of the long term behaviour of clays under load. Although Mariupol'skii assumes the problem to be elastic-plastic, the expressions derived for radial stress and ultimate uplift resistance in the soil contain terms for neither the modulus of elasticity nor Poisson's ratio.

Vesic's (2.3.B) solution for a sphere expanding under pressure from an explosive charge assumes that at ultimate cavity pressure p_{uc} a plastic zone around the sphere is formed and a volume change takes

place in this zone along with a volume change in the elastic region outside the zone such that the pressure remains at p_{uc} . The ultimate radius of the cavity will depend on the magnitude of the explosive charge. When a deep anchor is substituted for an expanding sphere, the radius of the anchor becomes the ultimate cavity radius. p_{uc} is then the uplift pressure at which sufficient volume change takes place in the plastic and elastic zones to allow the anchor to move, with no subsequent increase in p_{uc} . If the uplift pressure is below p_{uc} the zones will not expand enough to let the anchor through and the pushout or pullout load can continue to increase until p_{uc} is reached.

Vesic's expanding sphere solution for a $\phi = 0$ material (with no volume change in the plastic region) agrees with that obtained by Biship, Hill and Mott (1945) for the indentation of a frictionless material by a spherical indenting tool. Vesic subsequently improves this solution by making an allowance for the effect of volume change in the plastic zone. The rigidity index:

$$I_r = \frac{E}{(1+\nu)c} \qquad \cdots\cdots\cdots \quad (2.37a)$$

for purely cohesive soils is fundamentally a measure of the amount of strain which can be sustained by a clay before the onset of plasticity. Vesic tabulates values which he considers to be typical of I_r for clays, ranging from $I_r = 20$ for soft clays to $I_r = 500$ for stiff clays. These values of rigidity index imply that soft clays may deform as much as twenty five times more than stiff clays before plastic yielding occurs. However, with many types of soft clay, e.g. sensitive clays, plastic yielding commences at small strains, and the assumption of a general relationship between soil strength and rigidity index does not appear to be valid.

The uplift resistance problem for a deep anchor would not appear to be completely analagous to the expanding sphere problem. In the author's opinion, it would be better compared to the problem of a

charge expanding a hemisphere with a rigid boundary as its diameter, this boundary being equivalent to the circular anchor plate (see Fig. 2.12.). However, a hemisphere lacks the complete symmetry of a sphere and a preliminary investigation by the author has shown that no rigorous method of analysis of this problem at present exists.

It is difficult to compare the expression which Mariupol'skii obtains for the expansion of a cylindrical cavity with Vesic's expression for an expanding sphere, since their final equations for ultimate uplift resistance pressure are functions of different variables. However, Bishop et.al. (1945) compared theoretically the expansion of a spherical cavity to the expansion of a cylindrical cavity in a frictionless metal (neglecting volume changes in the plastic zone) and found the spherical expansion pressure to be approximately 15% greater than the cylindrical expansion pressure.

Meyerhof and Adams (2.3.C) employ experimental observations to evaluate certain factors in their equation for ultimate uplift resistance at great depths. The height wherein local failure occurs is determined from the observed extent of the slip failure surface. For the limiting value of ultimate uplift resistance they use Meyerhof's equation for bearing capacity at great depth. In this case they are assuming the soil to be an infinite mass (an assumption made by both Mariupol'skii and Vesic in their deep anchor theories).

In Ashbee's Finite Element analysis, the approximation used for the shear failure envelope of the soil for the model appears to be reasonable. The analysis shows that, for a general soil with friction and cohesion, peak stresses at various points in the soil mass are not reached simultaneously. This is an important observation which none of the previous theories (neither shallow nor deep) have considered. However, Ashbee's assumption of a uni-axial model, and the corresponding specification of stiffness coefficients, must reduce considerably

the validity of the results of this analysis.

E. Comparison of Existing Deep Anchor Theories

Fig. 2.13 illustrates the results of the three deep anchor theories which have been discussed. Since the expressions for ultimate uplift resistance are independent of depth, $p_u/\gamma_g D$ is plotted against $c/\gamma_g D$. For Vesic's theory, two values of rigidity index I_r and plastic volumetric strain Δ are considered. The curve for $I_r = 500$ and $\Delta = 0{\cdot}0$ represents a clay which will fail at a small strain and which shows no plastic volume change during the uplift resistance test. The curve for $I_r = 20$ and $\Delta = 0{\cdot}02$ represents a clay which can sustain a large amount of strain before failure and in which some plastic volume change will occur during the test. For Meyerhof and Adams's theory, two values of the ultimate bearing capacity coefficient N_u for deep anchors are considered. The curve for $N_u = 9{\cdot}34$ represents a rigid clay with no compressibility, and the curve for $N_u = 7{\cdot}0$ represents a compressible clay. For Mariupol'skii's theory, two values of ω, the function of volume compressibility due to consolidation, are considered. The curve for $\omega = 200$ represents a clay with small volume compressibility and the curve for $\omega = 25$ represents a clay with a high volume compressibility.

The values of $p_u/\gamma_g D$ in both Vesic's and Meyerhof and Adams's theories are linearly related to the values of $c/\gamma_g D$ since the theories may be expressed in the form:

$$p_u/\gamma_g D = X + (c/\gamma_g D)Y \qquad \cdots\cdots (2.43)$$

where X and Y are constants for fixed values of I_r, Δ and N_u. Mariupol'skii's theory, however, shows a concave downwards relationship, implying that as the shear strength of the soil increases, a smaller corresponding increase in the ultimate uplift resistance pressure will occur.

Although I_r, Δ, N_u and ω are defined in different ways,

Fig. 2.13 illustrates that the values of $p_u/\gamma_g D$ in each theory for the incompressible clays with small strain to failure are considerably higher, over the $c/\gamma_g D$ range considered, than those for the compressible clays with large strain to failure. This is an expected result, since the theories are based on the concept of the movement of the elastic-plastic boundary to allow movement of the anchor. If the clay is almost incompressible, then the radius of the elastic-plastic boundary must be large before anchor movement can occur. The ultimate uplift resistance will increase correspondingly, since a larger volume of clay is required to be compressed.

For the rigid, incompressible clay, Vesic's and Meyerhof and Adams's solutions give similar results. For the very compressible clays, Vesic's values are lower than those of Meyerhof and Adams. There are two possible reasons for this in the author's opinion. Firstly, Vesic takes into account plastic volume change which will tend to increase the value of compressibility of the clay. Secondly, it is possible that the compressibility of Vesic's material with a rigidity index of 20 is less than that of Meyerhof and Adams's material with a bearing capacity coefficient of 7.0, since high compressibility is not strictly defined.

For both incompressible and compressible clays, Mariupol'skii's solution gives values for $p_u/\gamma_g D$ below those of Vesic and Meyerhof and Adams. Because of the lack of explanation of the way in which Mariupol'skii derived his expression for ultimate uplift resistance, it is difficult to explain this difference in the results.

Fig. 2.14 illustrates the solutions of Vesic's deep and shallow anchor theories compared for two values of $c/\gamma_g D$. Vesic's solutions are chosen as being typical of those for the theories which have been discussed. The comparison shows that the theories predict a deep anchor failure coming into effect between $D/B = 1{\cdot}25$ and $D/B = 2{\cdot}25$. Since the uplift resistance mechanism of the soil for anchors at these

shallow depths must be influenced by the proximity of the anchor to the ground surface, this result does not accord with the assumptions of no surface effect in existing deep anchor theories. However, the results of model tests on deep anchors, performed by the author (chapter 4), demonstrate good agreement with Vesic's deep anchor predictions, whereas the values of ultimate uplift resistance obtained by the author in shallow anchor model tests are considerably lower than those predicted by Vesic. The model tests also showed that a large intermediate range of depths exists where both shallow and deep effects occur.

2.6. Conclusions about Foregoing Procedures

A. Shallow Anchor Theories

For the existing shallow anchor theories which have been considered, as applied to purely cohesive soils, and within their limitations regarding soil behaviour, the theories of Vesic, Matsuo and Meyerhof and Adams appear to have a sound formulation and give reasonably similar solutions for ultimate uplift resistance in the range $D/B = 0$ to $D/B = 2{\cdot}0$. When the soil has no friction, Mariupol'skii's less conventional assumptions of failure mechanism do not come into effect and his solution becomes equivalent to that of Meyerhof and Adams and the Shearing theory. Due to some apparently incorrect assumptions and calculations, Balla's solution gives values of uplift resistance which are considerably higher than those of the other theories.

The inherent weakness of all of the existing shallow anchor theories is their assumption that no movement occurs before failure, which means that they provide no way of predicting the load-displacement relationship of the soil under uplift conditions. Also, no account is taken of tension and the resulting cracking in the soil, and the alteration of the physical dimensions of the problem produced by movements of the anchor. In addition, as Ashbee's analysis demonstrated, movements of the anchor may mean that some of the soil mass will have

passed its value of peak shear stress and be in a residual stress state before the ultimate uplift resistance is reached. This will lessen the theoretical ultimate uplift resistance.

B. Deep Anchor Theories

Vesic and Meyerhof and Adams employ different approaches to the problem but obtain similar solutions. Unlike the shallow anchor theories, both of these theories make allowance for the elasticity and compressibility of the soil. Meyerhof and Adams's equation for the limiting value of ultimate uplift resistance of deep anchors and Vesic's adaptation of the expanding cavity theory are identical to Meyerhof's equation for the ultimate bearing capacity of deep foundations and Bishop, Hill and Mott's equation for indentation respectively. Since theoretical values of bearing capacity and indentation pressure predicted by the latter two equations have shown good agreement with experimental results, it is reasonable to assume that Meyerhof and Adams's and Vesic's deep anchor theories will provide a reasonably accurate prediction of the ultimate uplift resistance values of deep anchors in an ideal, homogeneous, isotropic clay.

2.7. Tests Performed in Purely Cohesive Soils by Previous Authors

A study of the literature reveals that a large range of uplift resistance tests have been performed by previous authors, mostly in sand or in sandy clay. There has been comparatively little model testing in purely cohesive soils and only a few of the results which have been published provide enough information about soil properties and anchor dimensions to enable a comparison between them to be made. All of these tests were laboratory model tests.

Ali (1968) performed a series of model pullout tests on a bentonite-water clay mixture of very low shear strength. Suction below the anchor caused an increase in the values of uplift resistance load of over 50% in his shallow anchor tests and of about 20% in his deep anchor

tests, and the results shown in Fig. 2.15 are for values of ultimate uplift resistance without suction. Ali estimated the suctional effect by performing some pullout tests with the anchor plate on the surface of the clay.

Bhatnagar (1969), using the same pullout apparatus as Ali, performed a series of tests on a firm silty clay, which possessed negligible frictional properties. His tests were free from suctional effects, since suction below the anchor plate is normally encountered only in soft clays with a high moisture content.

Adams and Hayes (1967) conducted several series of pullout tests on brick clay and Niagara clay. Only the results of tests in brick clay (a firm clay with relatively low moisture content) are shown in Fig. 2.15 since the results of their tests in Niagara clay included suctional effects, no accurate estimation of which was published by them.

Fig. 2.15 shows the results obtained by these three authors, plotted on a graph of $\bar{F}_u \vee D/B$. $\bar{F}_u$ is a dimensionless parameter which is the value of the ultimate uplift resistance of a soil divided by its shear strength and adjusted for the effect of soil weight on the anchor. Section 3.5 of chapter 3 describes the derivation of $\bar{F}_u$. Fig. 2.15 includes also a curve of $\bar{F}_u \vee D/B$ for Vesic's shallow and deep anchor theories. The significant difference between the values of ultimate uplift resistance obtained in the three series of model tests described above and also the considerable divergence between the model test results and the theoretical predictions of Vesic prompted the author to perform a series of model tests (described in chapter 4) and to develop a finite element analysis of the problem (described in chapter 5), in order to examine the problem in greater detail. However, before the author's model tests and finite element analysis are described, a dimensional analysis of the problem will be outlined in the next chapter.

TABLE 2.1. SHALLOW ANCHOR THEORIES

THEORY	FIG.	$P_u/\gamma_g D$: soils with both friction and cohesion	$P_u/\gamma_g D$: purely cohesive soils $\phi = 0$
Earth Cone	2.1	$1 + 2(D/B)\tan\alpha + 4/3\,(D/B)^2\tan^2\alpha$	$1 + 2(D/B)\tan\alpha + 4/3\,(D/B)^2\tan^2\alpha$
Earth Pressure	2.2	$1 + 2K_o(D/B)\tan\delta$	1
Shearing	2.2	$1 + 2K(D/B)\tan\phi + 4(C/\gamma_g B)$	$1 + 4(C/\gamma_g B)$
Balla	2.3	$(4D^2/\pi B^2)[F_1 + (C/\gamma_g D)F_2 + F_3]$	$(4D^2/\pi B^2)[F_1 + (C/\gamma_g D)F_2]$
Mariupol'skii	2.4	$[1 + 2K_o(D/B)\tan\phi + 4(C/\gamma_g B)]/[1 - 2n(D/B)]$	$1 + 4(C/\gamma_g B)$
Vesic	2.5	$(C/\gamma_g D)F_c + F_q + B/3D$	$(C/\gamma_g D)F_c + F_q + B/3D$
Matsuo	2.6	$(4/\pi B^2 D)[B_2^3 K_1 + cB_2^2 f(K_2')/(\gamma_g)]$	$(4/\pi B^2 D)[B_2^3 K_1 + cB_2^2 K_2'/(\gamma_g)]$
Meyerhof and Adams	2.7	$1 + 2SK_u(D/B)\tan\phi + 4(C/\gamma_g B)$	$1 + 4(C/\gamma_g B)$

Note: In order to obtain a general comparison between the various theories, the radius of the anchor shaft and the thickness of the anchor plate are assumed to be negligibly small.

TABLE 2.2. DEEP ANCHOR THEORIES

THEORY	FIG.	$p_u/\gamma_g D$: soils with both friction and cohesion	$p_u/\gamma_g D$: purely cohesive soils $\phi = 0$
Mariupol'skii	2.8	$\sigma_r / [\gamma_g D (1 - 0.5 \tan \phi)]$	$\sigma_r /(\gamma_g D)$
Vesic	2.9	$(c/\gamma_g D)(\bar{F}_c + 1) + (q/\gamma_g D)\bar{F}_q$	$(c/\gamma_g D)(\bar{F}_c + 1) + (q/\gamma_g D)\bar{F}_q$
Meyerhof and Adams	2.7	$1 + (4/\gamma_g BD)[cH + (\gamma_g/2) SH(2D-H) K_u \tan \phi]$	$1 + 4cH/(\gamma_g BD)$
	/	$(c/\gamma_g D) N_c + N_q + 1$ (ultimate) Note: N_c and N_q are bearing capacity factors, Meyerhof (1951)	$(c/\gamma_g D) N_u + 1$ (ultimate)

Note: In order to obtain a general comparison between the various theories, the radius of the anchor shaft and the thickness of the anchor plate are assumed to be negligibly small.

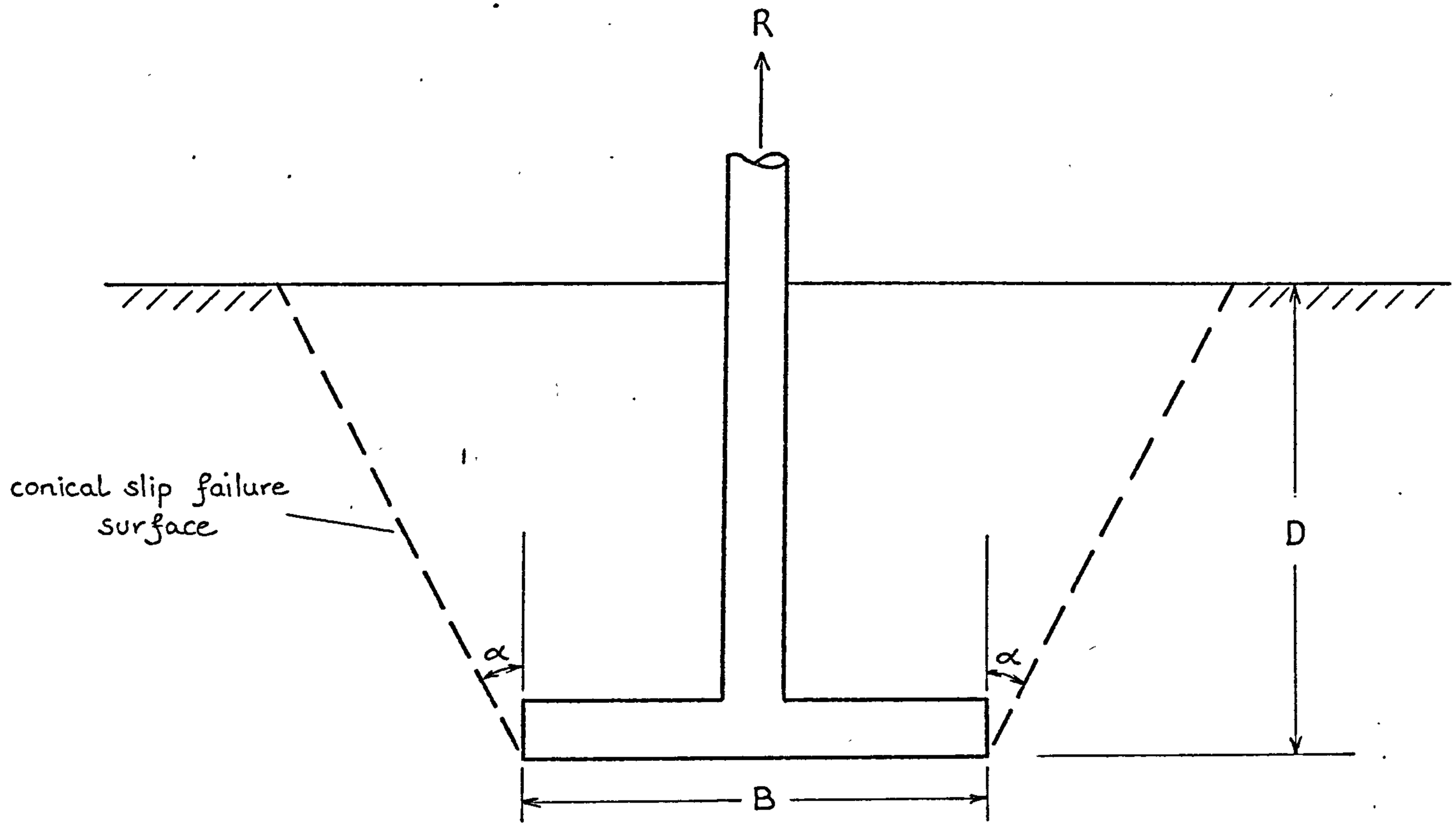

FIG. 2.1. EARTH CONE THEORY: CONICAL SLIP FAILURE SURFACE

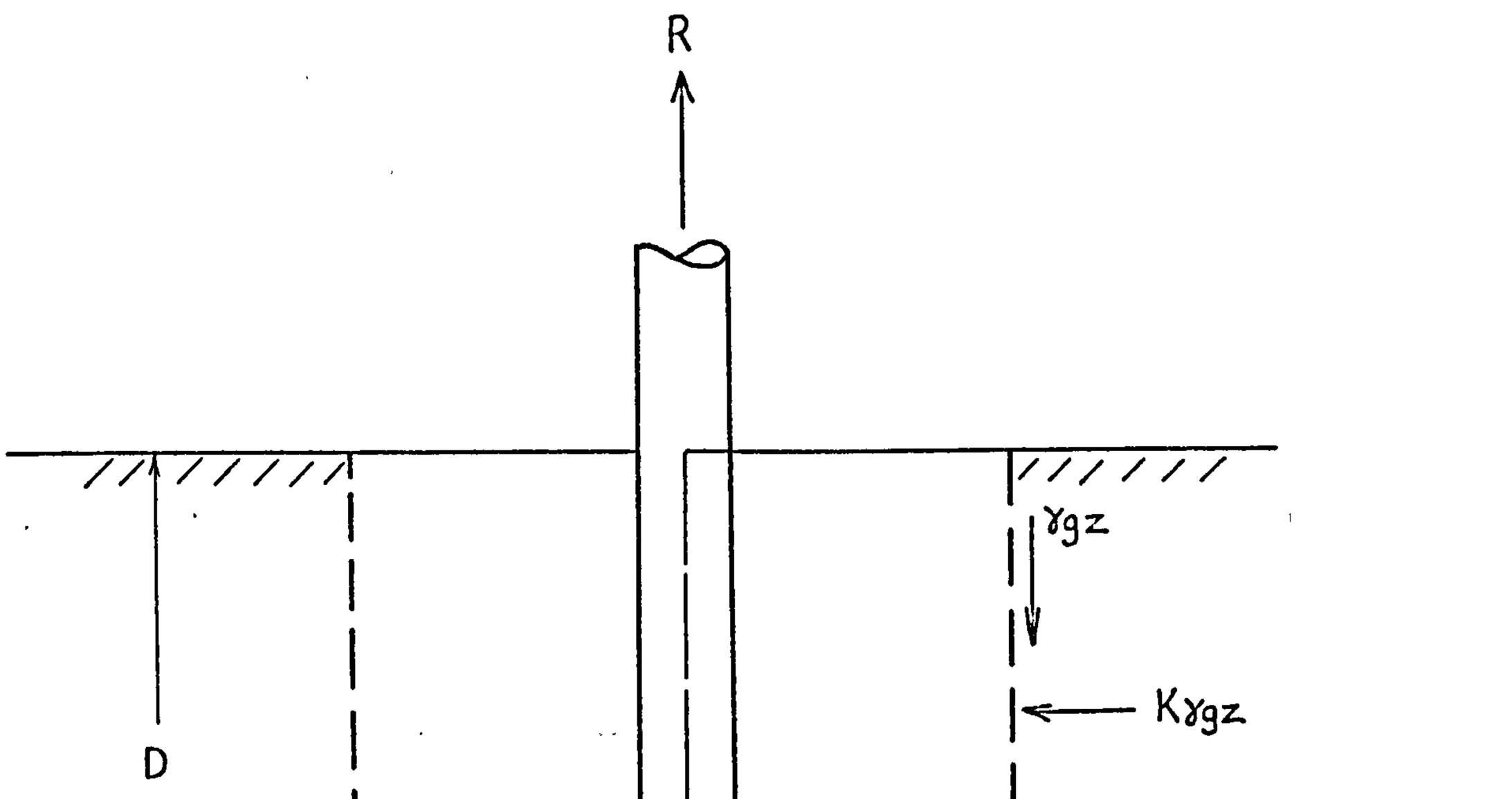

FIG. 2.2. EARTH PRESSURE AND SHEARING THEORIES:

CYLINDRICAL SLIP FAILURE SURFACE

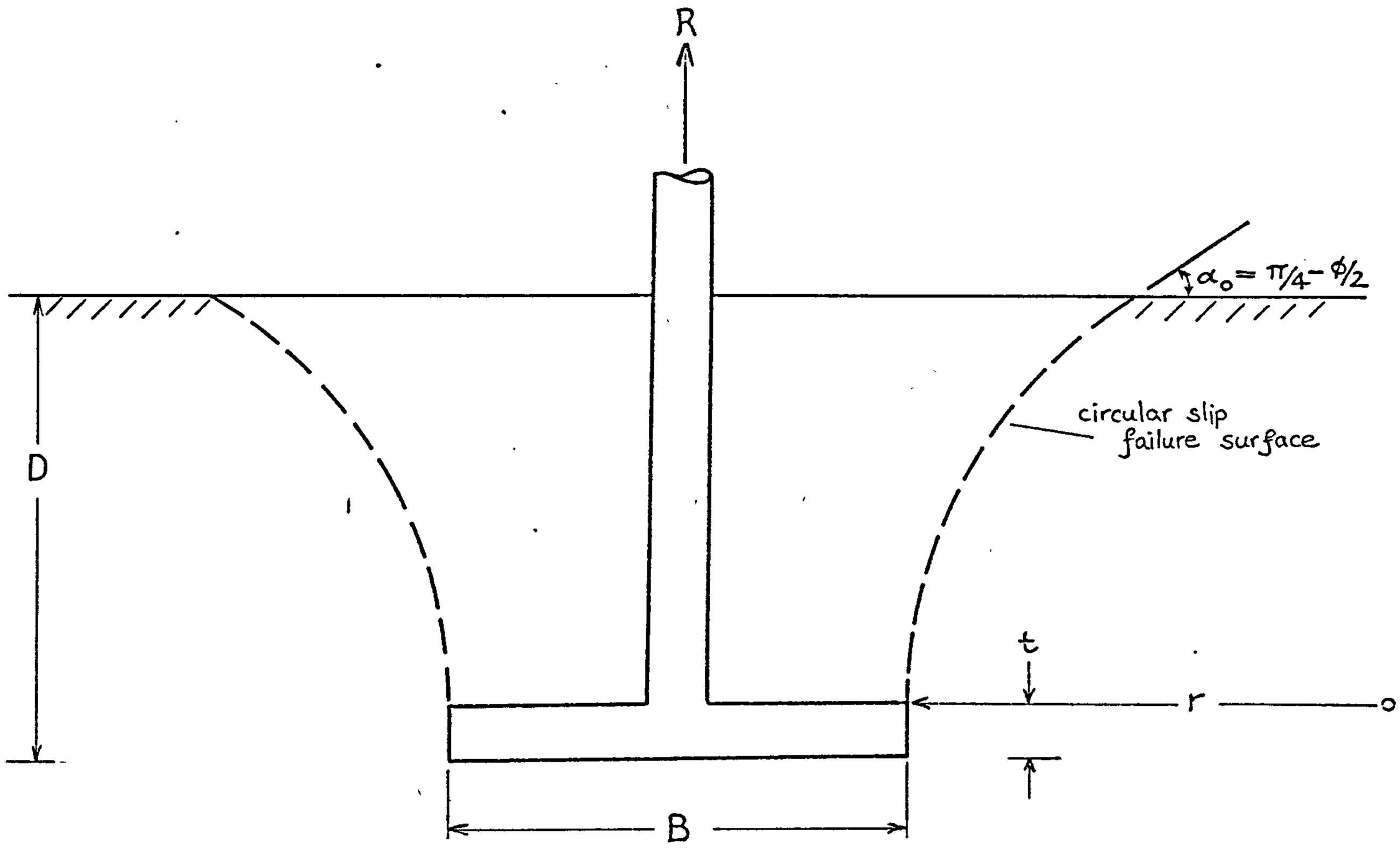

FIG. 2.3. BALLA'S THEORY: CIRCULAR SLIP FAILURE SURFACE

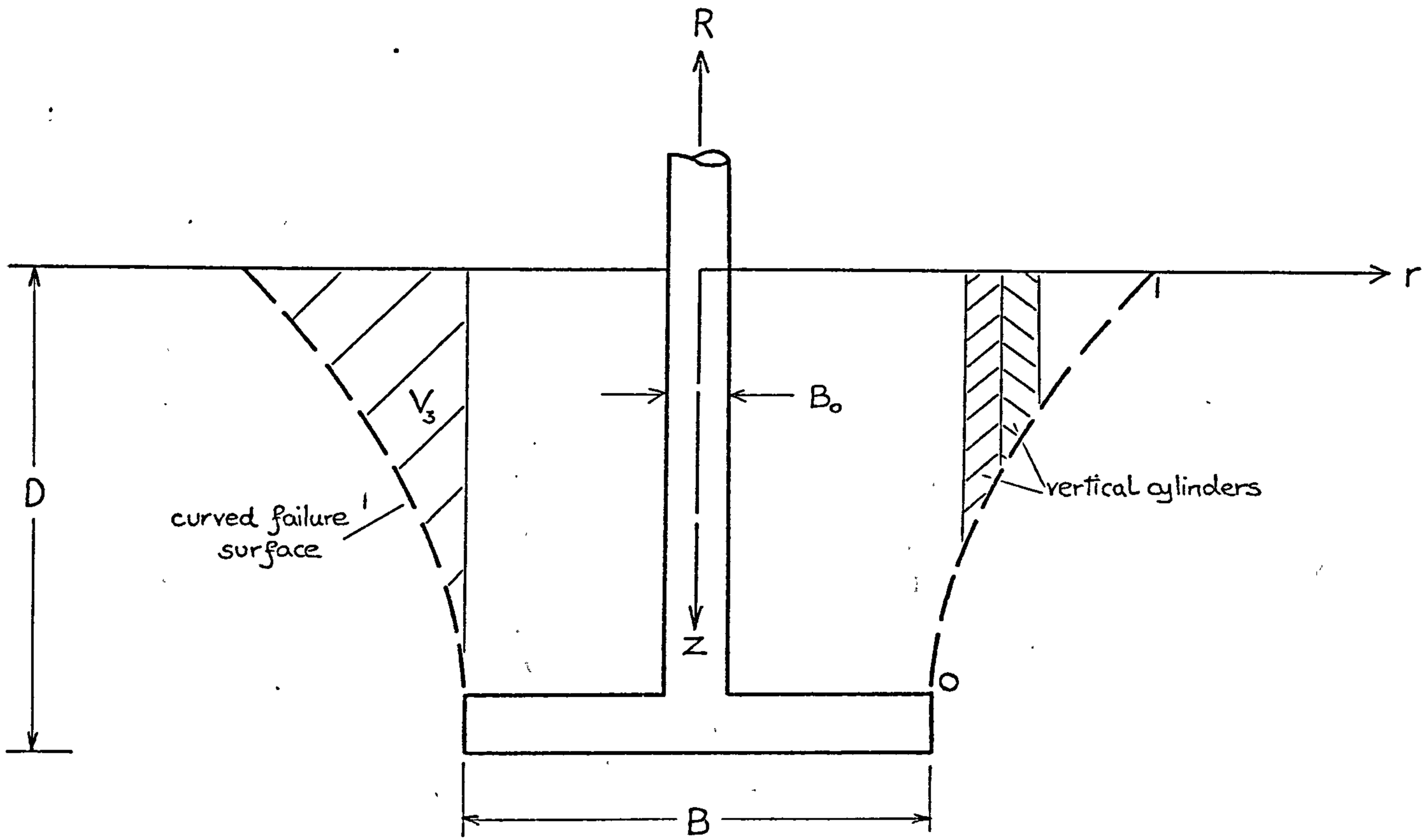

FIG. 2.4. MARIUPOL'SKII'S THEORY: CURVED FAILURE SURFACE

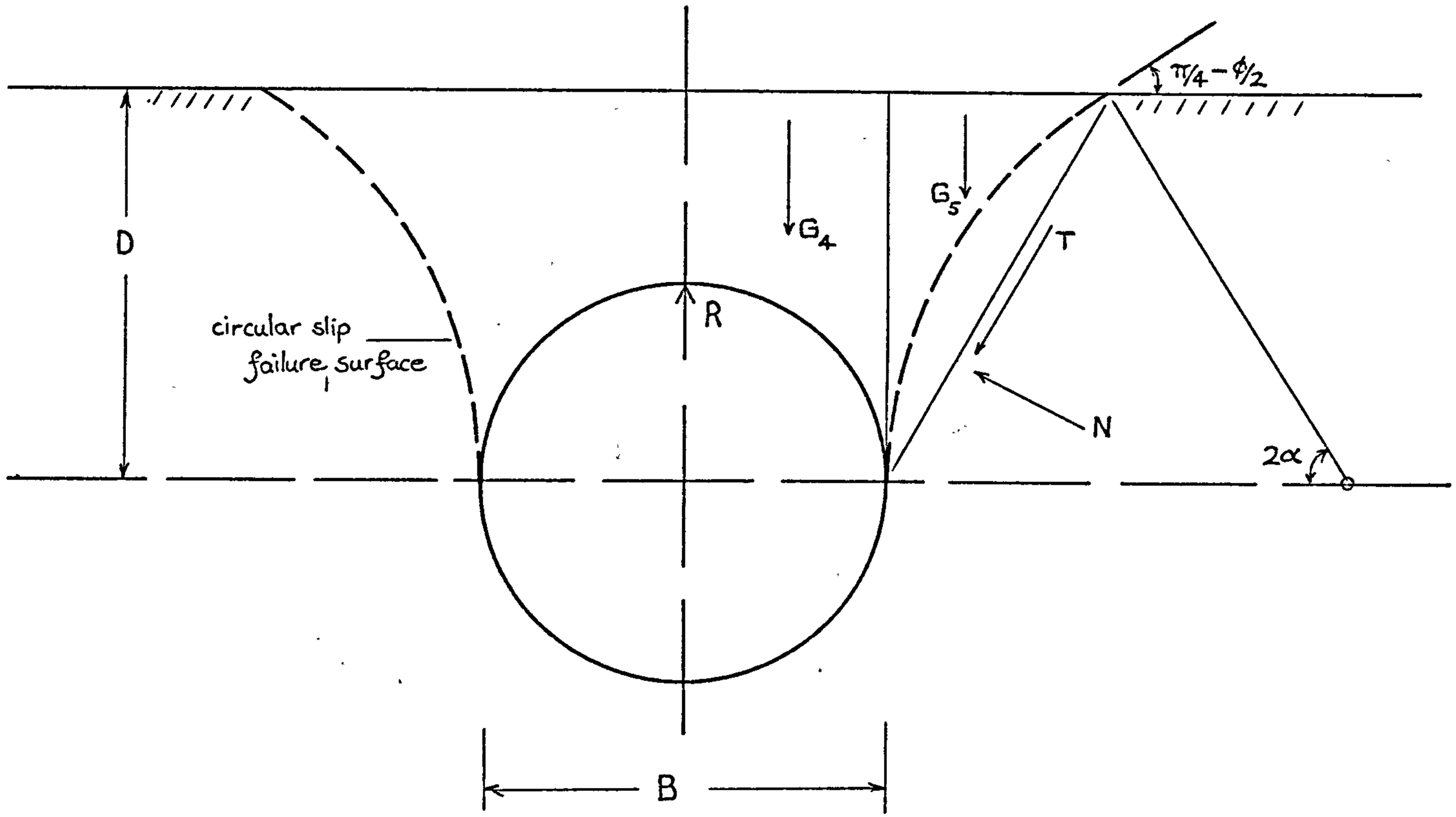

FIG. 2.5. VESIC'S THEORY: EXPANSION OF A SPHERICAL CAVITY CLOSE TO THE GROUND SURFACE: CIRCULAR SLIP FAILURE SURFACE

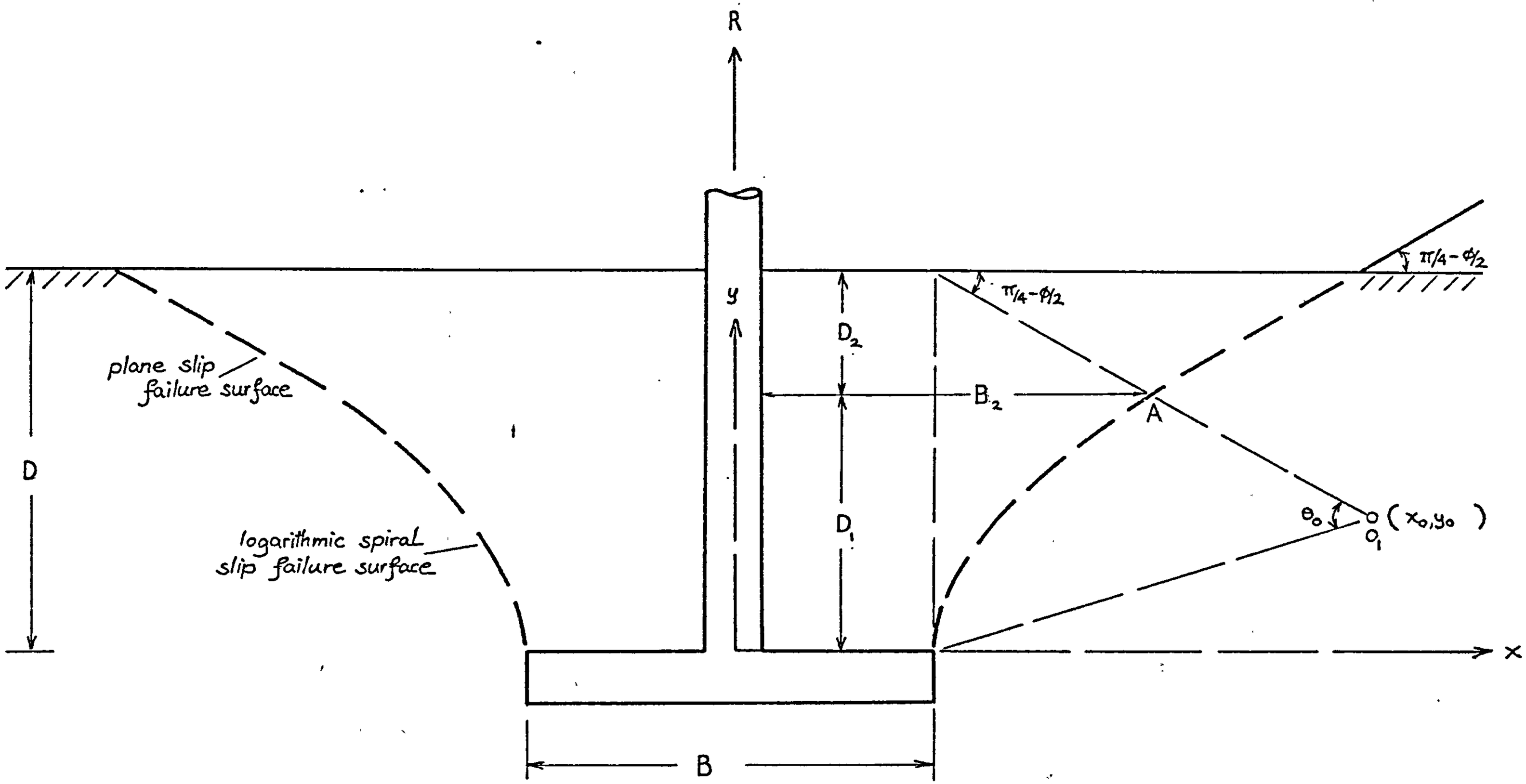

FIG. 2.6. MATSUO'S THEORY: LOGARITHMIC SPIRAL AND PLANE SLIP FAILURE SURFACES

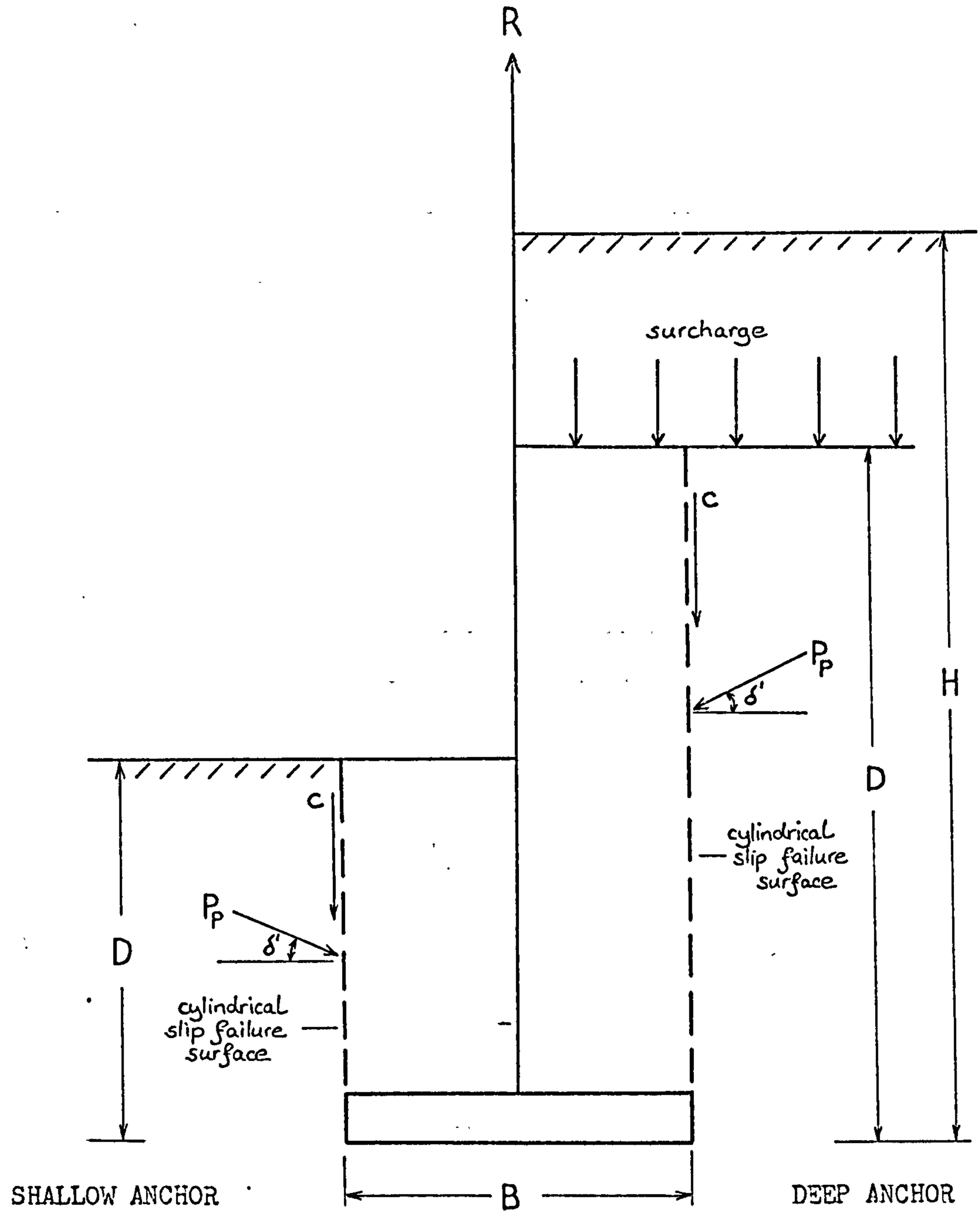

FIG. 2.7. MEYERHOF AND ADAMS'S THEORY FOR SHALLOW AND DEEP ANALYSES: CYLINDRICAL SLIP FAILURE SURFACES

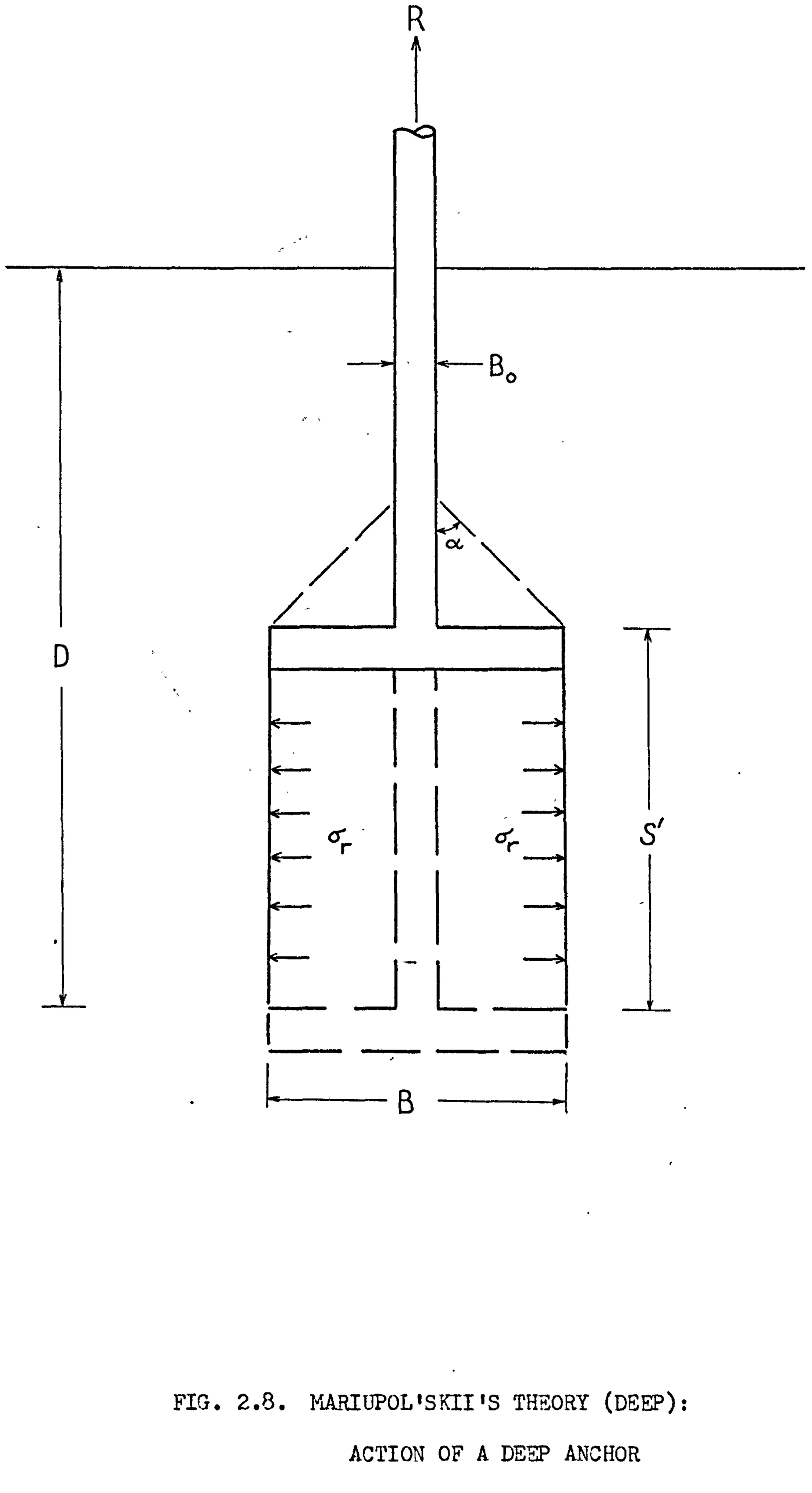

FIG. 2.8. MARIUPOL'SKII'S THEORY (DEEP):

ACTION OF A DEEP ANCHOR

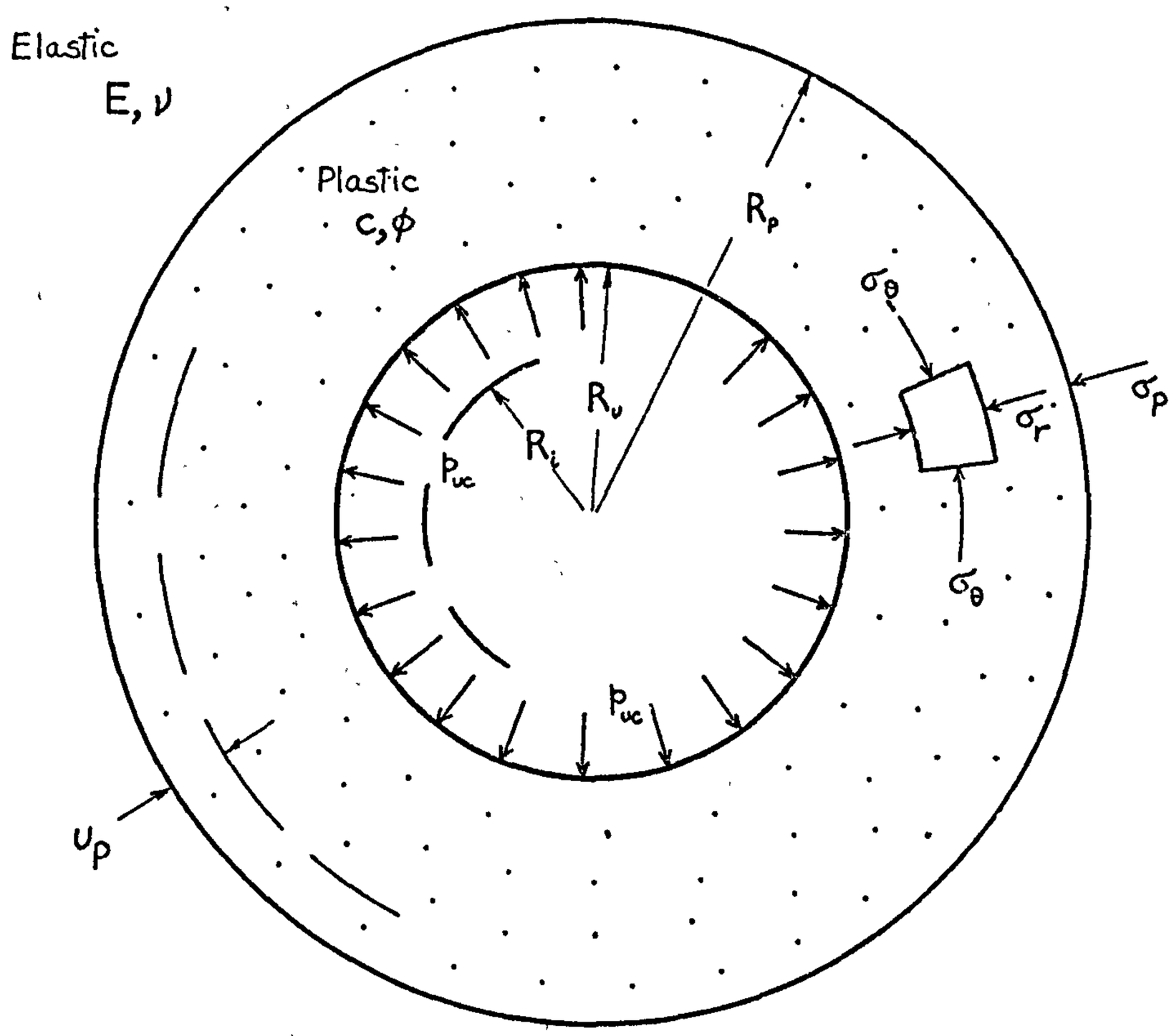

FIG. 2.9. VESIC'S THEORY: EXPANSION OF A DEEP SPHERICAL CAVITY

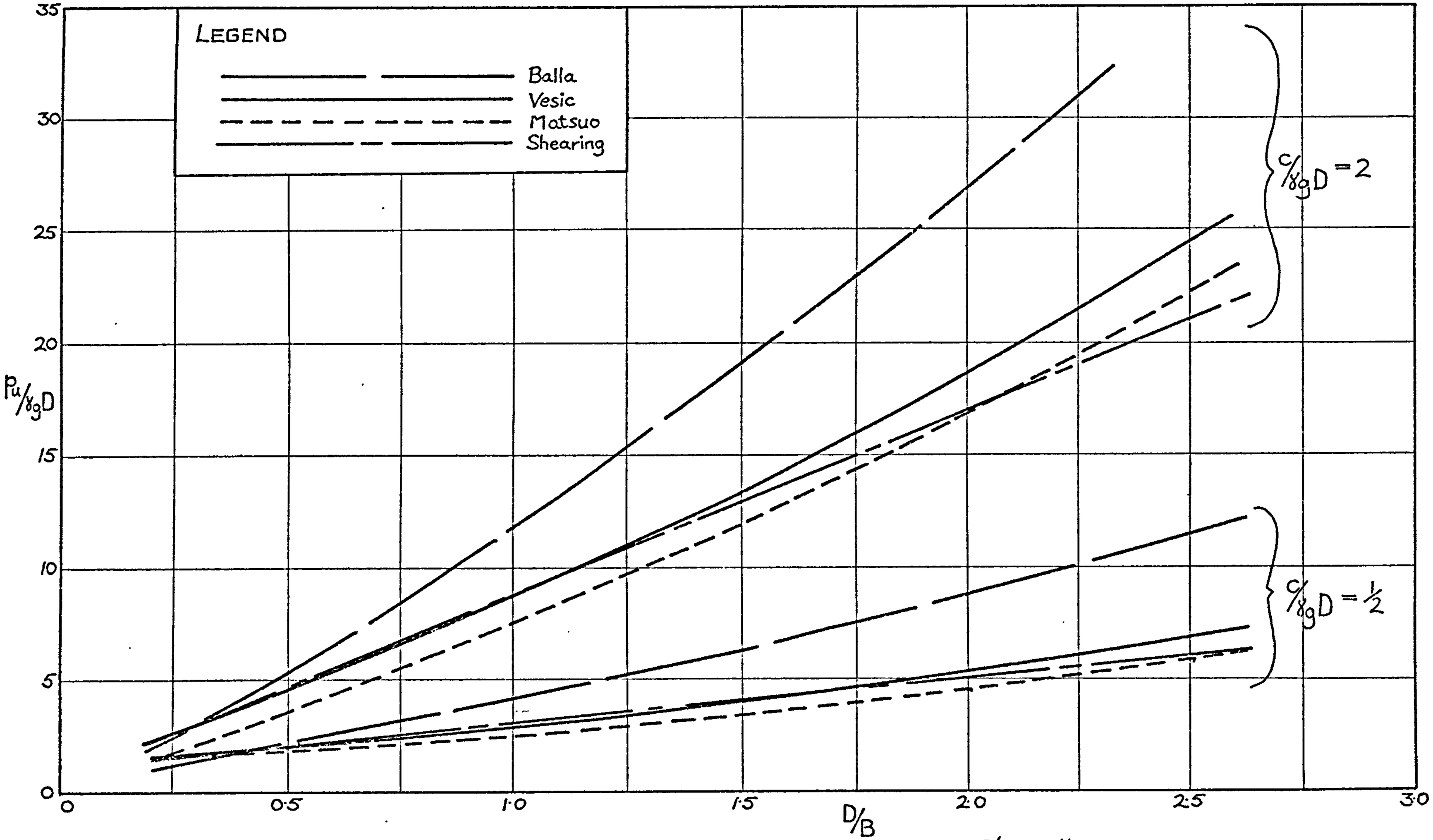

FIG. 2.10. COMPARISON OF THEORIES: SHALLOW ANCHORS: $c/\gamma_g D = \frac{1}{2}$ and 2

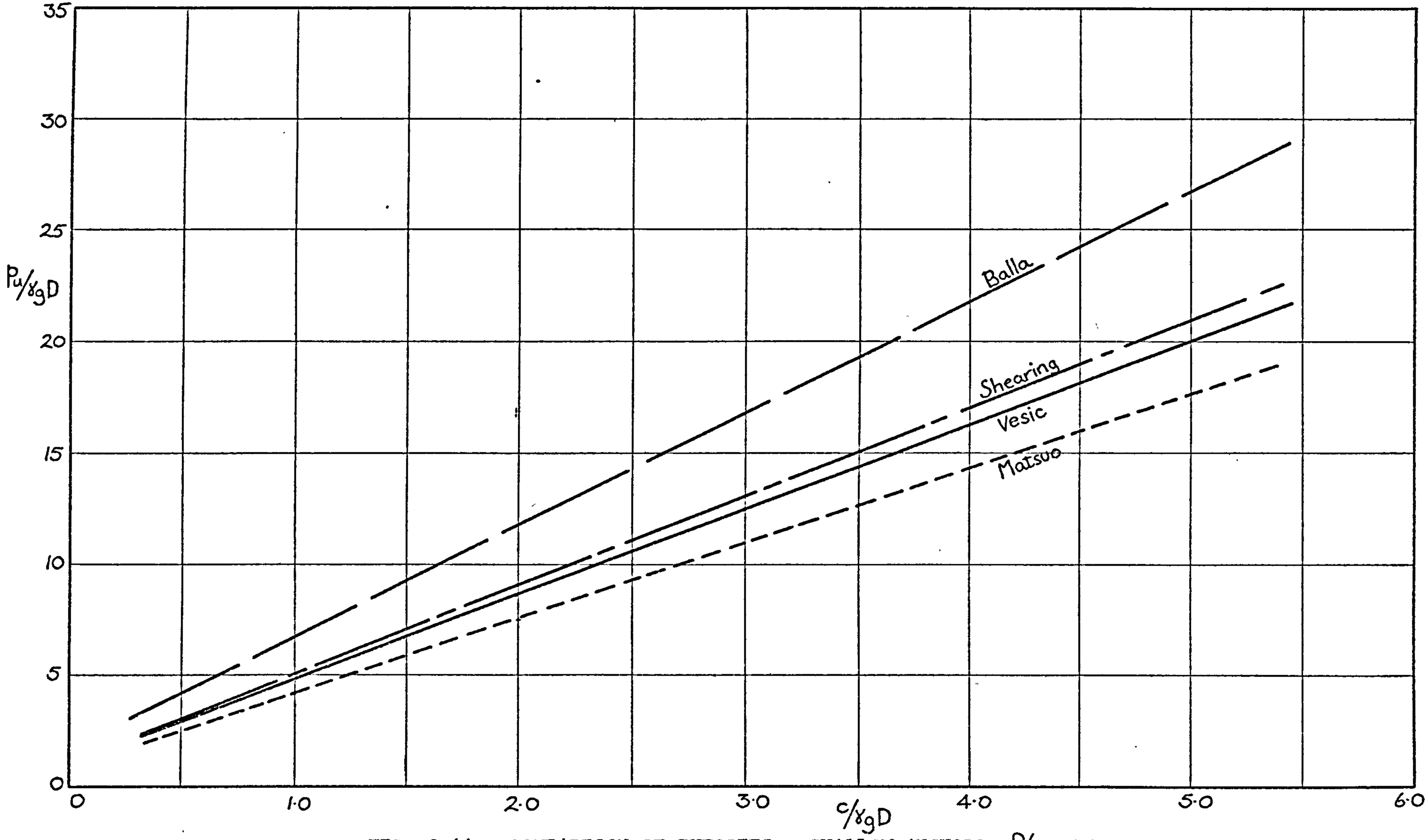

FIG. 2.11. COMPARISON OF THEORIES: SHALLOW ANCHORS: $D/B = 1{\cdot}0$

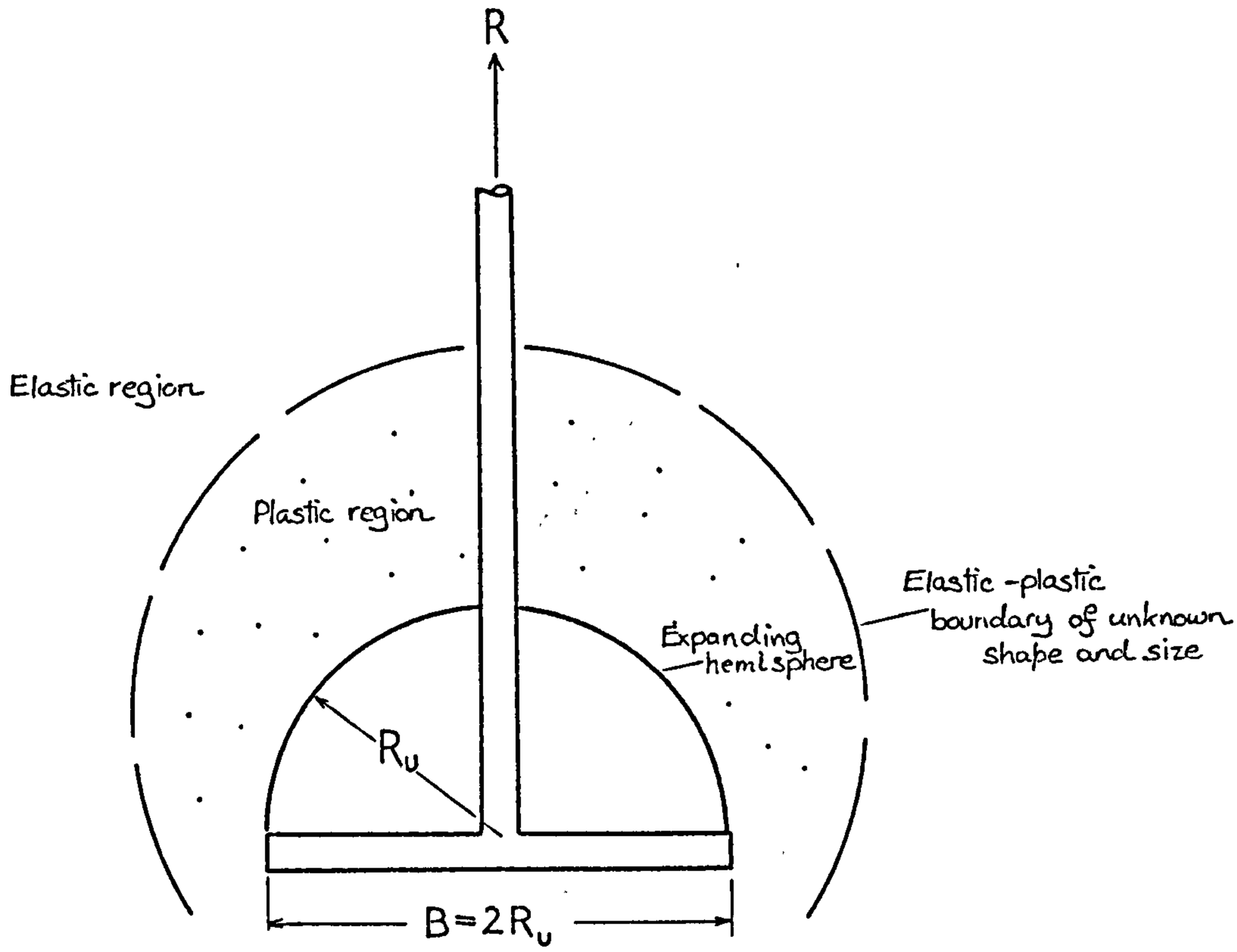

FIG. 2.12. EXPANSION OF A HEMISPHERICAL CAVITY

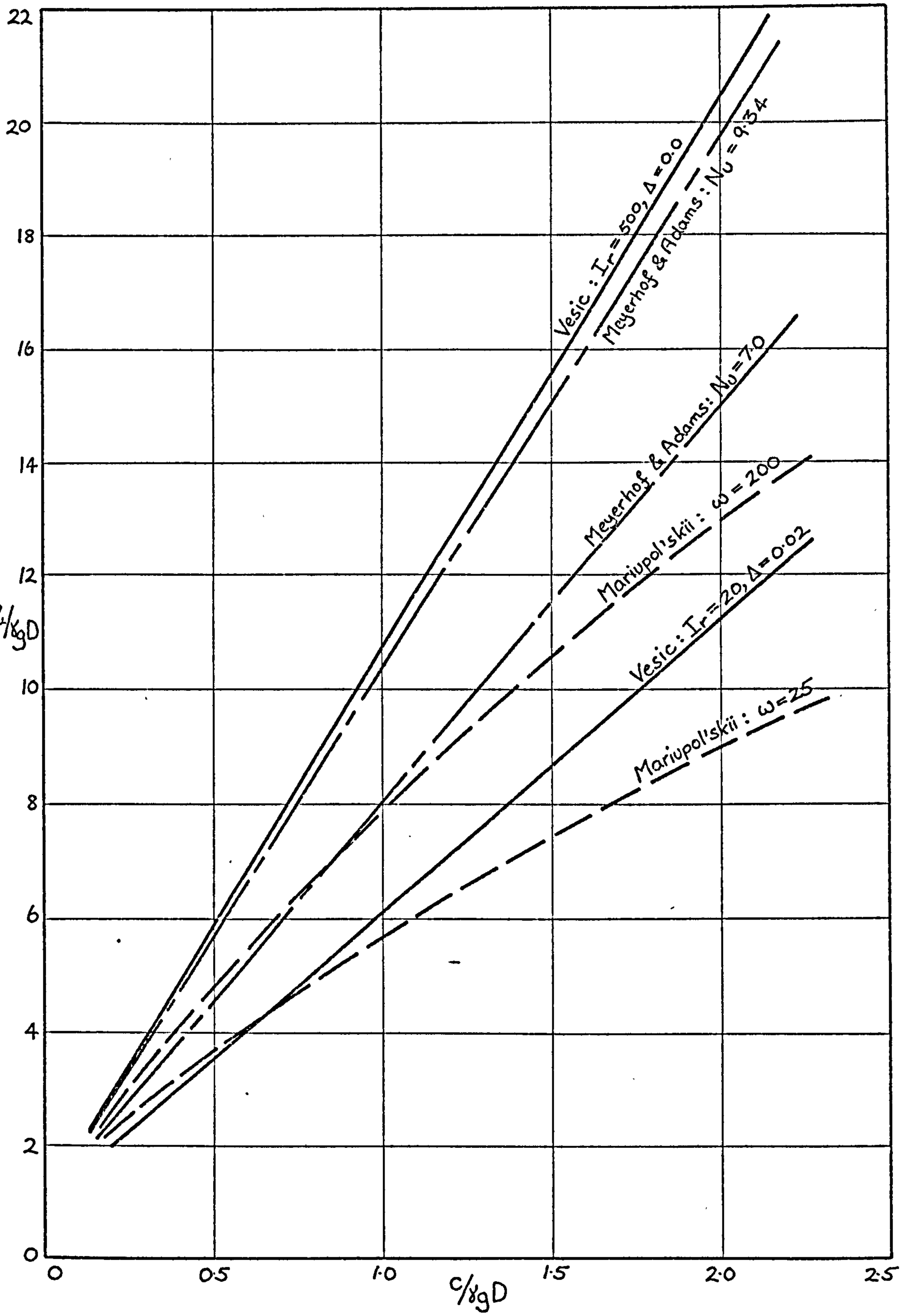

FIG. 2.13. COMPARISON OF THEORIES: DEEP ANCHORS

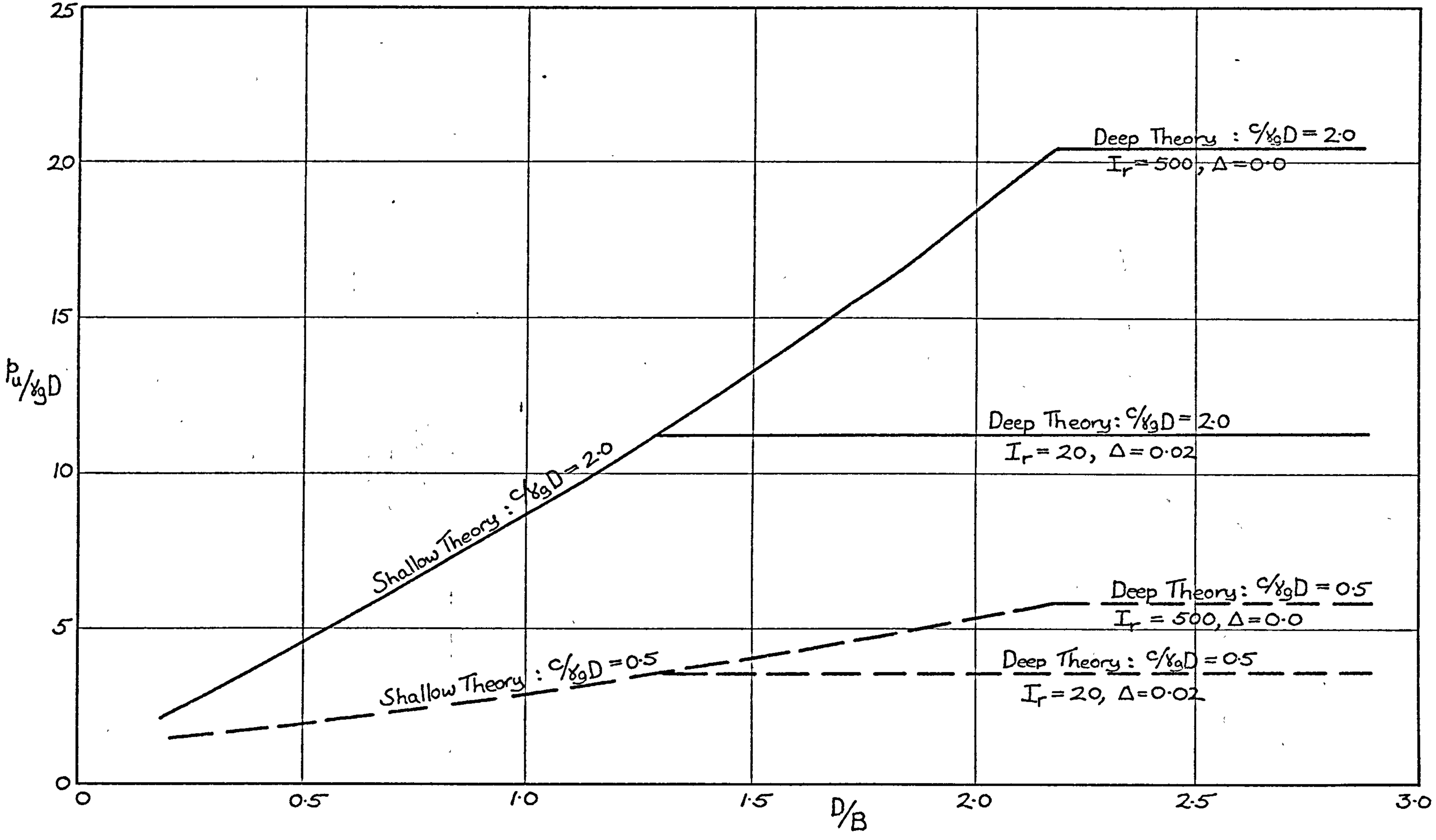

FIG. 2.14. COMPARISON OF VESIC'S SHALLOW AND DEEP ANCHOR THEORIES

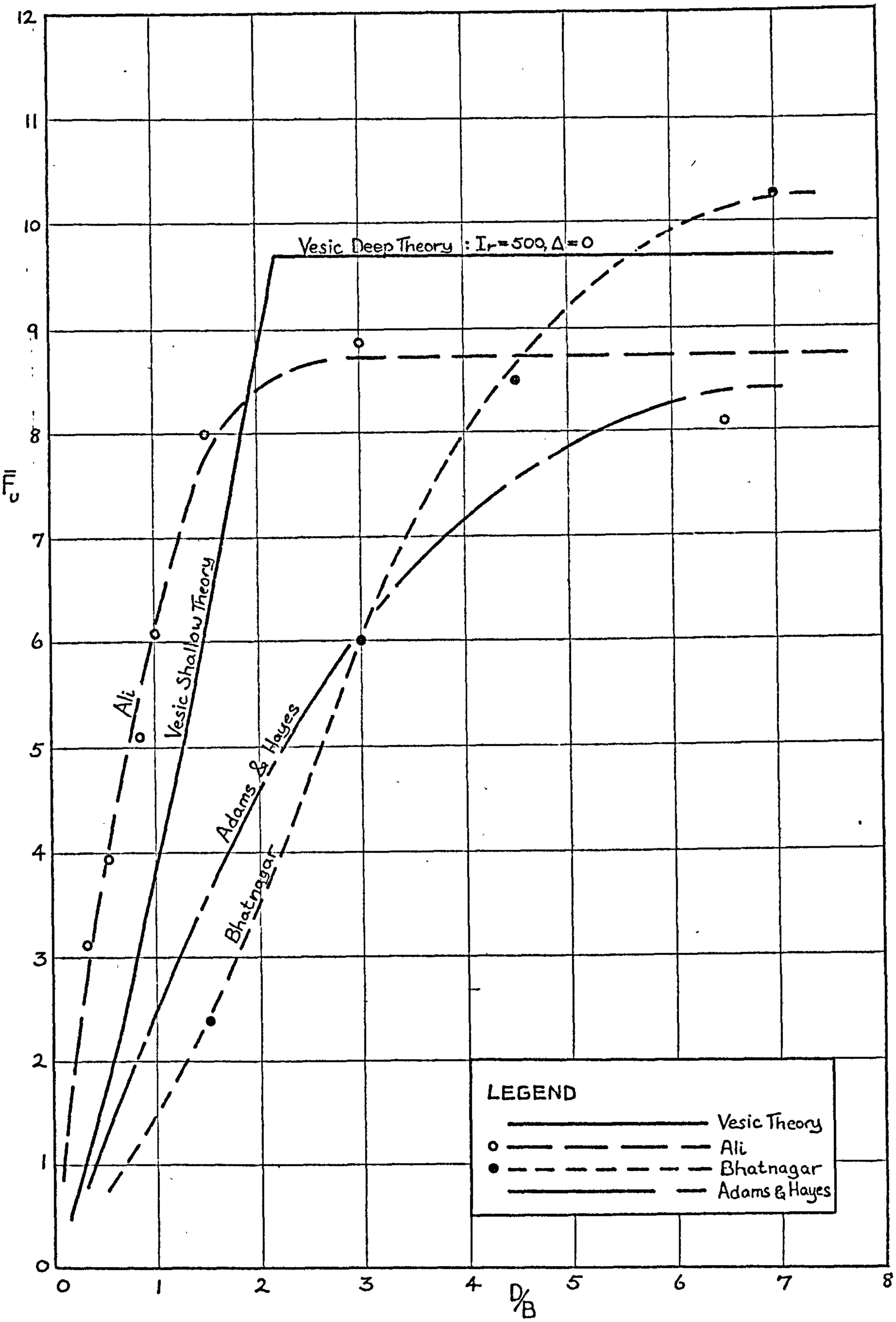

FIG. 2.15. MODEL TEST RESULTS BY ALI, BHATNAGAR, AND ADAMS AND HAYES, AND VESIC'S SHALLOW AND DEEP ANCHOR THEORIES

CHAPTER THREE

DIMENSIONAL ANALYSIS

3.1. Introduction

In order to conduct model tests which can be interpreted accurately in terms of the prototype, geometric and dynamic similarity between prototype and model must be established to as high a degree as possible. Where complete dimensional similarity cannot be achieved, attempts must be made to estimate the effect on model test results of any factors which cannot be made to conform to similarity conditions.

This chapter has two main purposes:

(a) to examine the uplift resistance problem with respect to soil properties and anchor dimensions, and to perform a dimensional analysis of the problem;

(b) to estimate the factors in the dimensional analysis which have a major influence on the problem, and to examine the effect on test results of any dimensional dissimilarity of these factors between model and prototype.

3.2. Parameters which affect Uplift Resistance

The parameters which affect uplift resistance can be divided into two main categories:

A. parameters of the materials used in the model;

B. parameters of the physical dimensions of the model.

A. Parameters of the Materials used in the Model

Soil parameters. The basic parameters of a soil water mixture may be described as soil particle size, soil particle shape, specific gravity of the soil particles, hardness of the soil particles, electric charge (if any) on the soil particles, properties of the interstitial water (e.g. salt content), and the void ratio and water content of the

mixture. A set of secondary parameters, which are functions of the primary parameters and which in general describe the behaviour of the soil water mix are listed below:

γ = the bulk density of the soil

ϕ = the internal angle of friction of the soil

c = the cohesion of the soil

t = the tensile strength of the soil

E = the modulus of elasticity of the soil

ν = Poisson's ratio of the soil

Δ = the plastic volumetric strain of the soil

Additional secondary parameters are consolidation properties, compressibility, permeability, viscosity, and creep.

All of the above secondary parameters will affect the value of the uplift resistance of the soil to a greater or lesser extent. However, the dimensional analysis will be simplified if those soil parameters which have a very small effect upon the problem can be eliminated. Examination and discussion of previous theories (chapter 2) and some preliminary model testing by the author have indicated clearly the parameters which must be included in the dimensional analysis.

Material bulk density must be included since any upward movement of the anchor will be resisted by the weight of material above it. The parameters of limiting material strength will be important. Since only purely cohesive soils are being considered in the present investigation, the angle of internal friction will be omitted. Existing theories take the value of shear strength of the soil to be the limiting value of soil strength. However, it will be shown (chapters 4 and 5) that considerable tensile regions exist throughout the material under uplift forces, and the tensile strength of the material must also be considered.

The values of the elastic modulus and Poisson's ratio of the soil will affect the deformation characteristics of the soil during both

shallow and deep anchor tests. This in turn may affect the mode of ultimate failure. In addition, existing deep anchor theories postulate that these parameters play a direct part in the determination of the value of the ultimate uplift resistance of soils. The plastic volumetric strain in the plastic zones of stress can also play a part in the determination of the value of ultimate uplift resistance.

In the dimensional analysis, only rapid (undrained) tests on fully saturated clays will be considered. Therefore, the time dependent parameters of compression consolidation and permeability will be neglected. In very soft materials under stress, viscous effects may be encountered. It will be assumed that the materials being used will display negligible viscous effects. The effect of creep will not be considered. It will be assumed that any suctional effect which may occur below the anchor during uplift resistance testing will be relieved by the use of a hollow shafted anchor.

Anchor material parameters. It will be assumed that the anchor is rigid enough to undergo negligible deformation compared to the soil during uplift resistance tests. The weight of the anchor footing, both in the prototype and in the model, is always known and therefore its part in the total uplift resistance force can be calculated. It can thus be omitted from the dimensional analysis. On the anchor plate, adhesion (c_a) may be developed between the anchor material and the soil. This parameter will be included in the dimensional analysis.

B. Parameters of the Physical Dimensions of the Model

The diameter of the anchor plate B and the initial depth of placement of the anchor D are of fundamental importance in the uplift resistance problem and must be included in the dimensional analysis. Model tests are normally carried out inside a container, diameter B_c. If the diameter of the container is too small, considerable boundary effects may be encountered. Since the prototype has no container, the

model container must be large enough to eliminate, as far as possible, these side effects and the parameter B_c must therefore be included in the dimensional analysis.

A preliminary analysis by the author has shown that if the anchor plate is made only thick enough to retain rigidity, then the effect of this thickness on the total uplift resistance of the soil will be negligible. The parameter of anchor plate thickness will therefore not be included in the dimensional analysis. The present investigation is concerned primarily with the uplift resistance of soil due to the anchor plate movement and not with the uplift resistance due to the adhesion between the soil and the anchor shaft. In the dimensional analysis, it will be assumed that the anchor shaft is of negligible thickness.

The uplift resistance of the soil prevents anchors from being pulled out of the ground in the high mast situation or from being pushed out of the ground in the shaft raising situation. The value of this uplift resistance may be affected if the values of the strength and the weight of the soil are altered due to the rate of pullout or pushout. However, if the rate of anchor movement in the uplift resistance test is similar to the rate of movement used in the testing of the soil strength, e.g. the rate of testing in the triaxial apparatus, then the rate of uplift resistance testing may be neglected, assuming that it is not great enough to affect the weight of the soil.

3.3. Dimensional Analysis of the Uplift Resistance Problem

For a rapid (undrained) uplift resistance test on a saturated clay, with the assumptions stated earlier, the uplift resistance pressure experienced by the soil may be assumed to be a function:

$$p = f(g, \gamma, c, t, E, \nu, \Delta, c_a, D, B, B_c)$$

The dimensions of the various parameters are tabulated in Table 3.1.

By the Buckingham pi method of inspection, using as a dimensionless group D, γ, and g :

$$p/\gamma_g D = f\left(c/\gamma_g D, t/\gamma_g D, E/\gamma_g D, c_a/\gamma_g D, \nu, \Delta, B/D, B_c/D\right) \quad (3.1)$$

now, $f(B/D) = (B/D)^a$ (say) $= (D/B)^{-a}$

if $a = -b$, then $f(B/D) = (D/B)^b$

Since D is usually greater than B in the uplift resistance problems, the ratio D/B is simpler to work with than B/D.

3.4. Effects of Dissimilarity of Dimensionless Groups in Model and Prototype

The dimensional analysis indicates that, with some simplifying assumptions, eight dimensionless groups must be the same in both model and prototype to obtain identical values for $p_u/\gamma_g D$ in rapid (undrained) uplift resistance tests in saturated clay.

In model testing in soil mechanics, it is common practice to use the same soil in the model as in the prototype, with the result that the parameters which describe soil behaviour, i.e. γ, c, t, E, ν and Δ are the same in both model and prototype. This implies that in order to achieve dimensional similarity between model and prototype for groups $c/\gamma_g D$, $t/\gamma_g D$ and $E/\gamma_g D$, assuming acceleration due to gravity to be constant, then $D_{mod.} = D_{pro.}$ and consequently to satisfy D/B then $B_{mod.} = B_{pro.}$. In other words, if the same soil is used in both model and prototype, then for complete dimensional similarity under normal gravity conditions, the model must be identical to the prototype.

If dimensional similarity is required between a model, scaled down by a length factor x, and the prototype, then the groups c/γ_g, t/γ_g and E/γ_g must be scaled down by the factor x whilst ν and Δ remain the same. It is known that the bulk densities γ of most saturated clays do not vary by much over a large range of strengths and thus γ may be assumed to be constant. Therefore, in order to achieve dimensional similarity, there exist two alternative methods:

(a) Reduce the values of c, t and E of the clay by a factor x,

whilst keeping ν and Δ the same. However, if the values of the cohesion, tensile strength, and the elastic modulus of the clay are reduced, even assuming that ν and Δ can be kept constant, the way in which the soil behaves under stress may alter. Parameters which were neglected in the dimensional analysis such as viscosity (if the soil has to be very soft) and creep may affect the displacement characteristics, and the manner in which cracking propagates throughout the soil may be altered.

(b) Increase the value of acceleration due to gravity g by model testing in a centrifuge. The difficulties are:

(i) the cost of equipment which is large enough to test a reasonably sized model;

(ii) the incorporation of an anchor loading mechanism into a centrifuge and the measurement of the relevant parameters, e.g. surface displacements, during testing.

The dimensional analysis indicates the groups of parameters which must be identical to give dimensional similarity between model and prototype. However, it does not indicate to what extent dimensional dissimilarity will affect model test results. Theories for predicting uplift resistance pressures already exist (chapter 2) and a theory which is considered to be representative will be examined to find the extent to which the relationship between $(p_u)_{mod.}$ and $(p_u)_{pro.}$ will be affected if dimensional similarity does not existing between model and prototype.

A. Shallow Anchor Theories

All of the existing shallow anchor theories assume ultimate shearing failure and ignore the effects of the elastic and tensile properties of the soil. Thus:

$$p_u/\gamma g D = f(c/\gamma g D, D/B) \qquad \cdots\cdots (3.2)$$

An examination of the values of $P_u/\gamma_g D$ in these theories (Table 2.1.) shows that the uplift resistance of the soil depends on the weight of the material and its shear strength (cohesion). Since the unit weight of soil is defined in terms of force per unit volume (weight is a function of volume) and the strength of the soil (stress, pressure) is defined in terms of force per unit area (stress is a function of area), then the larger the scale of the model, the greater the relative effect of the weight of the soil on the value of the uplift resistance of the model, assuming that the value of acceleration due to gravity is the same in both model and prototype. Therefore, if the same soil is used in both model and prototype, the soil weight contribution to the total ultimate uplift resistance in the model will be reduced. However, if the value of the shear strength of the soil is high, the contribution of the soil weight to the total ultimate uplift resistance in the prototype itself will be small since the unit weight of the soil is approximately constant and is not a function of the strength of the soil. Thus, the contribution of the soil weight to the total ultimate uplift resistance of the soil is a function of anchor size (depth and breadth) and the strength of the soil as well as the value of the unit weight of the soil, i.e. a function of $c/\gamma_g B$ (or $c/\gamma_g D$).

The above argument can be demonstrated with reference to Vesic's Shallow Anchor Theory, a theory which can be considered as representative of the shallow anchor theories examined in chapter 2. Fig. 3.1 shows the percentage contribution of soil weight to the total ultimate uplift resistance (expressed as $P_u/\gamma_g D$) when plotted against $c/\gamma_g B$. Appendix A provides details of the derivation of Fig. 3.1 by the author from Vesic's theory. In a theory which assumes a cylindrical or conical shaped slip failure surface, the contribution of soil weight to the total ultimate uplift resistance will be constant with varying depth.

However, since Vesic's Shallow Anchor Theory assumes a circular slip failure surface, the contribution of soil weight to the total ultimate uplift resistance will be a function of D/B . Values of $D/B = 0.5$ and $D/B = 1.5$ are plotted. Since $p_u/\gamma_g D$ is a function of both $c/\gamma_g D$ and D/B (eq.3.2) and $c/\gamma_g B = c/\gamma_g D \cdot D/B$, then $c/\gamma_g B$ is plotted in Fig. 3.1 since it combines both $c/\gamma_g D$ and D/B .

Before the implications of Fig. 3.1 are discussed, values of $c/\gamma_g B$ for some typical prototype anchor dimensions and soil properties are presented in Table 3.2. A normal range of $c/\gamma_g B$ values for prototype shallow anchors will be of the order of 0.46 (for large diameter anchors in soft clays) to 7.5 (for small diameter anchors in stiff clays). Models are normally scaled down by length factors of the order of 5 to 50, resulting in model tests being in the $c/\gamma_g B$ range 2.3 to 375, provided that the soils used in the model tests are similar to those described in Table 3.2.

The problems which may occur when two limiting cases of prototype shallow anchors are modelled without a centrifuge will be considered in the following sections. The first anchor to be considered will be a large prototype shallow anchor in a soft clay with a $c/\gamma_g B$ value of 0.46, which is considered to be the lower limit of typical prototype $c/\gamma_g B$ values (Table 3.2). The second anchor to be considered will be a small prototype anchor in a stiff clay with a $c/\gamma_g B$ value of 7.5, which is considered to be the upper limit of typical prototype $c/\gamma_g B$ values (Table 3.2).

<u>Large prototype shallow anchor in soft clay</u>. The dimensions of this prototype anchor and the parameters of the soil are considered to provide a lower limit of $c/\gamma_g B$ for typical prototype shallow anchors.

Diamater of anchor (B) = 3 m

Depth of anchor (D) = 3 m

D/B = 1

Shear strength of clay (c) = 25 kN/m^2

Unit weight of clay (γ_g) = 18 kN/m^3

$c/\gamma_g B$ = 0.46

According to Vesic's Shallow Anchor Theory (Fig. 3.1), the percentage contribution of soil weight to the total ultimate uplift resistance of this prototype will be approximately 37%.

Two methods of modelling this prototype will be considered: (a) a model which uses the prototype soil, implying that dimensional similarity between model and prototype will not be achieved, and (b) a model which uses a different soil and which attempts to achieve dimensional similarity between model and prototype.

(a) Model which uses the prototype soil. For modelling purposes, the prototype is scaled down by a length factor of 15 (i.e. the diameter of the model anchor is 0.2m) and the prototype soil is used, with a resulting model $c/\gamma_g B$ value of 6.9, i.e. dimensional similarity does not exist between model and prototype. Fig. 3.1 shows that in this model, the percentage contribution of soil weight to the total ultimate uplift resistance (according to Vesic's theory) will be approximately 4%, compared to 37% for the prototype.

Vesic's theory assumes that the total ultimate uplift resistance of the soil is made up of (i) the uplift resistance due to the weight of the soil and (ii) the uplift resistance due to the shear strength of the soil. In the case being considered, the value of the uplift resistance pressure on both the model and prototype anchors due to the shear strength of the soil will be the same, since the same soil is being used in both tests. However, according to Fig. 3.1, this will account for 96% (i.e. 100% -4%)of the total ultimate uplift resistance pressure in the model but only 63% (i.e. 100% - 37%) of the total ultimate uplift resistance

pressure in the prototype. Therefore, if no account is taken of the different contributions of soil weight to the total ultimate uplift resistance between model and prototype, and if the ultimate uplift resistance pressure predicted for the prototype is assumed to be the value measured in the model, an underestimation of prototype ultimate uplift resistance pressure of over 50% will occur, according to Vesic's theory. In the high mast foundation situation, an underestimation of the ultimate uplift resistance of the soil will lead to a conservative foundation design. However, in the shaft-raising situation, where the use of large diameter shafts (anchors) in soft clay beneath the sea bed is probable, an underestimation of this nature could lead to the provision of jacking equipment of inadequate capacity.

(b) Model which attempts to achieve dimensional similarity with the prototype. Tests by the author on soft clays (chapter 4) have shown that below a value of shear strength of approximately 5 kN/m^2, clays become viscous and difficult to handle and to compact, and this is therefore taken to be a limiting lower value of shear strength for model testing. If the model uses a very soft clay with a shear strength of 5 kN/m^2, i.e. the strength of the prototype clay ($c = 25\ kN/m^2$) is reduced by a factor of 5, then to achieve dimensional similarity, the diameter of the model anchor must be reduced by a factor of 5, i.e. the diameter of the model must be 0.6 m. Limitations of size must be placed on model tests, and no uplift resistance model tests by previous researchers have been performed with anchors exceeding 0.4 m in diameter, which may be taken as a limiting value for model testing. A 0.4 m diameter anchor in a soil of shear strength 5 kN/m^2 will yield a model $c/\gamma_g B$ value of approximately 0.7, which can be considered to be the minimum possible obtainable $c/\gamma_g B$ value. Large diameter

prototype anchors in soft clays which have $c/\gamma_g B$ values of less than 0.7 will therefore not be able to be modelled in a dimensionally similar manner. Fig. 3.1 shows that, according to Vesic's theory, the percentage contribution of soil weight to the total ultimate uplift resistance in this model will be approximately 27%, compared to 37% for the prototype.

Small prototype shallow anchor in stiff clay. The dimensions of this prototype anchor and the parameters of the soil are considered to provide an upper limit of $c/\gamma_g B$ for typical prototype shallow anchors (Table 3.2).

Diameter of anchor	(B)	= 1 m
Depth of anchor	(D)	= 1 m
	D/B	= 1
Shear strength of clay	(c)	= 150 kN/m^2
Unit weight of clay	(γ_g)	= 20 kN/m^2
	$c/\gamma_g B$	= 7.5

According to Vesic's Shallow Anchor Theory (Fig. 3.1), the percentage contribution of soil weight to the total ultimate uplift resistance of this prototype will be approximately 3%. Two methods of modelling this prototype will be considered: (a) a model which uses the protype soil, implying that dimensional similarity between model and prototype will not be achieved, and (b) a model which uses a different soil and which attempts to achieve dimensional similarity between model and prototype.

(a) Model which uses the prototype soil. For modelling purposes the prototype anchor is scaled down by a factor of 15 to give a model anchor diameter of 0.067 m, and the prototype soil is used, with a resulting model $c/\gamma_g B$ value of 112.5. Fig. 3.1 shows that the percentage contribution of soil weight to the total ultimate uplift resistance in this model will be less than 0.5%. Since

the same soil is being used in both model and prototype, the uplift resistance pressure on both the model and the prototype anchors due to the shear strength of the soil will be the same. However, since this accounts for 97% of the total ultimate uplift resistance in the prototype and approximately 99.5% of the total ultimate uplift resistance in the model, an underestimation of the total ultimate uplift resistance pressure in the prototype of less than 3% will occur if the total ultimate uplift resistance pressure of the prototype is assumed to be the value which is measured in the model.

(b) Model which attempts to achieve dimensional similarity with the prototype. Dimensional similarity can be achieved between model and prototype by using a model soil with a shear strength of 30 kN/m^2 and an anchor of diameter 0.2 m. Previous discussion has demonstrated that both of these values are reasonable for model testing. It can thus be concluded that dimensional similarity between model and prototype can be achieved without difficulty for small prototype anchors in stiff clays with high values of $c/\gamma_g B$.

The two limiting cases of $c/\gamma_g B$ of 0.46 and 7.5 for typical prototype shallow anchors have been considered. The values of $c/\gamma_g B$ for all typical prototype shallow anchors will lie between these limiting values. In this range of shallow prototype anchors, the ease of modelling the prototype and the contribution of soil weight to the total ultimate uplift resistance of the prototype will depend on the prototype value of $c/\gamma_g B$ and will be on a sliding scale between the two limiting cases discussed.

B. Deep Anchor Theories

Vesic's expanding cavity theorem adapted for deep anchors is

considered to be representative of the existing deep anchor theories which were examined in chapter 2. This theory expresses the ultimate uplift resistance of the soil as a function of the elastic and plastic properties of the soil:

$$p_u/\gamma_g D = f\,(c/\gamma_g D, I_r, \Delta) \qquad \cdots\cdots(3.3)$$

According to this theory, the ultimate uplift resistance of a deep anchor in clay is a function of soil parameters c, E, ν and Δ, and the overburden pressure of the soil on the anchor $\gamma_g D$. If a homogeneous soil is assumed, the deep anchor theory states that the contributions of c, E, ν, and Δ to the total ultimate uplift resistance are independent of depth. However, since the overburden pressure on the anchor is a function of depth, the scale of the prototype or model will affect the contribution of soil weight to the total ultimate uplift resistance of the soil. Nevertheless, it should be noted that according to Vesic's Deep Anchor Theory, the contribution of soil weight to the total ultimate uplift resistance pressure at any depth is independent of the diameter of the anchor. Fig. 3.2 shows the percentage contribution of soil weight to the total ultimate uplift resistance of the soil (expressed as $p_u/\gamma_g D$) when plotted against $c/\gamma_g D$. $c/\gamma_g D$ is plotted in the deep anchor case since the percentage contribution of soil weight to the total ultimate uplift resistance is independent of B. Values are plotted for an incompressible clay (small strain to yield) with $I_r = 500$ and $\Delta = 0.0$ and a compressible clay (large strain to yield) with $I_r = 20$ and $\Delta = 0.02$. These values of I_r and Δ were discussed in chapter 2. Details of the derivation of Fig. 3.2 by the author from Vesic's Deep Anchor Theory are given in Appendix A.

Before the implications of Fig. 3.2 are discussed, values of $c/\gamma_g D$ for some typical prototype anchor dimensions and soil properties are presented in Table 3.3. A normal range of values of $c/\gamma_g D$ for prototype anchors will be of the order of 0.15 for very deep anchors in

soft clay to 2.5 for moderately deep anchors in stiff clay, resulting in model $c/\gamma_g D$ values in a range from 0.75 to 125, assuming once more that models are scaled down by length factors from 5 to 50 and that the prototype range of soils is used for modelling purposes.

The problems which may occur when two prototype deep anchors are modelled without a centrifuge will be considered in the following sections. The first anchor to be considered will be a very deep prototype anchor in a soft clay which has a $c/\gamma_g D$ value of 0.155, considered to be the lower limit of typical prototype $c/\gamma_g D$ values (Table 3.3). The second anchor to be considered will be a moderately deep anchor in a stiff clay which has a $c/\gamma_g D$ value of 2.5, considered to be the upper limit of typical prototype $c/\gamma_g D$ values (Table 3.3).

Very deep prototype anchor in soft clay. The dimensions of this prototype anchor and the parameters of the soil are considered to provide a lower limit of $c/\gamma_g D$ for typical prototype deep anchors (Table 3.3).

Diameter of anchor is arbitrary, provided "deep anchor" failure occurs.

Depth of anchor (D)	=	9 m
Shear strength of clay (c)	=	25 kN/m^2
Unit weight of clay (γ_g)	=	18 kN/m^3
Rigidity Index of clay (I_r)	=	20
Plastic Volumetric Strain (Δ)	=	0.02
$c/\gamma_g D$	=	0.155

According to Vesic's Deep Anchor Theory (Fig. 3.2), the percentage contribution of soil weight to the total ultimate uplift resistance of this prototype will be approximately 56%.

Two methods of modelling this prototype will be considered: (a) a model which uses the prototype soil, implying that dimensional similarity between model and prototype will not be achieved, and (b) a model which uses a different soil and which attempts to achieve

dimensional similarity between model and prototype.

(a) Model which uses prototype soil. In order to model the anchor, the prototype depth of placement is scaled down by a factor of 15 to give a model depth of placement of 0.6 m, and the prototype soil is used, resulting in a model $c/\gamma_g D$ value of 2.32. Fig. 3.2 shows that in this model, the percentage contribution of soil weight to the total ultimate uplift resistance will be approximately 8%, compared to 56% in the prototype. If no account is taken of the different contributions of soil weight to the total ultimate uplift resistance between model and prototype and if the ultimate uplift resistance pressure which is predicted for the prototype is assumed to be the value which is measured in the model, and underestimation of prototype ultimate uplift resistance pressure of over 100% will occur, according to Vesic's theory. This underestimation of ultimate uplift resistance in the prototype would lead to a very conservative foundation design in the case of high mast footings but could lead to quite inadequate jacking power being provided in the shaft-raising situation.

(b) Model which attempts to achieve dimensional similarity with the prototype. As previously discussed, a soil with a shear strength below about 5 kN/m^2 is difficult to handle and compact. Practical considerations limit the depth of clay which may be used in model tests of this nature, and no previous researchers have performed model uplift resistance tests in clays of depths greater than 1.0m. This depth will be taken as a limiting value in the subsequent discussion. For the model being considered, an anchor at a depth of 1.0 m in a clay with a shear strength of 5 kN/m^2 will have a $c/\gamma_g D$ value of 0.28, compared with a $c/\gamma_g D$ value of the prototype of 0.155, i.e. dimensional similarity between model and prototype cannot be achieved in this case. This $c/\gamma_g D$ value of 0.28 can be

considered as being the minimum model $c/\gamma_g D$ value which can be attained and very deep anchors in soft clays with a $c/\gamma_g D$ value of less than 0.28 cannot be modelled in a dimensionally similar manner. Fig. 3.2 shows that, according to Vesic's theory, the percentage contribution of soil weight to the total ultimate uplift resistance in the model with $c/\gamma_g D = 0.28$ will be approximately 42%, compared to 56% for the prototype.

Since only the overburden pressure on the anchor is affected by the variation of anchor depth in deep uplift resistance tests in clay, the overburden pressures experienced by the prototype anchor may be simulated in model tests by the superimposition of a loading on the model clay surface. Thus, in the case being considered, where $(c/\gamma_g D)_{mod.}$ cannot be made equal to $(c/\gamma_g D)_{pro.}$, a surface loading p_s may be superimposed on the model such that $(c/\gamma_g D)_{pro.} = \left(\frac{c}{\gamma_g D + p_s}\right)_{mod.}$. Where superimposed loading is employed, the prototype soil can always be used in the model. The superimposed loading method has been used by Hanna et. al.(1972) in model uplift resistance tests in cohesionless soils. It must be noted that, in the author's opinion, this technique should not be employed in shallow anchor model tests since the superimposed loading may affect the surface deformation and the shape of the slip failure surface in the shallow anchor model.

Moderately deep prototype anchors in stiff clay. The dimensions of the prototype anchor and the parameters of the soil are considered to provide an upper limit of $c/\gamma_g D$ for typical prototype deep anchors (Table 3.3).

Diameter of anchor is arbritary, provided a "deep anchor" failure occurs.

Depth of anchor (D) = 3 m

Shear strength of clay (c) = 150 kN/m^2

Unit weight of clay (γ_g) = 20 kN/m^3

Rigidity Index of clay (I_r) = 500

Plastic volumetric strain (Δ) = 0.0

$c/\gamma_g D$ = 2.5

According to Vesic's Deep Anchor Theory (Fig. 3.3), the percentage contribution of soil weight to the total ultimate uplift resistance of this prototype will be approximately 3%.

Two methods of modelling this prototype will be considered: (a) a model which uses the prototype soil, implying that dimensional similarity between model and prototype will not be achieved, and (b) a model which uses a different soil and which attempts to achieve dimensional similarity between model and prototype.

(a) Model which uses prototype soil. For modelling purposes, the depth of placement of the prototype anchor is scaled down by a factor of 15 to give a model depth of placement of 0.2 m, and the prototype soil is used, resulting in a model $c/\gamma_g D$ value of 37.5. According to Vesic's theory (Fig. 3.2), the percentage contribution of soil weight to the total ultimate uplift resistance of this model will be approximately 0.5%. If no account is taken of the different contributions of soil weight to the total ultimate uplift resistance between model and prototype, and if the ultimate uplift resistance pressure which is predicted for the prototype is assumed to be the value which is measured in the model, an underestimation of the prototype ultimate uplift resistance pressure of less than 3% will occur.

(b) Model which attempts to achieve dimensional similarity with the prototype. Dimensional similarity between model and prototype can be achieved in this case if a model soil with a shear strength of 30 kN/m^2 is used with an anchor at a depth of 0.6 m, and there is therefore no need to superimpose surface loading in order to simulate dimensional similarity.

The two limiting cases of $c/\gamma_g D$ of 0.155 and 2.5 for typical prototype deep anchors have been considered. The values of $c/\gamma_g D$ for all typical prototype deep anchors will lie between these limiting values. In this range of deep prototype anchors, the ease of modelling the prototype and the contribution of soil weight to the total ultimate uplift resistance of the prototype will depend on the prototype value of $c/\gamma_g D$ and will be on a sliding scale between the two limiting cases discussed.

3.5. A Note on the Presentation and Comparison of Uplift Resistance Values obtained from Model Tests

The dimensional analysis in section 3.3 demonstrated that in the uplift resistance problem, values of D/B, $c/\gamma_g D$, $t/\gamma_g D$, $E/\gamma_g D$, $c_a/\gamma_g D$, B_c/D, ν and Δ must ideally be the same in both prototype and model to give the same value of $p_u/\gamma_g D$ in prototype and model. Ideally in uplift resistance model testing, the soil strength and the anchor dimensions of the model should be selected so that, in a series of tests, $c/\gamma_g D$, $t/\gamma_g D$, $E/\gamma_g D$, $c_a/\gamma_g D$, B_c/D, ν and Δ will be constant for varying values of D/B, to giving corresponding values for $p_u/\gamma_g D$. Various series of model tests can be performed with values $c/\gamma_g D$ (or $c/\gamma_g B$), $E/\gamma_g D$ etc. in the model which are representative of prototype values, wherever dimensional similarity between model and prototype can be achieved. An overall set of values for $p_u/\gamma_g D$ will thus be obtained which will enable the ultimate uplift resistance values of prototypes to be predicted if the soil properties and the anchor dimensions of the prototype are known, or conversely to indicate suitable anchor dimensions if the soil properties and total uplift force are known. Chapter 4 describes a series of model uplift resistance tests which were performed by the author with anchor dimensions and soil properties selected to allow the results to be plotted in the manner described above.

Figs. 3.1 and 3.2 illustrate that, according to Vesic's theory, the percentage contribution of soil weight to the total ultimate uplift resistance of the soil is less than 5% in any case where the value of $c/\gamma_g B$ is greater than 5 (shallow anchors) or $c/\gamma_g D$ is greater than 3 (deep anchors). This indicates that, for these anchors, the shear strength of the soil provides over 95% of the ultimate uplift resistance of the soil. Therefore, when comparing a series of model uplift resistance tests in which the values of $c/\gamma_g B$ are greater than 5 or $c/\gamma_g D$ are greater than 3, little error will generally occur if the ultimate uplift resistance of the soil is assumed to be proportional to the shear strength of the soil, i.e. p_u/c may be plotted against D/B.

In order to compare model test values of uplift resistance in purely cohesive soils, Vesic (1969) has derived an uplift resistance factor F_c which combines the uplift resistance pressure in the model test with the value of the shear strength of the soil, and also takes into account an assumed pressure due to the weight of the soil above the anchor. Meyerhof and Adams (1968) derived a similar uplift resistance factor N_u.

In chapter 4, the term $\bar{F}$ and $\bar{F}_u$ which are equivalent to the factors F_c and N_u, will be employed by the author in the comparison of uplift resistance values in model tests:

$$\bar{F} = \frac{p - \gamma_g D}{c} \qquad \cdots\cdots (3.4)$$

$$\bar{F}_u = \frac{p_u - \gamma_g D}{c} \qquad \cdots\cdots (3.5)$$

where the pressure due to the soil weight on the anchor plate is assumed to be the depth of the anchor times the unit weight of the soil ($\gamma_g D$).

A plot of $\bar{F}_u$ v D/B for model test results will provide only an approximate estimate of the value of the prototype ultimate uplift resistance, since the value of $\bar{F}_u$ will be dependent on the accuracy of the assumption of the value of overburden pressure on the anchor.

However, for soils which have the same values of c/t , c/E , ν , , I_r and Δ (and if it is assumed that the unit weight of purely cohesive soil is approximately constant), a unique curve of $\bar{F}_u$ v D/B will exist, compared to the large series of curves for $p_u/\gamma_g D$ v $c/\gamma_g D$ v D/B (and the correspondingly large number of model tests) which will be required for these soils if completely accurate predictions are to be made for the value of prototype ultimate uplift resistance from model tests.

3.6. Summary

Due to the large number of topics covered in this chapter, a summary of the points which were discussed is included.

(a) In rapid (undrained) uplift resistance tests on saturated clays, if the creep, viscous, consolidation compression and permeability effects are neglected and a very thin anchor plate and small diameter of anchor shaft are assumed, then:

$$p/\gamma_g D = f\,(c/\gamma_g D,\ t/\gamma_g D,\ E/\gamma_g D,\ c_a/\gamma_g D,\ \nu,\ \Delta,\ D/B,\ B_c/D) \quad (3.1\text{ bis})$$

(b) For shallow uplift resistance anchors, it was demonstrated that dimensional similarity between a model and a prototype cannot be achieved without a centrifuge if the prototype $c/\gamma_g B$ value is below approximately 0.7. This means that dimensional similarity cannot always be achieved for models of large prototype anchors in soft clays with low $c/\gamma_g B$ values, but can be achieved without difficulty for small prototype anchors in stiff clays with large $c/\gamma_g B$ values.

(c) For shallow uplift resistance anchors, it was shown that, according to Vesic's theory, the attainment of dimensional similarity of the value of $c/\gamma_g B$ between model and prototype will only be of importance where the prototype $c/\gamma_g B$ value is low, i.e. in cases where dimensional similarity cannot always be achieved, since only

in these cases is the percentage contribution of soil weight to the total ultimate uplift resistance high, e.g. of the order of 37% in the case considered.

(d) If the ultimate uplift resistance pressure of a prototype large shallow anchor in soft clay is assumed to be the value of the ultimate uplift resistance pressure measured in a model test which uses the prototype soil and which is scaled down by a length factor of 15, an underestimation of the prototype ultimate uplift resistance pressure of the order of 50% will occur, according to Vesic's theory. This will produce a conservative design for a high mast footing but could lead to the provision of inadequate jacking power in the shaft-raising situation.

(e) For deep uplift resistance anchors, it was demonstrated that dimensional similarity between model and prototype cannot be achieved, without the use of a centrifuge or superimposed surface loading, if the prototype $c/\gamma_g D$ value is below approximately 0.28. This means that, in general, it will be difficult to achieve dimensional similarity in models of very deep prototype anchors in soft clays, where the contribution of soil weight to the total ultimate uplift resistance will be high, e.g. of the order of 56% in the case considered.

(f) If the prototype $c/\gamma_g D$ value is less than 0.28 in the deep anchor case, dimensional similarity between model and prototype may be simulated by superimposing an appropriate surface loading on the model. If dimensional similarity is not simulated in this manner and if the value of prototype ultimate uplift resistance pressure is assumed to be the value which is measured in a model which uses the prototype soil but whose depth has been reduced by a factor of 15, an underestimation of the value of prototype ultimate uplift resistance of approximately 100% will occur,

according to Vesic's theory.

(g) For deep uplift resistance anchors, it was shown that, according to Vesic's theory, the attainment of dimensional similarity of the value of $c/\gamma_g D$ between model and prototype will only be of importance where the prototype $c/\gamma_g D$ value is low, i.e. in cases where dimensional similarity cannot always be achieved, since only in these cases is the percentage contribution of soil weight to the total ultimate uplift resistance high, e.g. of the order of 56% in the case considered.

(h) For presentation and comparison of model test results, it was demonstrated from dimensional considerations that values of ultimate uplift resistance obtained from model tests could be plotted in the form of $p_u/\gamma_g D$ v D/B for various values of $c/\gamma_g D$, $E/\gamma_g D$, $t/\gamma_g D$, $c_a/\gamma_g D$, Δ, ν and B_c/D in order to obtain an overall set of dimensionless values which can be applied to any size of prototype anchor and type of soil. Since the soil weight contribution to the total ultimate uplift resistance of a soil is less than 5% (according to Vesic) in cases where $c/\gamma_g B$ is greater than 5 (shallow anchors) or $c/\gamma_g D$ is greater than 3 (deep anchors), the ultimate uplift resistance in these situations is approximately proportional to the shear strength of the soil and p_u/c may be plotted against D/B with little resulting error. Alternatively, a factor such as $\bar{F}_u$, which combines the value of the ultimate uplift resistance of the soil, the value of the shear strength of the soil and a value of the estimated soil weight contribution to the total ultimate uplift resistance may be plotted against D/B .

TABLE 3.1 PARAMETERS CONSIDERED IN THE DIMENSIONAL ANALYSIS

Symbol	Parameter	Dimension
p	uplift resistance pressure	$ML^{-1}T^{-2}$
g	acceleration due to gravity	LT^{-2}
γ	bulk density of soil mass	ML^{-3}
γg	unit weight of soil	$ML^{-2}T^{-2}$
c	cohesive strength of soil	$ML^{-1}T^{-2}$
t	tensile strength of soil	$ML^{-1}T^{-2}$
E	elastic modulus of soil	$ML^{-1}T^{-2}$
ν	Poisson's ratio of soil	$M^{\circ}L^{\circ}T^{\circ}$
Δ	plastic volumetric strain of soil	$M^{\circ}L^{\circ}T^{\circ}$
c_a	adhesion between soil and anchor material	$ML^{-1}T^{-2}$
D	depth of placement of anchor	L
B	diameter of anchor plate	L
B_c	diameter of test box	L

L = Length M = Mass T = Time

TABLE 3.2. TYPICAL $c/\gamma_g B$ VALUES FOR SHALLOW PROTOTYPE ANCHORS

Clay Type / B(m)	Soft $c = 25\ kN/m^2$ $\gamma_g = 18\ kN/m^3$	Firm to Stiff $c = 75 kN/m^2$ $\gamma_g = 19 kN/m^3$	Stiff $c = 150\ kN/m^2$ $\gamma_g = 20 kN/m^3$
1	1·39	3·95	7·50
2	0·695	1·975	3·75
3	0·46	1·315	2·50

TABLE 3.3. TYPICAL $c/\gamma_g D$ VALUES FOR DEEP PROTOTYPE ANCHORS

Clay Type / D(m)	Soft $c = 25\ kN/m^2$ $\gamma_g = 18 kN/m^3$	Firm to Stiff $c = 75\ kN/m^2$ $\gamma_g = 19 kN/m^3$	Stiff $c = 150 kN/m^2$ $\gamma_g = 20 kN/m^3$
3·	0·46	1·315	2·5
6	0·23	0·66	1·25
9	0·155	0·44	0·83

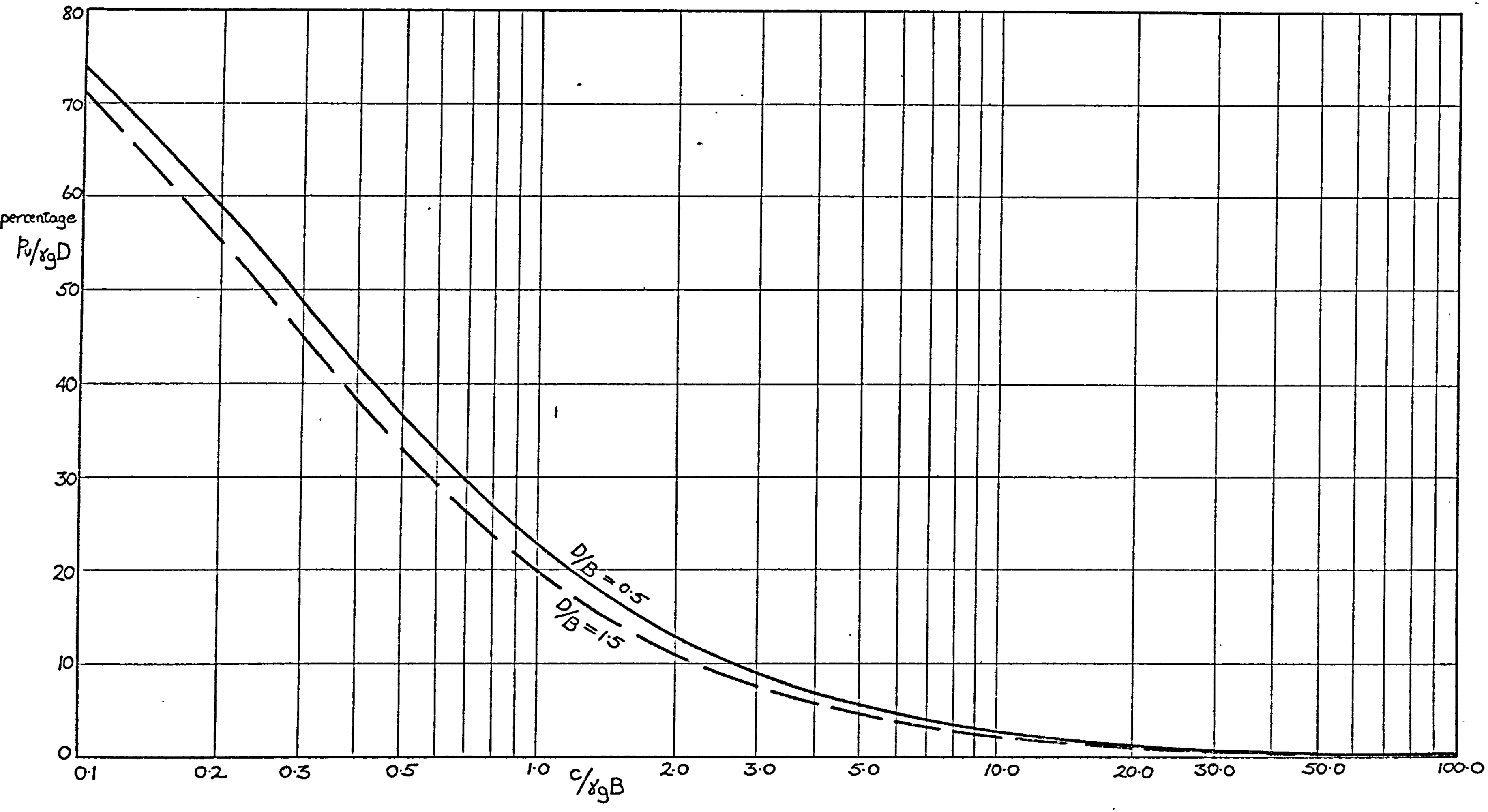

FIG. 3.1. PERCENTAGE CONTRIBUTION OF SOIL WEIGHT TO THE TOTAL ULTIMATE UPLIFT RESISTANCE OF THE SOIL ACCORDING TO VESIC'S SHALLOW ANCHOR THEORY

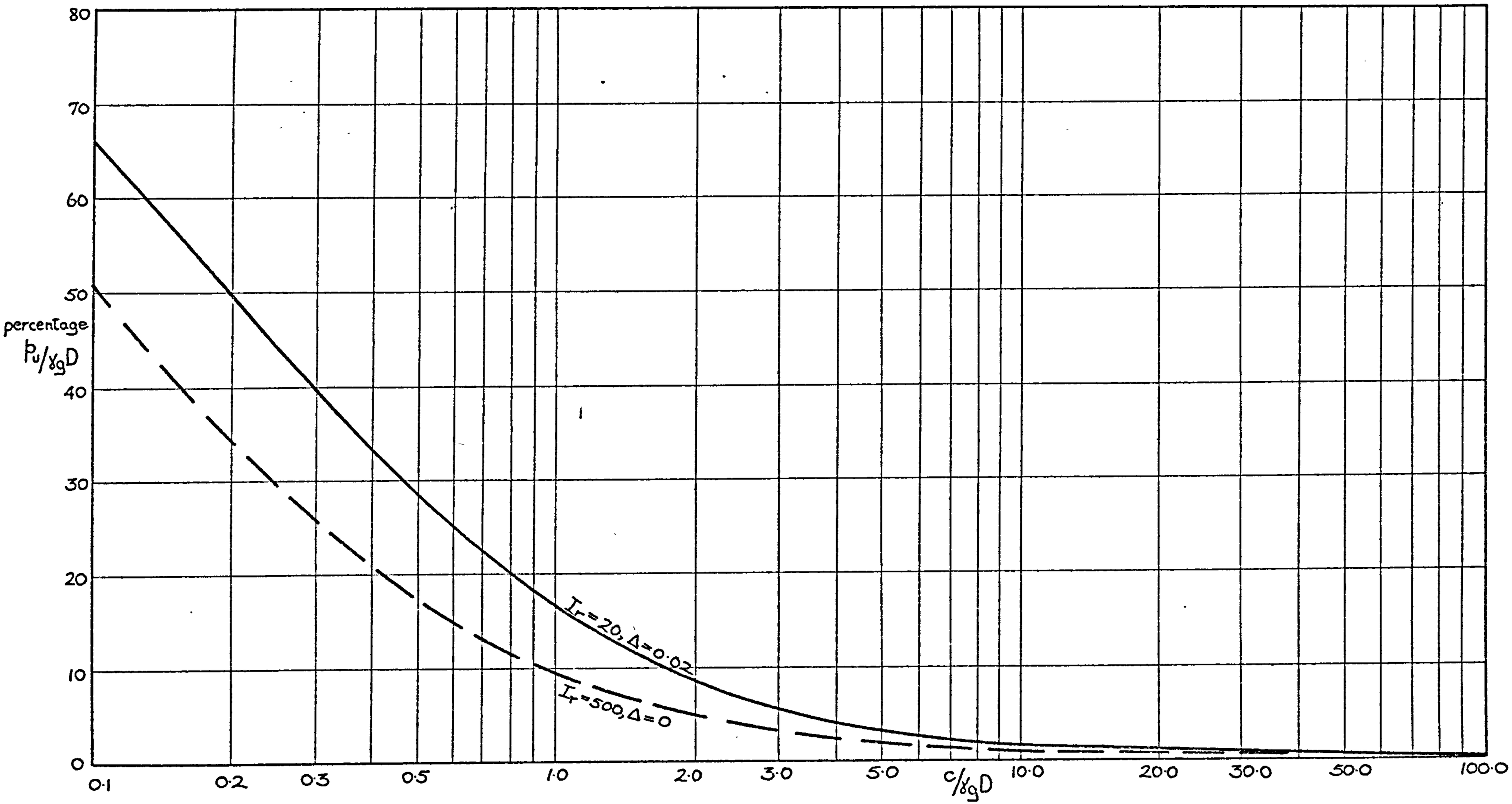

FIG. 3.2. PERCENTAGE CONTRIBUTION OF SOIL WEIGHT TO THE TOTAL ULTIMATE UPLIFT RESISTANCE OF THE SOIL ACCORDING TO VESIC'S DEEP ANCHOR THEORY

CHAPTER FOUR

LABORATORY INVESTIGATIONS

4.1. Introduction

In this chapter, the laboratory model testing program will be described and the results presented. The results will be discussed in chapter 6.

Uplift resistance tests in the laboratory on models of purely cohesive soils can provide the following information:

(a) a relationship between the load on the anchor and the corresponding displacement of the anchor in the soil, up to and beyond the ultimate uplift resistance of the soil;

(b) measurements of the surface deformation of the soil due to anchor displacement;

(c) measurements of the deformation and cracking within the soil mass due to anchor displacement;

(d) measurement of the porewater pressure distribution in the soil.

In the present program of laboratory model uplift resistance tests, the tests were performed in purely cohesive soils to obtain information relating to parts (a), (b) and (c) above. No measurement of the porewater pressure distribution in the soil (part (d)) was made, since it was considered that the difficulties involved in (i) assuring complete saturation of the uplift resistance sample, (ii) assuring the accurate placement of porewater measuring devices, (iii) assuring that the presence of these devices did not affect the soil behaviour, and (iv) assuring the placement of sufficient porewater pressure measuring devices to obtain an accurate picture of porewater pressure distribution, could not be overcome sufficiently to ensure accurate porewater pressure data.

With reference to part (c) above, the technique of placing

horizontal and vertical coloured layers in the sample before testing was adopted where measurement of the internal deformation of the soil was required. Details of this technique are described in section 4.4 of this chapter. Some recent researchers in soil mechanics, e.g. Burland and Roscoe (1969), have used X-ray techniques, by which the displacements inside the soil during a test could be measured by tracing the path of the lead shot which was placed in the sample during preparation. However, even assuming that the most powerful X-ray equipment was used, a penetration of not more than 250 mm was considered to be the maximum possible. This would limit an uplift resistance model test to such a reduced scale that the displacements of the lead shot due to anchor displacement would be extremely small and would require most sophisticated equipment to measure them accurately. In addition, the accurate placement of lead shot in the clay sample would be difficult.

In order to predict the magnitude and distribution of the radial and vertical normal stresses and shear stresses and the magnitude and direction of the principal stresses in the soil during the uplift resistance tests in the soil, a finite element analysis was developed by the author. This is described in chapter 5.

4.2. Properties of Soils used in the Uplift Resistance Tests

No naturally occurring soils were found which were considered to be suitable for modelling the uplift resistance problem, and so two clay soils were prepared in the laboratory for the investigations:

(a) a mixture of a sodium-bentonite clay (Fulbent 150) and glycerine. This clay is termed glyben. Four batches of glyben of different shear strengths were prepared.

(b) a mixture of clay from the Grangemouth area and Fayles Blue clay. This clay is termed modified Grangemouth clay. Only one batch of this clay was prepared.

Bentonite and glycerine has been used successfully as a laboratory material by Mayfield (1963) in order to simulate a saturated clay. Mayfield proposed that the mixture of "platy" particles of very small size (see Fig.4.1) which are present in Fulbent 150 with a liquid "binder" of low volatility and high polarity would produce a purely cohesive clay with stable mechanical properties. Undrained triaxial tests by Mayfield and by the author on various glyben mixtures have shown the material to be almost completely frictionless. Glyben possesses several advantages as a laboratory testing material. Since no perceptible evaporation of glycerine occurs at normal room temperatures and since glyben is completely insensitive to handling, repeated tests can be conducted using the same batch of material. Different strengths of glyben can be obtained by varying the proportions of bentonite and glycerine as shown in Fig. 4.2. The percentage glyben is defined as:

$$\frac{\text{the weight of glycerine}}{\text{the weight of bentonite}} \times 100$$

The main disadvantage of glyben is that the use of glycerine instead of water precludes the measurement of porewater pressure. In addition, samples of glyben cannot be sedimented from a slurry but must be formed by compaction, with the result that small quantities of air are unavoidably trapped in the sample.

The second clay which was prepared for the investigation was modified Grangemouth clay. Since the clay collected from the Grangemouth area had a high silt content, approximately 15% (by weight) of Fayles Blue clay (which is made up of a mixture of approximately 50% illite, 40% kaolinite, 5% quartz and 5% chlorite clay mineral particles) was mixed with it to increase its clay content and plasticity. However, from the results of uplift resistance tests and triaxial tests on partially-consolidated and partially-drained samples of this clay, it appears that some consolidation of the modified Grangemouth clay

took place at high values of stress, as discussed fully in chapter 6.

Particle size distribution curves for the two materials are shown in Fig. 4.1. Table 4.1 gives the values of liquid limit, plastic limit and the plasticity index for the modified Grangemouth clay. These tests are not applicable to glyben since it contains glycerine instead of water. Values of the specific gravity of the clays are also given in Table 4.1 along with the average water content of the modified Grangemouth clay during uplift resistance tests.

TABLE 4.1. SOIL PROPERTIES

Material / Property	Bentonite and Glycerine (Glyben)	Modified Grangemouth Clay
Liquid Limit (mc %)	—	34
Plastic Limit (mc %)	—	18
Plasticity Index (mc %)	—	16
mc % during tests	—	23.5 to 24.5
Specific Gravity of clay particles	2.76	2.92

mc = moisture content

It was suspected that samples of glyben and modified Grangemouth clay might be thixotropic. However, tests on samples of the two clays showed that neither was thixotropic. The values of the strength of the glyben varied with temperature, but the variation was found to be small over the range of temperatures which normally existed in the laboratory. To obviate any temperature effects however, samples were tested for strength immediately prior to uplift resistance testing, to ensure that the temperature of the glyben was the same during the strength tests as during the uplift resistance tests. The strength of the modified Grangemouth clay was found to be independent of temperature, in the range which existed in the laboratory. Glyben was found to be

hygroscopic in the long-term, due to the glycerine content, and was consequently stored inside polythene sheeting in a dry atmosphere.

4.3. A Description of the Apparati used in the Uplift Resistance Tests

A. Description of Loading

In chapter 1, two variations of the uplift resistance problem were illustrated, namely the high-mast foundation (pullout) problem and the shaft-raising (pushout) problem. In the high-mast foundation situation, the loading on the anchor is termed load-controlled, whereas in the shaft-raising (jacking-out) operation, the loading which is provided by the jack is termed displacement-controlled. Load-controlled loading is where discrete loads are applied to the anchor, and displacement-controlled loading is where the anchor is displaced by discrete or continucus amounts. A model uplift resistance apparatus must be capable of simulating not only pullout and pushout testing but also load-controlled and displacement-controlled loading.

B. General Apparatus

The primary purpose of this apparatus was to provide a means for determining the load-displacement relationships of the samples of clay under test, up to and beyond ultimate uplift resistance, and for the examination of the surface deformation of the samples during the test. The apparatus is illustrated in Figs. 4.3 and 4.4. Fig. 4.5 (a) and Fig. 4.5 (b) show photographs of the set-up which is illustrated in Fig. 4.4 (a), although the box in the photograph is the split-box, which is described in part C of this section.

The soil was compacted into one of three deep perspex boxes whose base dimensions were 300 mm, 500 mm and 900 mm square. The box was supported by a metal frame beneath which was the motor, gearbox and converter unit for displacement-controlled tests. For pullout tests, the loading was applied via a system of pulleys attached to a portal frame above the box. The round anchor plate could be positioned at any

height above the base of the box. Any suction effect which was generated below the anchor during the test could be eliminated by enabling atmospheric pressure to penetrate to the void below the anchor via a thin tube which connected a small hole through the base of the box to the anchor plate. The anchor plates were constructed of brass or steel and had smooth polished faces. The diameters of these plates ranged from 25 mm to 200 mm with the smaller anchor plates (25 mm to 100 mm diameter) being 3 mm thick, the larger ones 6 mm thick. For a particular test, the size of the box was chosen to give a suitable ratio of box-base to anchor diameter. In shallow tests with D/B less than or equal to 2, B_c/B ratios of the order of 4 (in very shallow tests) to 8 were used. In the deeper tests, larger B_c/B ratios were required because of possible boundary effects, and silicone grease was applied or PTFE sheets were provided between the clay and the perspex box sides to minimise these effects. For displacement-controlled tests, the anchor displacement rates could be varied by an alteration of the gearing in the gearbox. A Wykeham Farrance rotating bush was employed in pushout tests to ensure that friction on the pushout piston was reduced to a minimum. Vibration in the apparatus was minimised by the positioning of foam-rubber insulation beneath the motor for the loading mechanism, the motor for the rotating bush and the printout apparatus.

The apparatus could be simply adjusted for four combinations of testing and loading:

(a) Pushout test with displacement-controlled loading as illustrated in Fig. 4.4 (a).

(b) Pushout test with load-controlled loading as illustrated in Fig. 4.4.(b)

(c) Pullout test with displacement-controlled loading as illustrated in Fig. 4.3.

(d) Pullout test with load-controlled loading. If the threaded cable-end, shown as Ⓐ in Fig. 4.3 was detached from the lever arm, a weight-carrier and weights could be attached to the cable-end for the load-controlled test.

Two methods were employed to measure the surface deformations of the soil during uplift resistance testing. In the majority of tests a series of displacement transducers, attached to a gantry above the box, measured continuously during the test the vertical displacements at selected points on the surface of the clay as shown in Fig. 4.5 (b). In three tests, a time-lapse movie-camera was used to record, at one second intervals, the surface displacements during the test. The load on the anchor was measured by a load cell. Details of this cell, the displacement transducers which recorded the anchor displacement and the surface deformations, and the data processing, printing and punching equipment are given in Appendix B.

C. Split-Box Apparatus

The primary purpose of this apparatus was to provide a method for examining the displacements and cracking patterns (if any) which existed within the soil mass after the completion of an uplift resistance test. The apparatus is illustrated in Figs. 4.5, 4.6 and 4.7. The basic difference from the general apparatus occurred in the box construction. The perspex box was constructed in separate halves, which, when joined together, gave base dimensions of 600 mm square and a height of 450 mm. The base of each box-half was attached to a separate aluminium base plate. One of these base plates was bolted permanently to a large aluminium plate which was attached to the supporting frame. The other base plate was free to swivel, about a hinge-pin, on a layer of ball-bearings which were placed between the base plate and the large aluminium plate. During the compaction of the soil and the subsequent testing, the box-halves were clamped together and the set-up was similar to that

of the general test. It was essential that, after the completion of a test, the soil in the box was split apart, as opposed to being cut apart by a wire saw. The former arrangement ensured that details of soil texture and of cracking in the soil were not obscured by the smearing effect produced by a wire saw on soft clays. The photograph in Fig. 4.15 shows that all of the details of soil texture on the extreme left-hand side of the picture have been removed. This was where a wire saw was used and is in contrast to the rest of the clay face where the soil was "split" rather than cut.

After the completion of the test, the clamps were removed and the two halves of the box were jacked apart, one half remaining fixed, and the other half swivelling about the hinge-pin. By this method, a face of soil on a vertical plane which passed through the centre of the anchor plate could be exposed. As an alternative to splitting the soil by the swivelling action, the two halves of the box could be pulled apart directly. In order to achieve this, one box-half was freed from its aluminium base plate and was then slid directly backwards over a layer of ball-bearings which were placed between the base of the perspex box and the aluminium base plate. To facilitate sliding, the metal box-side supports were coated with PTFE. These side supports were a necessary part of the apparatus since the split box arrangement offered no resistance to bulging of the box sides when the box was filled with clay. Fig. 4.7 shows the swivelling and the direct splitting actions in diagrammatic form.

4.4. Methods of Preparation of Samples for Uplift Resistance Tests

A. Tests which used the General Apparatus

Glyben tests. Two methods of preparing the glyben samples were employed. In the first method, the glyben was kneaded manually into the box. This was a time-consuming process which required great care to ensure that as little air as possible was entrapped in the clay.

The samples which were prepared by this method were termed "layered" samples. In each box, a series of laboratory vane tests to measure the shear strength of the glyben were conducted at various stages of compaction. The results of these tests showed that a consistent strength of glyben could be achieved throughout the sample prepared in this manner. Initial uplift resistance tests and strength tests revealed that the bond in tension between the kneaded layers in samples of this material was weaker than in equivalent samples of unlayered material. In order to remove this weak tension bonding effect caused by the layering of the glyben, a second method of compaction was devised. An approximately cubical block of glyben was made up, outside the box, by kneading together small balls of the clay in a manner which ensured there was no preferred direction of compaction. The block was kneaded, rolled and handled until it was considered to be homogeneous and isotropic. The cubical block, which had sides of the order of three times the diameter of the anchor plate, was then placed in the box, on top of the anchor plate. The remaining clay in the box was then compacted by the "layering" method. The samples which were prepared by this method were termed "non-layered" samples.

Modified Grangemouth clay tests. It was found that samples which were prepared by the "layering" method, i.e. by the manual kneading of the clay into the box, did not exhibit the loss of tension bond between layers which was shown by "layered" glyben. This was the only method of compaction adopted for this material. Samples of this clay were always prepared and stored in a high humidity room in order to minimise any loss of moisture in the soil due to evaporation, and were only transferred to the testing rig immediately prior to testing.

B. Tests which used the Split-Box Apparatus

Glyben tests. Tests which used the split-box apparatus were divided into two basic categories: (a) tests in which coloured layers

were not inserted into the clay during sample preparation; (b) tests in which coloured layers were inserted into the clay during sample preparation.

(a) No coloured layers. The primary purpose of this test was to examine any cracking pattern in the clay which resulted from the upward displacement of the anchor. One sample of glyben was tested in this manner and was prepared by the "layered" method of compaction described earlier. After the completion of the test, the box was split open and the cracking pattern on the exposed clay face was examined and photographed. As with the other tests, the results of this test will be presented in sections 4.6 and 4.7 of this chapter.

(b) Coloured layers. Where coloured layers were required in the clay to demonstrate the internal movement of the clay due to anchor displacement, variations of the "layered" and "non-layered" techniques of compaction were devised. When glyben was kneaded into the box by hand, approximately horizontal layers of the clay were formed. However, it was recognised by the author that the simple compaction of alternate different coloured layers would not produce the desired horizontal layering appearance. In addition, this method precluded the insertion of vertical coloured layers into the clay in order to produce a "grid-iron" effect. Since the model tests being conducted by the author were axially-symmetric (assuming the clay in the square box to be a cylinder whose diameter was the width of the box) it was considered by the author that complete layers of coloured clay were unnecessary and that only thin strips of coloured clay, inserted on any vertical plane which passed through the centre of the anchor, were required. Two different methods of inserting horizontal and vertical coloured strips into the clay were devised.

The first method, illustrated in Fig. 4.8, did not make use of the split-box apparatus. The glyben was compacted into a box by the "layered" method of compaction. The box was similar to that used in the general apparatus except that the anchor plate, the rotating bush and the piston were located in the centre of one side of the box instead of on the base. The glyben was compacted to a level mid-way up the anchor plate. At this stage, strips of coloured glyben were inserted into the surface of the clay in a "grid-iron" pattern as shown in Fig. 4.8 (a). The glyben was then compacted up to the top of the box, much care being taken not to disturb the position of the coloured strips, as shown in Fig. 4.8 (b). The box was then rotated through an angle of 90^{o} so that the side which contained the anchor plate, rotating bush and piston formed the base of the box. The layer which contained the coloured strips was then on a vertical plane which passed through the centre of the anchor. The side which formed the closed top of the box (side @) was removed and placed on the open side which had previously been the open top of the box, as illustrated in Fig. 4.8 (c). The pushout test was then performed and afterwards the glyben was carefully removed to reveal the displaced coloured layers and cracking patterns in the clay, as shown in Fig. 4.8 (d). The samples which were prepared by this method were termed "rotated-box" samples. A series of five tests was performed using this method and one test was performed using this method of compaction and rotation but without the insertion of the coloured strips.

The second method of inserting coloured strips used the split-box apparatus and one sample of glyben was prepared and tested. The sample was compacted into the box by the "layered" method. It was then cut in half by a wire saw and the halves of the box were

unclamped and pulled apart using the swivelling action of the split-box apparatus. Horizontal and vertical strips of coloured glyben were inserted into one of the exposed clay faces. The halves of the split-box were then clamped together again and the test was commenced. After completion of the test, the box was split open and the displaced coloured layers and internal cracking were examined and photographed. The sample which was prepared by this method was termed the "split-box coloured layer" sample.

Modified Grangemouth clay. No coloured layer tests were performed in this clay. However, one sample was prepared by the "split-box coloured layer" method with the coloured layers omitted. The cracking pattern in the exposed face of the clay was examined and photographed after the completion of the test.

4.5. Tests to Measure the Strength, Bulk Density and Volume Change of the Clay Samples

The bulk densities of each of the four batches of glyben and the batch of modified Grangemouth clay were measured by compacting them into six-inch concrete cube moulds, which provided an extremely accurate measure of volume, and calculating the net weight of the clay in the mould. The samples were compacted in either a "layered" or "non-layered" manner to simulate compaction of the clays in the uplift resistance tests. No difference was found between the bulk densities of the "layered" and"non-layered" samples. The bulk densities of the batches of clay are given in Table 4.2.

The values of the strengths of the clays were measured by laboratory vane tests, undrained triaxial compression tests and tension tests. Details of the equipment and testing procedures are given in Appendix C. Because of the dimensional considerations which were discussed in chapter 3, the clays were prepared in order to give low values of shear strength, which allowed them to be compacted manually for use in the

model uplift resistance test samples. Below a value of shear strength of the order 5 kN/m^2, the clays became sticky and viscous and were difficult to handle and compact. Above a value of shear strength of the order of 15 kN/m^2, the clays became too stiff for manual compaction. Table 4.2 shows a summary of the strength values obtained for the two clays by the various strength testing procedures. The results of these tests will be discussed fully in chapter 6. Fig. 4.9 is included at this stage to show representative curves of values of deviatoric stress versus strain, plotted from the results of tests to measure the compressive strength and tensile strength of glyben. Fig. 4.10 shows similar curves for modified Grangemouth clay.

Standard Volume Change Measurement tests were conducted on samples of glyben and modified Grangemouth clay to investigate the possible significance of the small amount of air entrapped in the uplift resistance test samples during compaction. Details of these experiments and the test samples are given in Appendix D. The volume change of the sample was measured under two separate forms of loading, namely a change in cell pressure and an axial (deviatoric) loading. Fig. 4.11 illustrates the relationship between the cell pressure applied to the samples and the resulting percentage change in the volume of the samples. The significance of these volume changes will be discussed in chapter 6. Deviatoric stresses were applied to the samples up to failure, but did not cause any measurable volume change in either glyben or modified Grangemouth clay.

4.6. Details of Unlift Resistance Testing Program performed by the Author

A total number of 65 model uplift resistance tests were performed by the author, and details of the testing program are shown in Table 4.3. The majority of tests were displacement-controlled pushout tests since a considerably greater degree of control could be exercised over the location of the anchor plate in the pushout tests. In addition,

the soil above the anchor in these tests could be compacted more easily, due to the absence of the anchor shaft necessary in pullout tests. This was of particular importance in the "non-layered" compaction of glyben.

One shallow and one deep model anchor pullout test were conducted in "layered" glyben with the suction effect eliminated, and one shallow and one deep model anchor pullout test were conducted with the suction effect included. In addition, a pullout test using only the anchor shaft was performed in order to calculate the value of the adhesion between the shaft and the glyben. This value of adhesion was subtracted from the values of the ultimate uplift resistance of the non-suction pullout tests and the resulting adjusted values of ultimate uplift resistance of these tests were found to be similar to the values of ultimate uplift resistance for the equivalent non-suction pushout tests. Similarity between the mechanisms of pushout and pullout had previously been hypothesized in chapter 1, and, in view of the similar pushout and pullout results, it was considered by the author unnecessary to perform any additional pullout tests.

In the load-controlled tests in glyben, as the clay neared its ultimate uplift resistance, the effects of creep in the glyben on the displacement of the anchor were noted. These creep effects are discussed in chapter 6. Two load-controlled pushout tests (one shallow anchor and one deep anchor test) were performed in "layered" glyben in order to compare the results with equivalent displacement-controlled tests. No load-controlled tests were conducted in modified Grangemouth clay. In view of the argument presented in the previous paragraph, no load-controlled pullout tests were conducted in glyben.

The majority of the tests which used the general apparatus were conducted with the anchor plate located at the base of the box at the start of the test. However, a number of tests were carried out with the anchor plate located above the base of the box, in order to test

whether there was any significant difference in the results. In the "rotated-box" tests, the anchor plate had to be located at the base of the box at the start of each test. In all of the split-box tests, the anchor plate was located above the base of the box.

4.7. Presentation of Uplift Resistance Test Results

In this section the details and results of the model uplift resistance tests which were conducted by the author will be presented. The results of these tests will be compared and discussed in chapter 6.

Table 4.4 gives a summary of the details and the results of all of the model uplift resistance tests which were performed by the author. The table includes details of the soil, anchor, and box parameters of each test, i.e. the anchor plate diameter B, the width of the base of the box B_c, the bulk density of the clay γ, and the value of shear strength of the clay c which was measured by laboratory vane test in each box prior to testing. The dimensionless ratios $c/\gamma_g B$, $c/\gamma_g D$ and D/B are also included. The ultimate uplift resistance pressure p_u for each test and the resulting values of $p_u/\gamma_g D$ and the ultimate uplift resistance factor $\bar{F}_u$ are shown. The displacement of the anchor at any stage of the test is symbolised by d_a and the displacement of the anchor at ultimate-uplift resistance $d_{a(max)}$ in each test is given in the table. The last column of the table gives values of the ratio $\frac{d_a \text{ at } 0{\cdot}9\, p_u}{B}$ for each test. d_a at $0{\cdot}9\, p_u$ represents the amount of displacement which the anchor has undergone from the start of the test until the uplift resistance of the soil is at 90% of its ultimate value. The values of d_a at $0{\cdot}9\, p_u$ were obtained from the uplift resistance pressure versus the anchor displacement curves which were calculated for each test. The value of d_a at $0{\cdot}9\, p_u$ is used instead of the value of d_a at p_u since, as the ultimate uplift resistance of the clay was approached in each test, very large increments of anchor displacement occurred for

correspondingly small increments in the value of uplift resistance and the precise value of anchor displacement at ultimate uplift resistance was difficult to estimate.

The results of the uplift resistance tests can be divided into three sections for presentation purposes.

A. Measurement of internal and surface displacement and cracking in the clay.

B. Relationship between uplift resistance and anchor displacement during the tests.

C. Values of ultimate uplift resistance of the clays.

The order in which the results are presented in this chapter will be the order in which they are discussed in chapter 6.

A. Measurement of Internal and Surface Deformation and Cracking of the Clay

Internal deformation and cracking measurement of the clay. It was considered that a knowledge of the deformation and cracking patterns which existed within the clay at ultimate uplift resistance would assist in determining the mechanism of ultimate failure of the clay. An interpretation of the sample cross-sections which are shown in the photographs, described in the following paragraph, is made in chapter 6 in terms of the mechanism of ultimate failure of the samples.

Fig. 4.12 shows a photograph of the displacement of the coloured strips and the cracking within a sample of glyben at ultimate uplift resistance on a section taken through the centre of the anchor plate (test no. 49 with D/B = 1.6). Figs. 4.13 and 4.14 illustrate the corresponding displacements and cracking patterns at ultimate uplift resistance for values of D/B = 3 in test no. 50 and D/B = 4.5 in test no. 52 respectively. These three samples were prepared by the "rotated-box" method. Fig. 4.15 shows a photograph of the cracking which occurred at ultimate uplift resistance within "layered" glyben in test no. 53 with D/B = 1.5, prepared without coloured strips in the

split-box apparatus. Fig. 4.16 shows a photograph of the displacement of the coloured strips and the cracking which occurred at ultimate uplift resistance within "layered" glyben test no. 54 with D/B = 1.5, prepared in the split-box apparatus. Fig. 4.17 shows a photograph of the cracking which occurred at ultimate uplift resistance within the sample of modified Grangemouth clay in test no. 65 with D/B = 1.42, prepared without coloured strips in the split-box apparatus.

Measurement of deformation and cracking on the surface of the clay.

It was considered that, in addition to a knowledge of the internal deformation and cracking within the clay, a knowledge of the deformation and cracking patterns which occurred at the surface of the clay during testing would assist in determining the mechanism of ultimate failure of the clay. An interpretation and discussion of the results which are described in the following paragraphs are given in chapter 6.

Before the ultimate uplift resistance of the clay was reached in shallow anchor tests with D/B less than approximately 2, considerable surface deformation and surface cracking occurred in the samples of both glyben and modified Grangemouth clay. In tests in the intermediate range of depths with D/B values from approximately 2 to 4.5, considerably less surface deformation and cracking were observed, and in the deep anchor tests with D/B greater than approximately 4.5, no surface cracking was noted and very little surface deformation was recorded before ultimate uplift resistance.

The symbol d_s is used to represent the vertical displacement of the sample surface directly above the centre of the anchor plate.

Fig. 4.18 illustrates the values of $\frac{d_s \text{ at } 0{\cdot}9\, p_u}{d_a \text{ at } 0{\cdot}9\, p_u}$ v D/B for each displacement-controlled model uplift resistance pushout test performed by the author. $\frac{d_s \text{ at } 0{\cdot}9\, p_u}{d_a \text{ at } 0{\cdot}9\, p_u}$ is the ratio of the surface displacement above the anchor plate to the displacement of the anchor plate

at 90% of ultimate uplift resistance. Values of displacement at 90% of the ultimate uplift resistance of the clay were chosen for reasons outlined at the beginning of this section. The best-fitting curve has been drawn through the points which represent the results for "layered" glyben in Fig. 4.18.

In shallow anchor tests, the deformed surface of the sample took the form of a bulge (which exhibited considerable cracking) as the ultimate uplift resistance of the clay was approached. Fig. 4.19 shows photographs of the surface of a sample of "layered" glyben in both elevation (Fig. 4.19(a)) and plan (Fig. 4.19 (b)) at an anchor displacement of 2.6 times the displacement to ultimate uplift resistance. In those uplift resistance tests in which the sizes and shapes of the surface bulges were clearly defined, the diameters of the surface bulges ω were measured and are shown in Fig. 4.20, plotted as ω/B v D/B.

B. Relationship between Uplift Resistance and Anchor Displacement

Since a knowledge of the amount of anchor displacement corresponding to various levels of anchor load is essential in both the high-mast foundation and jacking-out situations, it was considered important that the curves which depicted the extent to which various factors influenced the load-displacement relationship between anchor and clay be included. An interpretation of the curves which are described in the following paragraphs will be given in chapter 6.

As described in chapter 3, the uplift resistance of the clay can be represented by the dimensionless uplift resistance factor $\bar{F}$, where $\bar{F} = \frac{b - \gamma_g D}{c}$. The displacement of the anchor d_a is shown in terms of the dimensionless ratio d_a/B. Fig. 4.21 illustrates representative curves of $\bar{F}$ v d_a/B for a shallow, an intermediate depth and a deep anchor test in "layered" glyben. Fig. 4.22 and Fig. 4.23 depict $\bar{F}$ v d_a/B for "non-layered" glyben and modified Grangemouth

clay respectively.

Fig. 4.24 illustrates the difference between values of the uplift resistance factor versus the anchor displacement ratio demonstrated by shallow anchor pullout tests in "layered" glyben with $D/B = 1.5$, where one test was conducted with the suctional effect acting below the anchor (test no. 43), and one test was conducted without it (test no. 41). Fig. 4.25 shows the $\bar{F}$ v d_a/B curve for load-controlled test no. 46 with $D/B = 4.5$, compared to the curve for an equivalent displacement-controlled test (test no. 26).

In each test which was performed, it was observed that the amount of anchor displacement which occurred before the ultimate uplift resistance of the clay was reached varied with the D/B ratio of the test, with the clay type, and with its method of compaction. Fig. 4.26 illustrates the dimensionless ratio $\frac{d_a \text{ at } 0.9\, p_u}{B}$ plotted against D/B for each of the displacement-controlled model uplift tests. (The numbers of the points on the graph denote the test numbers). In Fig. 4.26, three best-fitting curves have been drawn through the points which represent the results of the tests in "layered" glyben, "non-layered" and "rotated-box" glyben, and modified Grangemouth clay.

C. Values of Ultimate Uplift Resistance of the Clays

One of the primary purposes of the present investigation was to find the values of the ultimate uplift resistance of purely cohesive soils at various depths, and to investigate the factors which influenced these values. The results which are presented in the following paragraphs are discussed fully in chapter 6.

As was mentioned in chapter 3, a series of model tests in "layered" glyben were conducted with the purpose of finding the values of $p_u/\gamma_g D$ which corresponded to a range of D/B values and selected values of $c/\gamma_g D$. Fig. 4.27 depicts the curves of $p_u/\gamma_g D$ v $c/\gamma_g D$ v D/B

which were obtained from these tests. (The numbers of the points on the graph denote the test numbers). The shear strengths of the samples of glyben and the anchor dimensions were chosen in order to provide values of $p_u/\gamma_g D$ v D/B for $c/\gamma_g D$ values of 1.75, 2.5 and 3.7. Because of slight variations in the strengths of the glyben in different tests, the values of $c/\gamma_g D$ were not always exactly those required, as can be seen from Table 4.4. The values of $p_u/\gamma_g D$ in Fig. 4.27 have been adjusted to make the corresponding values of $c/\gamma_g D$ exactly 1.75, 2.5 or 3.7 by assuming p_u to be proportional to c .

The values of the ultimate uplift resistance factor $\bar{F}_u$ versus D/B for the complete program of model uplift resistance tests performed by the author are shown in Fig. 4.28 Fig. 4.29 shows the values of $\bar{F}_u$ v D/B for all of the tests in which the value of D/B was less than 2.1. In both figures, three best-fitting curves have been drawn through the points which represent the results of tests in "layered" glyben, "non-layered" and "rotated-box" glyben, and modified Grangemouth clay.

In this chapter, details of the uplift resistance model tests which were conducted by the author have been outlined and the results from these tests have been presented. The results will be compared and discussed in chapter 6. In chapter 5, a description of the finite element analysis for the uplift resistance problem will be given and the results from the analysis will be presented.

TABLE 4.2. AVERAGE VALUES OF STRENGTH AND BULK DENSITY OF GLYBEN AND MODIFIED GRANGEMOUTH CLAY

Material \ Parameter		Average Shear Strength			Average Compressive and Tensile Strengths			Bulk Density of Clay (kg /m³)
		Laboratory vane test (kN/m²)	Unconfined Triaxial compression test (kN/m²)	Triaxial value / Vane value	Unconfined compressive strength (kN/m²)	Unconfined tensile strength (kN/m²)	tensile value / compressive value	
GLYBEN	BATCH No.1	5·10	3·40 *	0·67	6·80 *	—	—	1.64×10^3
	BATCH No.2	6·10	4·53 **	0·74	9·06 **	—	—	1.66×10^3
	BATCH No.3	8·84	7·55 **	0·85	15·10 **	—	—	1.70×10^3
	BATCH No.4	16·20	13·70 **	0·85	27·40 **	5·54 + 16·10 ++	0·20 + 0·59 ++	1.74×10^3
MODIFIED GRANGEMOUTH CLAY		9·67	10·10 **	1·04	20·20 **	7·5	0·37	2.00×10^3

* Samples extruded from 1½ inch diameter sampling tubes

** Samples trimmed from block of clay

\+ Tests on "layered" samples

++ Tests on "non-layered" samples

TABLE 4.3. DETAILS OF MODEL UPLIFT RESISTANCE TESTING PROGRAM

	Clay Type	Test Details	Displacement - controlled Loading		Load - controlled Loading
			Pushout	Pullout	Pushout
General Tests	Glyben	'Layered' compaction	GA 1 to 32 (inclusive)	GC 41, 42, 43^{+}, 44^{+}	GD 45, 46
		'Non-layered' compaction	GB 33 to 40 (inclusive)	—	—
	Modified Grangemouth Clay		MA 55 to 64 (inclusive)	—	—
Internal deformation and cracking Tests	Glyben	'Rotated-box'	GE 47, 48*, 49*, 50*, 51, 52*	—	—
		'Split-box'	GF 53, 54*	—	—
	Modified Grangemouth Clay		MF 65	—	—

* Tests using coloured strips

\+ Tests including full suction effect

Tests 10, 25, 26, 31, 43, 53, 54, 58 and 65 were carried out with the initial location of the anchor plate B above the base of the box, test 44 with the anchor plate 2B above the base. In the remaining tests, the initial location of the plate was on the base of the box.

TABLE 4.4 (a). DETAILS AND RESULTS OF UPLIFT RESISTANCE TESTS IN GLYBEN

Test Number	Category	Anchor dimensions			Box	Soil parameters			$d_{a(max)}$ (mm)	$c/\gamma_g B$	$c/\gamma_g D$	p_u (kN/m²)	$p_u/\gamma_g D$	F_u	$\frac{d_a \text{ at } 0.9 p_u}{B}$
		B (mm)	D (mm)	D/B	B_c (mm)	Batch Number	γ (kg/m³ x 10³)	c (kN/m²)							
1	GA	100	60	0·6	500	3	1·70	8·63	12	5·17	8·63	11·72	11·72	1·20	0·050
2	GA	100	75	0·75	300	2	1·66	6·13	15	3·77	5·02	9·51	7·79	1·35	0·063
3	GA	100	97·5	0·975	500	1	1·64	5·30	22	3·30	3·38	12·43	7·93	2·05	0·092
4	GA	66·7	66·7	1·0	300	4	1·74	18·14	18	15·94	15·94	33·14	29·12	1·76	0·117
5	GA	66·7	75	1·125	300	2	1·66	6·13	22	5·65	5·02	16·94	13·06	2·40	0·126
6	GA	200	230	1·15	900	3	1·70	6·96	68	2·11	1·82	20·54	5·36	2·40	0·130
7	GA	66·7	97·5	1·46	500	1	1·64	5·00	28	4·66	3·19	17·94	11·44	3·27	0·165
8	GA	100	150	1·50	500	2	1·66	6·18	32	3·80	2·53	21·55	8·83	3·09	0·147
9	GA	50	75	1·50	300	2	1·66	6·08	22·5	7·47	4·98	21·17	17·34	3·28	0·194
10	GA	100	150	1·50	500	3	1·70	9·02	47	5·41	3·61	30·40	12·16	3·09	0·230
11	GA	200	310	1·55	900	3	1·70	6·67	100	2·02	1·31	26·53	5·19	3·21	0·175
12	GA	100	195	1·95	500	1	1·64	5·00	40	3·10	1·59	22·88	7·04	3·93	0·196
13	GA	50	100	2·0	300	2	1·66	5·79	23	7·11	3·55	25·37	15·58	4·10	0·248
14	GA	33·3	75	2·25	300	2	1·66	5·88	17	10·85	4·82	29·18	23·90	4·76	0·273
15	GA	66·7	150	2·25	500	2	1·66	5·88	40	5·41	2·41	27·72	11·36	4·22	0·274
16	GA	66·7	195	2·925	500	1	1·64	5·00	43	4·66	1·59	29·21	9·31	5·21	0·285
17	GA	50	150	3·0	300	2	1·66	6·08	38	7·47	2·49	30·03	12·30	4·94	0·376
18	GA	33·3	100	3·0	300	2	1·66	5·88	22	10·85	3·61	34·61	21·26	5·61	0·370

continued on next page

TABLE 4.4 (a). CONTINUED

Test Number	Category	Anchor dimensions			Box	Soil parameters			d_a (max)	$c/\gamma_g B$	$c/\gamma_g D$	p_u	$p_u/\gamma_g D$	F_u	$\frac{d_a \text{ at } 0.9 p_u}{B}$
		B (mm)	D (mm)	D/B	B_c (mm)	Batch Number	γ ($kg/m^3 \times 10^3$)	c (kN/m^2)	(mm)			(kN/m^2)			
19	GA	25	75	3·0	300	2	1·66	6·03	19	14·81	4·94	35·07	28·73	5·61	0·372
20	GA	100	300	3·0	500	3	1·70	7·26	82	4·36	1·45	41·91	8·38	5·08	0·370
21	GA	33·3	120	3·6	300	4	1·74	15·40	30	27·10	7·52	100·34	49·01	6·38	0·390
22	GA	25	100	4·0	300	2	1·66	6·57	25	16·14	4·04	44·00	27·03	6·45	0·430
23	GA	50	200	4·0	300	2	1·66	5·88	50	7·22	1·81	35·82	11·00	5·54	0·450
24	GA	33·3	150	4·5	300	2	1·66	6·28	35	11·58	2·57	39·57	16·20	5·91	0·440
25	GA	33·3	150	4·5	500	3	1·70	9·90	36	17·84	3·96	72·14	29·55	7·04	0·342
26	GA	66·7	300	4·5	500	3	1·70	8·24	67	7·41	1·65	55·50	11·10	6·13	0·412
27	GA	66·7	300	4·5	500	3	1·70	8·29	65	7·45	1·66	55·63	11·12	6·11	0·560
28	GA	50	300	6·0	500	3	1·70	9·02	88	10·82	1·80	62·52	12·50	6·38	0·516
29	GA	25	150	6·0	300	2	1·66	6·28	38	15·43	2·57	45·34	18·57	6·83	0·544
30	GA	33·3	200	6·0	300	2	1·66	6·18	58	11·40	1·90	40·89	12·56	6·09	0·612
31	GA	33·3	200	6·0	500	3	1·70	9·90	42·5	17·84	2·97	73·72	22·11	7·10	0·510
32	GA	25	200	8·0	300	2	1·66	6·23	43	15·31	1·91	44·74	13·74	6·66	0·856
33	GB	100	40	0·4	500	3	1·70	8·43	11	5·05	12·64	7·80	11·70	0·85	0·048
34	GB	100	60	0·6	500	3	1·70	8·43	13	5·05	8·43	11·81	11·81	1·28	0·058
35	GB	66·7	66·7	1·0	300	4	1·74	16·38	12·5	14·40	14·40	38·90	34·18	2·31	0·066
36	GB	50	100	2·0	300	4	1·74	17·65	15	20·69	10·34	85·29	49·99	4·74	0·140

continued on next page

TABLE 4.4 (a). CONTINUED

Test Number	Category	Anchor dimensions			Box	Soil parameters									
		B (mm)	D (mm)	D/B	B_c (mm)	Batch Number	γ ($kg/m^3 \times 10^3$)	c (kN/m^2)	$d_{a(max)}$ (mm)	$c/\gamma_g B$	$c/\gamma_g D$	p_u (kN/m^2)	$p_u/\gamma_g D$	F_u	$\frac{d_a \text{ at } 9p_u}{B}$
37	GB	33·3	100	3·0	300	4	1·74	15·40	19·5	27·10	9·02	100·56	58·93	6·42	0·231
38	GB	33·3	133·3	4·0	300	4	1·74	15·30	21	26·93	6·73	107·41	47·22	6·83	0·258
39	GB	33·3	166·7	5·0	300	4	1·74	15·10	23	26·57	5·31	112·69	39·63	7·27	0·300
40	GB	66·7	350	7·0	500	3	1·70	8·24	66	7·41	1·41	67·41	11·55	7·47	0·285
41	GC	100	150	1·5	500	3	1·70	9·23	39	5·35	3·57	31·91	12·76	3·30	0·194
42	GC	66·7	300	4·5	500	3	1·70	9·81	87	8·82	1·96	62·29	12·45	5·84	0·350
43	GC	100	150	1·5	500	3	1·70	9·12	44	5·47	3·65	58·92	23·56	6·19	—
44	GC	66·7	250	3·75	500	3	1·70	8·92	36	8·02	2·14	85·77	20·58	9·15	—
45	GD	100	150	1·5	500	3	1·70	9·32	—	5·59	3·73	29·53	11·81	2·90	—
46	GD	66·7	300	4·5	500	3	1·70	9·32	—	8·38	1·86	67·68	13·53	6·73	—
47	GE	100	160	1·6	500	3	1·70	8·38	29	5·03	3·14	38·97	14·61	4·33	0·111
48	GE	100	160	1·6	500	3	1·70	8·38	27·5	5·03	3·14	39·65	14·87	4·41	0·125
49	GE	100	160	1·6	500	3	1·70	8·38	27	5·03	3·14	39·10	14·66	4·35	0·121
50	GE	66·7	200	3·0	500	3	1·70	9·81	35	8·82	2·94	66·00	19·79	6·39	0·180
51	GE	66·7	300	4·5	500	3	1·70	8·38	49	7·54	1·68	63·90	12·78	7·03	0·277
52	GE	66·7	300	4·5	500	3	1·70	8·24	50	7·41	1·65	63·50	12·70	7·10	0·277
53	GF	100	150	1·5	500	3	1·70	11·08	27	6·65	4·43	36·59	14·63	3·08	0·120
54	GF	100	150	1·5	500	3	1·70	11·67	24·5	7·00	4·67	41·01	16·40	3·30	0·110

continued on next page

TABLE 4.4 (b). DETAILS AND RESULTS OF UPLIFT RESISTANCE TESTS IN MODIFIED GRANGEMOUTH CLAY

Test Number	Category	Anchor dimensions			Box	Soil parameters			$d_{a(max)}$	$c/\gamma_g B$	$c/\gamma_g D$	p_u	$p_u/\gamma_g D$	F_u	$\frac{d_a \text{ at } 0.9 p_u}{B}$
		B (mm)	D (mm)	D/B	B_c (mm)	Batch Number	γ ($kg/m^3 \times 10^3$)	c (kN/m^2)	(mm)			(kN/m^2)			
55	MA	100	60	0·6	500	—	2·00	10·79	18·5	5·50	9·20	12·27	10·43	1·03	0·087
56	MA	100	100	1·0	500	—	2·00	9·90	33·9	5·05	5·05	2552	13·01	2·38	0·195
57	MA	100	150	1·5	500	—	2·00	8·92	44·3	4·55	3·03	38·95	13·24	4·04	0·265
58	MA	50	90	1·8	500	—	2·00	10·39	31·8	10·59	5·89	52·88	29·96	4·92	0·282
59	MA	66·7	150	2·25	500	—	2·00	8·92	46·2	6·82	3·03	59·12	20·10	6·30	0·457
60	MA	50	150	3·0	500	—	2·00	9·02	57·7	9·20	3·07	74·45	25·31	7·93	0·660
61	MA	50	187·5	3·75	500	—	2·00	9·22	70·9	9·40	2·51	84·64	23·02	8·78	0·720
62	MA	33·3	150	4·5	500	—	2·00	9·71	69·0	14·87	3·30	97·18	33·03	9·71	1·095
63	MA	33·3	175	5·25	500	—	2·00	9·90	67·5	15·16	2·89	103·84	30·25	10·14	0·960
64	MA	33·3	200	6·0	500	—	2·00	9·90	72·6	15·16	2·52	104·38	26·61	10·14	0·915
65	MF	50	71	1·42	500	—	2·00	10·79	20·4	11·00	7·75	43·93	31·55	3·94	0·230

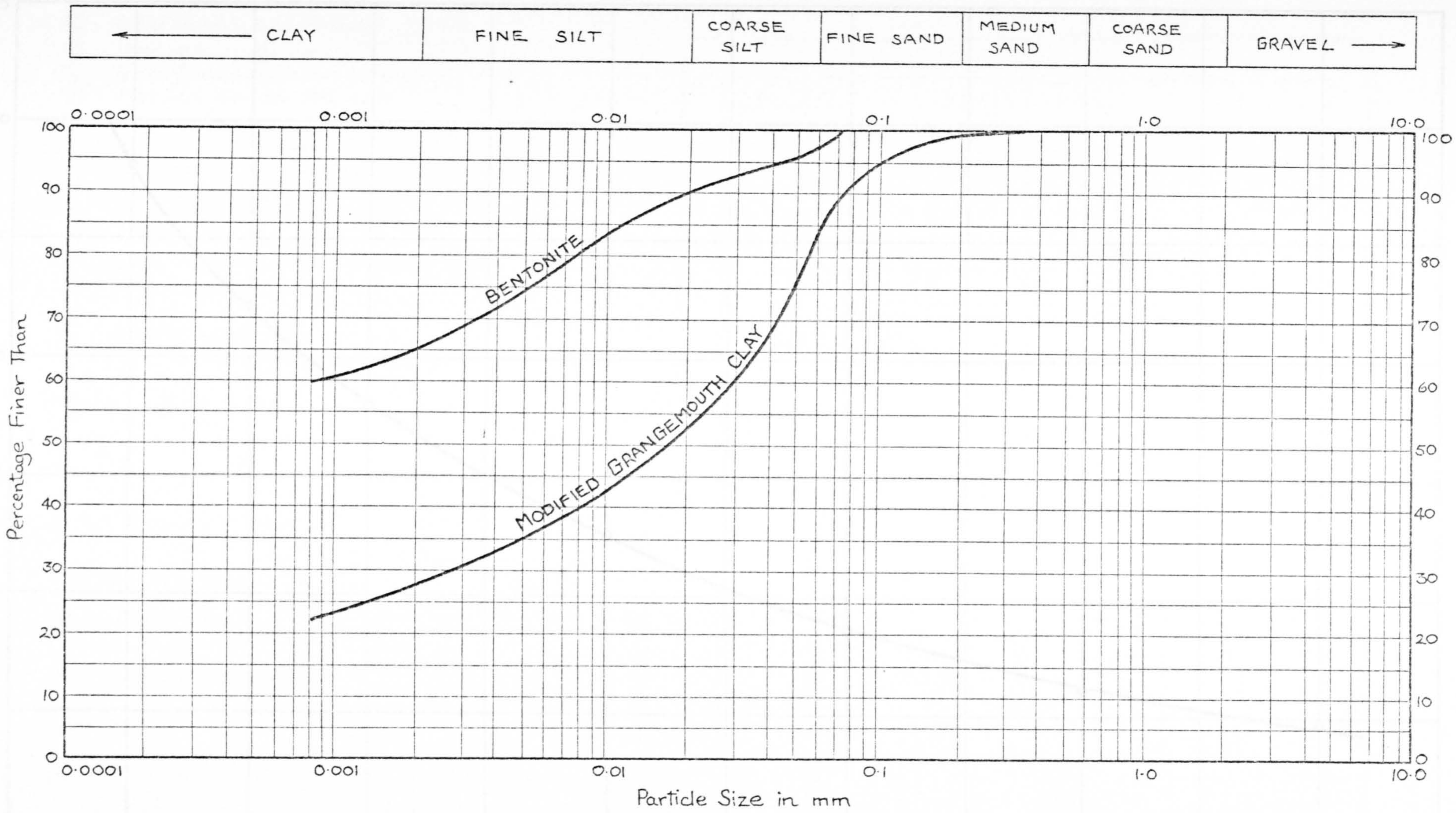

FIG. 4.1. PARTICLE SIZE DISTRIBUTION CHARTS FOR BENTONITE (FULBENT 150) AND MODIFIED GRANGEMOUTH CLAY

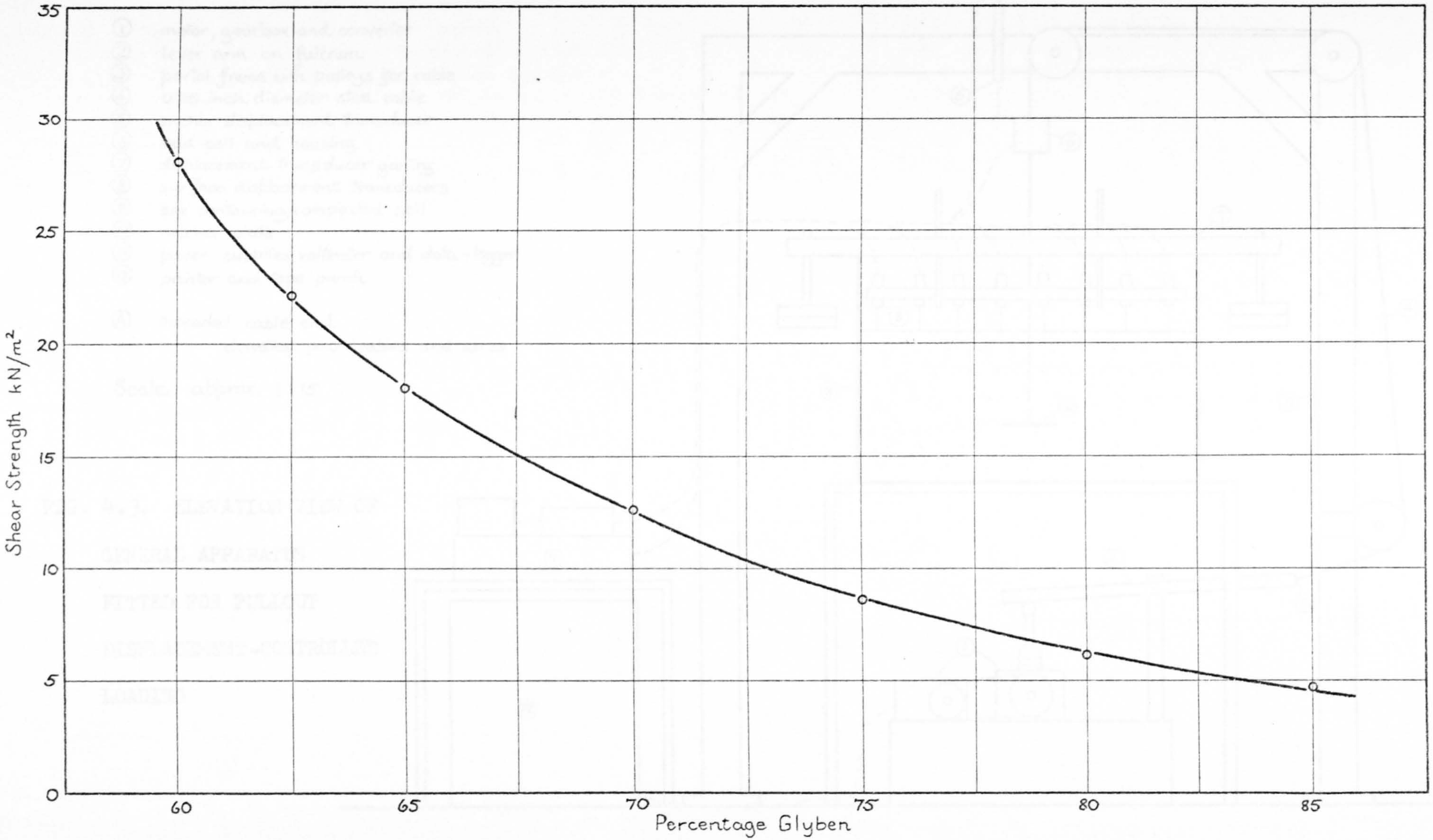

FIG. 4.2. SHEAR STRENGTH OF A RANGE OF GLYBEN MIXES

① motor, gearbox and converter
② lever arm on fulcrum
③ portal frame with pulleys for cable
④ 0·25 inch diameter steel cable
⑤ anchor displacement transducer
⑥ load cell and housing
⑦ displacement transducer gantry
⑧ surface displacement transducers
⑨ box containing compacted soil
⑩ anchor plate
⑪ power supplies, voltmeter and data-logger
⑫ printer and tape punch

Ⓐ threaded cable end
– – – – – denotes power cables and wires

Scale approx. 1 : 15

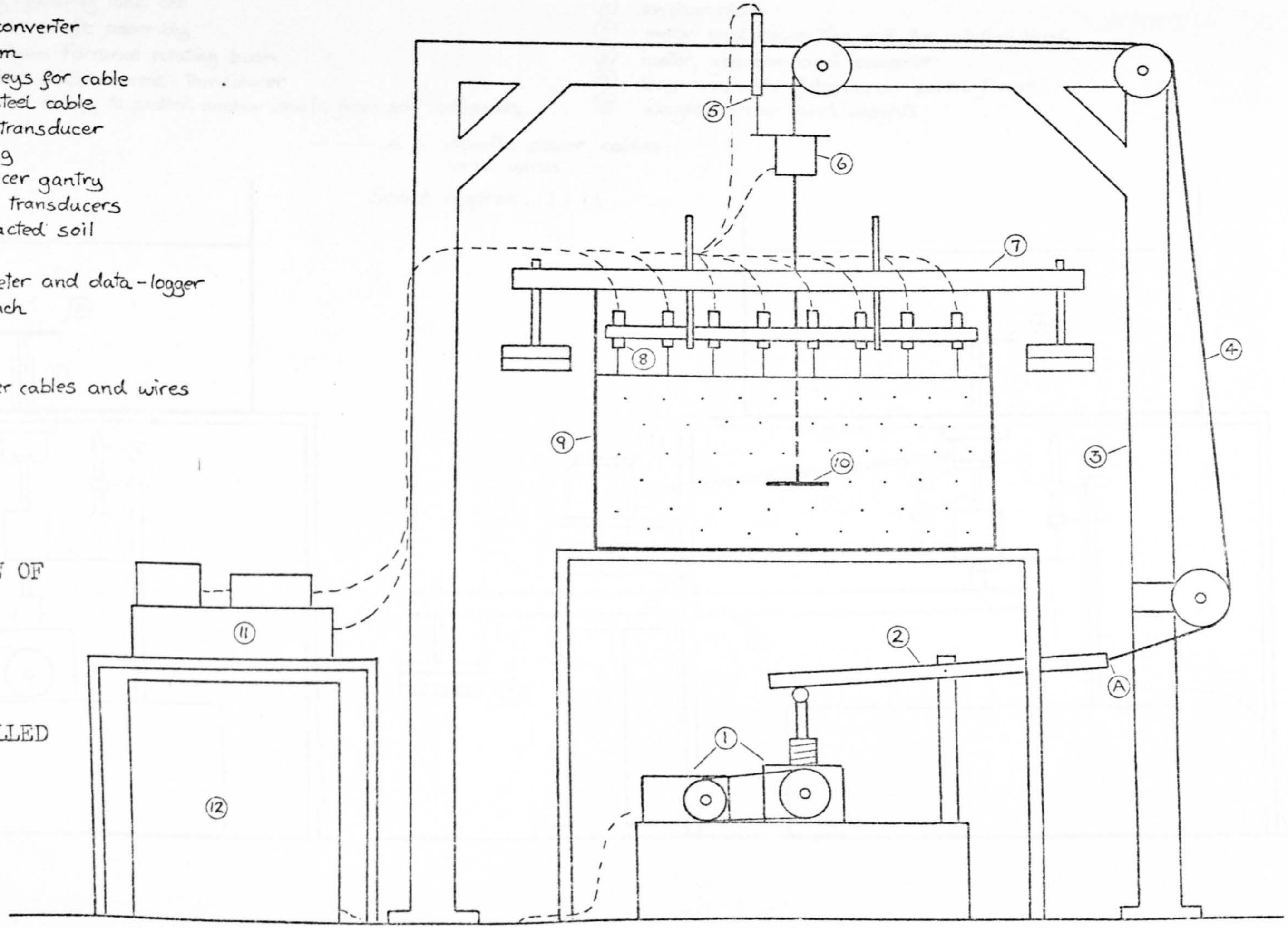

FIG. 4.3. ELEVATION VIEW OF GENERAL APPARATUS FITTED FOR PULLOUT DISPLACEMENT-CONTROLLED LOADING

① fully-floating load cell
② anchor shaft assembly
③ Wykeham Farrance rotating bush
④ anchor displacement transducer
⑤ threaded casing to protect anchor shaft from soil adhesion
⑥ anchor plate
⑦ motor and connecting rod for rotating bush
⑧ motor, gearbox and converter
⑨ lever arm with fulcrum on portal frame
⑩ weight carrier and weights

– – – – – denotes power cables and wires

Scale approx. 1:11

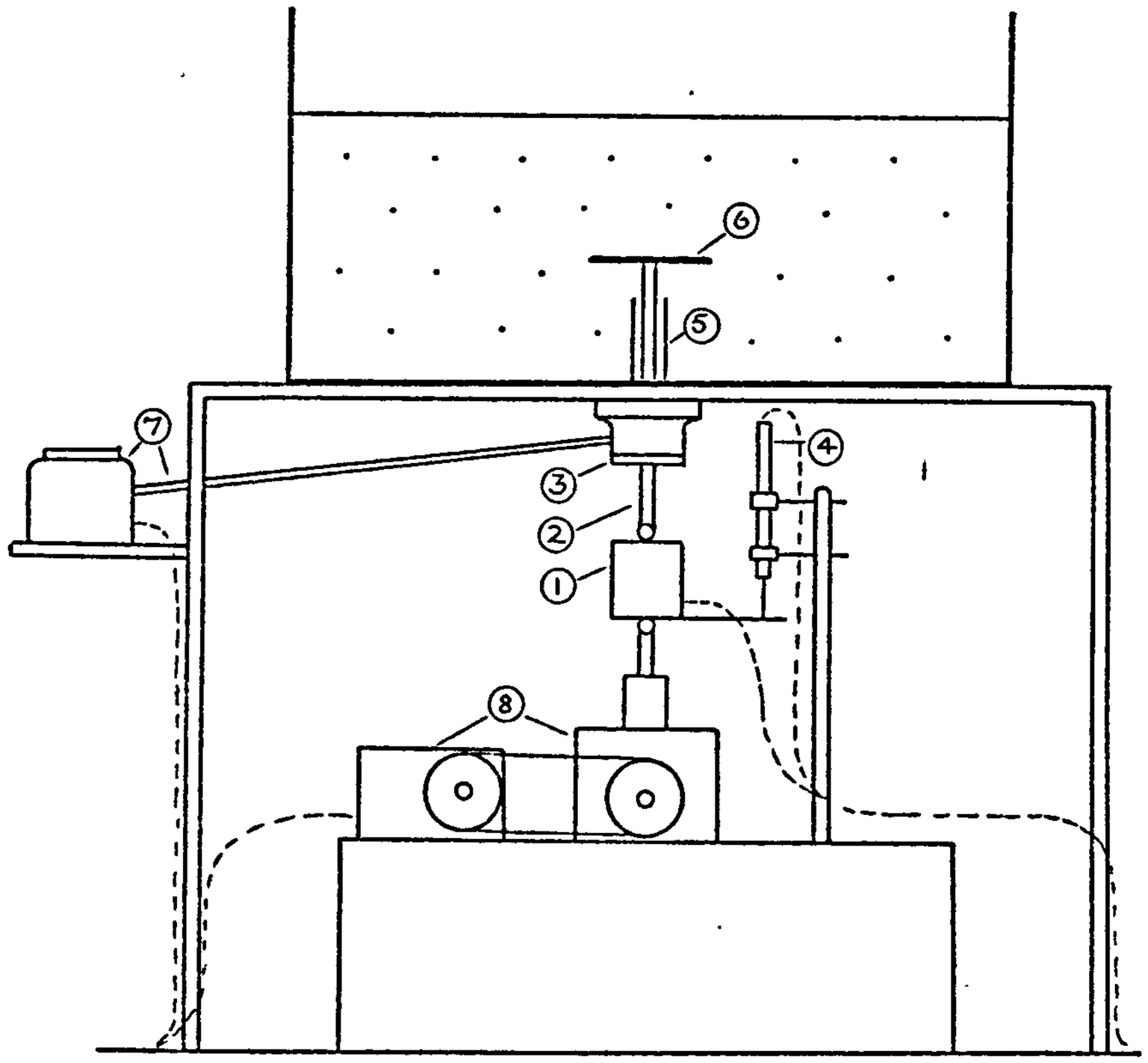

FIG. 4.4 (a). DISPLACEMENT-CONTROLLED PUSHOUT

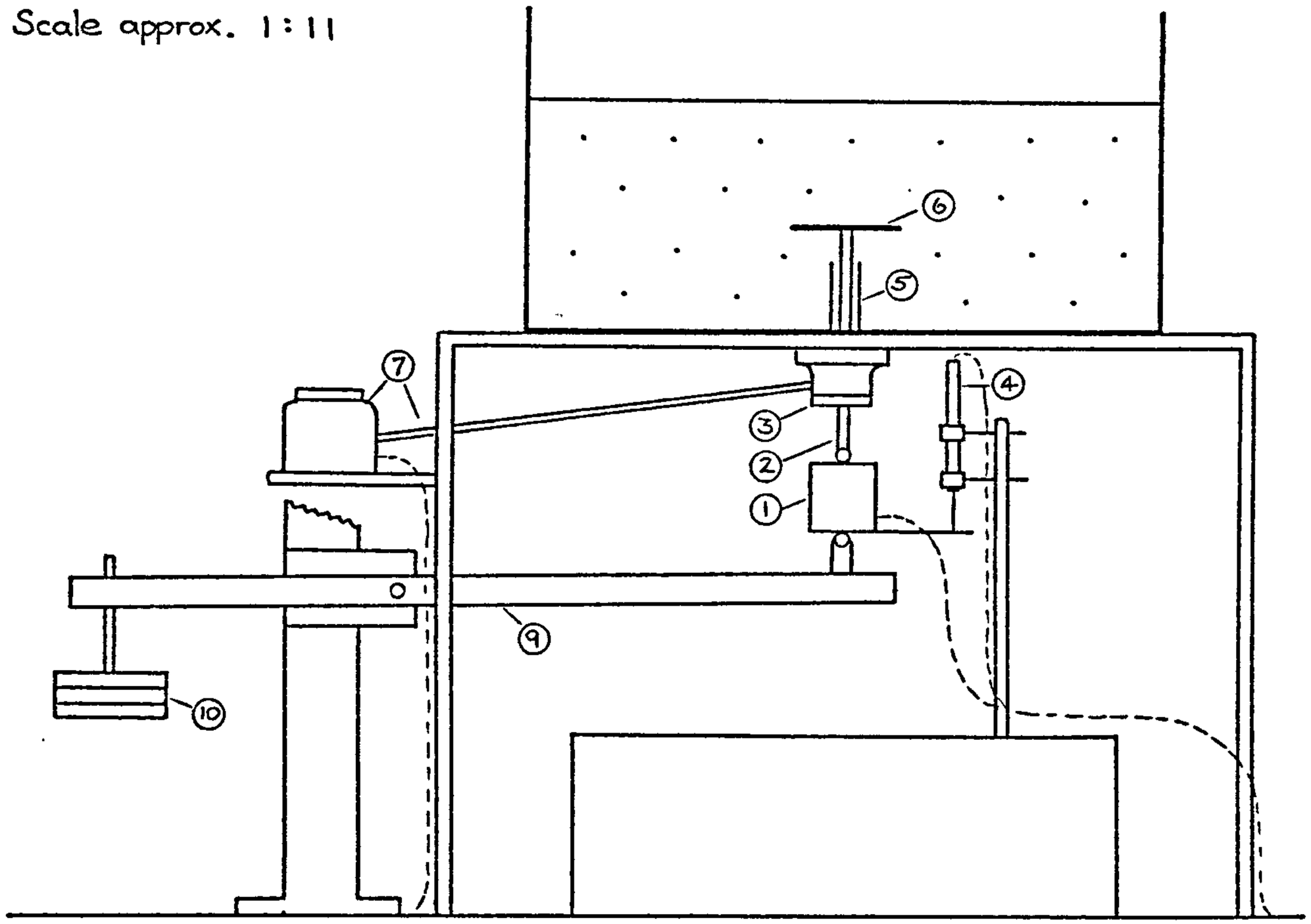

FIG. 4.4 (b). LOAD-CONTROLLED PUSHOUT

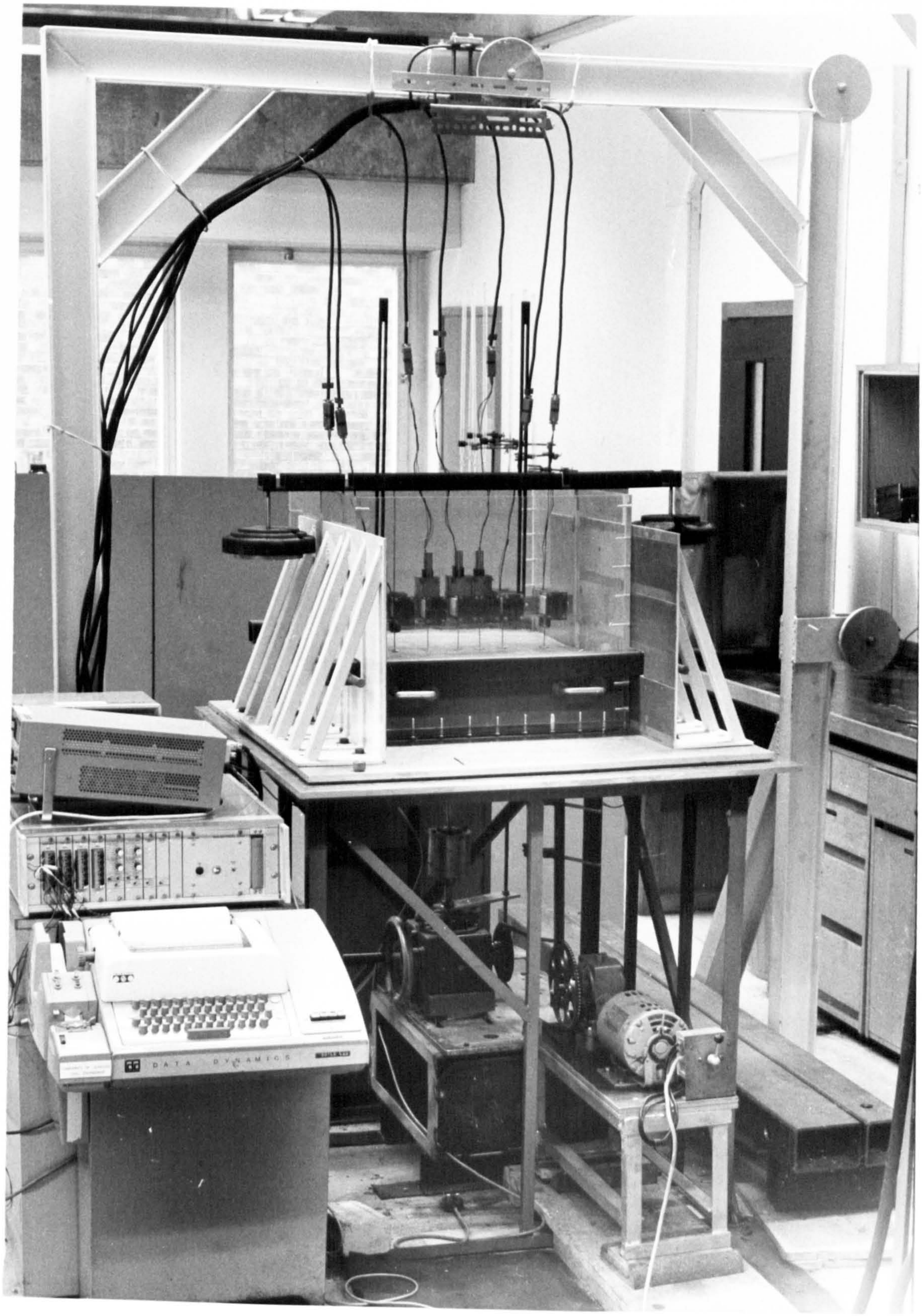

FIG. 4.5 (a). GENERAL VIEW OF UPLIFT RESISTANCE APPARATUS WITH SPLIT-BOX

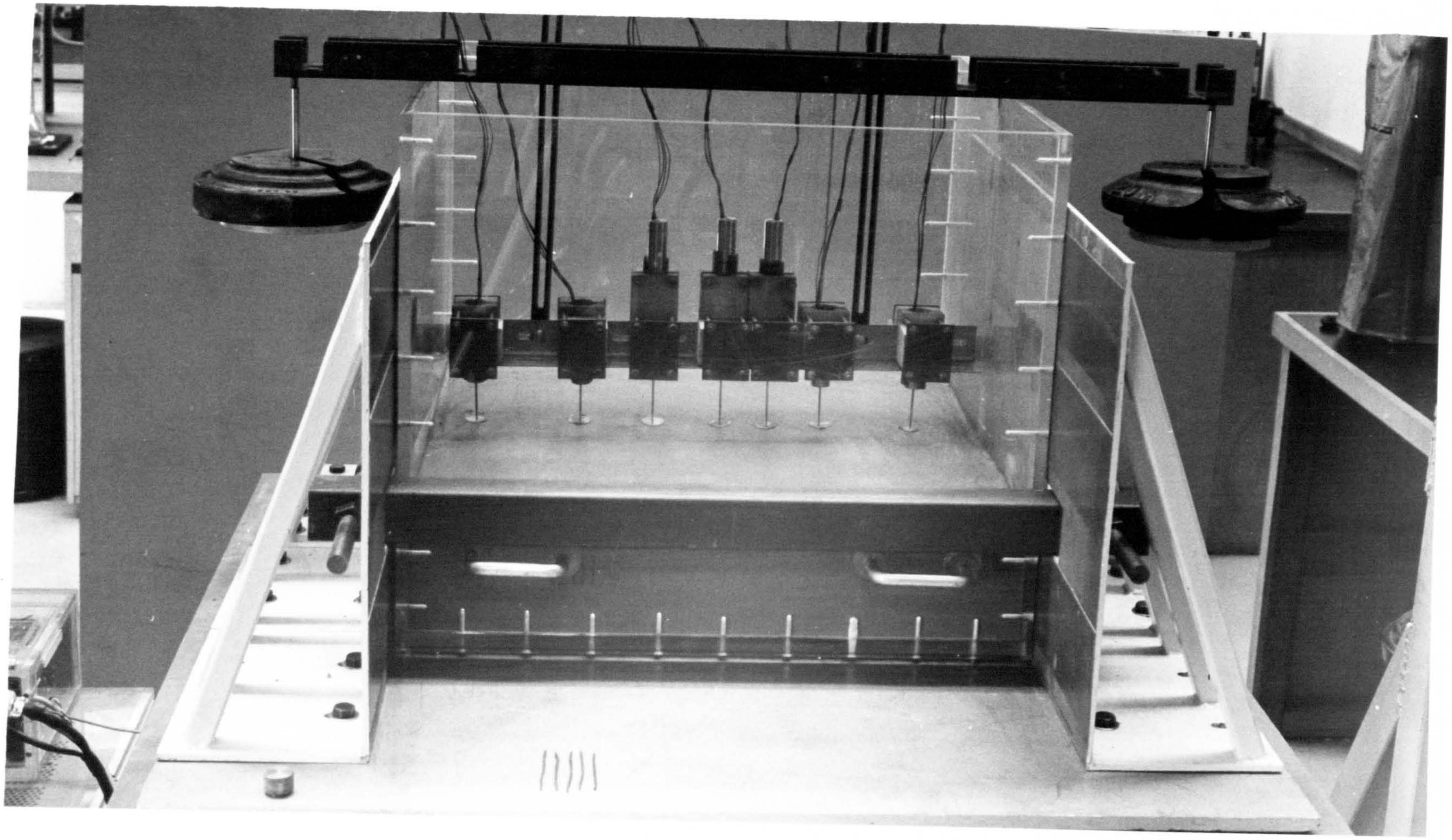

FIG. 4.5 (b). DETAIL OF SPLIT-BOX SHOWING SURFACE DEFORMATION MEASURING EQUIPMENT

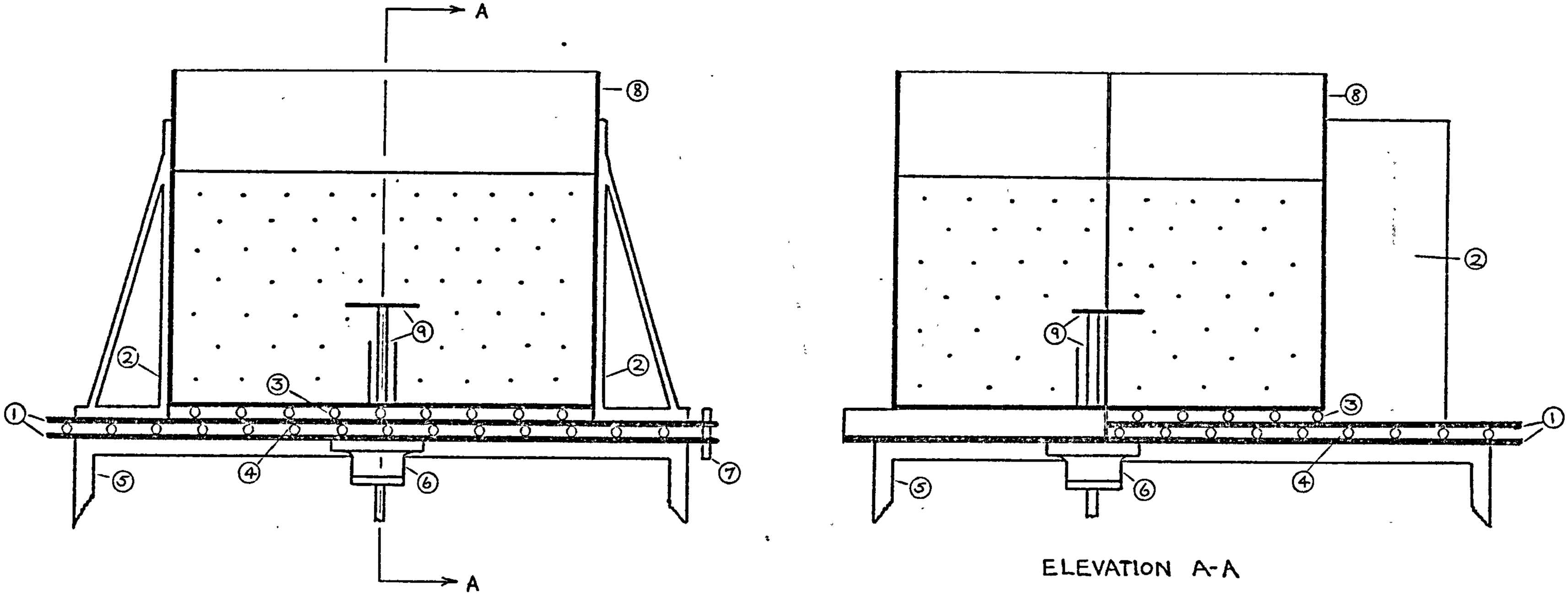

① aluminium base plates
② PTFE coated box-side supports
③ ball-bearings for direct-splitting action
④ ball-bearings for swivel-splitting action
⑤ supporting frame
⑥ Wykeham Farrance rotating bush
⑦ hinge-pin
⑧ split-box
⑨ off-centre shaft and casing, anchor plate attached eccentrically

Scale approx. 1:9

FIG. 4.6. ELEVATION VIEWS OF SPLIT-BOX APPARATUS

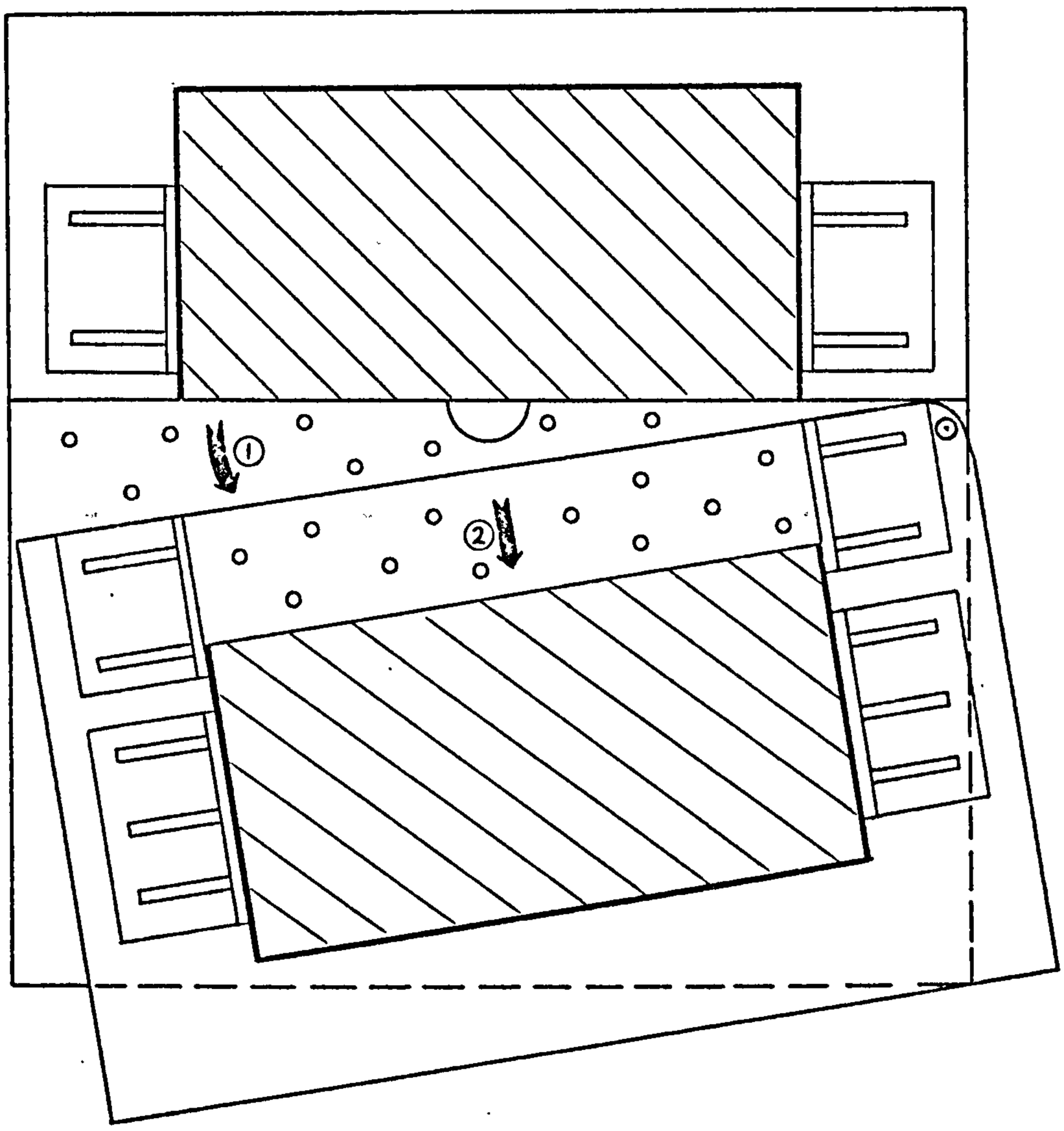

① swivel-splitting action
② direct-splitting action

FIG. 4.7. PLAN VIEW SHOWING SPLIT-BOX SPLITTING ACTIONS

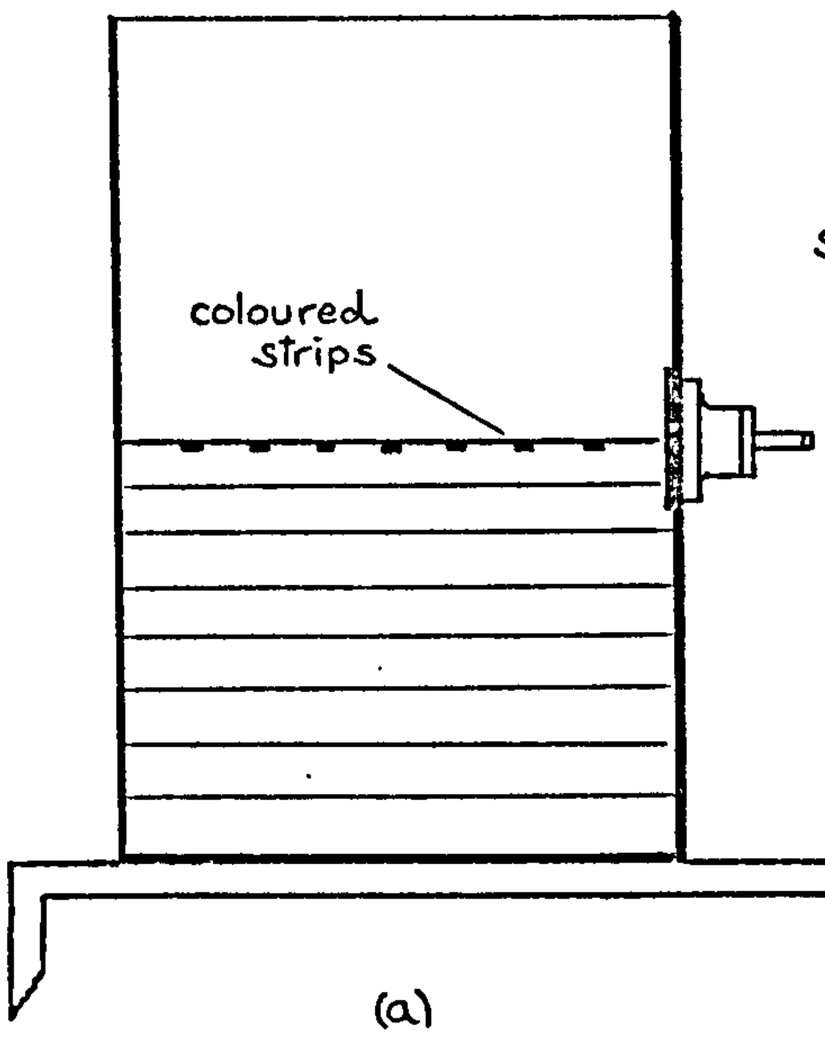

(a)
box half-filled with glyben and coloured strips placed

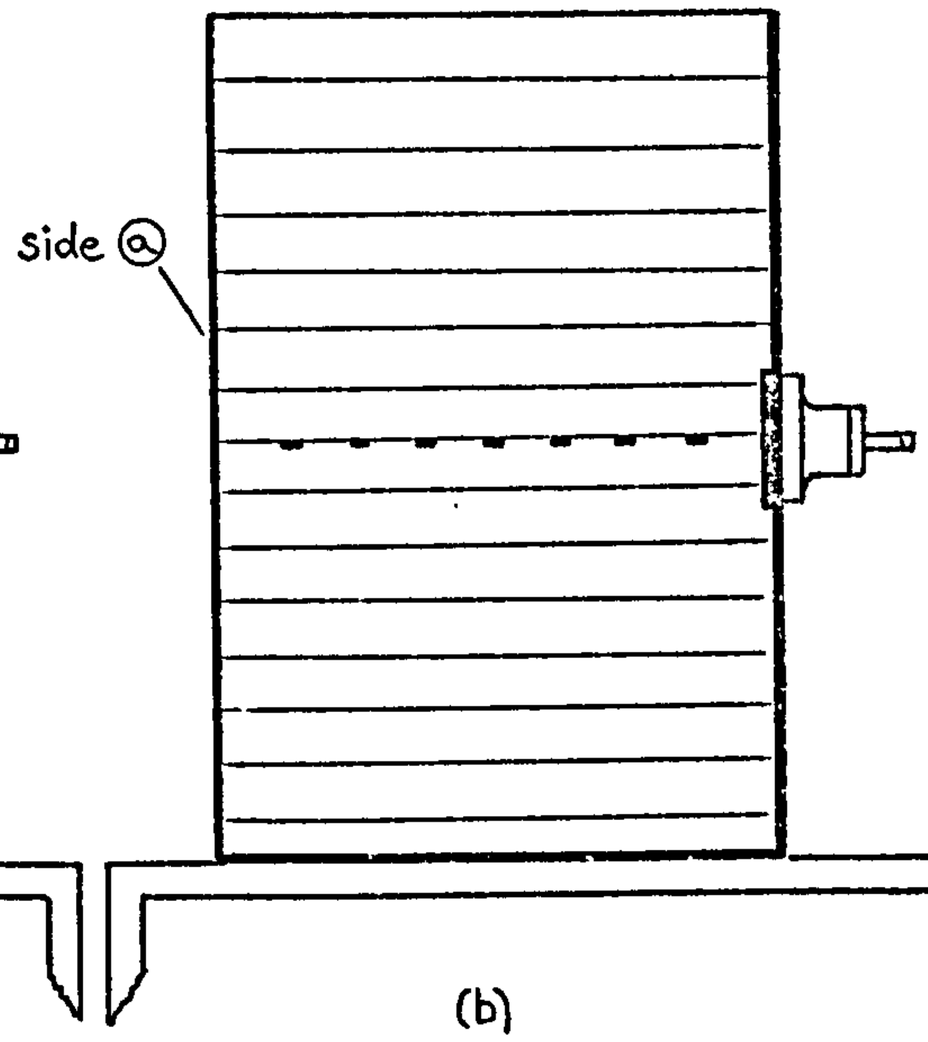

(b)
box completely filled with glyben

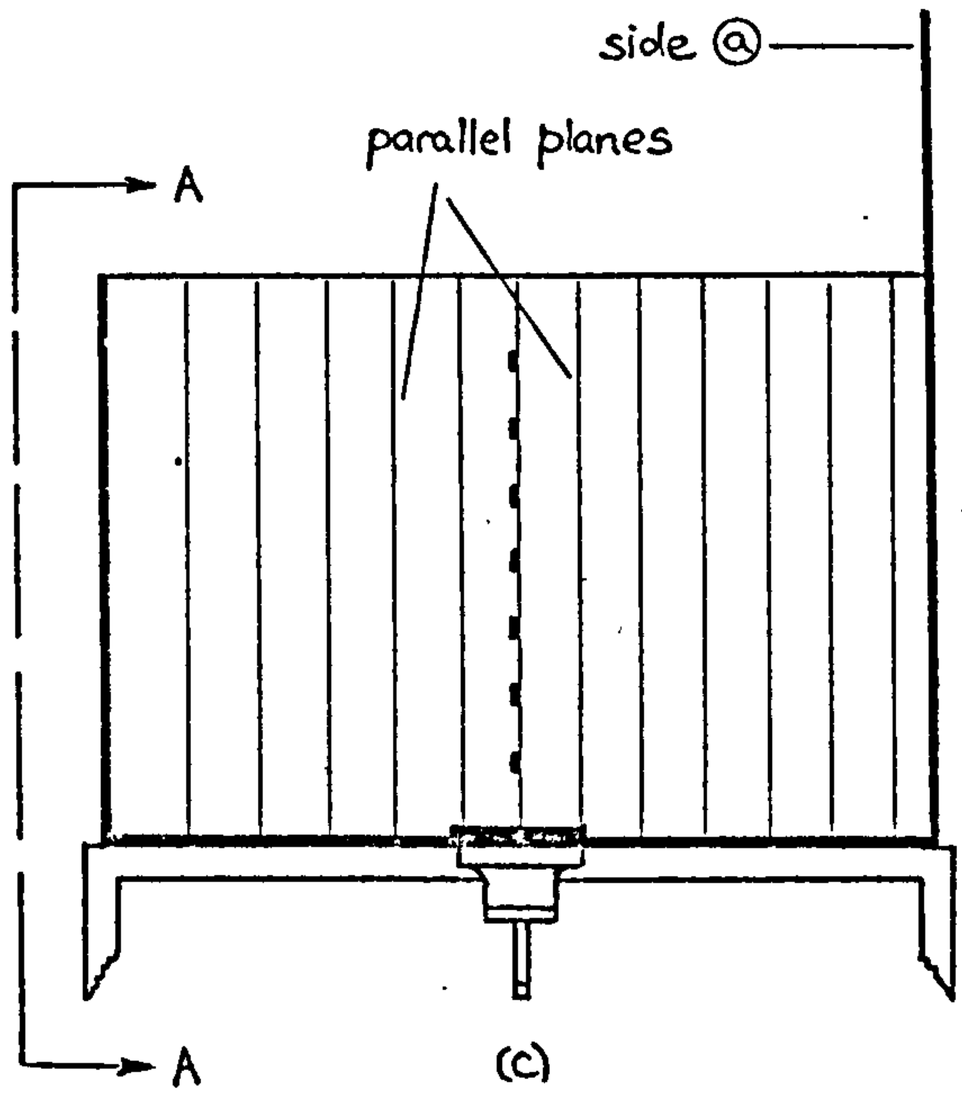

(c)
box rotated through 90° and side @ transferred

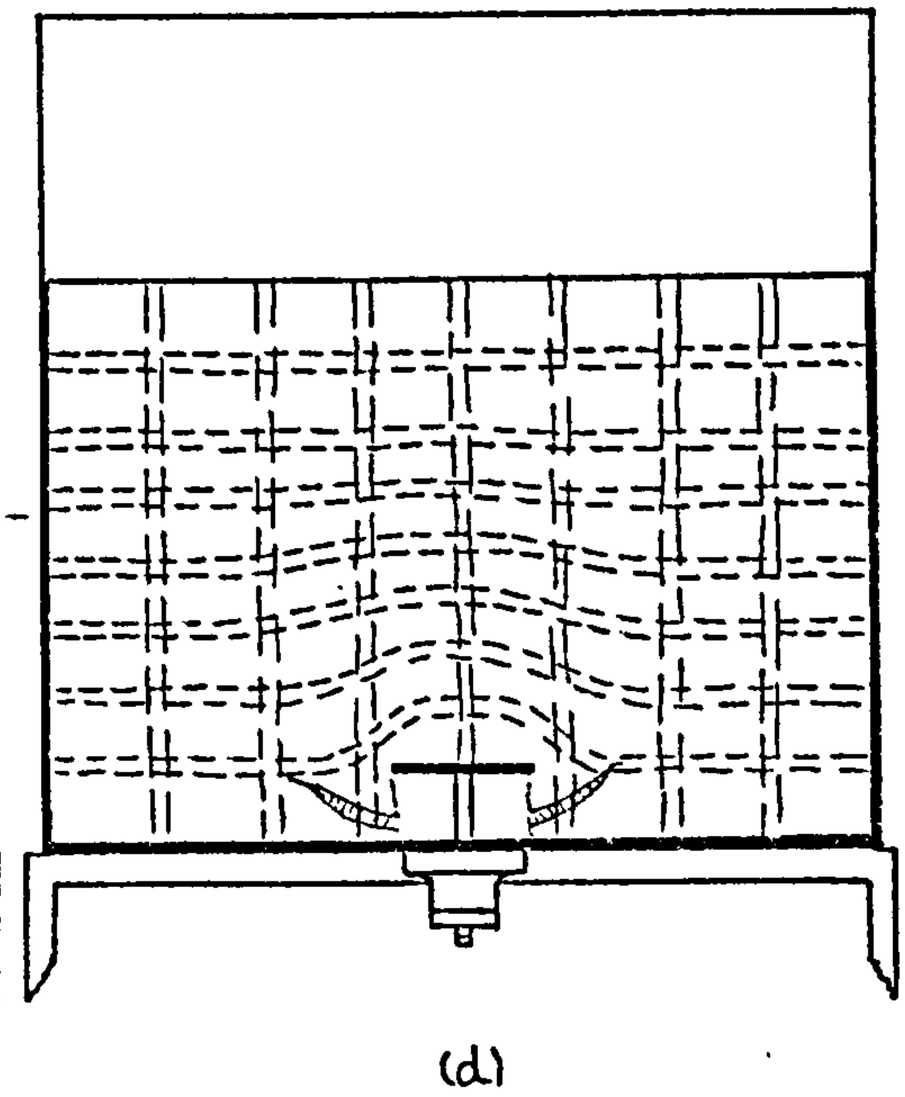

(d)
test completed and half of glyben removed to reveal displacements of strips and cracking

FIG. 4.8. FOUR STAGES IN THE PREPARATION OF "ROTATED-BOX" SAMPLES

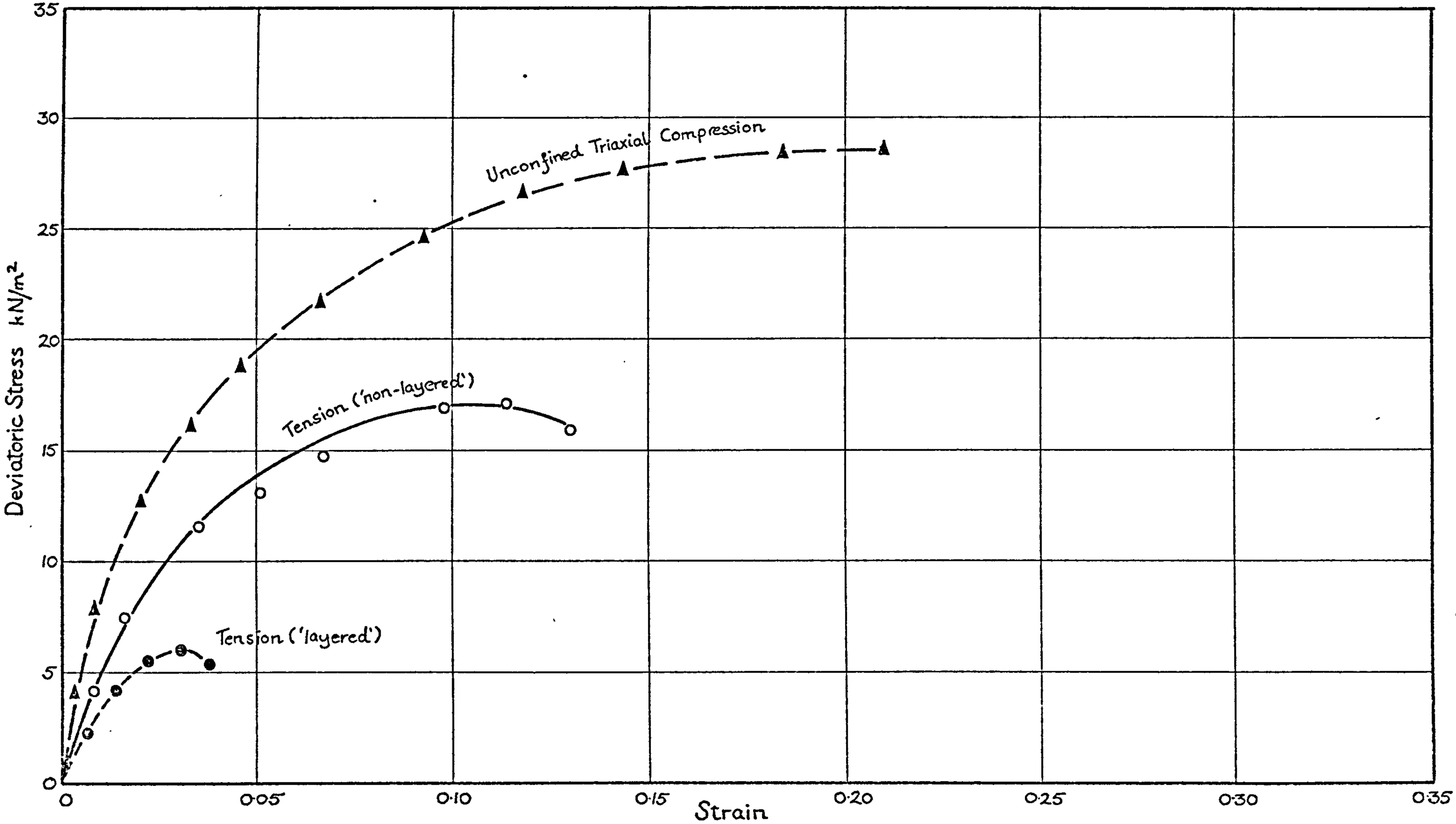

FIG. 4.9. STRESS-STRAIN CURVES OF GLYBEN BATCH No. 4 SAMPLES IN UNCONFINED COMPRESSION AND TENSION

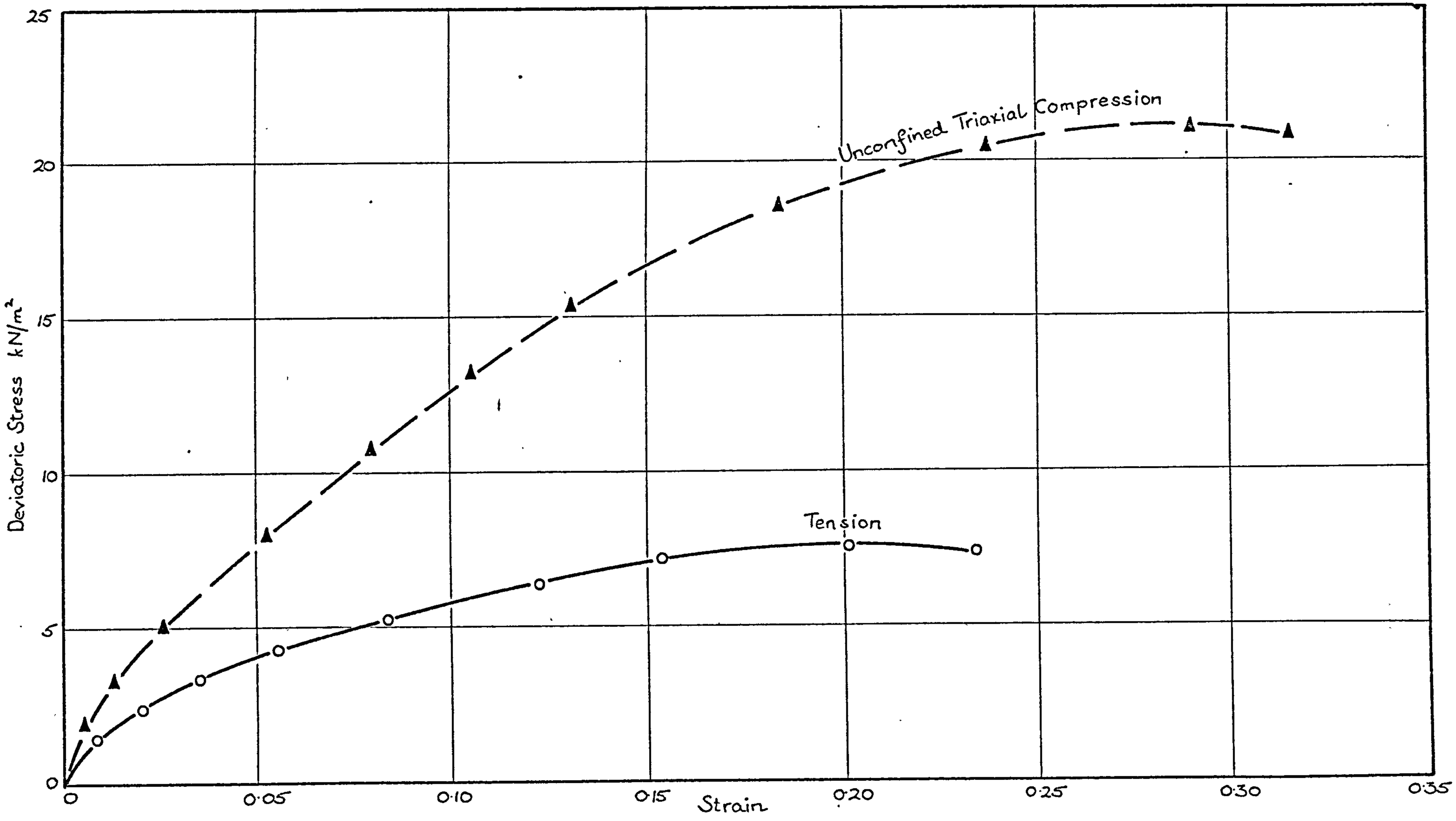

FIG. 4.10. STRESS-STRAIN CURVES OF MODIFIED GRANGEMOUTH CLAY SAMPLES IN UNCONFINED COMPRESSION AND TENSION

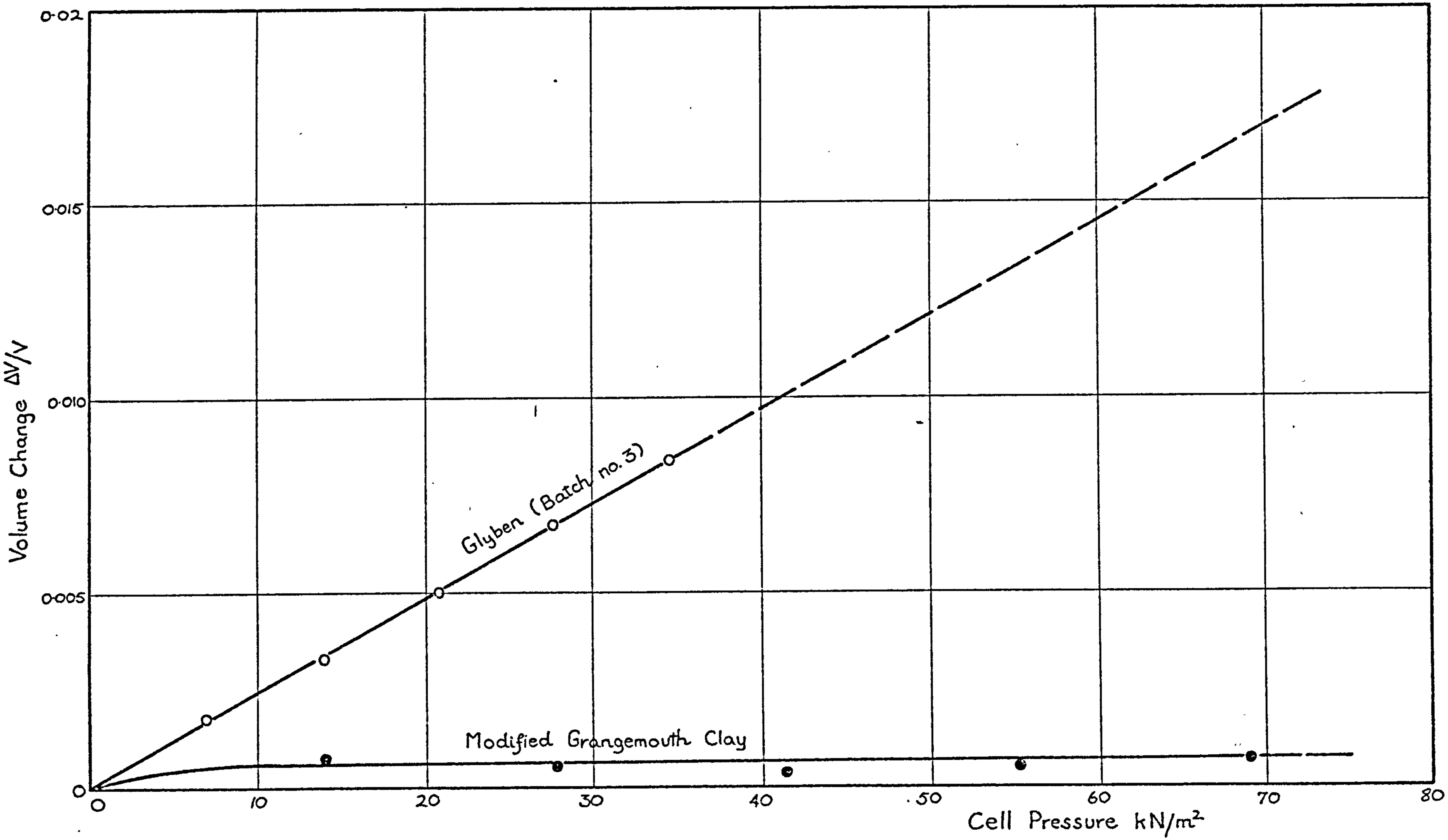

FIG. 4.11. VOLUME CHANGE VERSUS CELL PRESSURE FOR GLYBEN BATCH No. 3 AND MODIFIED GRANGEMOUTH CLAY

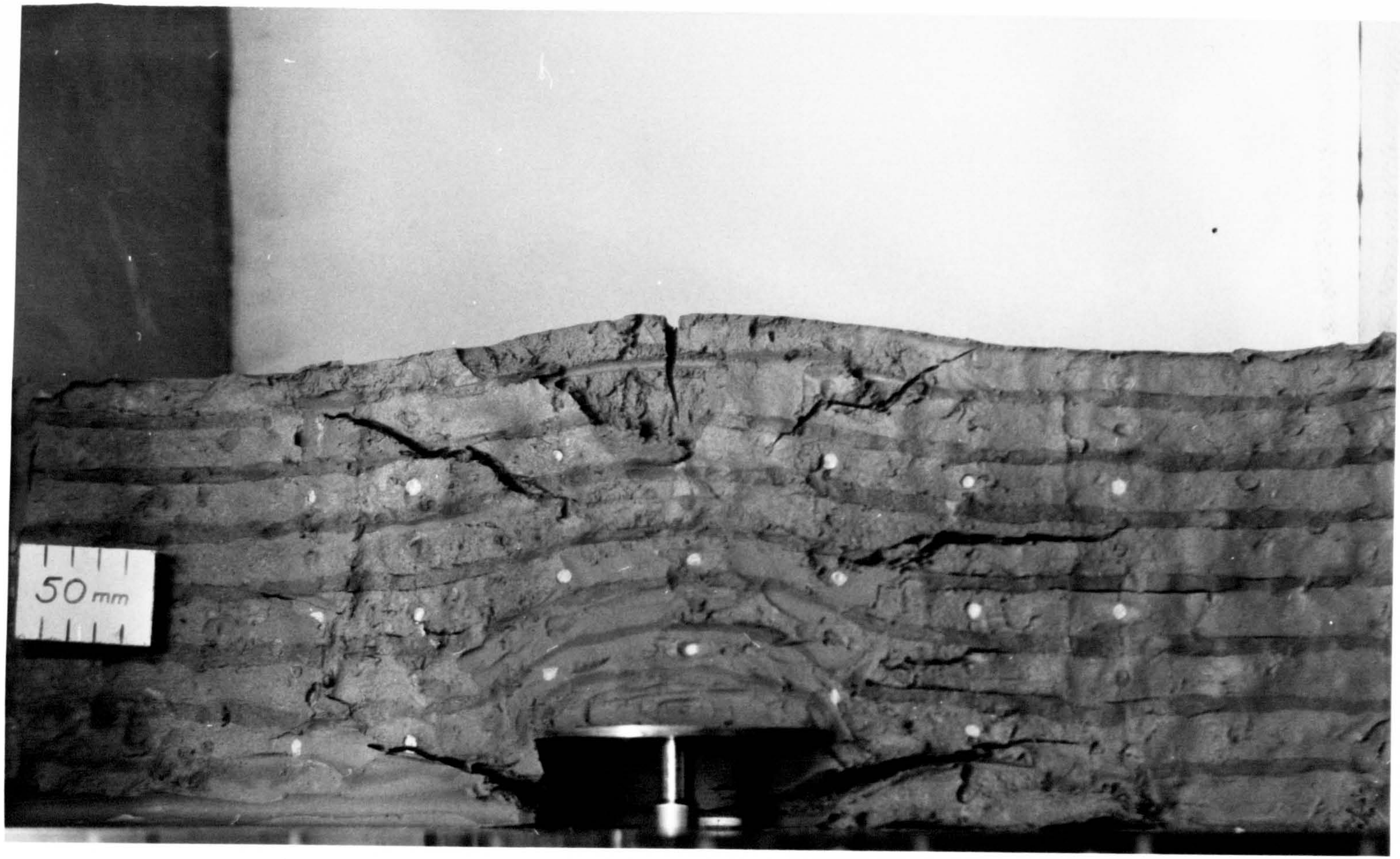

FIG. 4.12. DEFORMATION AND CRACKING AT ULTIMATE UPLIFT RESISTANCE IN "ROTATED-BOX" SAMPLE OF GLYBEN

SECTION THROUGH CENTRE OF SAMPLE: TEST No. 49, D/B = 1.6

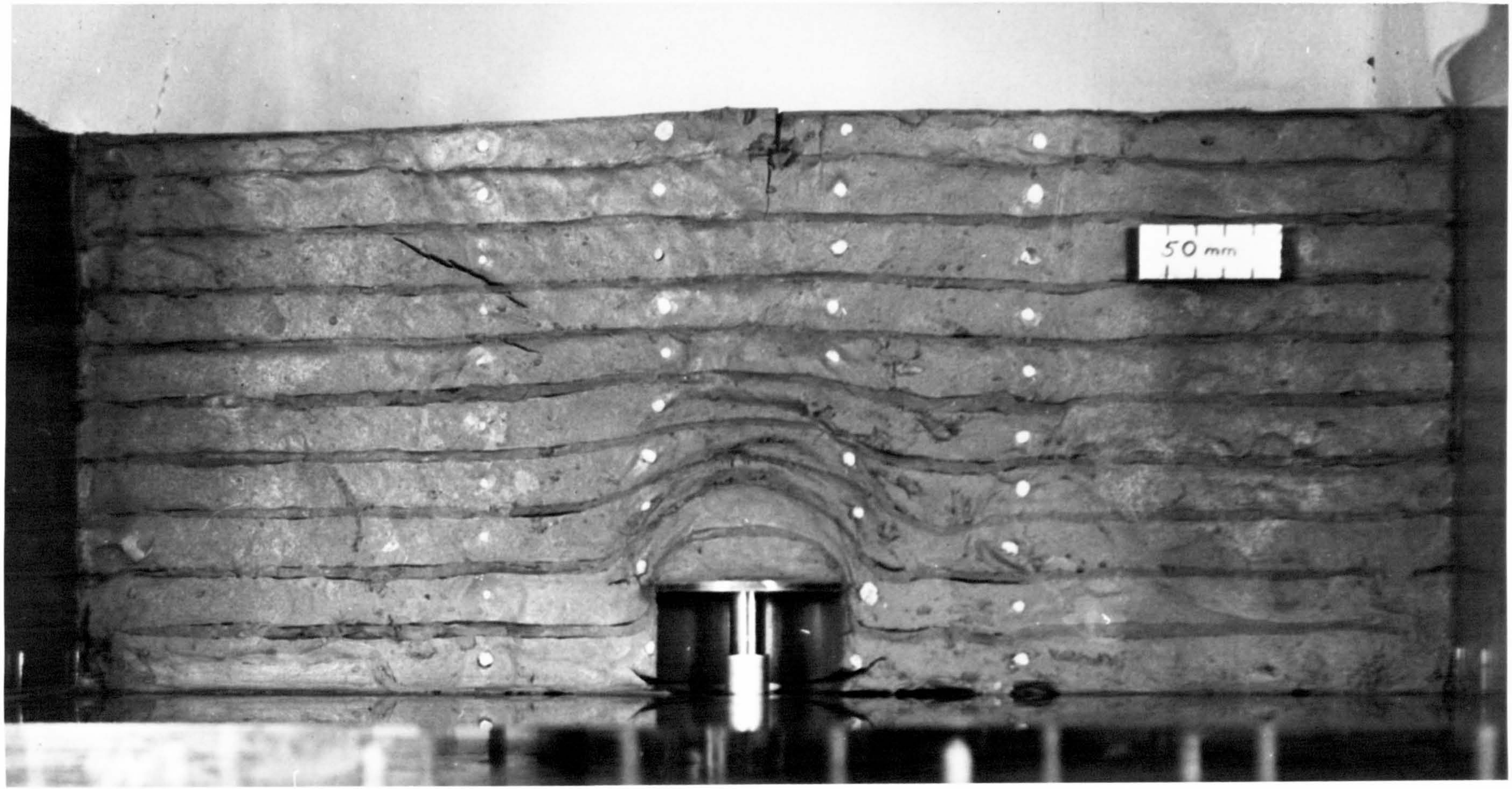

FIG. 4.13. DEFORMATION AND CRACKING AT ULTIMATE UPLIFT RESISTANCE IN "ROTATED-BOX" SAMPLE OF GLYBEN

SECTION THROUGH CENTRE OF SAMPLE: TEST No. 50, D/B = 3.0

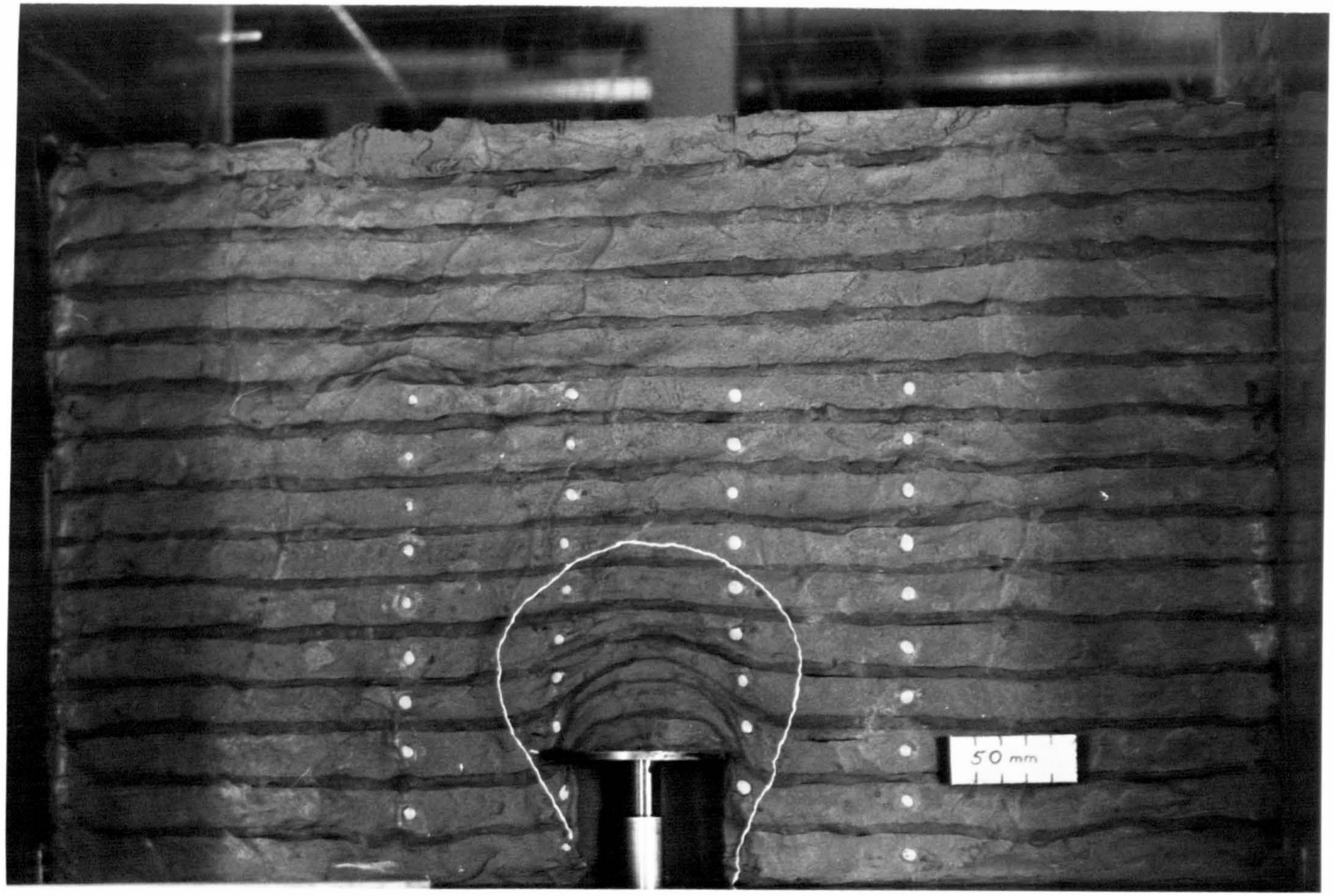

FIG. 4.14. DEFORMATION AT ULTIMATE UPLIFT RESISTANCE IN "ROTATED-BOX" SAMPLE OF GLYBEN SECTION THROUGH CENTRE OF SAMPLE. WHITE THREAD INDICATES REGION VISIBLY AFFECTED BY ANCHOR DISPLACEMENT. TEST No. 52, D/B = 4.5

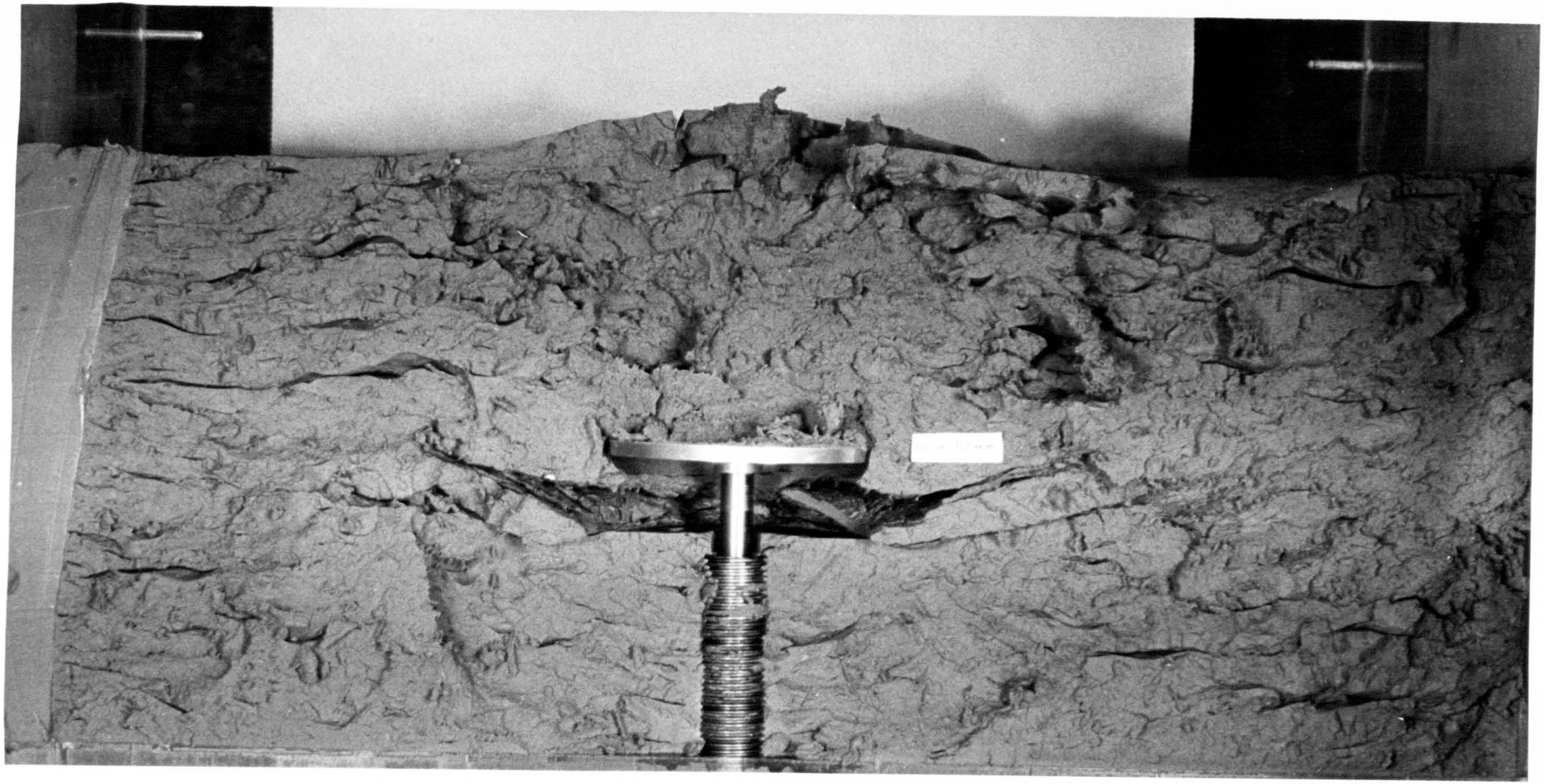

FIG. 4.15. CRACKING AT ULTIMATE UPLIFT RESISTANCE IN "SPLIT-BOX" SAMPLE OF GLYBEN

SECTION THROUGH CENTRE OF SAMPLE: TEST No. 53, D/B = 1.5

FIG. 4.16. DEFORMATION AND CRACKING AT ULTIMATE UPLIFT RESISTANCE IN "SPLIT-BOX" SAMPLE OF GLYBEN

SECTION THROUGH CENTRE OF SAMPLE: TEST No. 54, D/B = 1.5

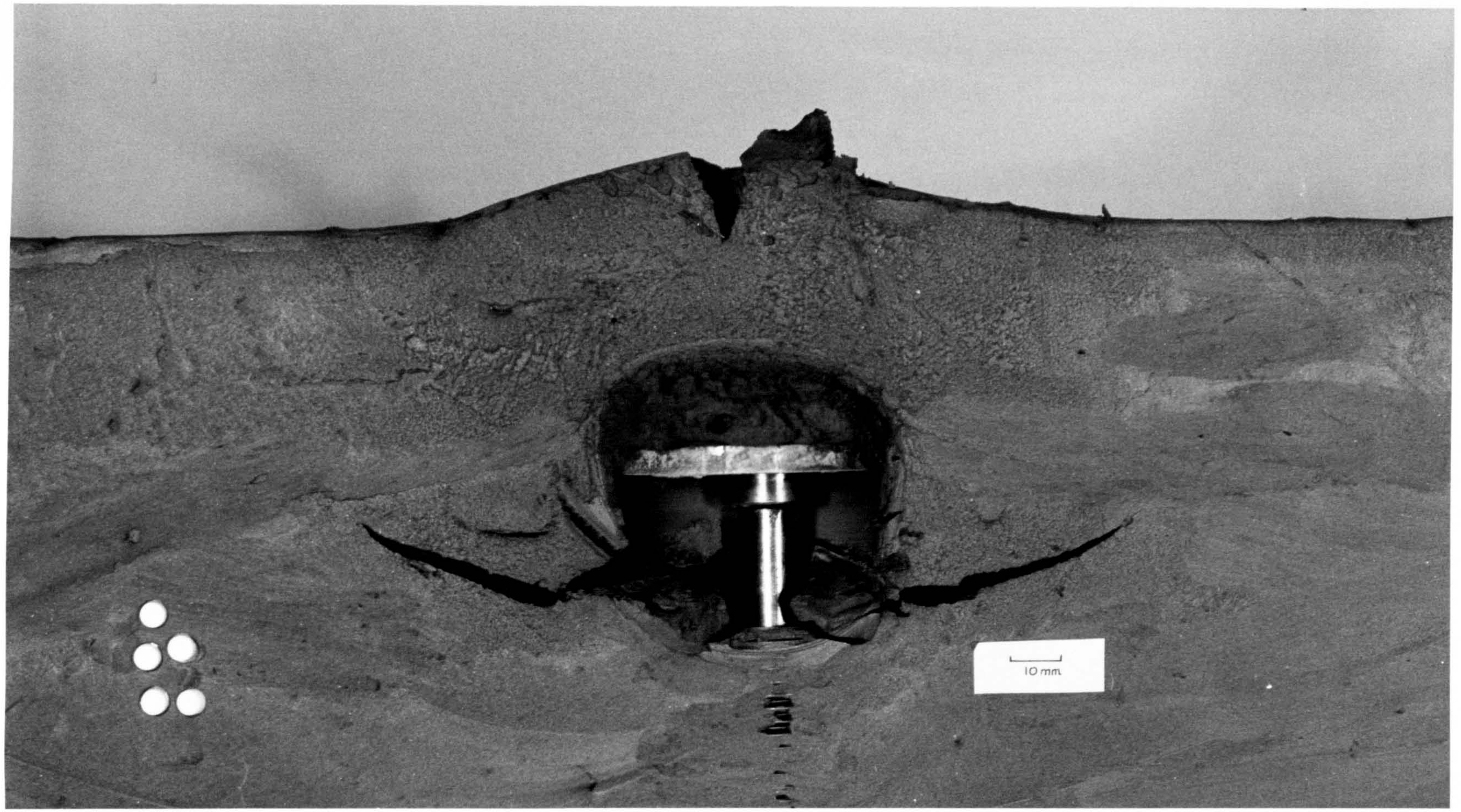

FIG. 4.17. CRACKING AT ULTIMATE UPLIFT RESISTANCE IN "SPLIT-BOX" SAMPLE OF MODIFIED GRANGEMOUTH CLAY

SECTION THROUGH CENTRE OF SAMPLE: TEST No. 65, D/B = 1.42

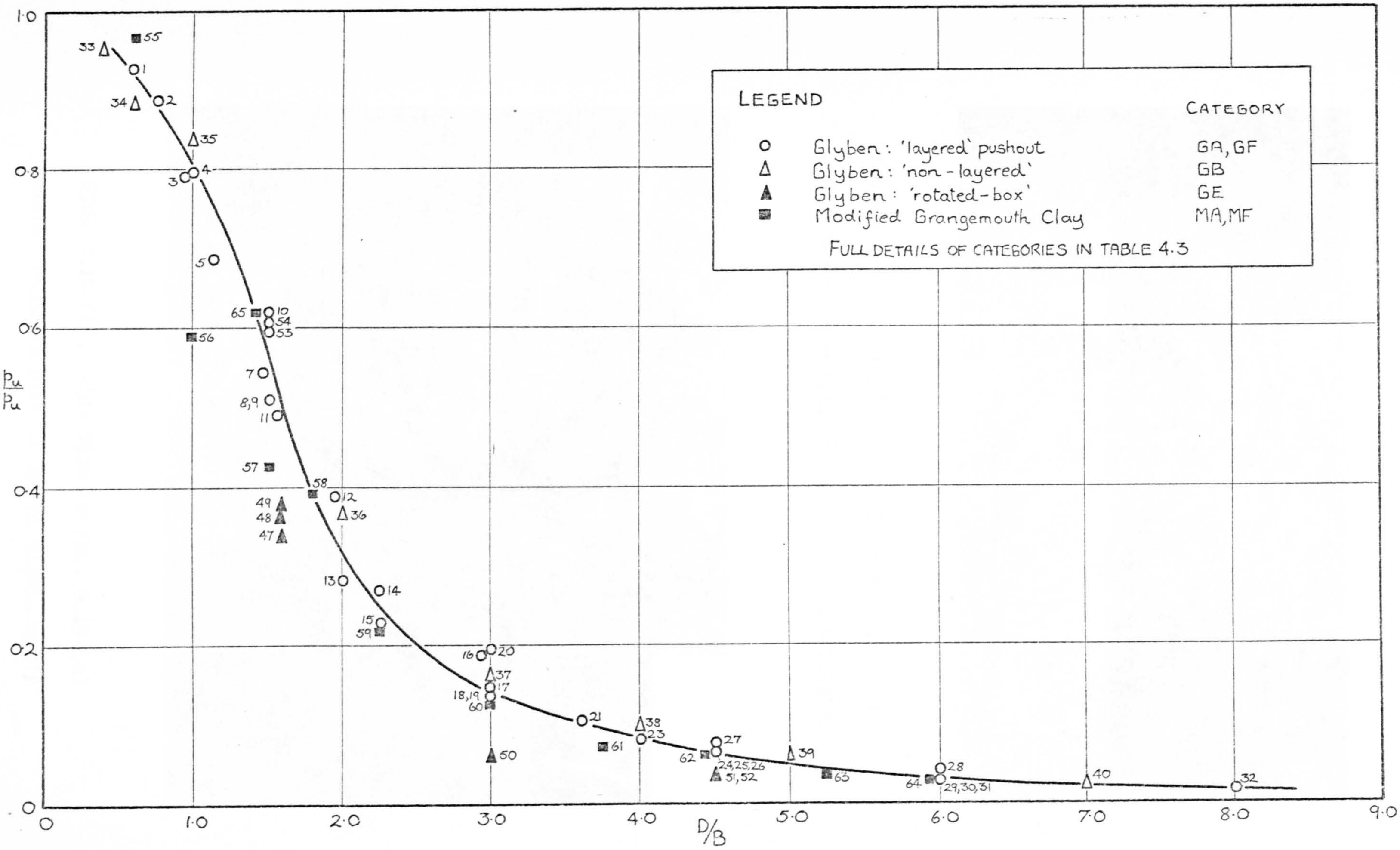

FIG. 4.18. RATIO OF SURFACE DISPLACEMENT TO ANCHOR DISPLACEMENT AT 90% OF ULTIMATE UPLIFT RESISTANCE VERSUS D/B

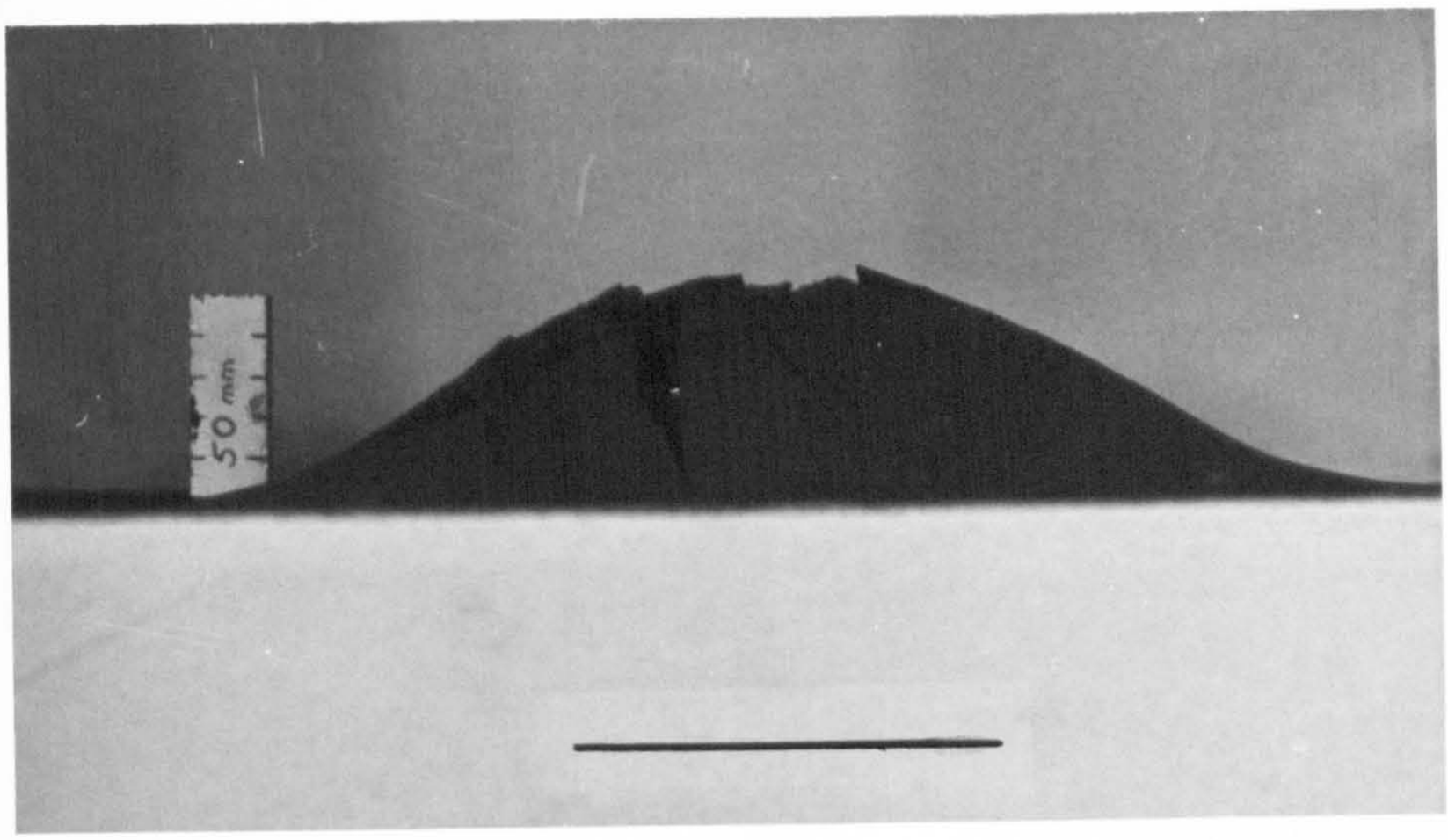

FIG. 4.19 (a). SURFACE BULGE IN "LAYERED" GLYBEN

TEST No. 8, D/B = 1.5. POSITION OF ANCHOR SHOWN

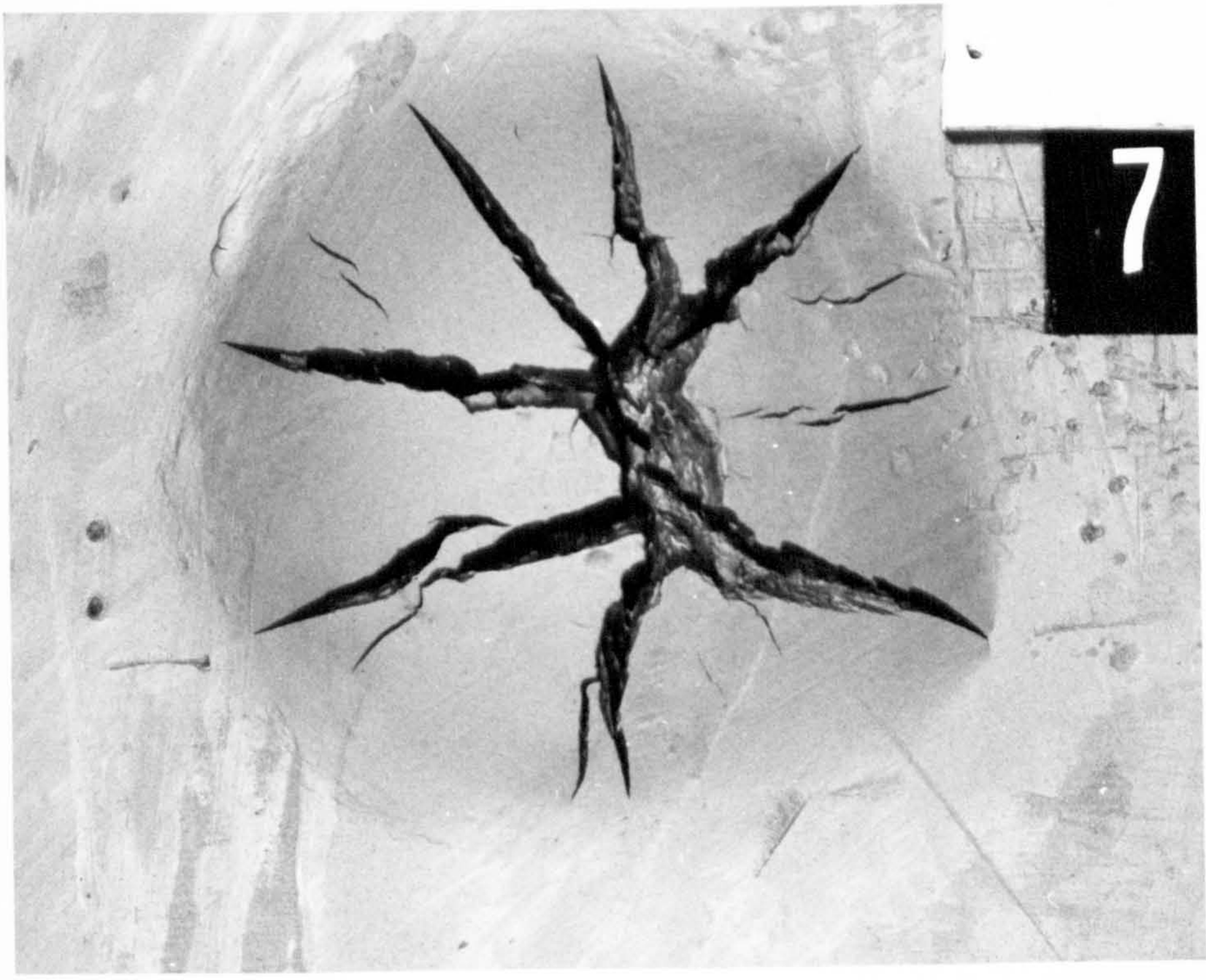

FIG. 4.19 (b). PLAN VIEW OF FIG. 4.19 (a)

BULGE CORRESPONDING TO ANCHOR DISPLACEMENT

AT 2.6 TIMES ULTIMATE UPLIFT RESISTANCE DISPLACEMENT

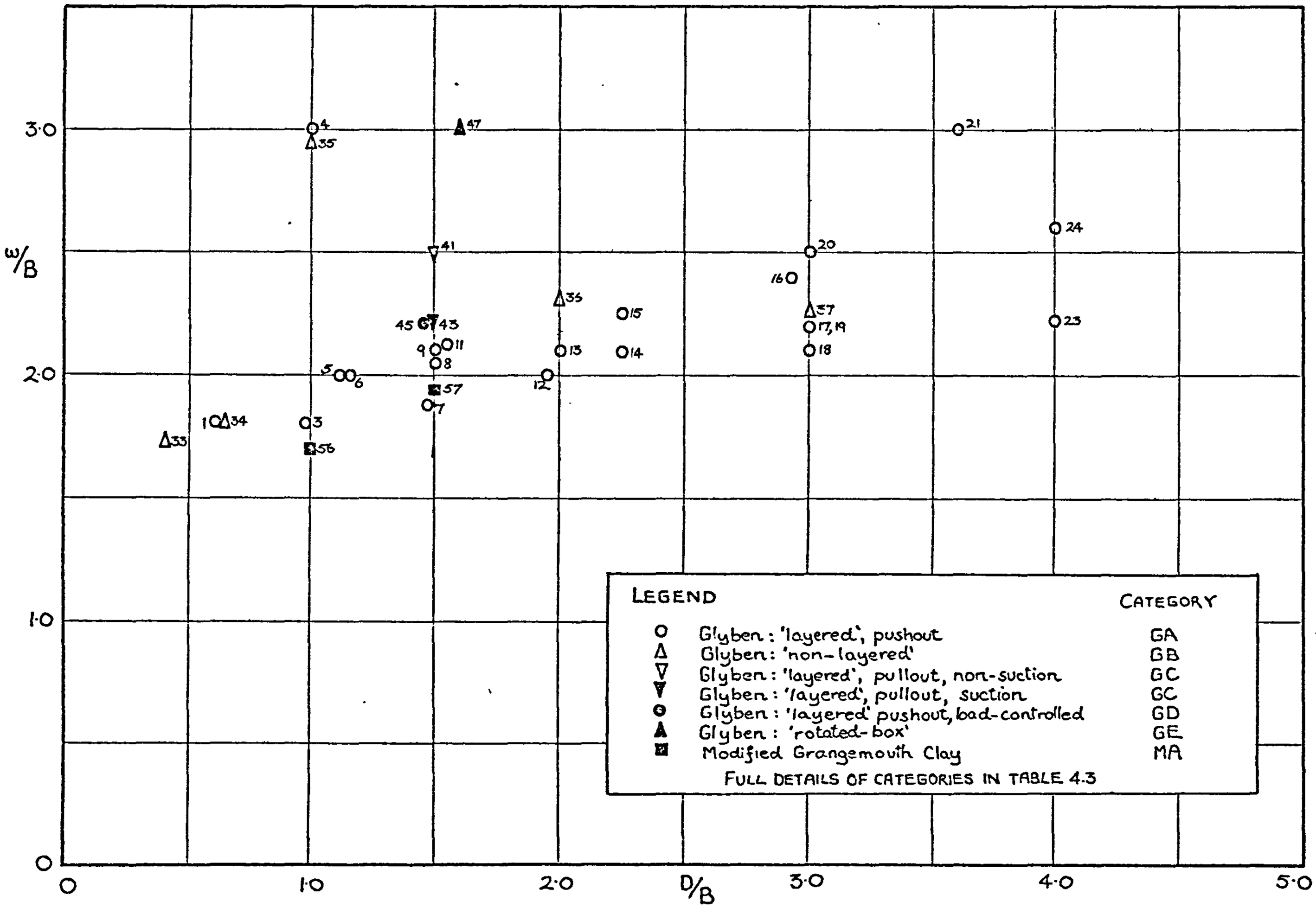

FIG. 4.20. RATIO OF SURFACE BULGE DIAMETER TO ANCHOR DIAMETER VERSUS D/B

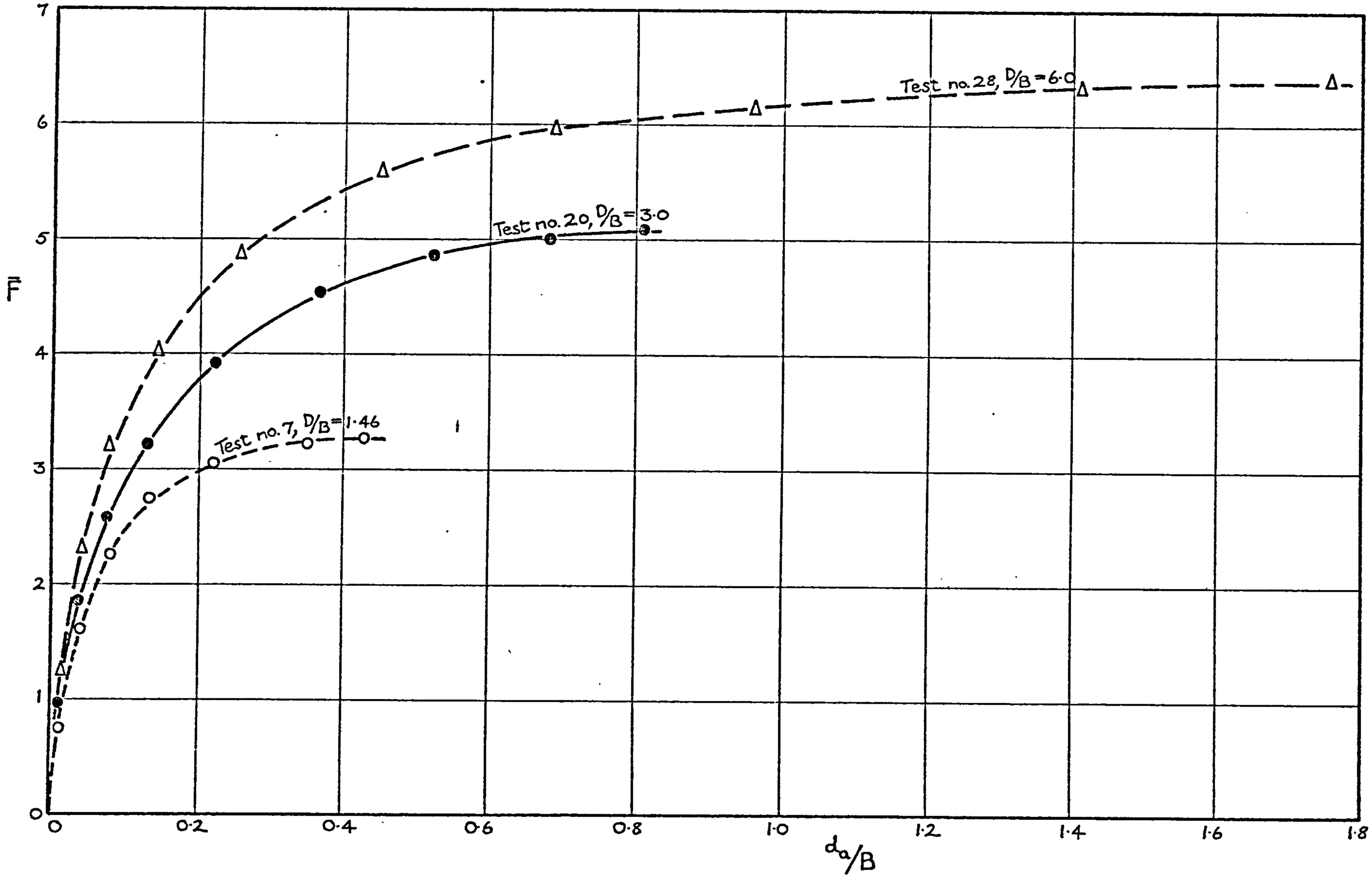

FIG. 4.21. UPLIFT RESISTANCE FACTOR VERSUS ANCHOR DISPLACEMENT RATIO FOR THREE TESTS IN "LAYERED" GLYBEN

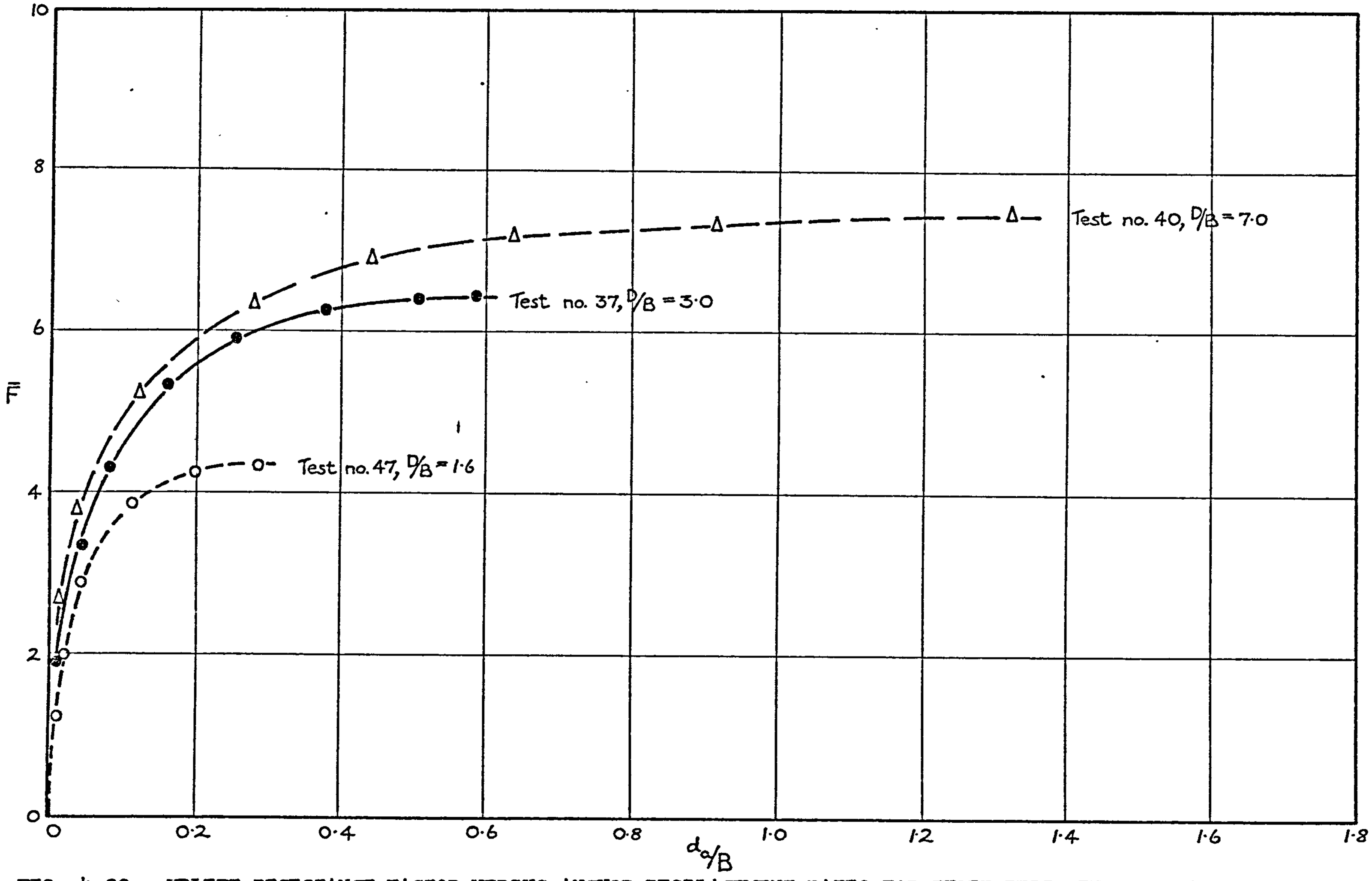

FIG. 4.22. UPLIFT RESISTANCE FACTOR VERSUS ANCHOR DISPLACEMENT RATIO FOR THREE TESTS IN "NON-LAYERED" GLYBEN

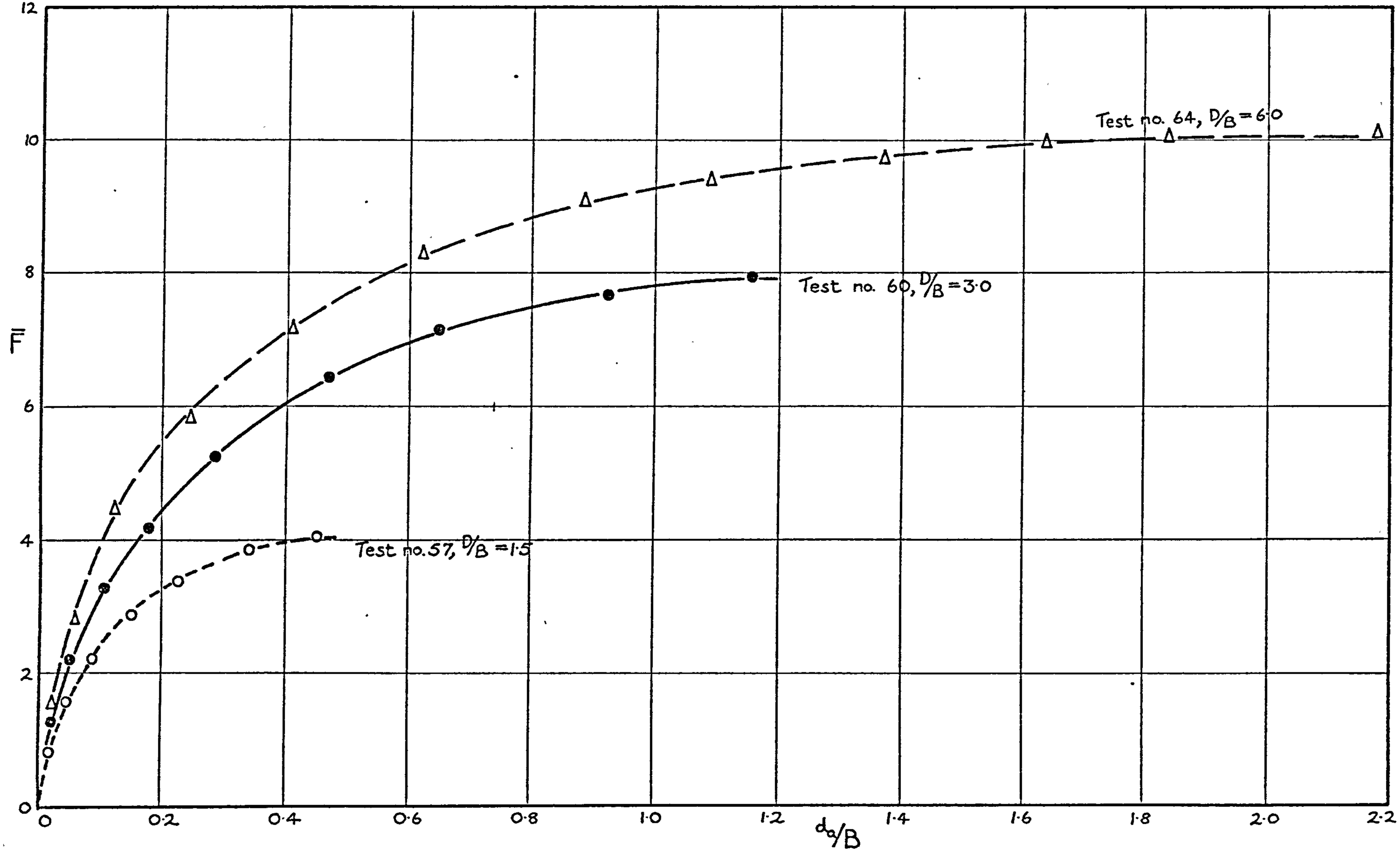

FIG. 4.23. UPLIFT RESISTANCE FACTOR VERSUS ANCHOR DISPLACEMENT RATIO FOR THREE TESTS IN MODIFIED GRANGEMOUTH CLAY

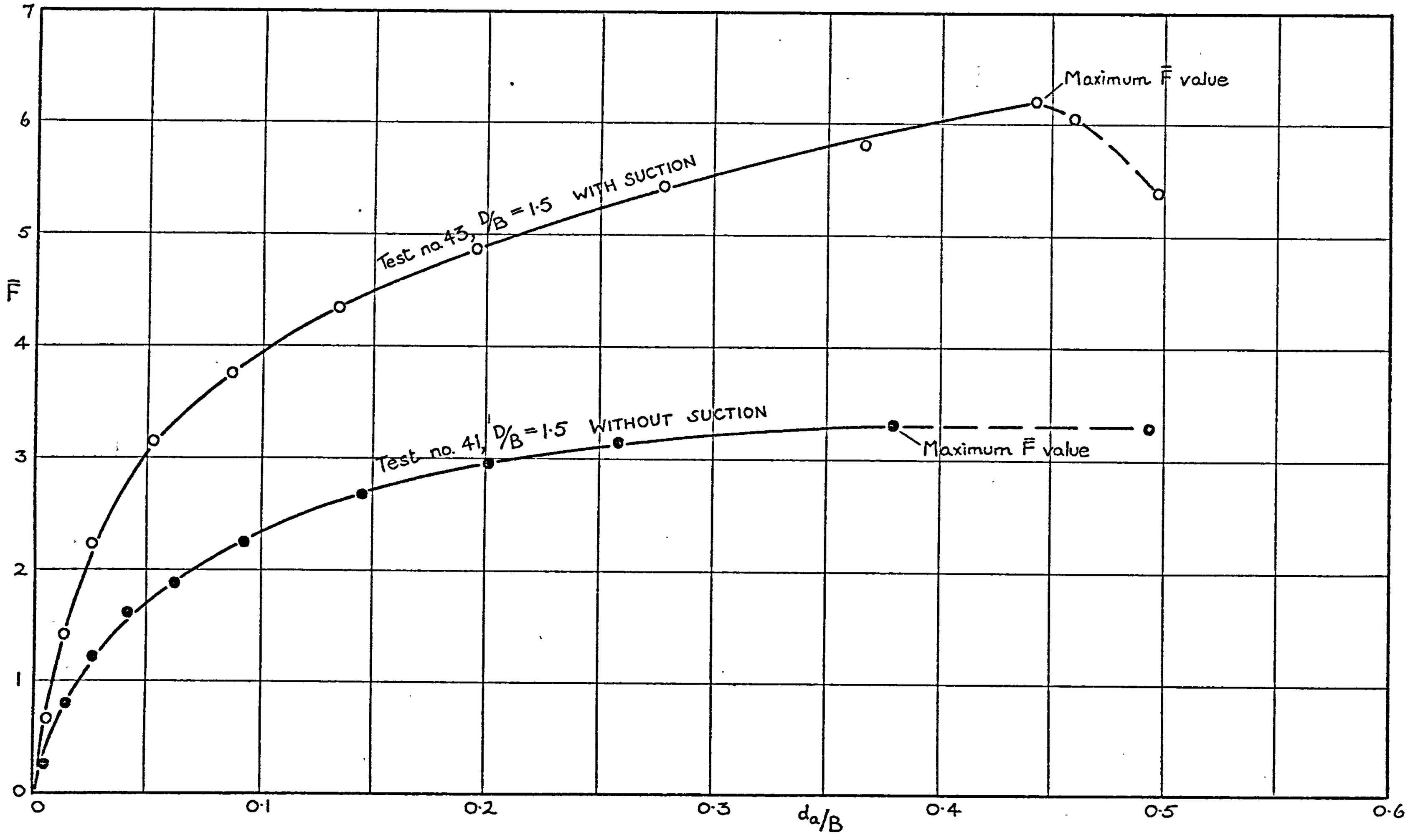

FIG. 4.24. UPLIFT RESISTANCE FACTOR VERSUS ANCHOR DISPLACEMENT RATIO FOR SHALLOW ANCHOR PULLOUT TESTS WITH AND WITHOUT SUCTION

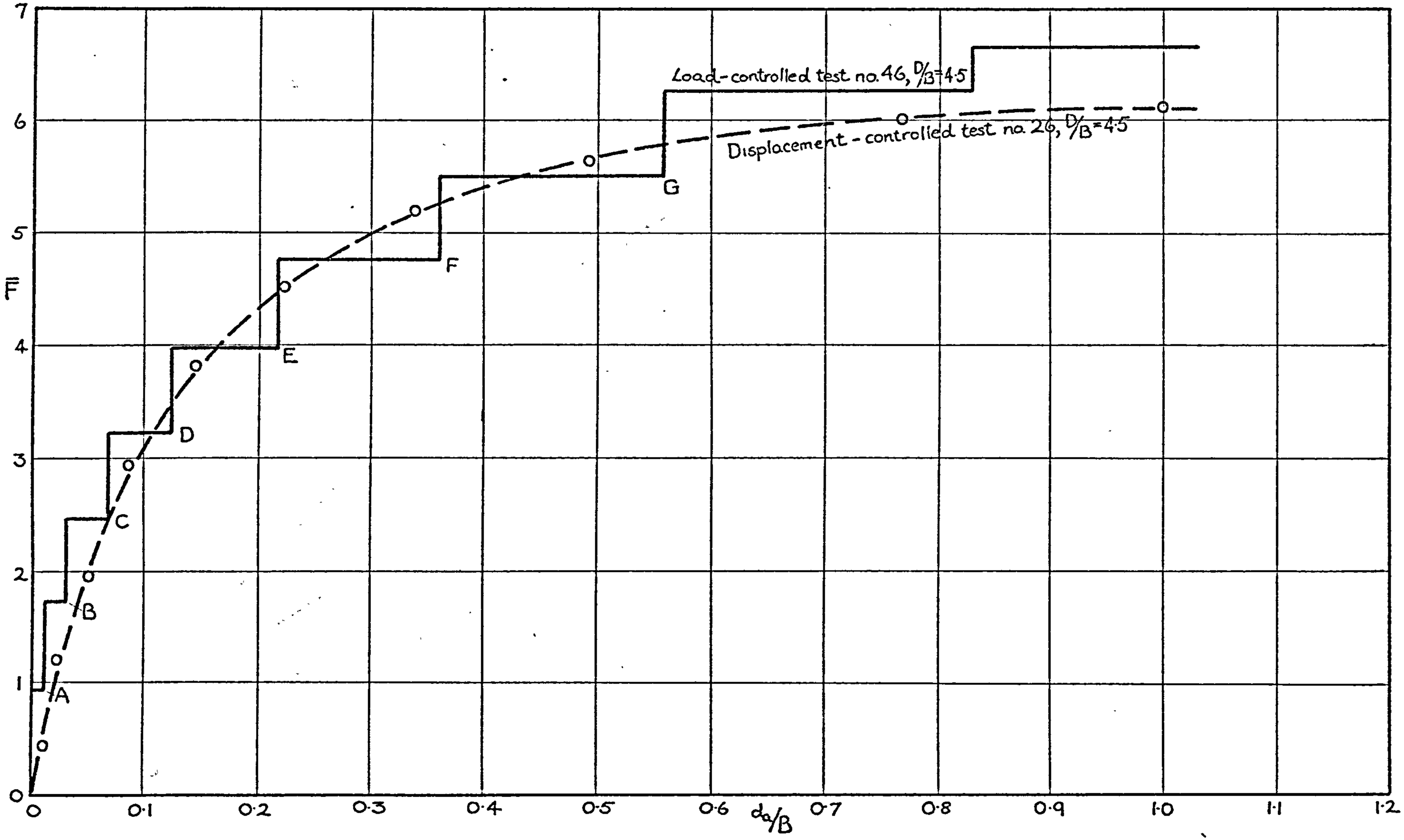

FIG. 4.25. UPLIFT RESISTANCE FACTOR V ANCHOR DISPLACEMENT RATIO FOR EQUIVALENT LOAD-CONTROLLED & DISPLACEMENT-CONTROLLED TESTS

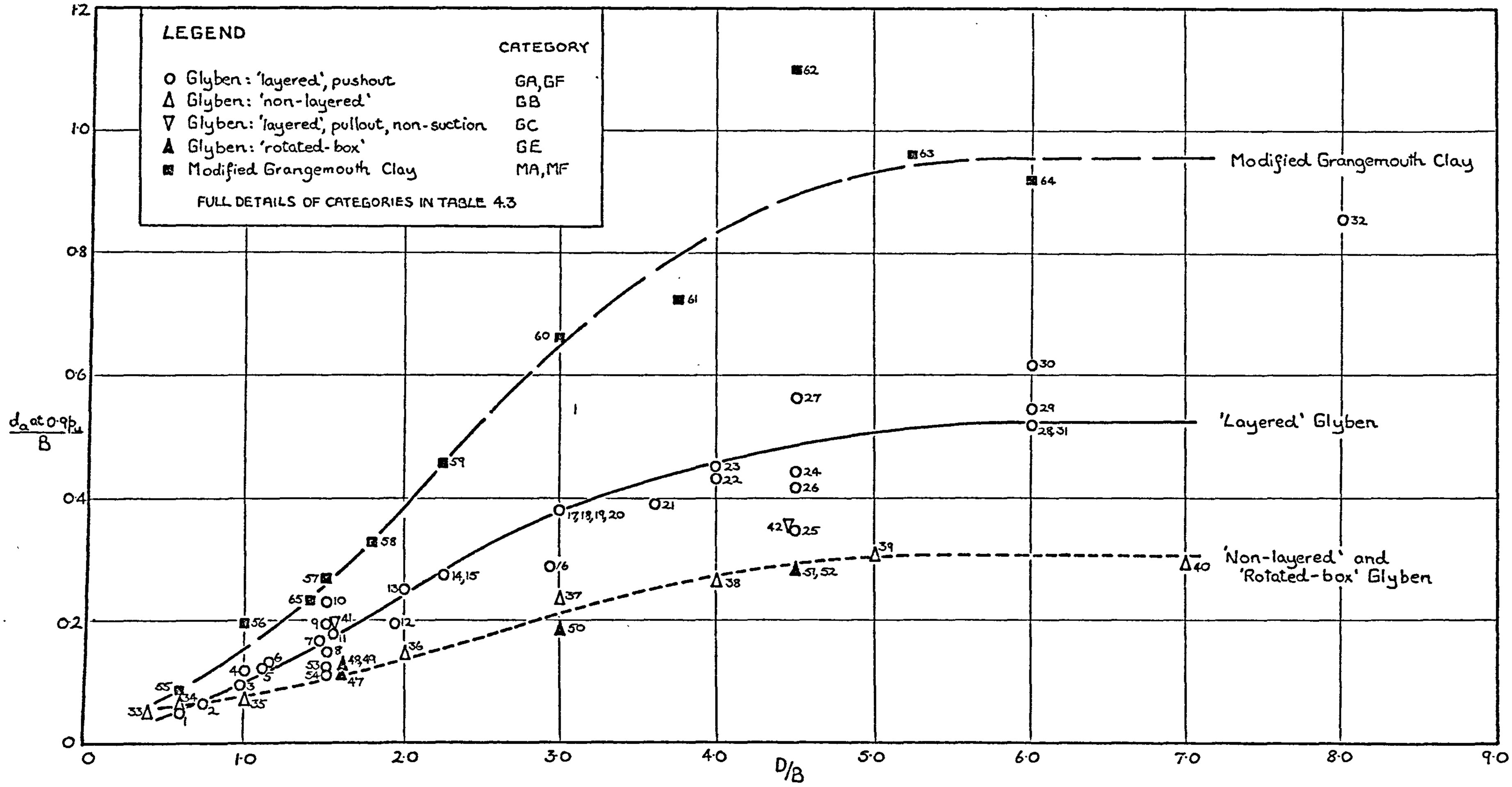

FIG. 4.26. ANCHOR DISPLACEMENT RATIO AT NINETY PERCENT OF ULTIMATE UPLIFT RESISTANCE VERSUS D/B

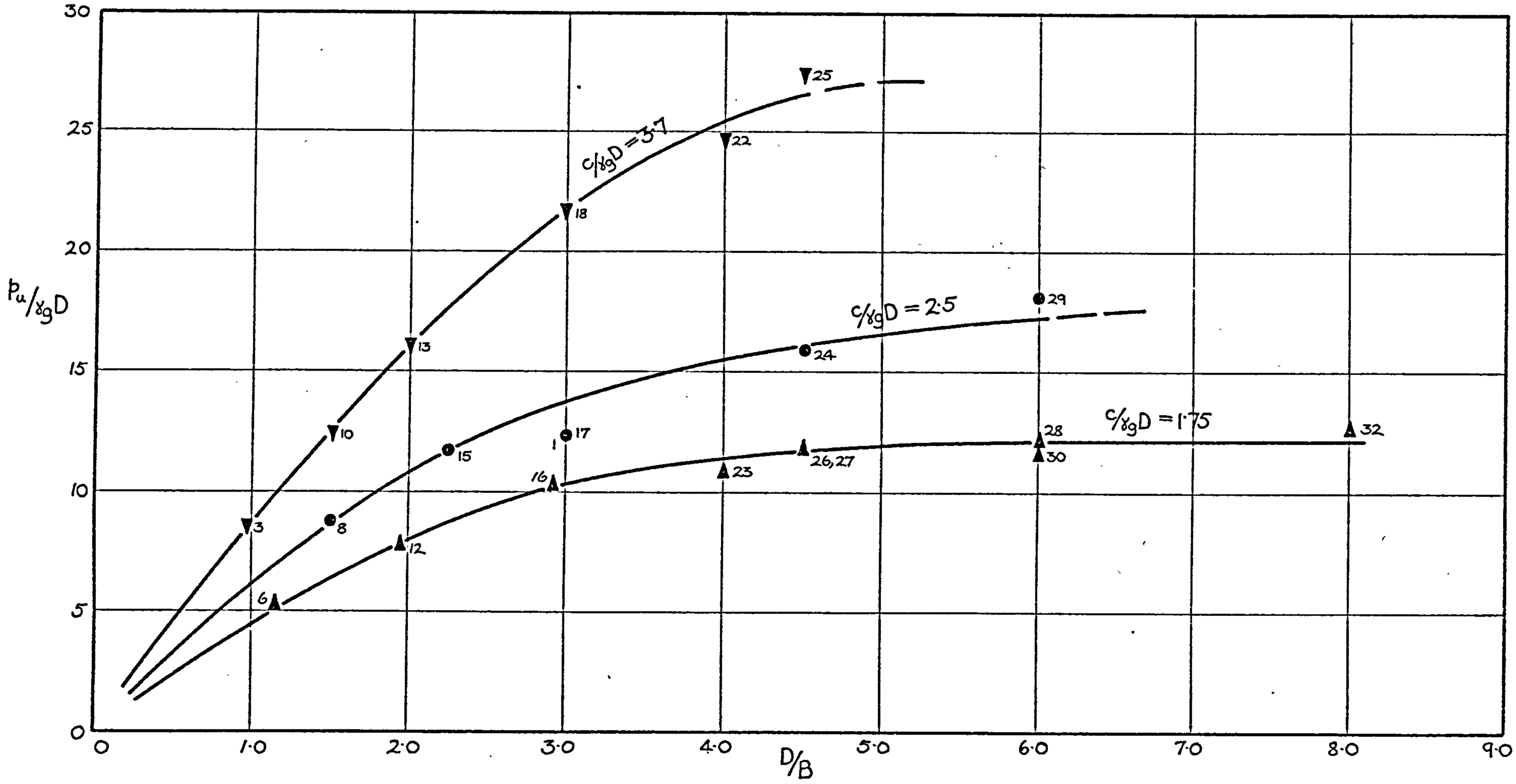

FIG. 4.27. $p_u/\gamma_g D$ v D/B v $c/\gamma_g D$ FOR UPLIFT RESISTANCE TESTS IN "LAYERED" GLYBEN

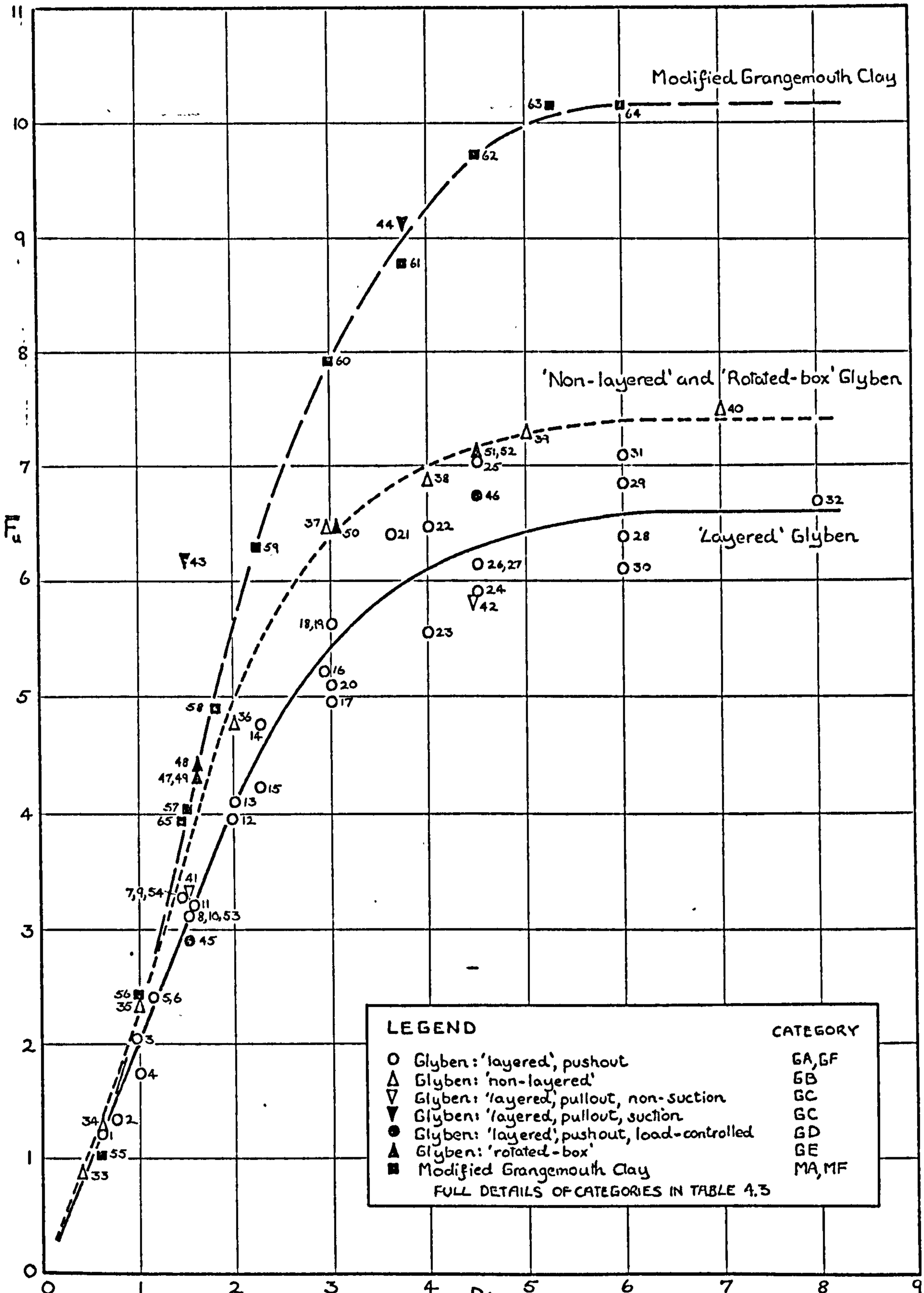

FIG. 4.28. $\bar{F}_u$ VERSUS D/B FOR ALL UPLIFT RESISTANCE TESTS

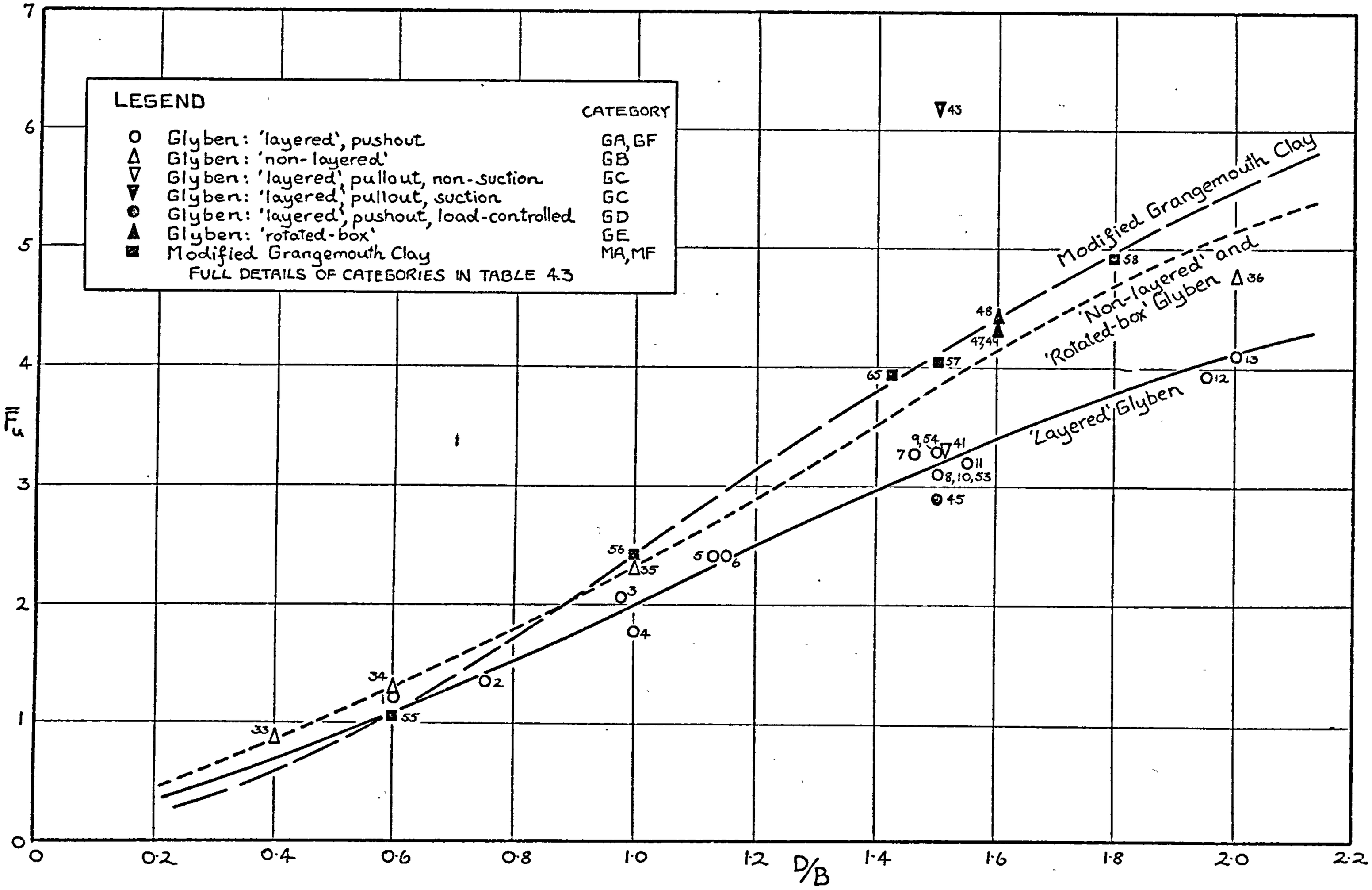

FIG. 4.29. $\bar{F}_u$ VERSUS D/B FOR UPLIFT RESISTANCE TESTS WITH D/B LESS THAN OR EQUAL TO 2.0

CHAPTER FIVE

FINITE ELEMENT ANALYSIS

5.1. Introduction

The details and the results of the laboratory investigations conducted by the author were outlined in chapter 4. These results included plots of the load-displacement relationship of clay samples measured during uplift resistance tests, the measurement of the values of ultimate uplift resistance of the clay samples, the measurement of the surface deformation of the samples during the tests and the examination of the internal displacement and cracking in the samples at ultimate uplift resistance. However, measurements were not taken to determine the magnitude and distribution of stresses in the samples during the uplift resistance tests and no method was devised to determine experimentally the manner in which the clay in the vicinity of the anchor yielded plastically during the tests. In addition, the internal displacement of the clay could only be estimated approximately and only after the completion of each test. It was therefore considered appropriate to develop a method of analysis in which the displacements and stresses in both the elastic and plastic regions of the samples could be predicted at any stage of the uplift resistance test. For these reasons, a finite element analysis of the problem was proposed.

At the present time, provided that sufficient computer facilities are available, a large range of problems in continuum mechanics can be analysed by the finite element method. However, the accuracy of the results obtained by this method will depend to a large extent on the accuracy of the data which is used in the analysis. In soil mechanics problems, this point is of particular importance, since soil behaviour is difficult to predict accurately. For example, although a series of laboratory triaxial strength tests on samples of soil may give a consistent stress-strain curve, it can seldom be determined

whether these samples are completely representative of the soil in the field and whether the soil will behave in the predicted manner under the complex stress patterns which are experienced in the field. However, this limitation in accuracy applies to any form of analysis which attempts to predict the behaviour of the soil in the field from data measured in the laboratory and must be recognised and allowed for by the investigator.

In the following sections, the features which were included in the finite element analysis will be outlined, the limitations of the program will be stated and the results from the analysis will be presented. A detailed description of the program is given in Appendix E.

The primary purpose of the finite element analysis used in this investigation was to examine the displacements and the stresses which occurred in the soil mass during uplift resistance. Although the results are presented in a quantitative form, they are intended only to be a guide to the way in which a clay will perform at various stages of an uplift resistance test rather than a prediction of the precise values of the stresses and displacements which will occur. This is because of the various assumptions and approximations inherent in the program and the properties of the ideal material which are assumed in the program, and which will be described in section 5.4 of this chapter.

5.2. General Features of the Finite Element Program used in the Investigation

The program which was used in this investigation was originally developed by Dr. I.M. Smith of the University of Manchester, but it had to be subsequently considerably modified by the author for use in the uplift resistance problem. Details of the program can be found in Appendix E. An outline of its features is as follows:

(a) It is an axi-symmetric program which uses isoparametric quadrilateral elements with two degrees of freedom, radial and vertical, per node.

(b) The integration to calculate the values of element stiffnesses is numerical and uses the Gaussian quadrature formulae.

(c) The Gaussian elimination procedure is employed to obtain nodal displacements from the structural stiffness matrix and the load vector.

(d) It is an elastic-plastic analysis which uses the "initial stress" method developed by Zienkiewicz et. al. (1969) and the elastic-plastic constitutive matrix derived by Yamada et. al. (1968).

(e) The magnitude of the anchor loads in the load vector can be increased by specified amounts. If, in any element, the resulting stresses are greater than the level of the defined yield stress for the material, according to Von Mises failure criterion, the excess stresses are redistributed to the remaining elements by an iterative procedure.

(f) For the initial load increment, if the elastic portion of the stress-strain curve is assumed to be linear, the values of the terms in the load vector can be proportionally increased or decreased by the program so that the value of stress in the "critical" element will be fractionally less than the specified value of Von Mises Yield Stress for the material, where the "critical" element is defined as the first element in the mesh to reach the specified value of Von Mises Yield Stress. This means that the initial load increment can be adjusted by the program so that it becomes the largest load under which all of the elements in the mesh remain on the elastic portion of the material stress-strain curve.

(g) The analysis makes provision for the inclusion of internal stresses due to material self-weight.

(h) The anchor plate is treated as being rigid in the analysis and this requires that all nodes on the plate are displaced by an equal

amount during loading.

(i) The magnitude of the residual loads (defined in Appendix E), corresponding to the applied load values which produce element stresses on the elastic portion of the material stress-strain curve, can be calculated.

Fig. 5.1 illustrates one of the meshes (mesh no. 1) which was used in the finite element analysis. Although the elements are depicted in the figure as being two-dimensional, since the problem is axi-symmetric, each element is a toroid with a volume approximately equal to $2\pi r A_e$, where r is the average distance of an element from the axis of symmetry and A_e is the area of the element, as shown in Fig. 5.1. Fig. 5.1. shows any half-section through the axis of symmetry of the cylindrical mesh, with A-A representing the position of the anchor plate. As described in part (h) above, the anchor plate is treated as being rigid, which requires that the nodes 1, 2, 3, 4 and 5 of elements ⓐ, ⓑ, ⓒ, ⓓ and ⓧ must always be displaced vertically by equal amounts to simulate the rigid anchor plate. Details of how this is achieved are given in Appendix E. To simulate the case of no suction below the anchor plate, the elements ⓔ, ⓕ, ⓖ, ⓗ and ⓨ have separate nodes 6, 7, 8, 9 and10, and this allows the elements above and below the anchor plate to separate freely when nodes 1, 2, 3, 4 and 5 are displaced. The nodes of the elements at the bottom and side extremities of the mesh are completely restrained, i.e. no radial or vertical movement is allowed, in order to simulate the rigid sides and base of a box with a high value of adhesion between soil and box. The nodes on the axis of symmetry of the mesh are restrained in a radial direction due to the symmetry of the problem. The elements which are close to the anchor plate are smallest, i.e. the mesh is finest, since details of stresses and displacements near the anchor plate are considered to be of greatest importance. As

the distance from the anchor plate increases, the elements become larger and the mesh correspondingly coarser.

5.3. Scope of the Finite Element Program used in the Investigation

In this section, the input data which is required by the program and the resulting information which is output by the program will be described. Although a printout of the program is not included in this thesis, a complete flow chart of the program can be found inside the back cover.

A. Input Data Required by the Program

Details of this data are given in Table 5.1.

B. Output given by the Program

By varying the input data described in Table 5.1, most of the parameters described in chapter 3 as being relevant to the problem may be varied, e.g. by varying the element sizes and the number and geometry of the elements and loaded nodes, various depth to breadth ratios and box sizes can be simulated; by restraining the horizontal degrees of freedom in the anchor nodes, the anchor can be made completely rough; by varying the values of E, ν, γ, and c, different purely cohesive soils can be simulated. The program supplied information which was employed directly or indirectly to show the following:

(a) the radial and vertical displacements of all nodes, corresponding to the applied loading. In the axi-symmetric case, there were no displacements of nodes in the circumferential direction because of the symmetry of the problem.

(b) the order in which the various elements in the mesh yielded, according to Von Mises failure criterion.

(c) the magnitude and direction of the principal stresses and the maximum shear stress in each element, corresponding to each load increment.

(d) the magnitude and distribution of the radial, vertical and circumferential normal stresses, both compressive and tensile, and the shear stresses in each element, corresponding to each load increment. In the axi-symmetric case, no shear stresses existed on the circumferential plane due to the symmetry of the problem.

(e) the load-displacement relationship of the anchor in the soil.

(f) the value of the residual loads on each node after the first load increment.

5.4. Limitations of the Finite Element Program used in the Investigation

In the Introduction to this chapter, it was stated that the accuracy of the results obtained by the finite element analysis depended to a large extent on the accuracy of the soil data which was employed in the analysis. In addition, the accuracy of the results was affected by the following limitations in the program:

(a) the values of the stresses obtained in each element were values for the stresses at the centre of the element only.

(b) the use of quadrilateral elements with two degrees of freedom per node assumed that all element sides would remain straight during deformation. This is not what occurs in real soil which, when stressed, deforms in a non-linear manner. The effect of this assumption may be seen in the figures which illustrate mesh deformation due to anchor displacements (Figs. 5.5, 5.6, 5.7 and 5.8.).

(c) element stiffness integration very near the axis in the axi-symmetric problem tended to be inaccurate. The effect of this inaccuracy was diminished by using a finer mesh near the axis.

(d) the use of a curved stress-strain relationship for the soil in the program increased computer time very considerably. Therefore, a linear elastic non-strain hardening plastic relationship was

used throughout this part of the investigation. The three linear elastic non-strain hardening plastic stress-strain curves which are assumed to simulate the actual stress-strain relationship of a clay are shown in Fig. 5.2. These curves will be described in section 5.5of this chapter and the significance of these approximations to the actual stress-strain relationship will be discussed in chapter 6. No cracking was assumed to occur in the material when subjected to tensile stresses, and the values of yield strength in compression and tension were assumed to be equal.

(e) only an approximate value of anchor plate loading corresponding to a specified anchor displacement could be obtained. In order to estimate the plate loading, the values of stresses at the centre of the elements which were adjacent to and directly above the anchor were integrated over the element volume to obtain the nodal loads. However, the "critical" element, shown as ⊗ in Fig. 5.1, will always have high values of compressive stress on the side nearer the axis, and high values of tensile stress on the side farther from the axis and the value of stress at the centre of this element will always be lower than the value of stress which corresponds to the load at the edge of the anchor. Therefore, the value of nodal load for node 5 in Fig. 5.1 will always be output as less than the actual value. Appendix E gives details of the way in which the level of inaccuracy of the value of the nodal loads obtained from the stresses in the "critical" element was estimated. The sign convention which was used in the finite element analysis is also presented in Appendix E.

(f) the program could only be used accurately in cases where the total strain on any element was small, because of the assumptions of small strain which were made in deriving the element characteristics.

(g) the program calculated nodal displacements and element strains and stresses for each load increment, taking into account the strains and stresses which existed in each element due to previous load increments. However, the program assumed the original geometry of the nodes at all times, i.e. at each new load increment the geometry of the mesh was assumed to be as illustrated in Fig. 5.3. Due to this limitation and that of (b) and (f) above, the program could not take into account local types of failure in the soil, such as predicted by Vesic (1963 and 1965) and Meyerhof and Adams (1968) for deep anchors, but continued to increase the loads until a general failure occurred.

5.5. Details of the Data used in the Finite Element Analysis

In section 5.3, the output of the program was outlined and it was stated that the values of the output were a function of the parameters which were described in chapter 3 as playing a significant part in the uplift resistance problem. Since eleven parameters were involved, a very large number of program runs would have been required to analyse and compare the output from the various combinations of these parameters. In view of this, it was decided to vary those parameters which the author considered to be most important and to keep the other parameters constant at representative values.

The parameters which were varied were the depth to breadth ratios, D/B, of the anchor plate. Runs were made with three different meshes corresponding to three values of D/B, namely 1.5, 3.2 and 5.25, in order to simulate shallow, intermediate depth and deep anchor tests respectively. These three D/B values were chosen by the author after an examination of the results from his laboratory model tests. Details of the meshes are given in Table 5.2, along with the values of the parameters which were kept constant. The meshes are illustrated in Fig. 5.2. Before a description of the output from these runs is made,

a brief explanation about the values of the parameters shown in Table 5.2 will be given.

Table 5.2 shows that the soil was assumed to be weightless in the three runs. As described in Appendix E, the value of stress in each element due to material self-weight could be included in the program and this stress would be a constant throughout the various load increments and iterations during the program run. The stresses in the elements adjacent to the anchor were integrated over their volume to find the load on the anchor. The load on the anchor plate due to material self-weight would be constant and equal to $\gamma_g DA$, where A is the area of the anchor plate. The values of self-weight stresses in the vertical, radial and circumferential directions in each element would also be constant throughout the entire program run, due to the geometry of the mesh remaining unaltered. Therefore, if the value of total stress in any element were required, the values of the stresses in the element due to material self-weight could be added to the values of the stresses which resulted from the displacement of the anchor plate. For the purposes of this investigation, the coefficient of earth pressure at rest was assumed to be unity, which was considered to be a reasonable assumption for a saturated clay. Under this assumption, the self-weight would have no effect on the value of the Von Mises stress for the element. In view of the above considerations, it was considered by the author that the three runs should be made without the addition of material self-weight stresses.

It is shown in Appendix E that in the finite element uplift resistance program the relationship between nodal loads and displacements and the relationship between element stresses and strains in both the elastic and plastic portions of the material stress-strain curve were inverse linear functions of the elastic modulus E . By considering the three stress-strain curves shown in Fig. 5.4, it will be shown that,

if a finite element program assumes a linear elastic non-strain hardening plastic stress-strain curve, then the values of stresses, strains, displacements, and loads resulting from that program can be proportioned to any required value of elastic modulus E or yield stress $\bar{\sigma}_y$. It must be emphasised that the three curves depicted in Fig. 5.4 are for demonstrating this point only, and have no connection with the stress-strain curves used in the uplift resistance finite element program. A comparison of (i) curves A and B in Fig. 5.4, and (ii) curves A and C in Fig. 5.4, will be considered.

Case (i) : curves A and B. In curve A, the value of the elastic modulus E , which corresponds to the slope of the elastic portion of the curve, is double that of curve B, but the value of yield stress $\bar{\sigma}_y$, which corresponds to the value of stress of the horizontal plastic portion of the curve, remains the same. For any value of nodal load in finite element program runs using these stress-strain curves, the corresponding value of nodal displacement for curve A will be half of that for curve B. For any value of element stress in either the elastic or plastic zone, the corresponding value of element strain for curve A will be half of that for curve B. If the value of the uplift resistance factor $\bar{F}$ ($= P/c$ in the weightless case) is plotted against the anchor displacement ratio $d_{a/B}$ for runs using material stress-strain curves A and B, the $d_{a/B}$ values for a material with curve A will be half of that for a material with curve B for the same value of $\bar{F}$.

Case (ii): curves A and C. The value of E in curve A is half of that in curve C, and the value of $\bar{\sigma}_y$ stress is also half, i.e. $\frac{E}{\bar{\sigma}_y}$ is the same for both curves. For any value of nodal displacement, the corresponding value of nodal load for curve A will be half of that for curve C and for any value of element strain in either the elastic or plastic zone, the corresponding value of element stress for curve A will be half of that for curve C. If the value of $\bar{F}$ is plotted

against $d_{a/B}$ for runs using material stress-strain curves A and C, the plots will be identical.

Cases (i) and (ii) demonstrate that, if a linear elastic non-strain hardening plastic material stress-strain curve is assumed, then the results from a program which uses nominal values of E and $\bar{\sigma}_y$ can be proportioned to any required value of E and $\bar{\sigma}_y$. It is therefore necessary to run the program with only one value of E and one value of $\bar{\sigma}_y$. However, as was explained in part (f) of section 5.4 of this chapter, the element characteristics have been derived under the assumption of small strains. Therefore, if a low value of E and a high value of $\bar{\sigma}_y$ are used, giving a small value of $\frac{E}{\bar{\sigma}_y}$, and the resulting element strains are large, then these results may be inaccurate since they do not conform to the basic assumption of small element strains.

In order to simulate values of elastic modulus and yield stress for a very soft clay, values of $E = 720$ kN/m^2 and $\bar{\sigma}_y = 18$ kN/m^2 were used in runs 1, 2 and 3. However, since a linear elastic non-strain hardening plastic stress-strain curve was assumed in the program, the results from the program could be proportioned to any values of E and $\bar{\sigma}_y$, bearing in mind the limitations on element strains described previously. The values of nodal displacements and corresponding stresses and strains obtained from the finite element runs using $E = 720$ kN/m^2 were proportioned to correspond to values of $E = 1200$ kN/m^2, $E = 430$ kN/m^2 and $E = 100$ kN/m^2 in order to simulate the tangent modulus, the chord modulus at one half of the yield stress and the chord modulus at total yield stress respectively of the batch no. 3 glyben stress-strain curve illustrated in Fig. 5.2. The linear elastic non-strain hardening plastic curves for $E = 1200$ kN/m^2, 430 kN/m^2 and 100 kN/m^2 are also illustrated in Fig. 5.2. In all of the curves in this figure, the value of yield stress was 18 kN/m^2.

The values of the nodal displacements, stresses and strains are presented in section 5.6of this chapter and discussed in chapter 6.

It is also shown in Appendix E that the relationship between nodal loads and displacements and the relationship between element stresses and strains are functions of Poisson's ratio ν . However, unlike the function for the elastic modulus E , the function for ν is not a simple one. In the runs shown in Table 5.2, a value of $\nu = 0.495$ was employed, the clay being assumed to be almost incompressible. Two additional short runs, each using only six increments of load, were performed on mesh no. 2 with $\nu = 0.25$ and $\nu = 0.0$. Because of the higher values of compressibility of the materials with the small values of Poisson's ratio, the values of anchor displacements corresponding to a certain value of anchor load increased as the value of ν decreased. However, the relationship between nodal loads and displacements and between element stresses and strains corresponding to the various values of Poisson's ratio were complex and difficult to compare and will not be considered further in this investigation.

For the three runs shown in Table 5.2, a completely smooth anchor face was assumed, i.e. the radial degrees of freedom of the anchor nodes were not restrained. An additional short run was performed with mesh no. 2, employing restraints on the radial displacements of the anchor nodes to simulate a completely rough anchor. As in the short runs with the varying values of Poisson's ratio, a basis for comparison was difficult to find since, although small differences were noted between the values of element stresses in the rough and the smooth anchor cases, there was no consistent pattern in the differences, e.g. there was a small increase in the values of stresses in some elements and a small decrease in others. It is recommended in Future Work that a further investigation, using the finite element analysis, be conducted into the effects of varying the values of Poisson's ratio and anchor roughness.

The values of the ratio of box diameter to anchor diameter B_c/B used in runs 1, 2 and 3 were 5.75, 7.33 and 11.50 respectively. These were considered by the author to be ratios representative of those used in the laboratory model tests. In each mesh, the height of the anchor plate above the base of the box was approximately equal to B . Two additional short runs with mesh no. 2 were performed which used ratios of B_c/B of approximately double and half of that used in run no. 2. In both of these additional runs, the height of the anchor plate above the base of the box was altered proportionally. In the case where the value of B_c/B was doubled, the displacement of the anchor which was required to cause yielding in the "critical" element was increased by approximately 4%, which reflected the reduced structural stiffness of the mesh. However, the relationship of uplift resistance versus anchor displacement for the mesh was very similar to that of the original mesh. In the case in which the B_c/B ratio of the mesh was halved, the displacement of the anchor which was required to cause yielding in the "critical" element was reduced by approximately 13%, which reflected the increased structural stiffness of the mesh. The relationship of uplift resistance versus anchor displacement for this mesh was significantly different from that of the original mesh, the slope of the curve (not shown) being approximately 30% steeper than in the original. It may be concluded that, as the B_c/B ratio increases, the effect of its alteration on the values of stresses, strains, loads and displacements becomes correspondingly less. However, as the B_c/B ratio approaches unity, the effect of its alteration on the above values correspondingly increases.

5.6. Presentation of the Results of the Finite Element Runs

In this section, the results which were obtained from runs 1, 2 and 3 are presented. The results of these runs will be compared and discussed in chapter 6.

The results of the finite element runs can be divided into three sections for presentation purposes:

A. Prediction of nodal displacements in the meshes.

B. Relationship between uplift resistance and anchor displacements in the meshes.

C. Values of stresses in the elements.

The order in which the results are presented in this chapter will be the order in which they are discussed in chapter 6.

A. Prediction of Nodal Displacements in the Meshes

Fig. 5.5 shows the nodal displacements in the shallow anchor mesh for run no. 1, with $D/B = 1.5$, at the stage of the run when the value of the stress in the "critical" element was just below the value of the Von Mises Yield Stress. This stage is represented by point Ⓐ in Fig. 5.12. Fig. 5.12 shows plots of the uplift resistance factor F versus the anchor displacement ratio d_a/B for runs 1, 2 and 3, and will be described further in part B of this section. At this stage of the run, all of the elements in the mesh still remained on the elastic portion of the material stress-strain curve, although a fractional increase in anchor load would have caused the "critical" element to yield. Fig. 5.6 shows the nodal displacements in the shallow anchor mesh at ultimate uplift resistance, represented by point Ⓑ in Fig. 5.12. The values of both the radial and vertical displacements shown in Figs. 5.5 and 5.6 have been adjusted for $E = 430\ kN/m^2$, which corresponds to the chord modulus at half of the yield stress in Fig. 5.2, and have been scaled up by a factor of 8 for presentation purposes.

Fig. 5.7 shows the nodal displacements in the deep anchor mesh for run no. 3, with $D/B = 5.25$, at the point when the value of stress in the "critical" element was just below the value of Von Mises Yield Stress, and this point is represented by Ⓔ in Fig. 5.12. Fig. 5.8

shows the nodal displacements at a stage nearing the ultimate uplift resistance of the soil, represented by point Ⓕ in Fig. 5.12. The values of both the radial and vertical displacements shown in Figs. 5.7 and 5.8 have been adjusted for $E = 430\ kN/m^2$ and have been scaled up by factors of 17 and 5 respectively for presentation purposes.

B. Relationship between Uplift Resistance and Anchor Displacements in the Meshes

Fig. 5.9 illustrates curves of $\bar{F}$ v d_a/B plotted from the output obtained from run no. 1, with $D/B = 1.5$, and which correspond to the three values of E which are shown in Fig. 5.2. As described earlier, these values of E represent the initial tangent modulus ($E = 1200\ kN/m^2$), the chord modulus at one half of the yield stress ($E = 430\ kN/m^2$) and the chord modulus at the total yield stress ($E = 100\ kN/m^2$) of the average stress-strain curve obtained from an unconfined compression test on a sample of batch no. 3 glyben, also shown in Fig. 5.2. A curve of $\bar{F}$ v d_a/B for the shallow "rotated-box" glyben test no. 47, with $D/B = 1.6$, is included in Fig. 5.9 for comparative purposes. Fig. 5.10 shows $\bar{F}$ v d_a/B curves plotted from the output obtained from run no. 2, with $D/B = 3.2$, corresponding to the three values of elastic modulus E described above. The curve for "non-layered" glyben test no. 37, with $D/B = 3.0$, is included in Fig. 5.10 for comparative purposes. Fig. 5.11 shows $\bar{F}$ v d_a/B curves plotted from the output obtained from run no. 3, with $D/B = 5.25$, corresponding to the three values of E described above. The curve for "non-layered" glyben test no. 40, with $D/B = 7.0$, is included in Fig. 5.11 for comparative purposes. In Fig. 5.12, the $\bar{F}$ v d_a/B curves for runs 1, 2 and 3, with $E = 430\ kN/m^2$, are illustrated.

C. Values of Stresses in the Elements

Order of yielding of the elements. Figs. 5.3 (a), (b) and (c) show the order in which the elements yielded, according to the Von

Mises failure criterion, in runs 1, 2 and 3 respectively. For run no. 1, with D/B = 1.5, and run no. 2, with D/B = 3.2, the order of yielding up to ultimate failure of the soil is shown. For run no. 3, with D/B = 5.25, yielding up to ultimate failure is not shown since, as ultimate failure was approached, the output of the program became inconsistent, possibly due to the large number of yielded elements at that stage. As will be discussed in chapter 6, general ultimate failure occured only when all of the elements above the "critical" element had yielded plastically.

Magnitude and direction of principal stresses. Fig. 5.13 (a) depicts the direction of the major principal stress, i.e. the direction of the greatest compressive, or least tensile, stress in each element of the shallow anchor mesh in run no. 1, with D/B = 1.5, at the point when the value of stress in the "critical" element was just below the value of Von Mises Yield Stress. This stage of the test is represented by point Ⓐ in Fig. 5.12. The thickness of the lines which represent the stress directions give a guide to the size of the major principal stresses, but do not vary linearly with the magnitude of the stresses. The shaded areas in the figure represent the regions in which the major principal stresses were tensile and the unshaded areas represent the regions in which the major principal stresses were compressive. Dotted lines indicate the boundaries between these regions. Since the major principal stresses which are illustrated in Fig. 5.13 (a) are defined as being the greatest compressive, or least tensile, stresses in each element, the shaded areas depict elements in which the normal stresses on all planes in the elements were tensile, as shown on the Mohr circle representation in Fig. 5.16. Fig. 5.13 (b) depicts the magnitude and direction of the major principal stresses in run no. 1 at ultimate uplift resistance. Figs. 5.14 and 5.15 illustrate the magnitude and direction of the major principal stresses in runs 2 and 3

respectively. In Fig. 5.14, the stresses are shown corresponding to the stage of "critical" element yielding, represented by point Ⓒ in Fig. 5.12 and corresponding to ultimate uplift resistance, represented by point Ⓓ in Fig. 5.12. In Fig. 5.15, the stresses are shown corresponding to the stage of "critical" element yielding, represented by point Ⓔ in Fig. 5.12 and corresponding to a stage nearing ultimate uplift resistance, represented by point Ⓕ in Fig. 5.12.

Magnitude and distribution of normal and shear stresses. Fig. 5.17 (a) illustrates the distribution of vertical normal stress in run no. 1, with $D/B = 1.5$, when the value of stress in the "critical" element was just below the value of Von Mises Yield Stress, as shown by point Ⓐ in Fig. 5.12. Fig. 5.17 (b) illustrates the distribution of vertical normal stress in run no. 1 at ultimate uplift resistance, as shown by point Ⓑ in Fig. 5.12. The values of the stress contours are given as fractions of the value of the vertical normal stress in the "critical" element when it was on the point of yielding. The shaded areas in the figure represent the areas of tensile vertical normal stress and the unshaded areas represent areas of compressive vertical normal stress. Dotted lines indicate the boundaries between the regions of tensile and compressive stresses. Fig. 5.18 represents the distribution of radial normal stresses in run no. 1 and Fig. 5.19 represents the distribution of shear stresses on the radial plane in the vertical direction (which are identical to the shear stresses on the vertical plane in the radial direction) in run no. 1. The stresses in both of these figures are shown at stages corresponding to "critical" element yield and ultimate uplift resistance. Figs. 5.20, 5.21 and 5.22 represent the distribution of the vertical normal, radial normal and shear stresses respectively in run no. 3 for the deep anchor mesh. The stresses in these figures are shown at stages corresponding to "critical" element yield and nearing ultimate uplift resistance.

In the present chapter and in the previous chapter, the details of the finite element analysis and the laboratory investigation of the uplift resistance problem which were performed by the author have been outlined and the results presented. In chapter 6, these results will be compared and discussed.

TABLE 5.1 INPUT DATA REQUIRED BY THE FINITE ELEMENT PROGRAM

INFORMATION	DETAILS
Element Information	number of sides, number of degrees of freedom and the size of each element
Mesh Information	total number of elements, total number of nodes, number of restrained nodes, number of loaded nodes, total number of degrees of freedom and the position of the anchor plate in the mesh
Soil Parameter Information	values of: bulk density, elastic modulus, Poisson's ratio, and plastic yield stress of the soil
Loading Information	size of the loads (or displacements) applied to loaded nodes, number and size of the load increments and the number of iterations in each increment
Miscellaneous	half-band width of the structural stiffness matrix

TABLE 5.2. DETAILS OF MAIN FINITE ELEMENT RUNS

Run number	Mesh number	Number of elements	Number of nodes	Value of D/B	Value of B/B_c	Number of displacement increments	Number of iterations per increment	Ratio of value of successive increments to value of first increment	Length of run time on KDF9 computer
1	1	182	215	1·50	5·75	15	10	1 : 4	120 mins
2	2	187	220	3·20	7·33	20	10	1 : 2·5	180 mins
3	3	209	243	5·25	11·50	20	10	1 : 2·5	180 mins

Value of elastic modulus E in each run was $720\ kN/m^2$
Value of Poisson's ratio ν in each run was $0{\cdot}495$
Value of Von Mises Yield Stress $\bar{\sigma}_y$ in each run was $18{\cdot}0\ kN/m^2$
Material in each run was considered to be weightless

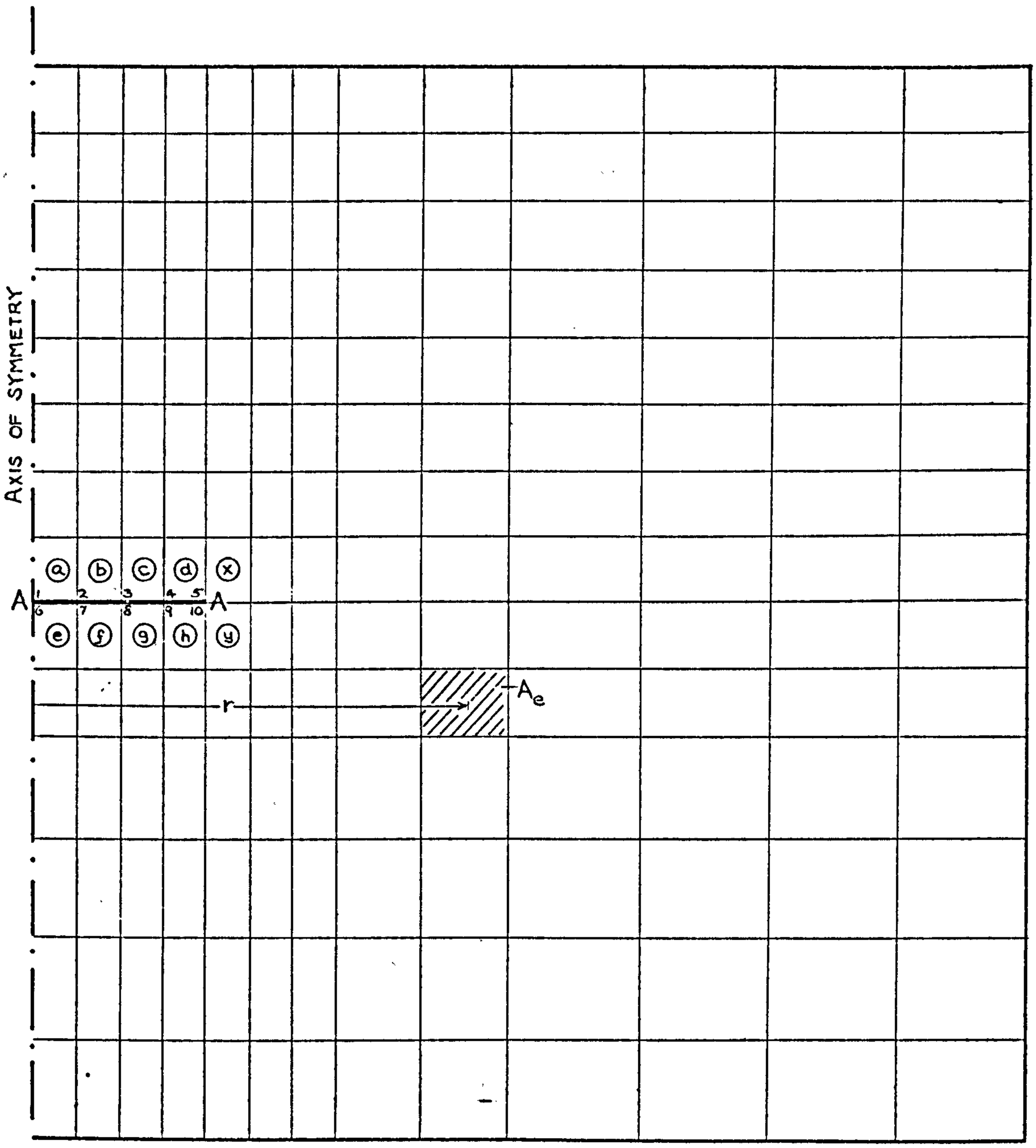

FIG. 5.1. MESH FOR D/B = 1.5, SHOWING ANCHOR NODE DETAILS

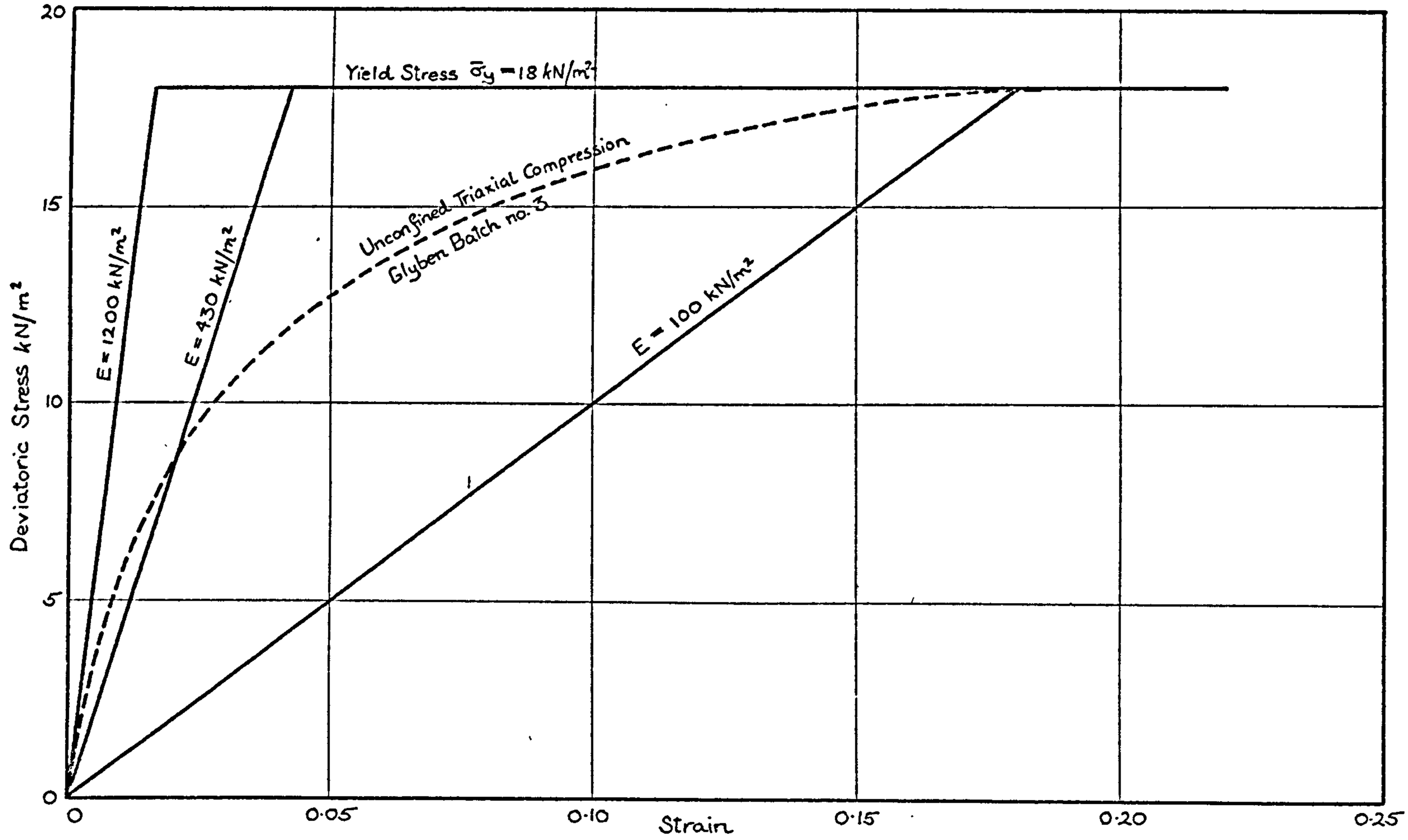

FIG. 5.2. DEVIATORIC STRESS VERSUS STRAIN FOR THE THREE LINEAR ELASTIC NON-STRAIN HARDENING CURVES USED IN THE CALCULATION OF RESULTS AND BASED ON THE CURVE SHOWN FOR BATCH No. 3 GLYBEN

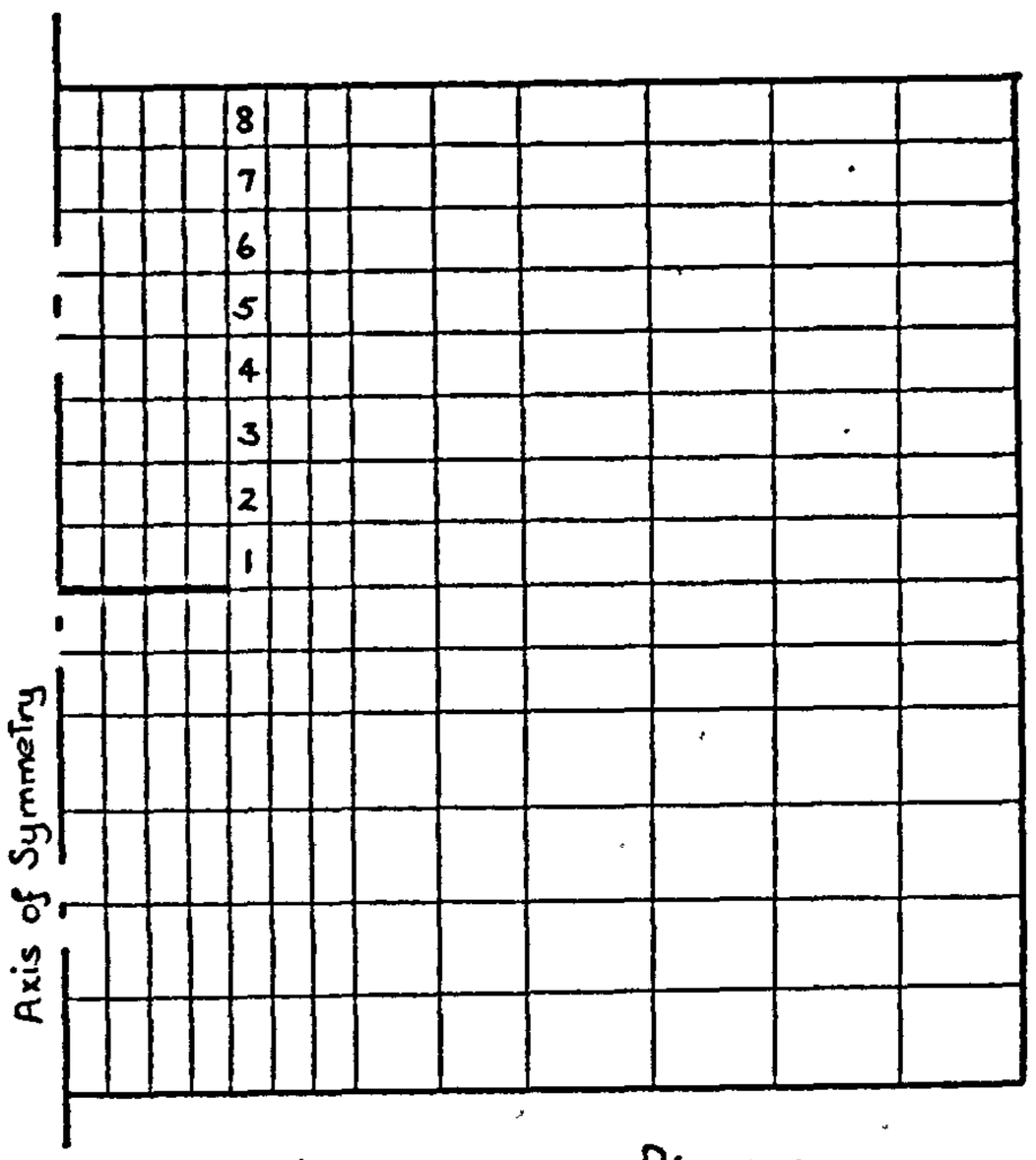

(a) MESH No. 1 $D/B = 1.5$

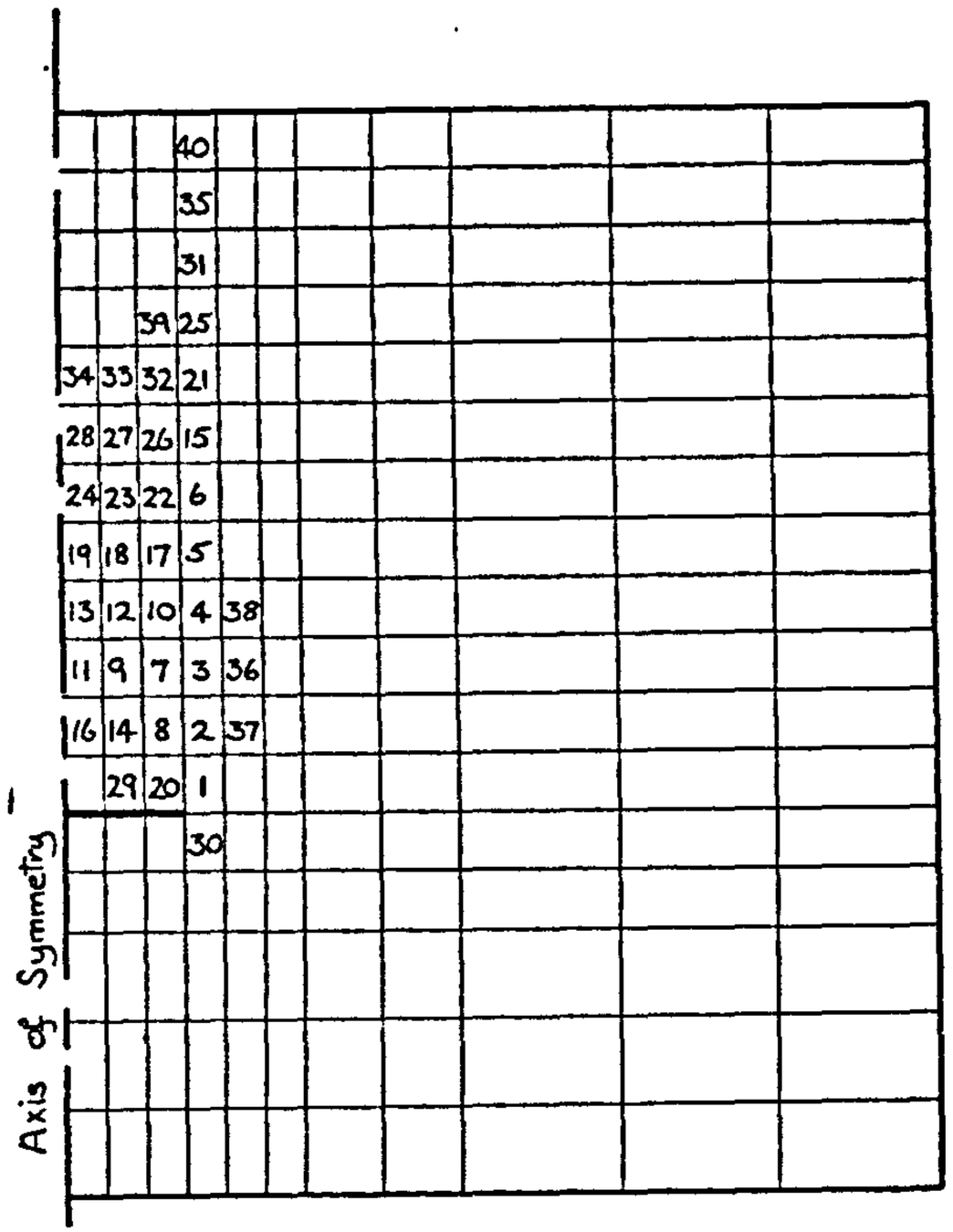

(b) MESH No. 2 $D/B = 3.2$

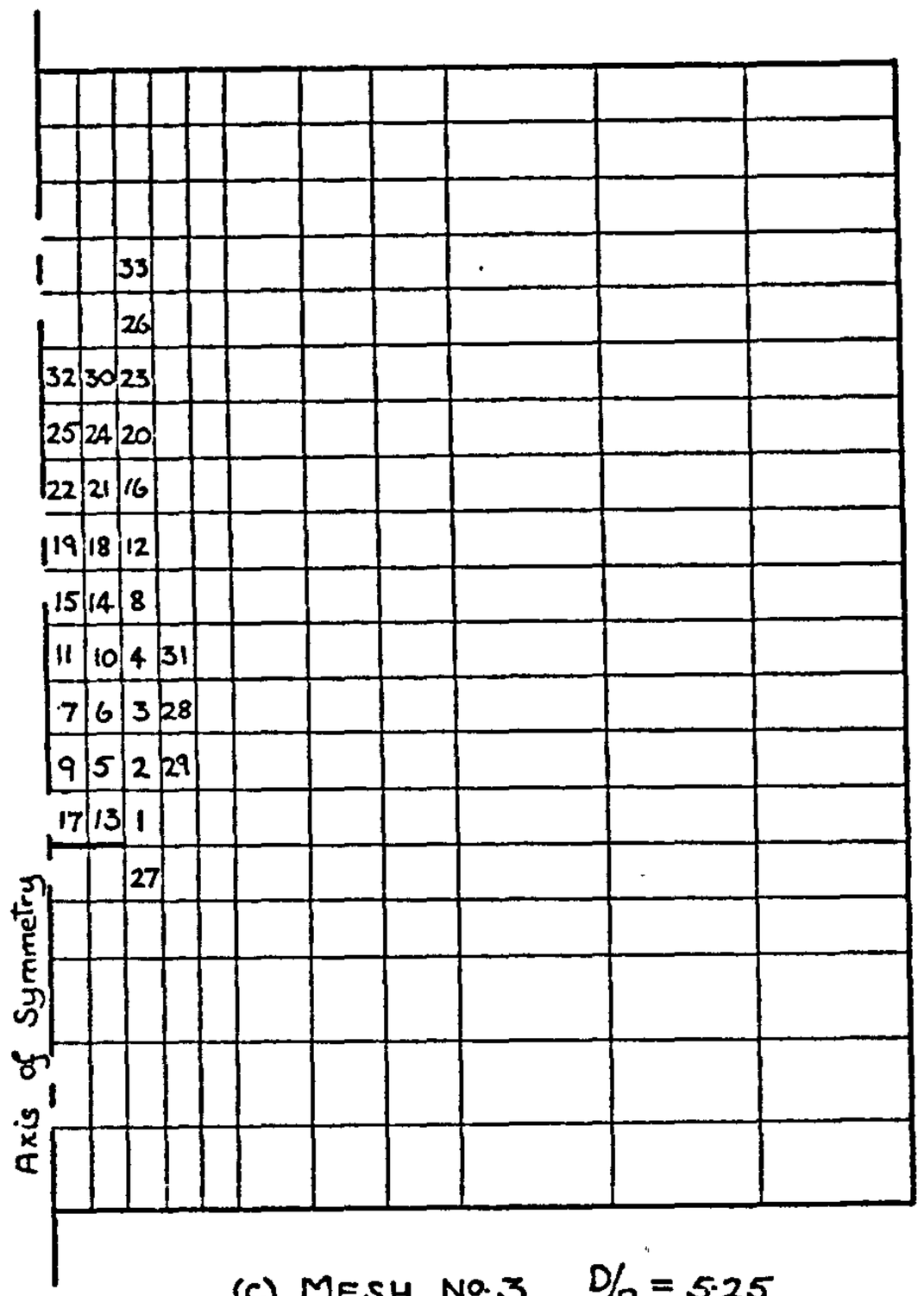

(c) MESH No. 3 $D/B = 5.25$

FIG. 5.3. DETAILS OF THE MESHES USED IN THE FINITE ELEMENT PROGRAM, ILLUSTRATING THE RELATIVE SIZE OF THE ANCHOR AND THE ORDER IN WHICH THE ELEMENTS YIELDED PLASTICALLY

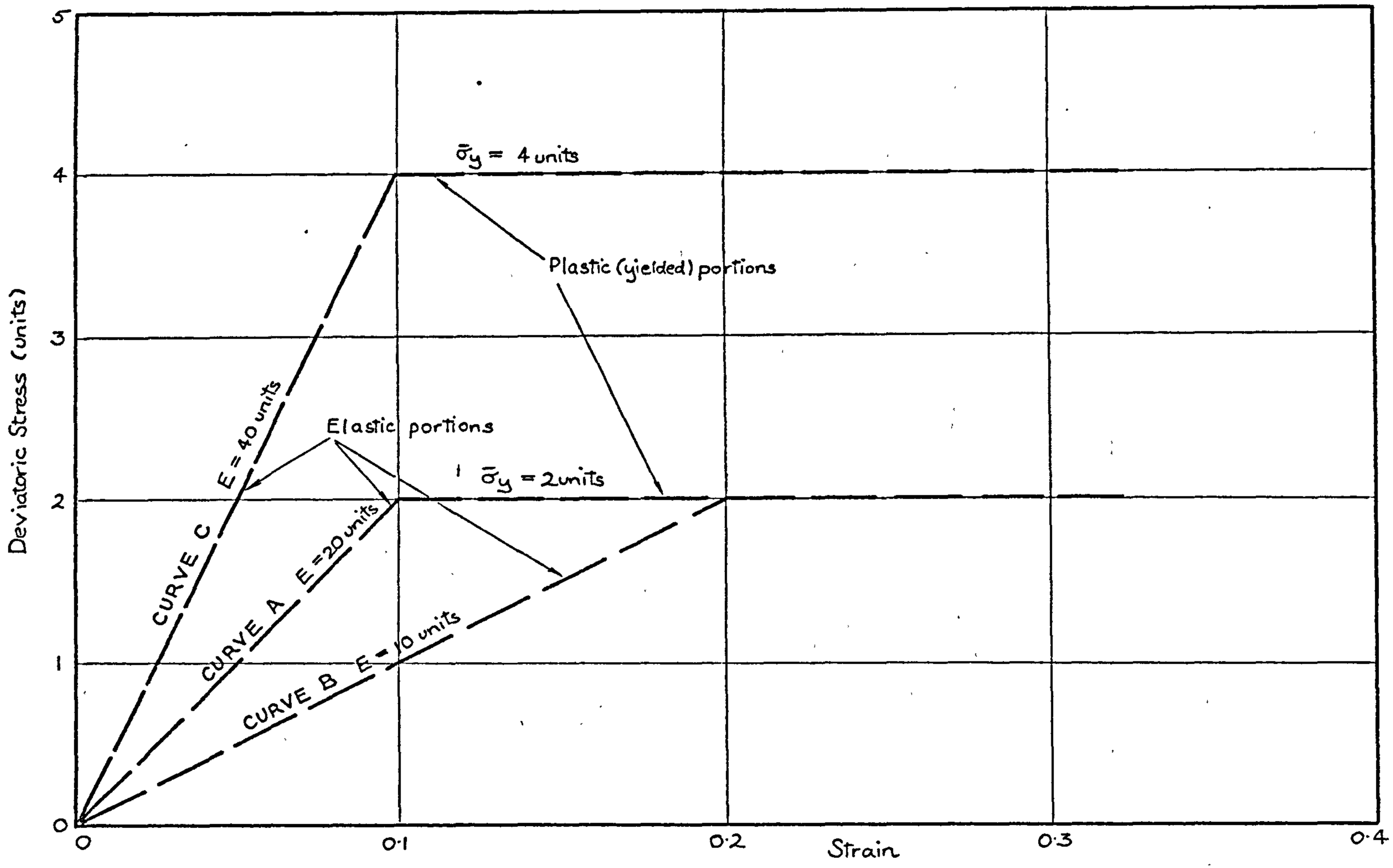

FIG. 5.4. DEVIATORIC STRESS VERSUS STRAIN CURVES FOR THREE LINEAR ELASTIC, NON-STRAIN HARDENING PLASTIC MATERIALS

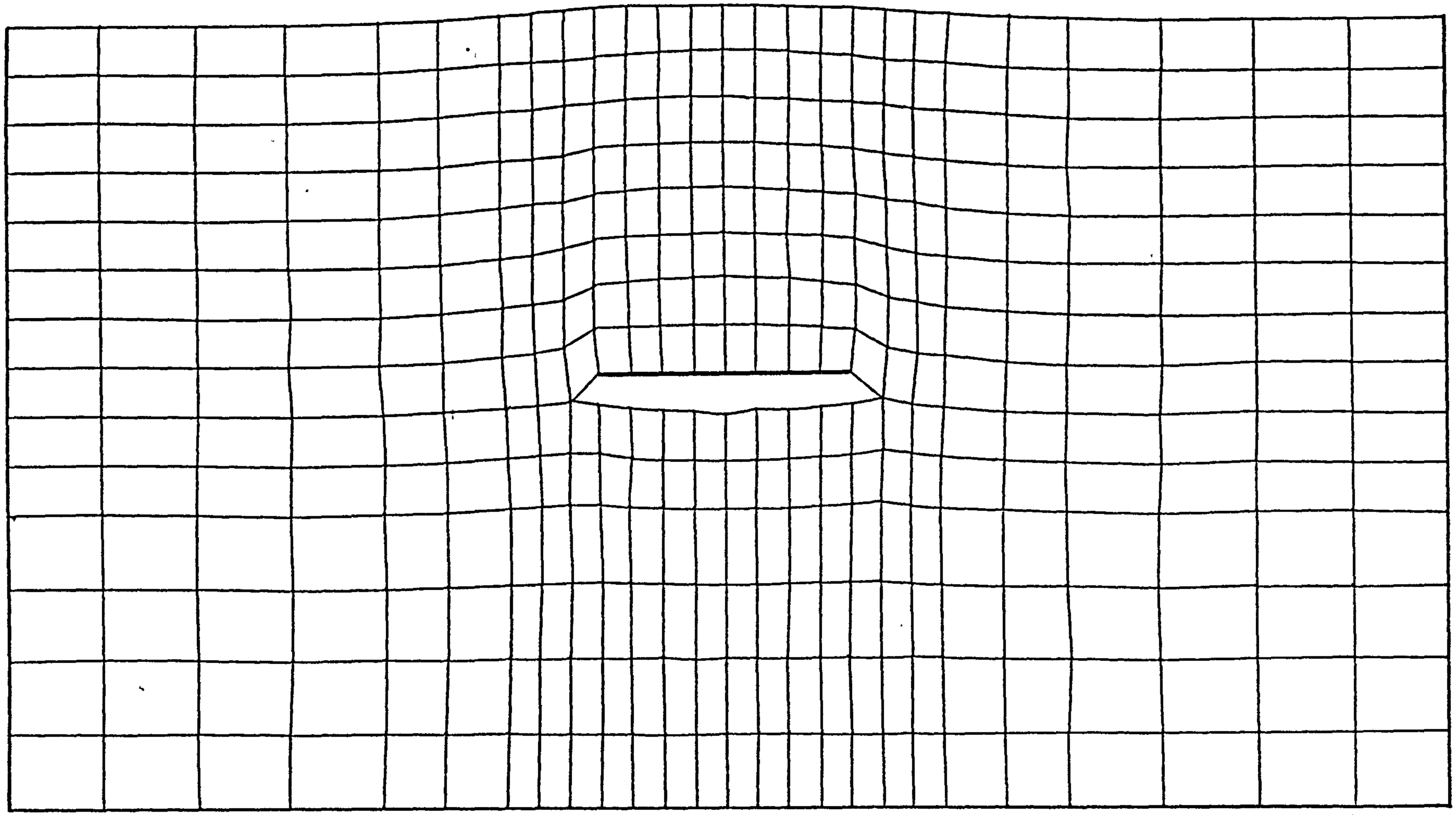

FIG. 5.5. NODAL POSITIONS AT POINT Ⓐ IN FIG. 5.12, RUN No. 1, D/B = 1.5. DISPLACEMENTS ENLARGED BY FACTOR OF 8

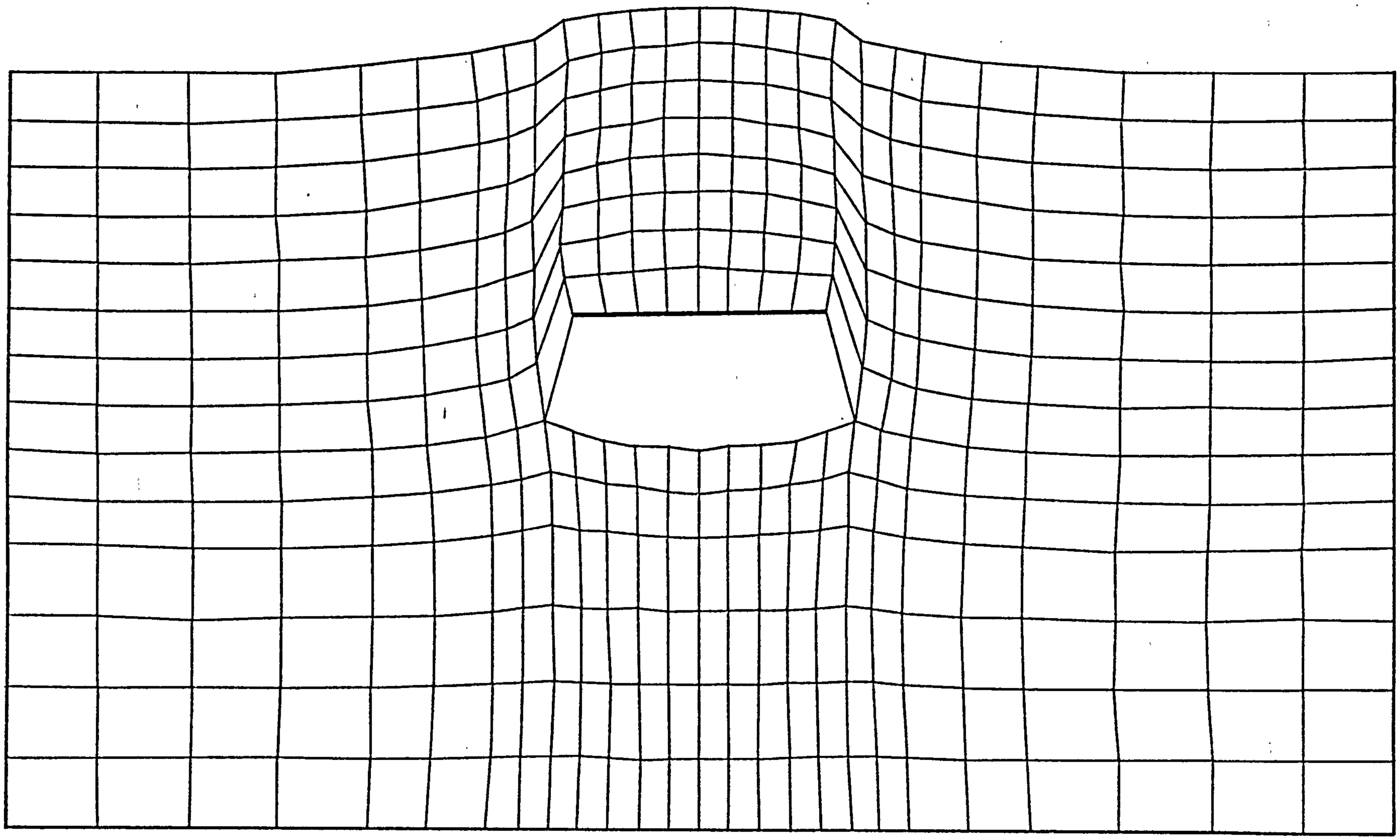

FIG. 5.6. NODAL POSITIONS AT POINT Ⓑ IN FIG. 5.12, RUN No. 1, D/B = 1.5. DISPLACEMENTS ENLARGED BY FACTOR OF 8

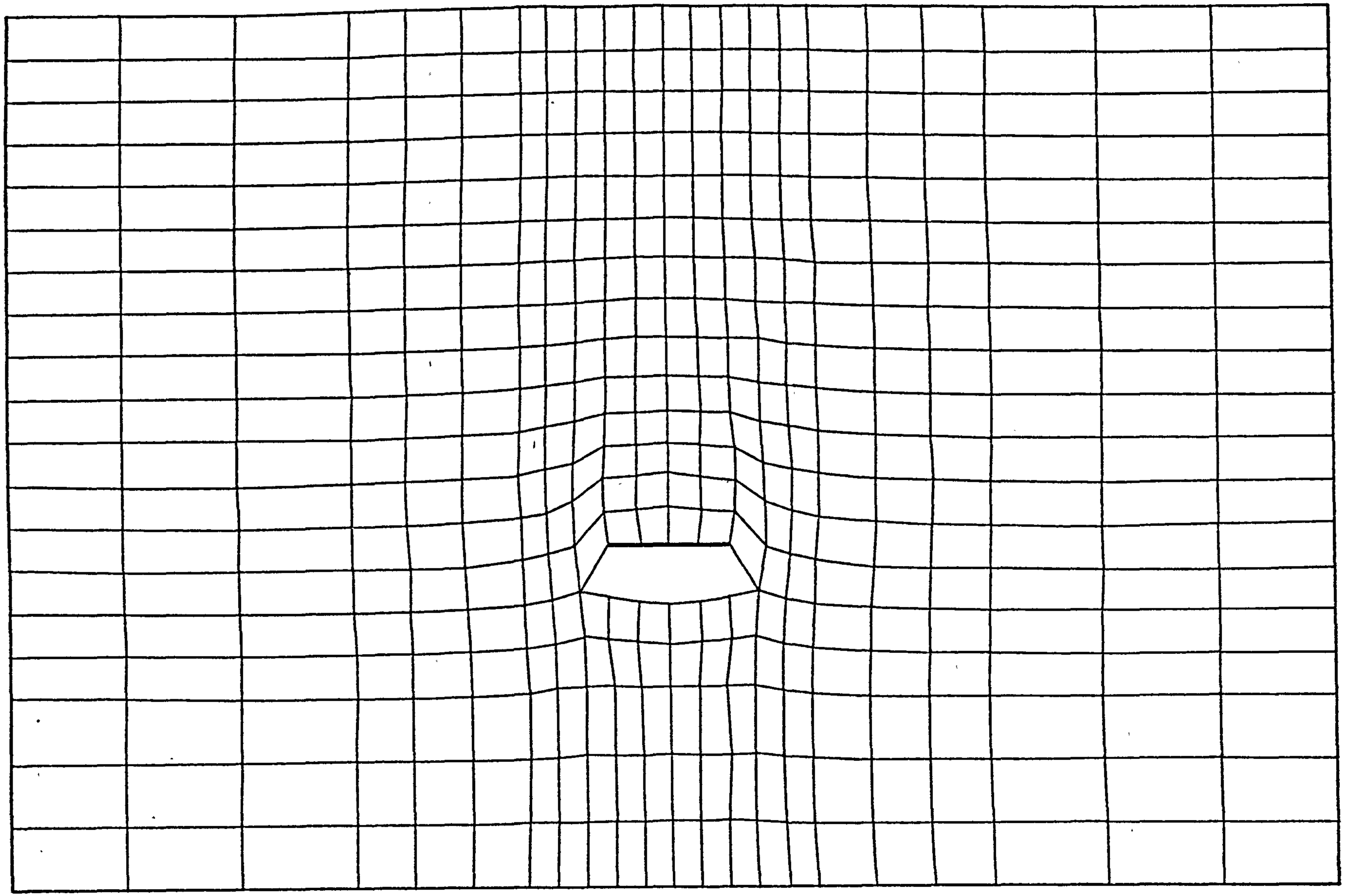

FIG. 5.7. NODAL POSITIONS AT POINT Ⓔ IN FIG. 5.12, RUN No. 3, D/B = 5.25. DISPLACEMENTS ENLARGED BY FACTOR OF 17

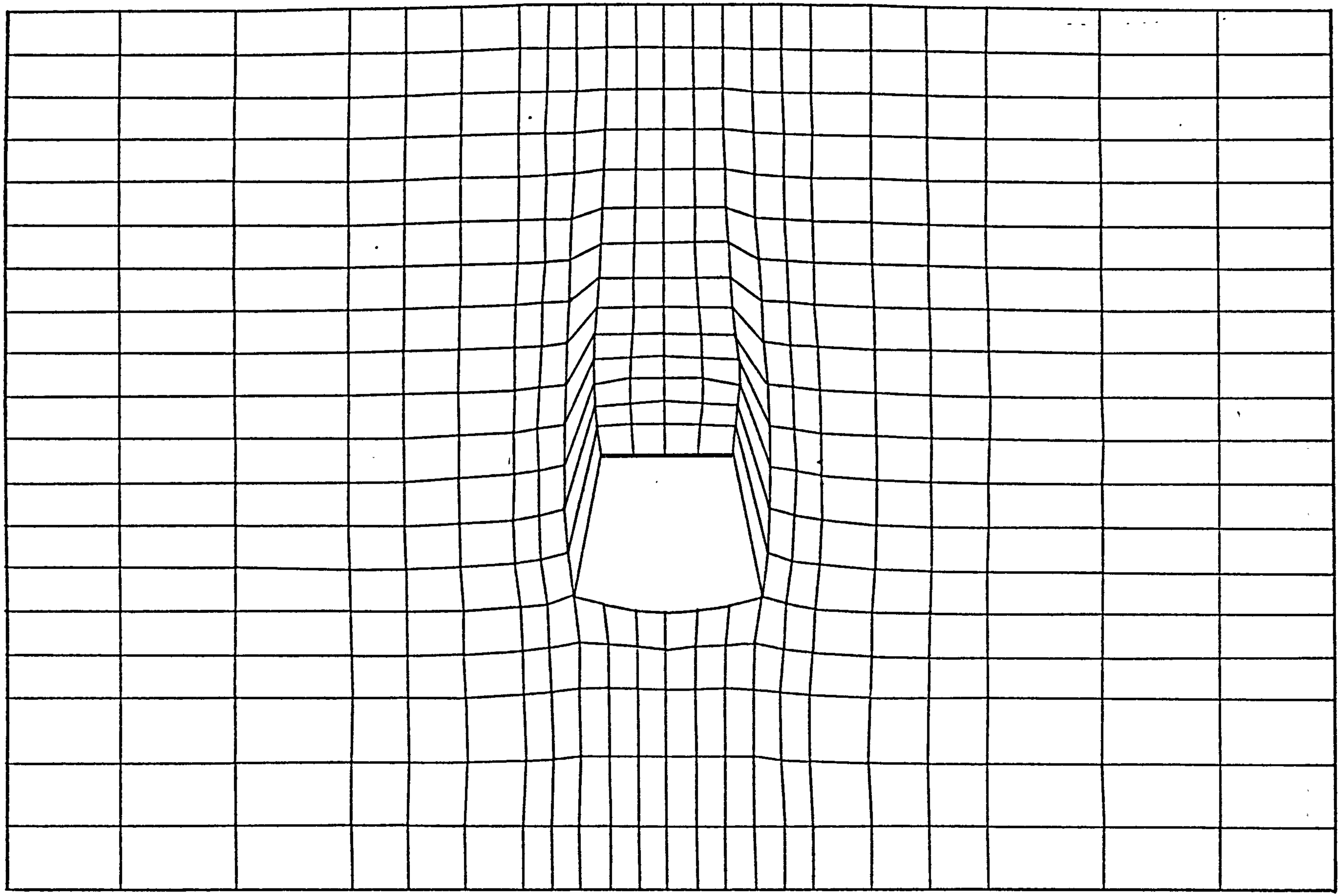

FIG. 5.8. NODAL POSITIONS AT POINT Ⓕ IN FIG. 5.12, RUN No. 3, D/B = 5.25. DISPLACEMENTS ENLARGED BY FACTOR OF 5

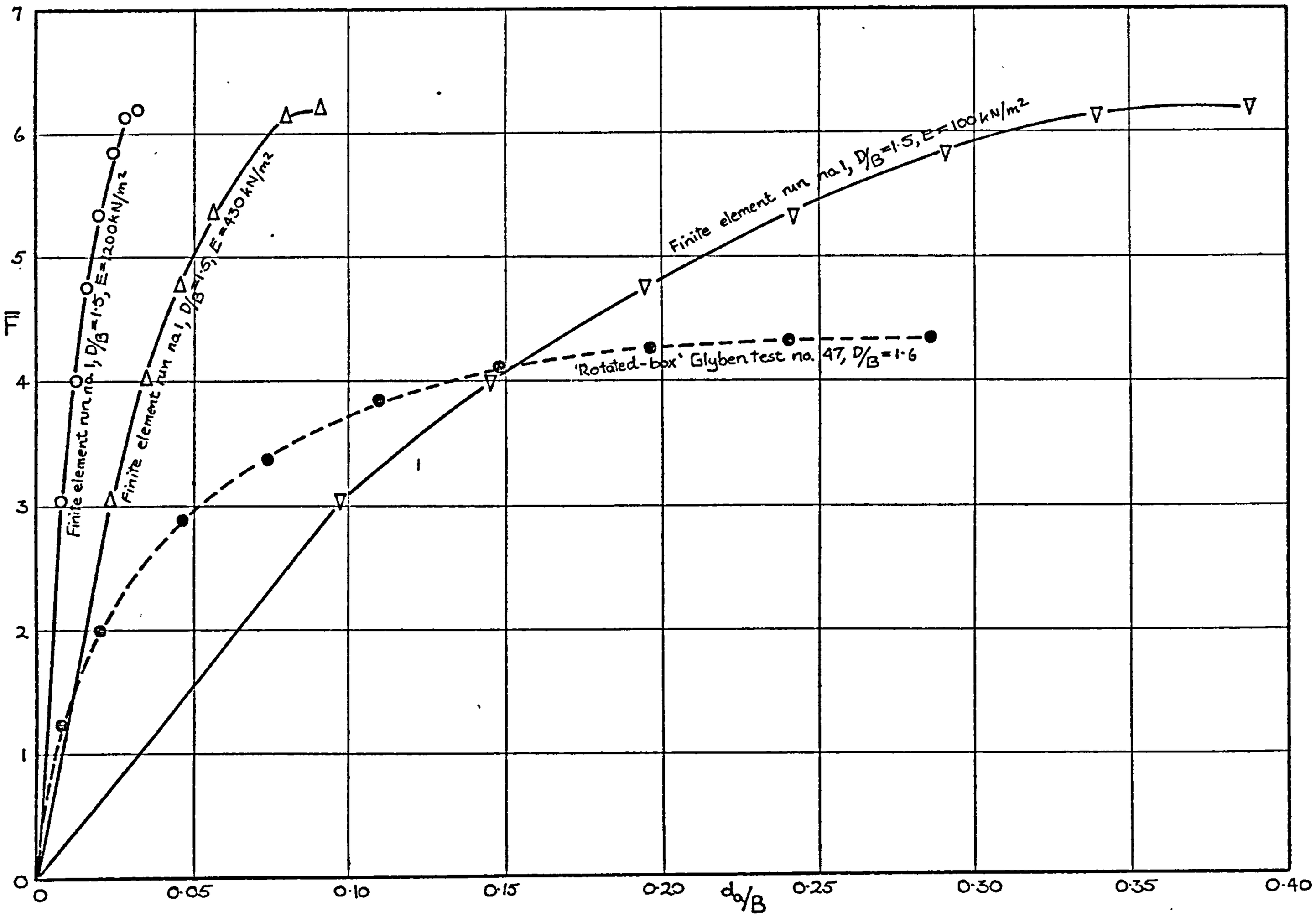

FIG. 5.9. $\bar{F}$ VERSUS d_o/B FOR SHALLOW ANCHOR MODEL TEST No. 47 AND FINITE ELEMENT RUN No. 1

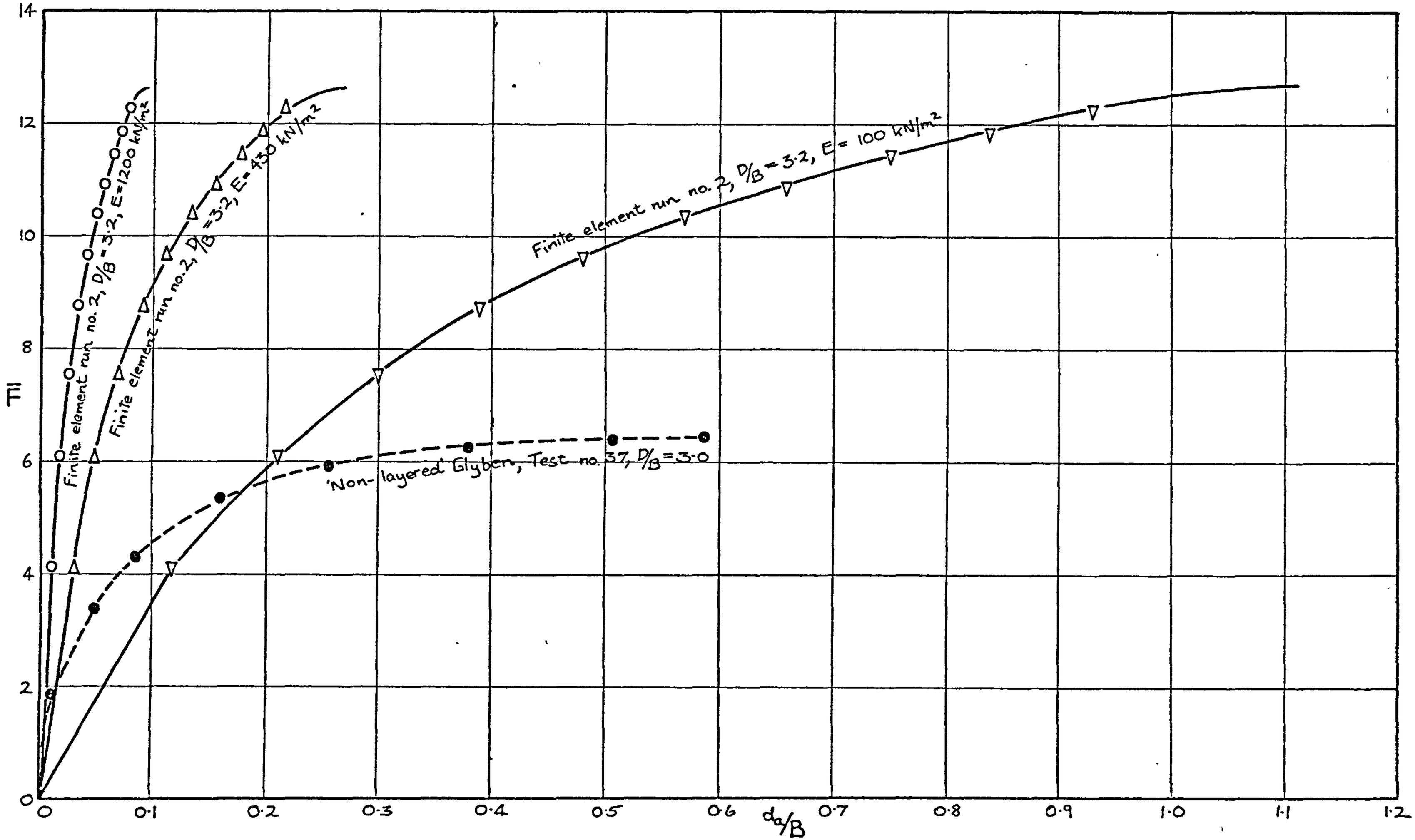

FIG. 5.10. F VERSUS d_a/B FOR INTERMEDIATE DEPTH ANCHOR MODEL TEST No. 37 AND FINITE ELEMENT RUN No. 2

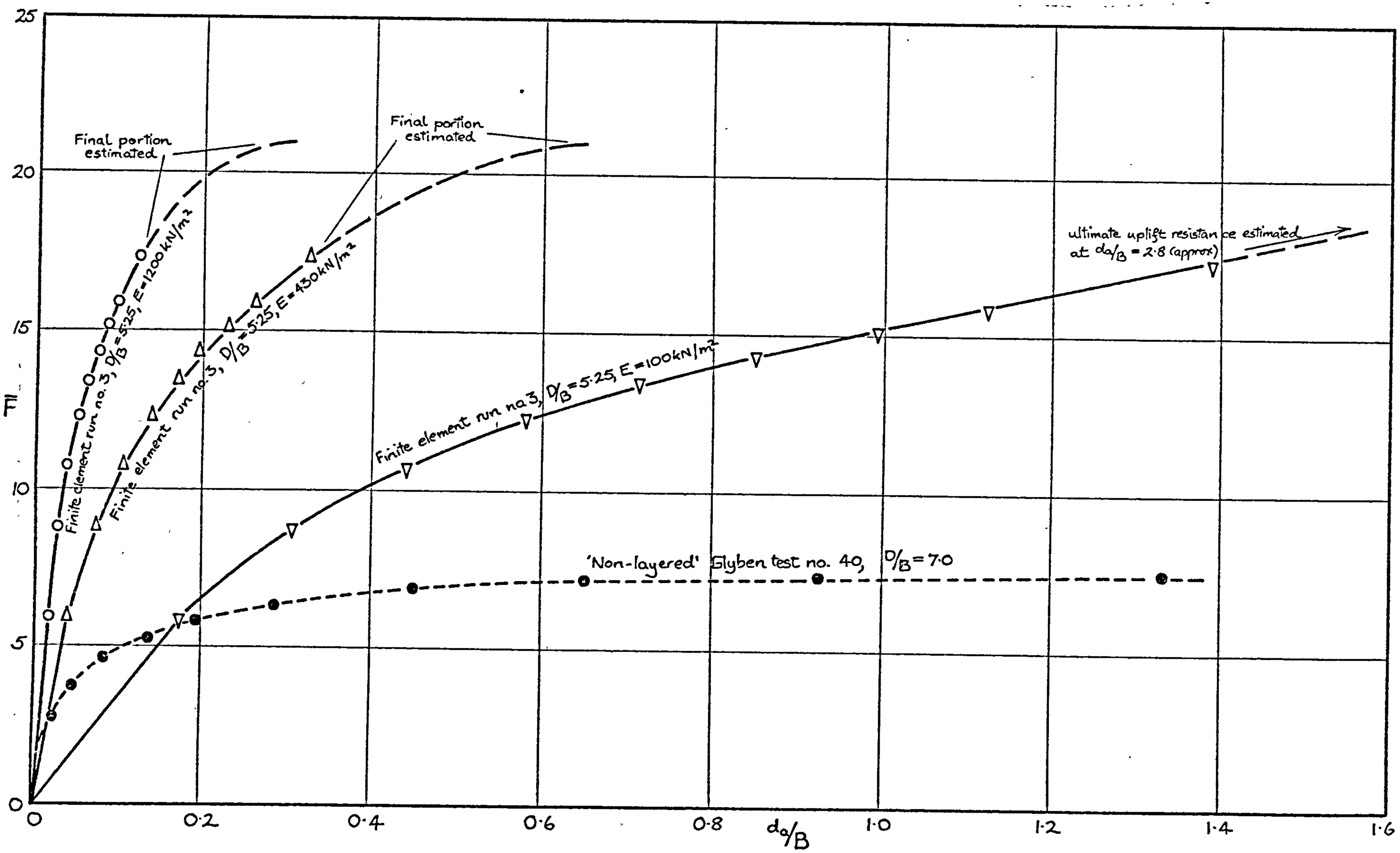

FIG. 5.11. $\bar{F}$ VERSUS d_a/B FOR DEEP ANCHOR MODEL TEST No. 40 AND FINITE ELEMENT RUN No. 3

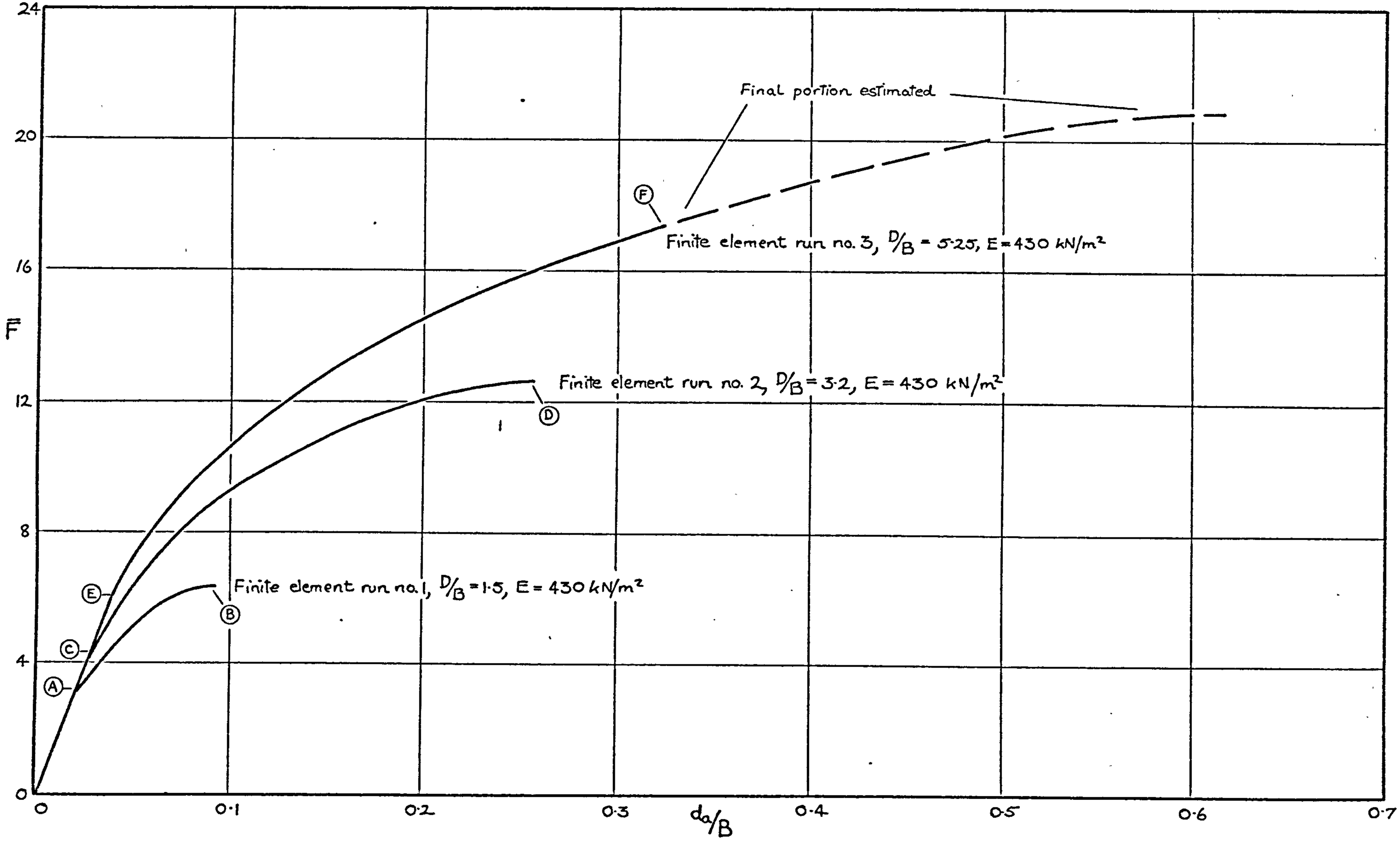

FIG. 5.12. $\bar{F}$ VERSUS d_a/B FOR FINITE ELEMENT RUNS 1, 2 AND 3

(a) AT STAGE Ⓐ IN FIG. 5.12--ELASTIC

(b) AT STAGE Ⓑ IN FIG. 5.12--ULTIMATE FAILURE

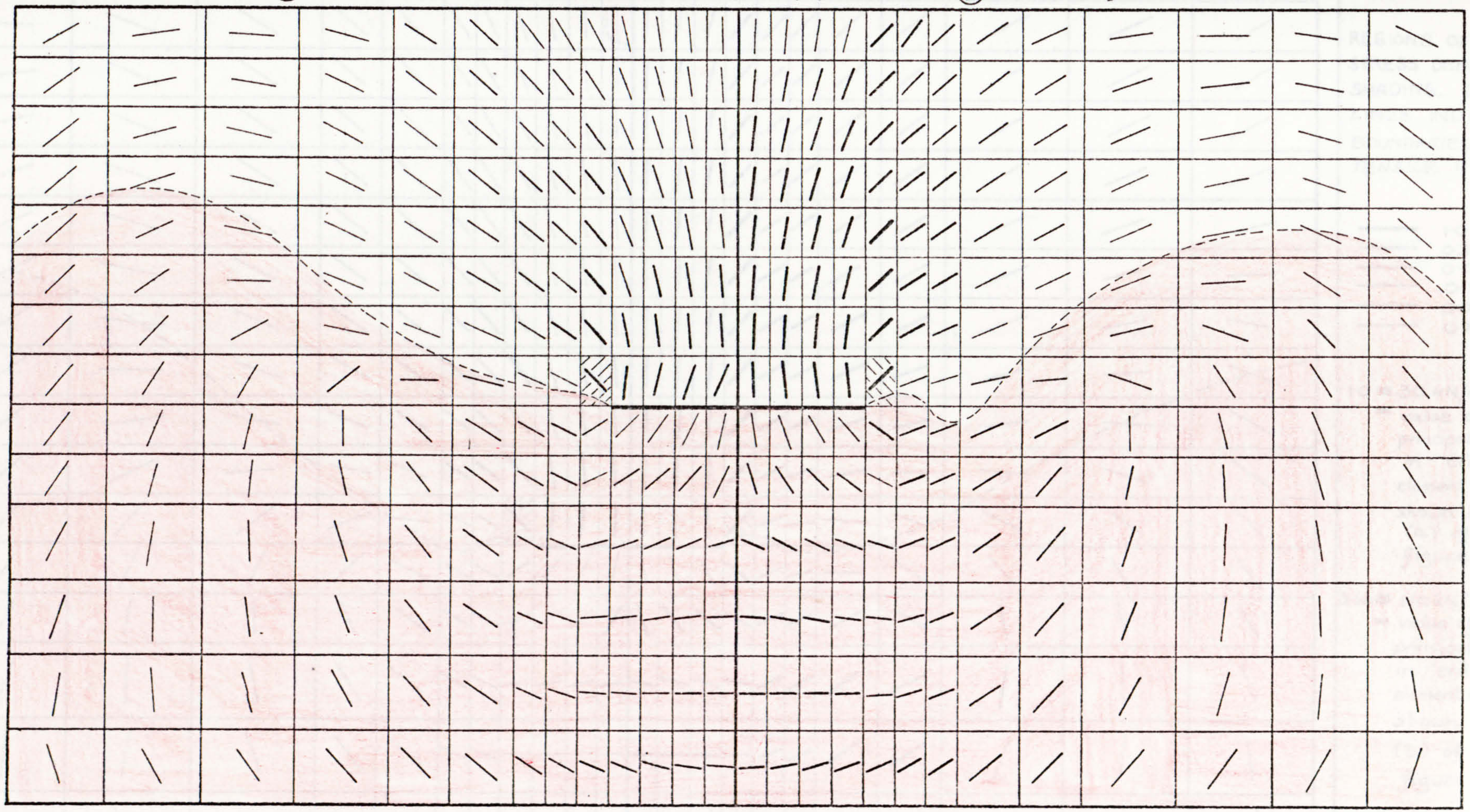

LEGEND

REGIONS OF TENSILE STRESS DENOTED BY SHADING. DOTTED LINES INDICATE BOUNDARIES OF TENSILE REGIONS

1·0 to 2·0
0·33 to 1·0
0·2 to 0·33
0·1 to 0·2
0·03 to 0·1
0 to 0·03

1·0 ≡ 30 kN/m² = value of major principal stress in 'critical' element (hatched) shown in part (a) of figure.

2·0 ≡ 60 kN/m² = value of major principal stress in 'critical' element (hatched) shown in part (b) of figure

FIG. 5.13. MAGNITUDE AND DIRECTION OF PRINCIPAL STRESSES FROM RUN No. 1, D/B = 1.5

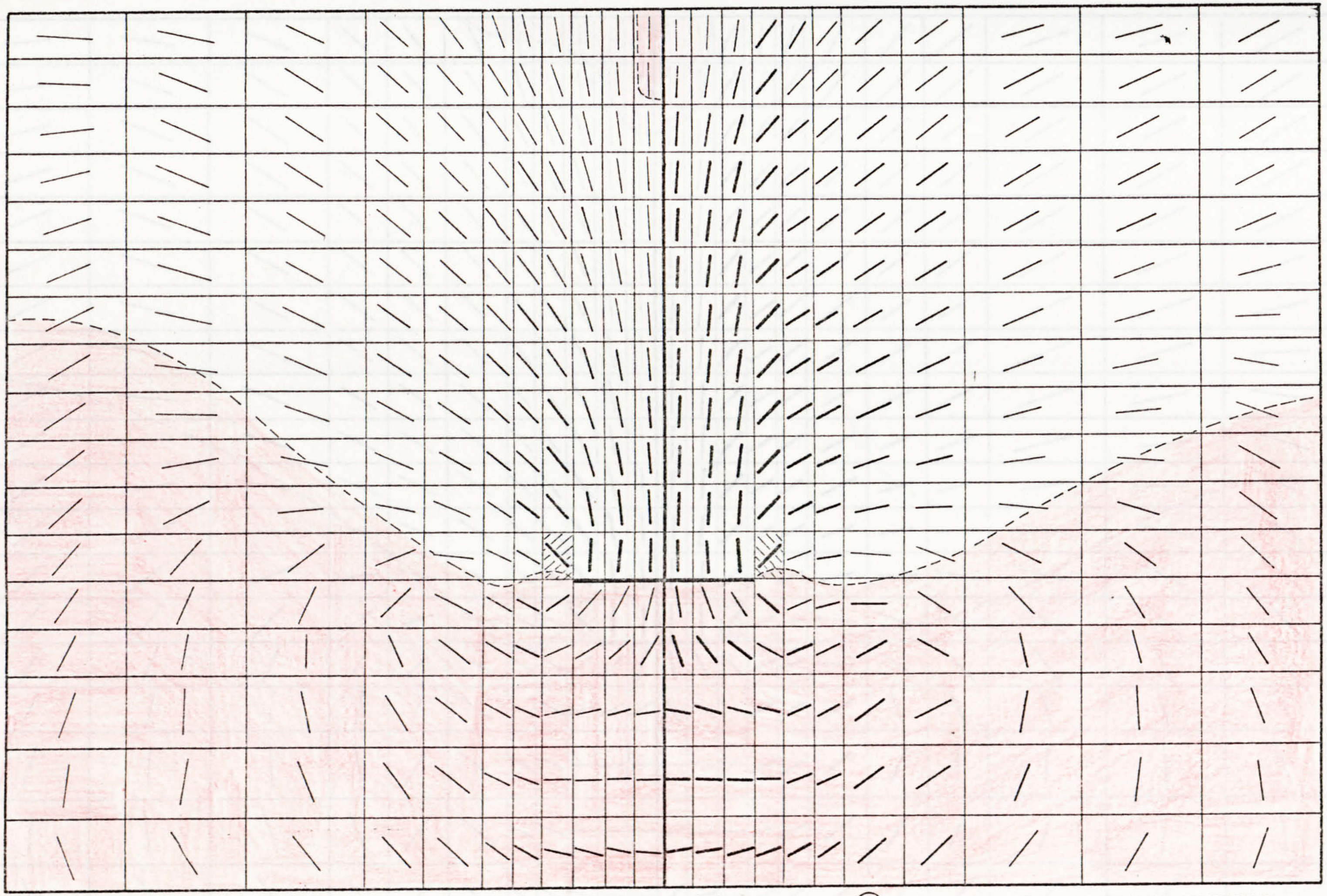

(a) AT STAGE Ⓒ IN FIG. 5.12--ELASTIC

(b) AT STAGE Ⓓ IN FIG. 5.12--ULTIMATE FAILURE

LEGEND

REGIONS OF TENSILE STRESS DENOTED BY SHADING. DOTTED LINES INDICATE BOUNDARIES OF TENSILE REGIONS

- 1·0 to 3·66
- 0·33 to 1·0
- 0·2 to 0·33
- 0·1 to 0·2
- 0·03 to 0·1
- 0 to 0·03

1·0 ≡ 30 kN/m² = value of major principal stress in 'critical' element (hatched) shown in part (a) of the figure.

3·66 ≡ 110kN/m² = value of major principal stress in 'critical' element (hatched) shown in part (b) of the figure

FIG. 5.14. MAGNITUDE AND DIRECTION OF PRINCIPAL STRESSES FROM RUN No. 2, D/B = 3.2

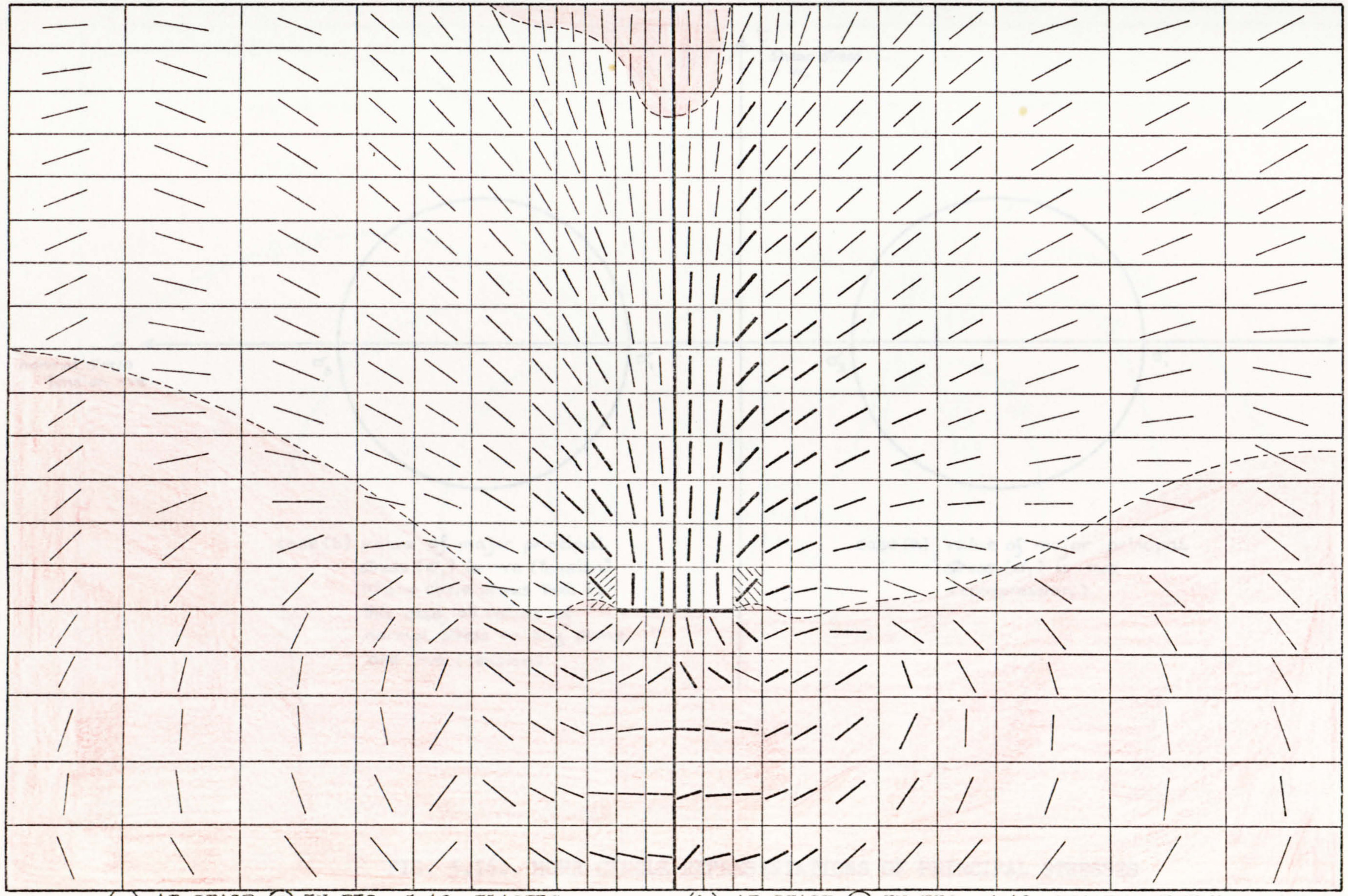

(a) AT STAGE (E) IN FIG. 5.12--ELASTIC (b) AT STAGE (F) IN FIG. 5.12--NEARING ULTIMATE FAILURE

FIG. 5.15. MAGNITUDE AND DIRECTION OF MAJOR PRINCIPAL STRESSES FROM RUN No. 3, D/B = 5.25

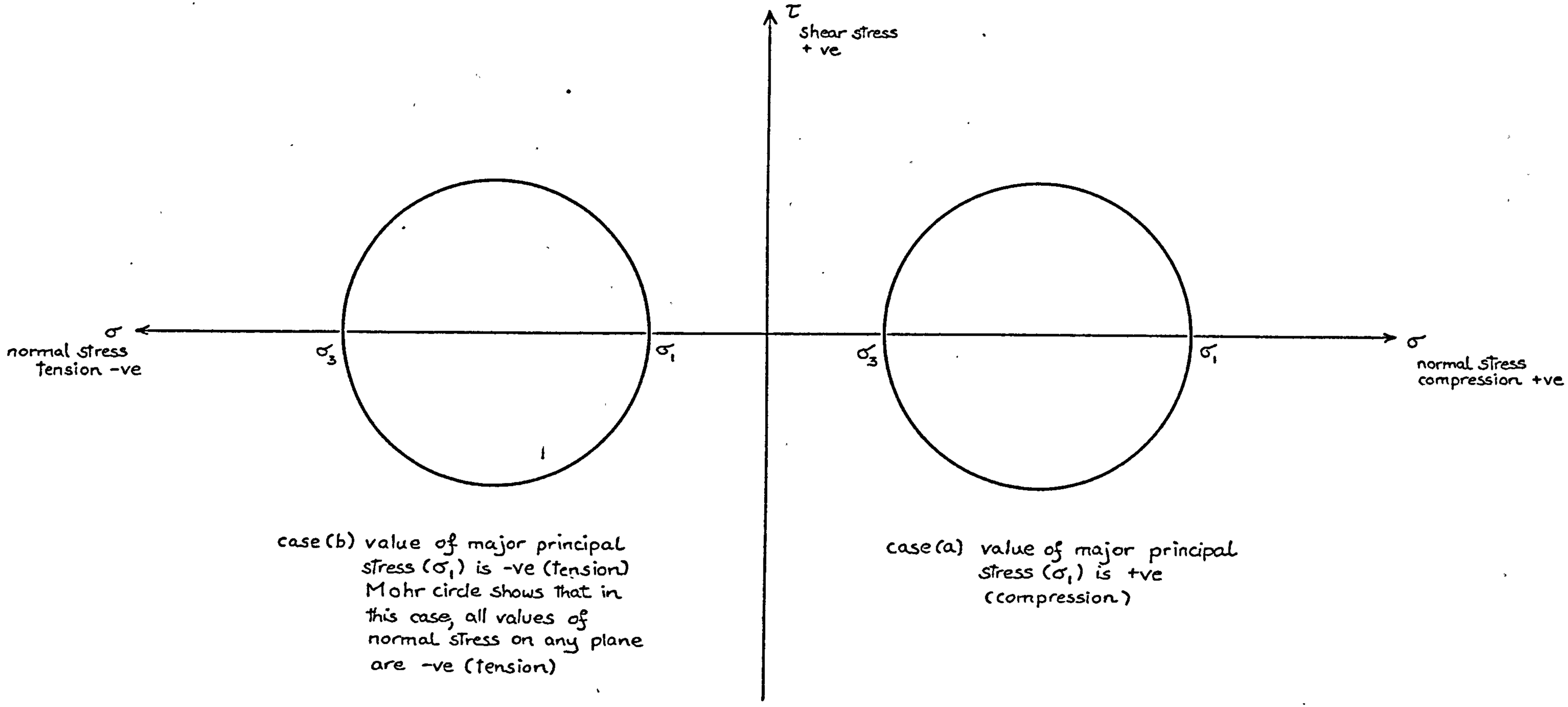

case (b) value of major principal stress (σ_1) is -ve (tension) Mohr circle shows that in this case, all values of normal stress on any plane are -ve (tension)

case (a) value of major principal stress (σ_1) is +ve (compression)

FIG. 5.16. MOHR CIRCLE REPRESENTATIONS OF PRINCIPAL STRESSES

(a) AT STAGE Ⓐ IN FIG. 5.12--ELASTIC

(b) AT STAGE Ⓑ IN FIG. 5.12--ULTIMATE FAILURE

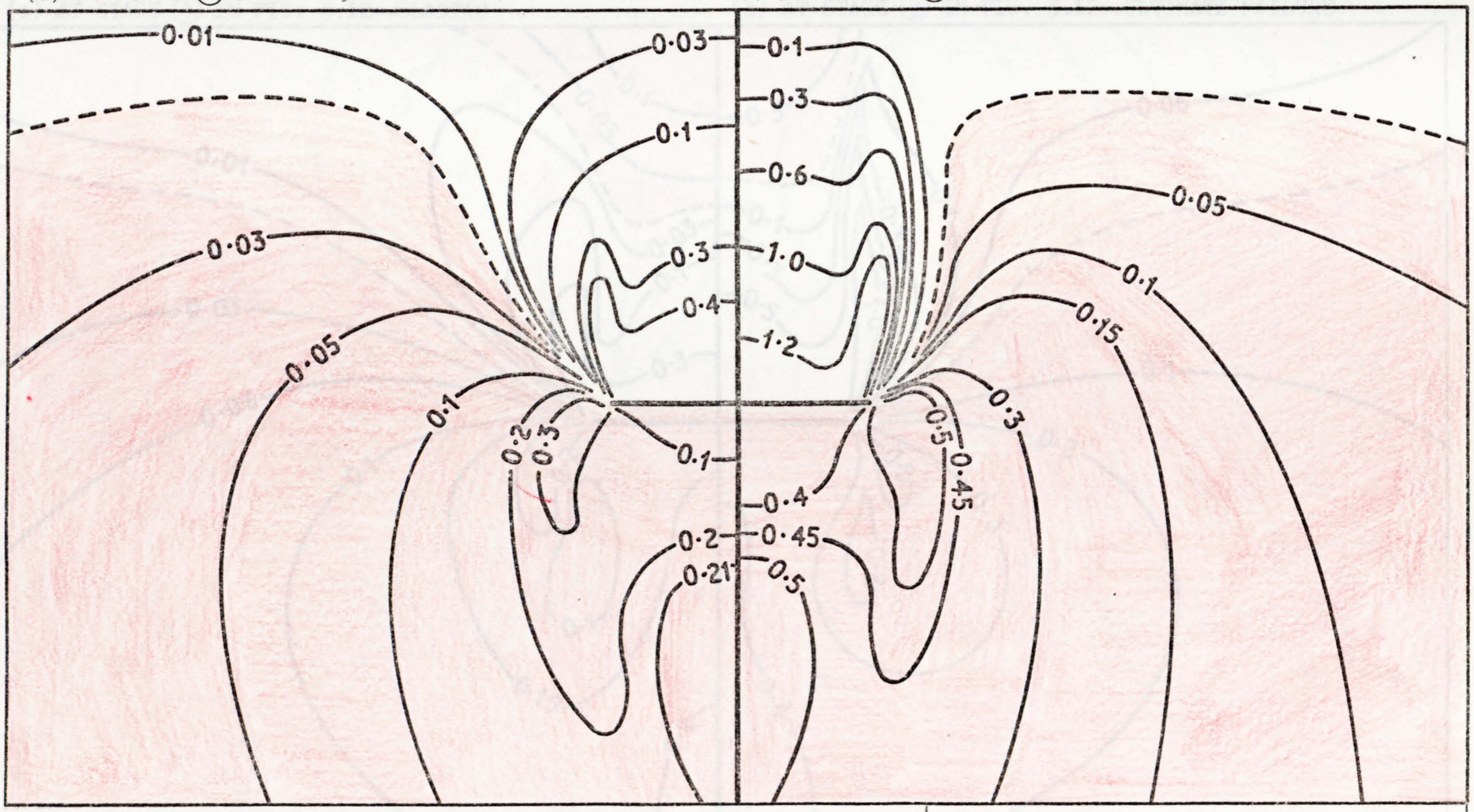

FIG. 5.17. DISTRIBUTION OF VERTICAL NORMAL STRESSES FROM FINITE ELEMENT RUN No. 1, D/B = 1.5

LEGEND REGIONS OF TENSILE STRESS DENOTED BY SHADING. DOTTED LINES INDICATE BOUNDARIES OF TENSILE REGIONS.

1·0 ≡ 19 kN/m² = value of vertical normal compressive stress at the centre of the 'critical' element at stage Ⓐ in Fig. 5.12

(a) AT STAGE Ⓐ IN FIG. 5.12--ELASTIC

(b) AT STAGE Ⓑ IN FIG. 5.12--ULTIMATE FAILURE

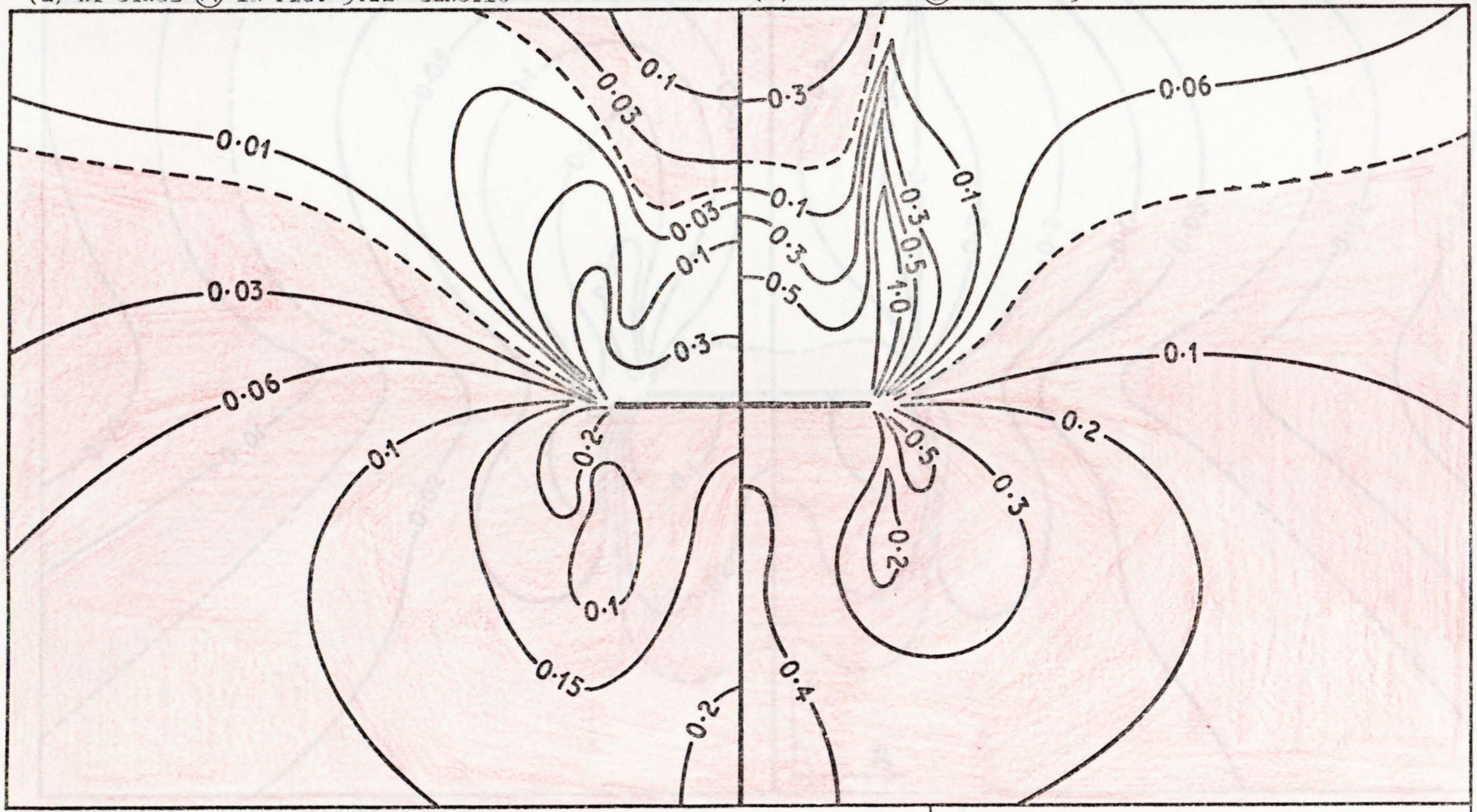

LEGEND REGIONS OF TENSILE STRESS DENOTED BY SHADING. DOTTED LINES INDICATE BOUNDARIES OF TENSILE REGIONS.

1·0 ≡ 18 kN/m² = value of radial normal compressive stress at the centre of the 'critical' element at stage Ⓐ in Fig 5.12.

FIG. 5.18. DISTRIBUTION OF RADIAL NORMAL STRESSES

FROM FINITE ELEMENT RUN No. 1, D/B = 1.5

(a) AT STAGE Ⓐ IN FIG. 5.12--ELASTIC

(b) AT STAGE Ⓑ IN FIG. 5.12--ULTIMATE FAILURE

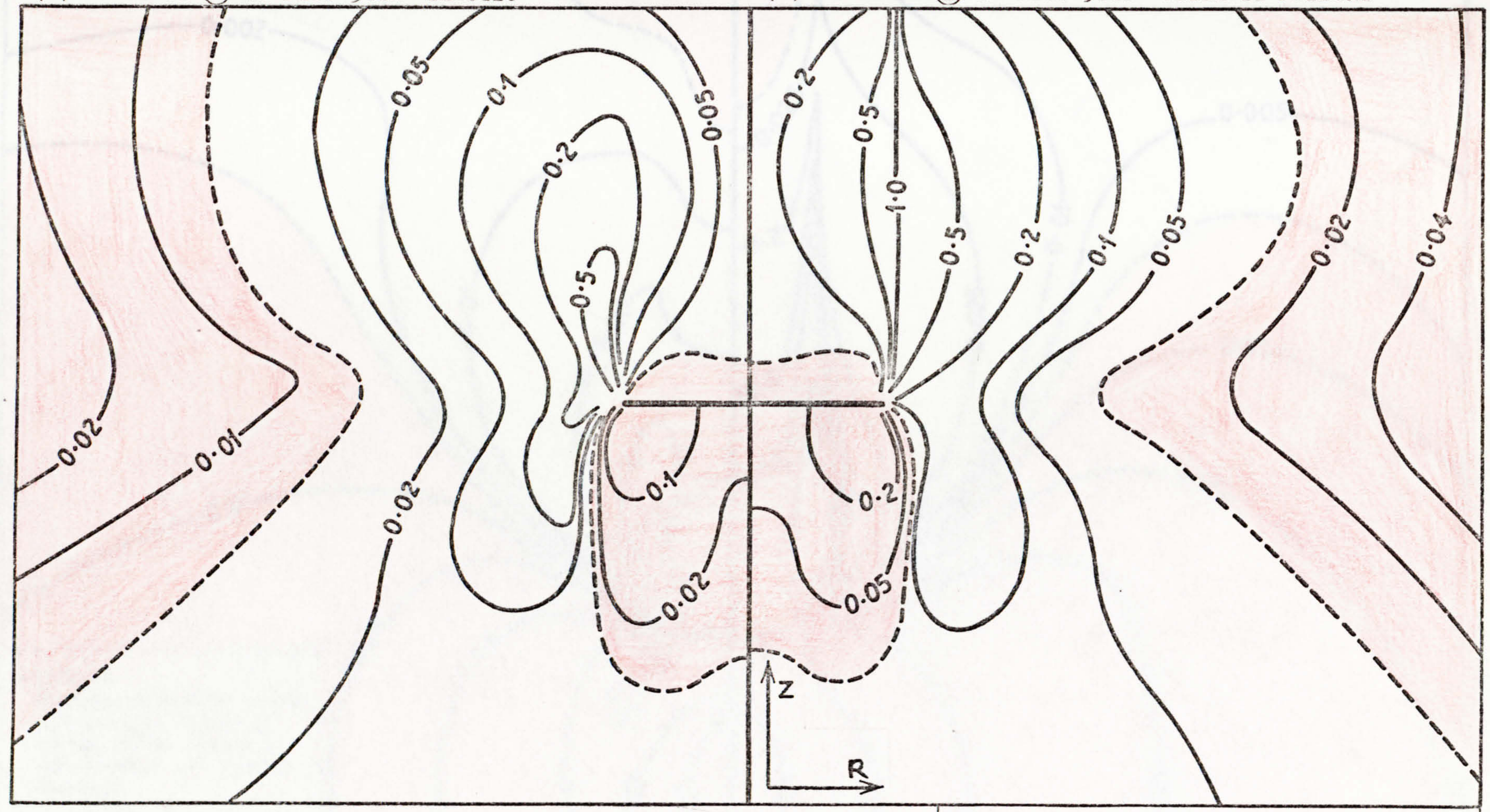

FIG. 5.19. DISTRIBUTION OF SHEAR STRESSES ON Z-R AND R-Z PLANES FROM RUN No. 1, D/B = 1.5

LEGEND REGIONS OF TENSILE STRESS DENOTED BY SHADING. DOTTED LINES INDICATE BOUNDARIES OF TENSILE REGIONS.

1·0 ≡ 10·4 kN/m² = value of limiting shear stress corresponding to a value of Von Mises Yield Stress of 18 kN/m².

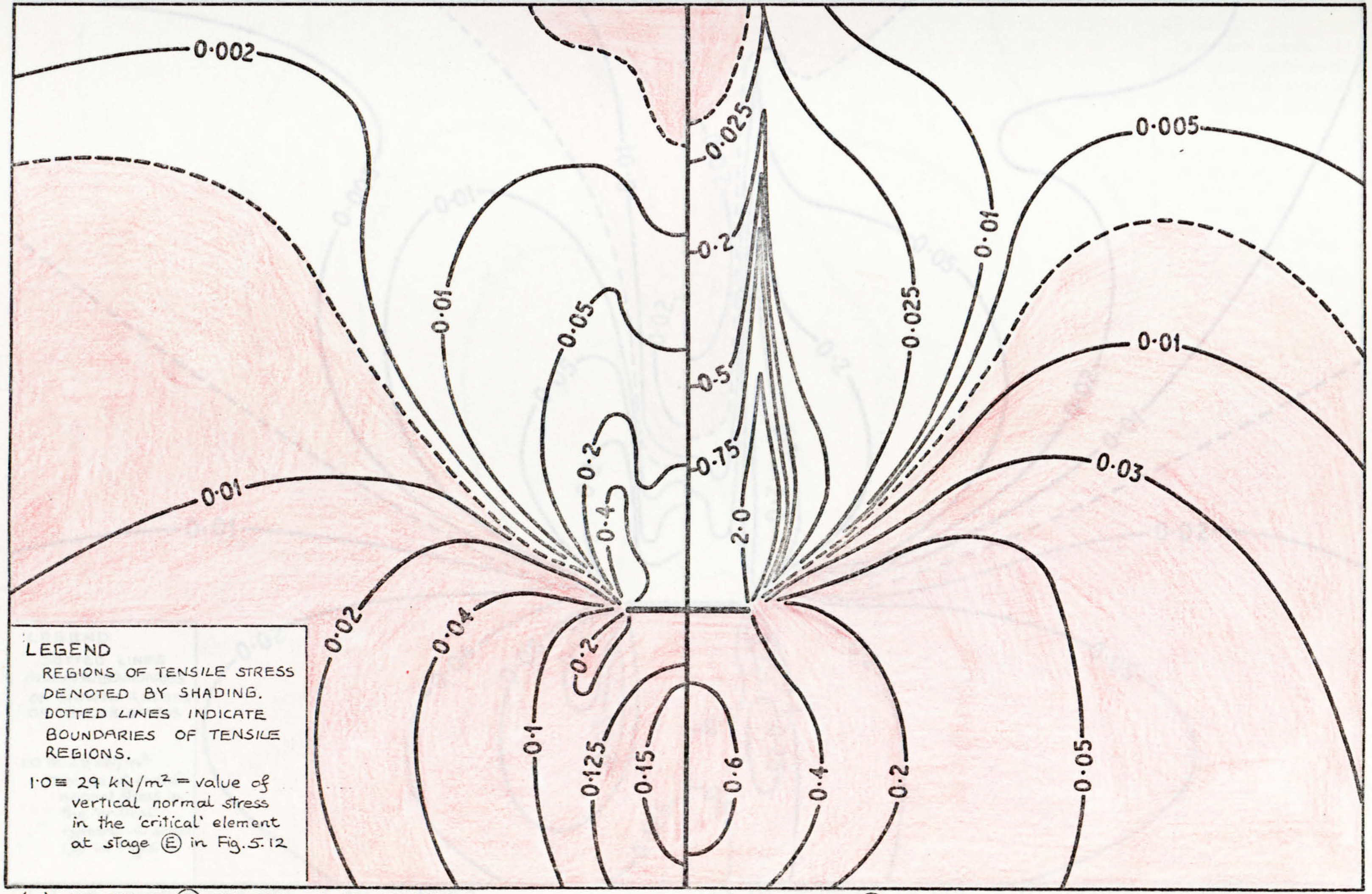

(a) AT STAGE (E) IN FIG. 5.12--ELASTIC

(b) AT STAGE (F) IN FIG. 5.12--NEARING ULTIMATE FAILURE

FIG. 5.20. DISTRIBUTION OF VERTICAL NORMAL STRESSES FROM FINITE ELEMENT RUN No. 3, D/B = 5.25

(a) AT STAGE Ⓔ IN FIG. 5.12--ELASTIC (b) AT STAGE Ⓕ IN FIG. 5.12--NEARING ULTIMATE FAILURE

FIG. 5.21. DISTRIBUTION OF RADIAL NORMAL STRESSES FROM FINITE ELEMENT RUN No. 3, D/B = 5.25

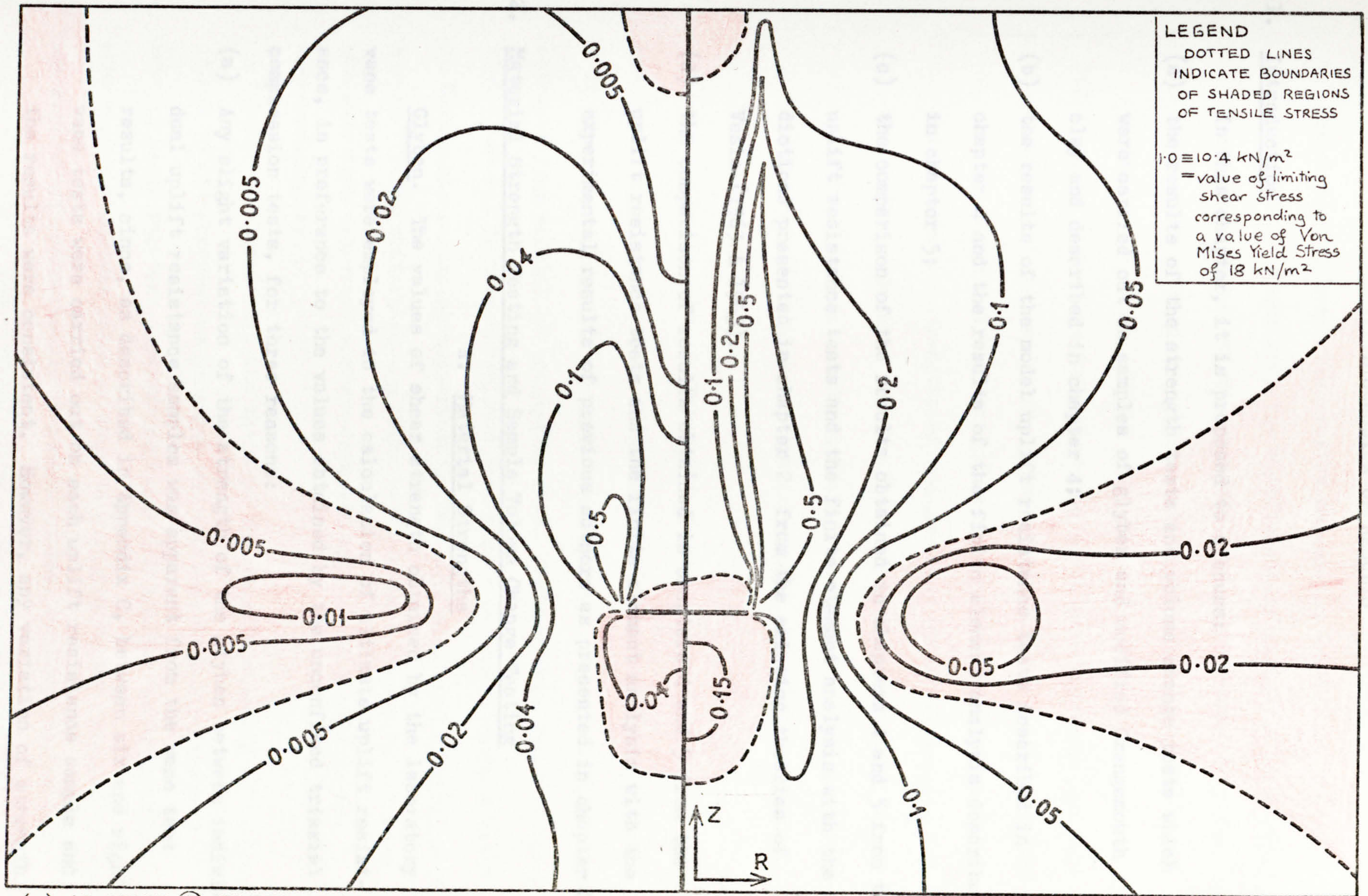

(a) AT STAGE Ⓔ IN FIG. 5.12--ELASTIC (b) AT STAGE Ⓕ IN FIG. 5.12--NEARING ULTIMATE FAILURE

FIG. 5.22. DISTRIBUTION OF SHEAR STRESSES ON Z-R AND R-Z PLANES FROM RUN No. 3, D/B = 5.25

CHAPTER SIX

DISCUSSION OF RESULTS

6.1. Introduction

In this chapter, it is proposed to discuss:

(a) the results of the strength tests and volume change tests which were carried out on samples of glyben and modified Grangemouth clay and described in chapter 4;

(b) the results of the model uplift resistance tests described in chapter 4 and the results of the finite element analysis described in chapter 5;

(c) the comparison of the results obtained in chapters 4 and 5 from the uplift resistance tests and the finite element analysis with the predictions presented in chapter 2 from the existing theories of Vesic (1963 & 1965).

(d) the comparison of results obtained in chapters 4 and 5 from the uplift resistance tests and the finite element analysis with the experimental results of previous authors as presented in chapter 2.

6.2. Material Strength Testing and Sample Volume Change Testing

A. Material Strengths

Glyben. The values of shear strength obtained by the laboratory vane tests were employed in the calculation of ultimate uplift resistance, in preference to the values obtained by the unconfined triaxial compression tests, for three reasons:

(a) Any slight variation of the strength of the glyben between individual uplift resistance samples was apparent from the vane test results, since, as described in Appendix C, between six and eight vane tests were carried out on each uplift resistance sample and the results were consistent. However, any variation of strength between the uplift resistance samples could not be detected from

the unconfined triaxial compression test results since each series of six triaxial tests was normally carried out only after the completion of every five uplift resistance tests.

(b) As noted in Appendix C, the coefficient of variation of shear strengths obtained by the triaxial tests was greater than the coefficient of variation of the strengths obtained by the vane tests.

(c) Although glyben was found to be an insensitive material, it was considered that the amount of disturbance caused to the triaxial samples of soft glyben during preparation could have reduced to some extent the strengths of the samples. This may account for the smaller values of average shear strength obtained by the unconfined triaxial compression tests compared to the values of shear strength obtained by the laboratory vane tests, as shown in Table 4.2.

The uppermost curve in Fig. 4.9 showed a representative stress-strain curve obtained by the unconfined triaxial compression test on a $1\frac{1}{2}$ inch diameter sample of batch no. 4 glyben. The stress-strain curves obtained from samples of batches 1, 2 and 3 glyben were found to have similar shapes to this curve, and the samples reached a maximum value of deviatoric stress at approximately the same amount of strain. Also, no significant difference was found between the stress-strain curves obtained from "layered" and "non-layered" samples of glyben in the compression test.

Table 4.2 shows that the ratio of the tensile strength of "layered" glyben to its compressive strength was approximately 1:5 compared to the 3:5 ratio for "non-layered" glyben. The tension curves in Fig. 4.9 show that the maximum value of tensile strength in the "layered" glyben was reached at approximately 3% sample strain, compared to the 10% sample strain for "non-layered" glyben. These results indicate the lack

of tensile bonding in the "layered" glyben samples. Fig. C.3(a) and Fig. C.3 (b) (Appendix C) show a plan view of the failed cross-sections of the "layered" and "non-layered" glyben tension samples respectively. A considerable difference in material texture is apparent, the smoother texture of the "layered" sample cross-section suggesting that failure has taken place on a plane between separate layers.

Modified Grangemouth Clay. The values of shear strength of modified Grangemouth clay obtained by the laboratory vane tests were employed in the calculation of ultimate uplift resistance, in preference to values obtained by the unconfined triaxial compression tests, for the reasons explained in parts (a) and (b) above for glyben. Table 4.2 shows that the average values of shear strength of the modified Grangemouth clay obtained by the triaxial tests were similar to those obtained by the vane tests, although, as noted previously, the coefficient of variation of the triaxial test results were greater than those for the vane test results.

Fig. 4.28 showed that the values of ultimate uplift resistance in deep tests in modified Grangemouth clay were considerably higher than in equivalent tests in glyben. Due to the particle size distribution of the modified Grangemouth clay, it was considered by the author that some degree of consolidation of the clay was taking place in the vicinity of the anchor plate during the deep uplift resistance tests. In order to find out if this were the case, four $1\frac{1}{2}$ inch triaxial samples of modified Grangemouth clay were prepared. Two samples were tested at a cell pressure of 140 kN/m^2, which was considered to be the maximum value of normal pressure experienced by the clay in the vicinity of the anchor during deep uplift resistance tests, and no drainage was allowed. In order to simulate as closely as possible the condition of the soil in the vicinity of the anchor plate at ultimate uplift resistance in the deep uplift resistance tests, the second pair of samples were tested at the same cell pressure

but were allowed to consolidate in a fully drained condition for approximately ten minutes before the deviatoric stress was applied and drainage was allowed during the application of the deviatoric stress. It was considered that the time taken to reach the maximum value of deviatoric stress, added to the initial ten minutes of consolidation, was approximately equal to the time taken to reach ultimate uplift resistance in the deep uplift resistance tests in modified Grangemouth clay. The results of the four triaxial tests are shown in Fig. 6.1. The maximum deviatoric stresses of the consolidated samples were of the order of two times those of the unconsolidated ones, which indicates that the short period of consolidation affected the structure of the second pair of samples, causing an increase in their shear strength. These results suggest that the level of pressure experienced in the vicinity of the anchor plate for the duration of the deep uplift resistance tests in modified Grangemouth clay caused consolidation and a consequent increase in the shear strength of the clay in the vicinity of the anchor, which may account for the higher values of uplift resistance obtained in the deep uplift resistance tests in this clay. Fig. 4.28 illustrated that, as the value of D/B decreased, the values of the ultimate uplift resistance factor $\bar{F}_u$ for modified Grangemouth clay became closer to those for glyben. In view of the above argument, this could be expected, since in the shallower tests, the pressures on the clay in the vicinity of the anchor were less than in the deeper tests and less time elapsed before ultimate uplift resistance was attained, and consequently less consolidation of the clay occurred.

The upper curve in Fig. 4.10 illustrates a representative stress-strain curve for an unconfined triaxial compression test on a $1\frac{1}{2}$ inch diameter sample of modified Grangemouth clay. The sample reached maximum deviatoric stress at approximately 27% sample strain. Table 4.2

shows that the ratio of tensile strength to compressive strength of the modified Grangemouth clay was of the order of 1:2.75 and the lower curve in Fig. 4.10 illustrates that the maximum tensile strength of the sample was attained at about 20% sample strain, which caused considerable "necking" in the sample prior to ultimate failure. Fig. C.3 (c) shows a plan view of the cross-section of the plane of failure and illustrates the considerable reduction in sample diameter due to "necking" compared with the "layered" glyben sample, shown in Fig. C.3(a), which failed at about 3% sample strain.

B. Volume Change Test

The volume change test is described in Appendix D and is essentially a test to determine the immediate compressibility of a sample of material. Since clays have low values of permeability, the change of volume due to the expulsion of porewater from a loaded sample of clay is a gradual process. However, any air which is entrapped in the sample will be reduced in volume when the pressure on the sample is increased and it is this reduction in volume which is measured in the Volume Change Test.

If any appreciable reduction in the volume of the uplift resistance sample occurred due to a compression of entrapped air voids during the uplift resistance tests, then some proportion of the total amount of anchor displacement in the tests could be attributed to this volume change. The purpose of the volume change test was to ascertain whether any significant proportion of the anchor displacement in the uplift resistance tests was due to the compression of air voids in the uplift resistance sample.

Glyben. Fig. 4.11 shows that the reduction of volume of the four inch diameter sample of batch no. 3 glyben, which was assumed to be a sample representative of all of the batches of glyben, varied almost linearly with the increase in cell pressure. However, it was found

that negligible volume change occurred due to deviatoric stresses applied to the sample up to failure. Table 4.4 shows that the maximum pressure to which batch no. 3 glyben was subjected in the uplift resistance tests by the anchor plate was of the order of 70 kN/m^2. If the curve for glyben shown in Fig. 4.11 is extended linearly, it shows that a cell pressure of 70 kN/m^2 would cause a volume change in the four inch diameter sample of approximately 1.7%. It is difficult to interpret this result in terms of the volume change in the uplift resistance sample. However, Figs. 5.17 to 5.22 do indicate that the high values of stress near the anchor dissipated rapidly in the soil with increasing distance from the anchor plate. Moreover, it can be assumed that the major part of the effect of the anchor pressure and movement in the soil was equivalent to the effect of the deviatoric stress which caused no perceptible volume change in the four inch diameter sample. In view of these considerations, it was concluded by the author that only a very small decrease in volume occurred in the glyben samples due to the compression of entrapped air voids during the uplift resistance tests and that a negligible proportion of the anchor displacement to ultimate uplift resistance in glyben tests was a result of this volume decrease.

Modified Grangemouth clay. Fig. 4.11 shows that the reduction of volume of the sample of modified Grangemouth clay due to an increase in cell pressure was almost negligible. It was also found that negligible volume change occurred due to deviatoric stresses applied to the sample up to failure. It was therefore concluded that a negligible fraction of the anchor displacement to ultimate uplift resistance in modified Grangemouth clay was the result of volume change due to the compression of air voids in the sample.

6.3. Discussion of the Results of the Model Uplift Resistance Tests and the Finite Element Analysis

In this section the results obtained from model uplift resistance tests conducted by the author and the results obtained from the finite element analysis will be discussed and compared. Table 6.1 lists the types of measurement which were exclusive to either the model testing method or the finite element analysis and also the types of measurement which could be obtained from both methods. The results of the model tests and finite element runs will be divided into five sections for discussion:

A. Internal displacements and cracking.

B. Surface displacements and cracking.

C. The relationship between uplift resistance and anchor displacement.

D. The values of ultimate uplift resistance.

E. The magnitude, direction and distribution of stresses.

Since the topics discussed in sections A to E are closely inter-related, they cannot be discussed satisfactorily in isolation and thus the headings for these sections denote only the primary subjects for discussion in each section but do not exclude the discussion of subjects from other sections when they are considered to be relevant.

Before a discussion and comparison of the model test results are made, consideration will be given to the effect of the method of preparation of (i) the "split-box" and (ii) the "rotated-box" samples described in chapter 4, on the results of the tests. This consideration is introduced at this stage since the assumptions which will be made concerning the "split-box" and "rotated-box" samples will be used extensively throughout the following discussion.

(i) Split-Box Samples. In test no. 53, a "layered" sample of glyben was prepared and tested in the split-box before being "split" open. In test no. 54, an equivalent sample was prepared, cut open and coloured strips were added before the sample was clamped together again and tested. After the test, the sample was "split" open. It

was found that the ultimate uplift resistance values of the two samples were almost identical, as shown in Fig. 4.29, and the anchor displacements to 90% of ultimate uplift resistance were similar, as was shown in Fig.4.26. The shape of the uplift resistance versus anchor displacement curves (not shown) and the shapes of the surface displacements at ultimate uplift resistance, as illustrated in Figs. 4.15 and 4.16 respectively, were also similar. It was concluded, on this evidence, that the weak bond on the vertical section through the centre of the anchor plate, caused by the cutting open of the sample prior to the addition of the coloured strips, had a negligible effect on the results of the tests.

(ii) "Rotated-Box"Samples. The shape of the surface bulge, caused by the anchor as it neared the surface of the uplift resistance sample during the test, appeared to differ between the "rotated-box" shallow samples and the "non-layered" shallow samples, being slightly elliptical in the "rotated-box" samples and circular in the "non-layered" samples. However, an examination of the values of ultimate uplift resistance of samples of "rotated-box" glyben showed them to be almost identical to those for "non-layered" glyben, as illustrated in Figs. 4.28 and 4.29. The amount of anchor displacement to 90% of ultimate uplift resistance was very similar in the two categories of tests, as shown in Fig. 4.26, and the shape of the uplift resistance versus anchor displacement curves (not shown) were also similar. In view of these results, the "rotated-box" samples will be assumed to be representative of "non-layered" samples except with respect to surface displacement.

A. Internal Displacements and Cracking

Internal displacement and cracking in shallow anchor tests. In this section the internal displacement and cracking patterns in the shallow anchor model tests will be discussed and compared with the

corresponding values of nodal displacements obtained from the finite element analysis. In addition, a theory concerning the possible modes of ultimate failure, based on observations of the model tests, will be proposed for shallow anchors in purely cohesive soils of relatively low tensile strength in which cracking occurred.

Fig. 6.2 shows sketches of the sections through the centre of the shallow anchor samples at ultimate uplift resistance which were illustrated in the photographs in (i) Fig. 4.12 for "rotated-box" glyben, (ii) Figs. 4.15 and 4.16 for "layered" glyben, and (iii) Fig. 4.17 for modified Grangemouth clay. Fig. 6.2 also includes a sketch of the shape of the mesh predicted in the shallow anchor finite element run at ultimate uplift resistance and shown in Fig. 5.6. In the sketches, lines were drawn from the edge of the anchor plate in its original position before the commencement of the test, to the point of inflexion of the clay surface at maximum uplift resistance. The angles between these lines and the vertical varied from approximately 20 to 26 degrees in the model tests but the angle was very small in the finite element case. The finite element analysis showed a cylindrical slip failure surface as predicted by the Shearing Theory (2.2.A), whereas the model tests showed that the soil which was displaced by the anchor movement was in the form of a truncated cone. This difference appears to be the result of cracking in the model soil samples. Each of the photographs of the sections of these samples indicates a major crack, shown as AB in Fig. 6.2, which propagated from the edge of the anchor plate in its original position at an angle of the order of 20 degrees to the horizontal to a distance of approximately one half of the anchor plate diameter from the edge of the anchor plate. This crack was a result of the relatively high tensile stresses created in this region by the anchor movement. An indication of the level of these tensile stresses is given in Figs. 5.17 and 5.18. In the following paragraphs,

possible modes of ultimate uplift failure for shallow anchors are proposed by the author.

Fig. 6.3 illustrates the mode of ultimate failure predicted by the finite element method for shallow anchors in purely cohesive soil in which the values of tensile strength and compressive strength were assumed to be equal and in which no cracking of the soil was assumed to occur. It was recognised that the assumption of a "non-cracking" material was unrealistic in as much as cracking will occur in most purely cohesive soils under certain conditions of stress. Fig. 6.4 illustrates the mode of ultimate failure proposed by the author for shallow anchors in purely cohesive soils in which the value of tensile strength was considerably less than the value of compressive strength and subsequent cracking in the tensile regions could occur. This soil will be referred to as "cracking" soil.

Considering both Figs. 6.3 and 6.4, an initial load of F_1 is applied to the anchor. In the "non-cracking" material shown in Fig. 6.3(a), a resulting vertical displacement δ_1 of the anchor occurs and the soil in the shaded region P_1 yields. This yield is due to the discontinuity of the edge of the anchor plate which causes very high values of stress in its immediate vicinity. Yielding occurs in region P_1 when the limiting value of shear stress in the material is exceeded. In the "cracking" material shown in Fig. 6.4(a), a similar type of yielding occurs in the shaded region P_1'. In addition, the load causes the limiting value of tensile stress in the region immediately below the edge of the anchor to be exceeded and crack A_1B_1 to be formed. This crack propagates and the displacement of the anchor plate continues to displacement δ_1', when the forces which are resisting the upward movement of the soil mass become equal to the anchor force F_1. These resisting forces are the force due to the weight of the soil and the force arising from the bending moment M_1, shown in

Fig. 6.4(a), due to the structural stiffness of the soil. Thus, after the initial load, the movement which has occurred in the "cracking" soil is considerably greater than in the "non-cracking" soil.

A second load, making the total load equal to F_2 , is now added to the anchor. In the "non-cracking" material shown in Fig. 6.3(b), the total anchor displacement becomes δ_2 and the yield zone extends to region P_2 . In the "cracking" soil shown in Fig. 6.4(b), yield occurs in the region P_2' but the crack A_2B_2 propagates until the downward forces due to the soil weight plus the force arising from the bending moment M_2 are equal to the anchor load F_2 . At this stage the total amount of displacement of the anchor δ_2' in the "cracking" case has caused a considerable radial tensile region T to form near the surface of the clay with possible resulting cracking.

A third load is now added to the anchor plate to bring the total load to F_3 . In the "non-cracking" case shown in Fig. 6.3(c), the total anchor displacement becomes δ_3 and the yield zone extends to P_3 . In the "cracking" case, yield extends to region P_3' and the crack propagates to A_3B_3 . However, in this case the anchor continues to displace under the load F_3 , indicating that ultimate failure of the soil has occurred in either of the following two ways:

(a) a crack CD , due to excessive tension in the region T , extends from the surface of the clay to the plastic yield zone P_3' , causing the general slip failure surface CDB_3 which is shown in Fig. 6.4(c). The cracking pattern in Fig. 4.12 indicates this type of failure. A similar mode of failure was proposed by Matsuo (1967) in his theory (2.2.E).

(b) a continuous extension, at limiting tensile stress, of the material shown in the regions X above the zone of shear failure P_3' shown in Fig. 6.4(d). Fig. 4.17 indicates this type of failure.

In both cases (a) and (b), failure is termed general failure since one surface of yielded material extends from the anchor plate to the soil surface. In section 6.3.C an explanation of why failure of type (a) occurred in some laboratory model tests and failure of type (b) occurred in others will be presented.

An additional load which makes a total load of F_4 can be added to the anchor in the "non-cracking" soil case in order to extend the yielded region to P_4, as shown in Fig. 6.4(d), and cause a cylindrical general slip failure surface.

To sum up, in shallow anchor tests on soils with high tensile strength in which cracking at limiting tensile stress in the material does not occur, ultimate failure is caused by a "punching" failure in which the ultimate uplift resistance of the soil is equal to the total value of limiting shear stress on a cylinder of soil of diameter equal to that of the anchor, and height equal to the depth of placement of the anchor, as postulated in the Shearing Theory (2.2.A). In the case of soils with relatively low tensile strength in which cracking can occur, ultimate failure is caused by a combination of shear failure and failure due to cracking or continuous extension in the regions of high tensile stress. These regions are a result of large displacements of the anchor and soil, caused by the propagation of a crack through the zone of soil in tension in the vicinity of the edge of the anchor in its initial position. This crack is allowed to propagate due to the lack of structural stiffness of the soil above the anchor plate in the shallow anchor tests. The value of ultimate uplift resistance in the "cracking" case will always be less than or equal to the "punching" value of ultimate uplift resistance.

Since most clays have values of tensile strength which are considerably below their values of compressive strength and also exhibit cracking under conditions of limiting tensile stress, stresses and

ultimate loads predicted by the finite element analysis will be an upper bound and most shallow anchors in clay will reach ultimate failure by the mode described above for "cracking" clays. The values of anchor displacement to failure and the values of ultimate uplift resistance in the shallow anchor model tests will be discussed in sections 6.3C and 6.3D respectively.

Internal displacement and cracking in deep anchor tests. Fig. 4.14 illustrated the amount of anchor displacement and the displacement pattern of the soil which occurred in "rotated-box" test no. 52, with $D/B = 4.5$, at ultimate uplift resistance. A length of white thread was placed around the area of clay which was visibly affected by the anchor movement, and showed that the extent of the failure was limited, indicating that a local type of failure had occurred. It is not possible to ascertain the extent of the plastic region from the photograph, but the values of ultimate uplift resistance obtained from the deep anchor model tests were in relatively close agreement with the ultimate values which were predicted by Vesic (1965) and Meyerhof and Adams (1968). These will be discussed further in section 6.4. The absence of any cracking may be noted. Although the same regions of high tensile stress which were found in the shallow tests will exist in the vicinity of the anchor plate in the deep tests, as indicated in Figs. 5.20 and 5.21, the combination of the high values of self weight and the large resistance moment due to the high value of the structural stiffness of the sample at depth will preclude the propagation of cracking. In this case, the load required to cause ultimate local failure will be less than the load required to cause cracking.

Fig. 5.8 showed the displacement of the deep anchor and the resulting displacement of the soil which was predicted by the finite element analysis as ultimate uplift resistance was approached. As stated in chapter 5, the finite element program has not been designed

to take account of the type of local failure predicted by Vesic (1965) and Meyerhof and Adams (1968). Fig. 5.8 shows therefore the form of displacement which would have occurred when a general type of failure was imminent. The value of ultimate uplift resistance in local failure, as demonstrated by the model tests, will always be less than the value of ultimate uplift resistance which occurs in general failure in deep anchors. Thus, in deep anchor situations, local type of failure will always occur and the general failure pattern predicted for deep anchors by the finite element analysis will be largely hypothetical.

Internal displacement and cracking in the intermediate depth of anchor tests. Fig. 4.13 illustrated the amount of anchor displacement and the displacement and cracking pattern of the soil which occurred at ultimate uplift resistance in "rotated-box" test no. 50 with D/B = 3.0. Some cracking was apparent, although considerably less cracking occurred than in the equivalent shallow anchor test shown in Fig. 4.12. There was also less displacement of the soil at and near the surface of the sample than in the shallow anchor case. It may therefore be assumed that ultimate failure at this depth comprised a combination of general failure and local failure characteristics.

B. Surface Displacements and Cracking

Fig. 4.18 illustrated the ratio of surface displacement immediately above the centre of the anchor plate to anchor displacement at 90% of ultimate uplift resistance, plotted against the anchor depth to breadth ratio for the displacement-controlled model pushout tests. In the very shallow tests the clay surface was displaced by virtually the same amount as the anchor plate, which suggests a general type of failure of the soil. In the deep anchor tests, very little surface displacement occurred, which supports the argument that proposed a

local type of failure of the soil in these tests. In Fig. 4.18 the results for the various categories of tests described in Table 4.3 appear in general to fall on or near to the best-fitting curve drawn through the points which represent the tests in "layered" glyben. However, the results for the "rotated-box" tests (nos. 47 to 52) are consistently well below this curve, and a reason for this will be postulated later in this section.

In order to illustrate clearly the bulging and cracking which occurred at the surface of a sample in a shallow anchor test, the displacement of the anchor in "layered" glyben test no. 8, with D/B = 1.5, was continued to a displacement of 2.6 times that at ultimate uplift resistance, and the resulting surface bulges were shown in elevation and plan view in Figs. 4.19(a) and (b) respectively. Fig. 4.19(a) also showed the position of the anchor plate relative to the soil surface at this stage in the test. It was noted that although the height of the bulge increased with increasing anchor displacement, the diameter of the bulge remained approximately constant. The shape of the bulge in elevation in Fig. 4.19(a) was typical of shallow anchor tests in both glyben and modified Grangemouth clay in the range $0.6 < D/B < 2.0$. In very shallow anchor tests with D/B less than 0.6, the bulge had a flatter top surface and steeper sides than shown in Fig. 4.19 (a). In deep anchor tests, little bulging of the surface occurred at ultimate uplift resistance.

Fig. 4.20 illustrated ω/B, the ratio of the diameters of the bulges to the diameters of the anchors, plotted against D/B, the anchor depth to breadth ratios, for tests in which these measurements could be made. The ω/B values ranged from approximately 1.75 at D/B = 0.5 to 2.5 at D/B = 4.0. In the tests in which D/B was greater than about 2.0, no measureable bulge was formed on the surface at ultimate uplift resistance and anchor displacement was continued beyond ultimate uplift resistance in order to obtain the measurement of bulge

diameter.

Although an accurate measurement of the surface bulge diameter was obtained for only one test (no. 47) of the "rotated-box" series, it was noted that the surface bulges in all three shallow anchor "rotated-box" tests (nos. 47 to 49) were slightly elliptical in shape, as opposed to the normal circular shape shown in Fig. 4.19. It was also noted that the average diameters of these bulges were significantly greater than in each of the other categories of tests shown in Table 4.3. These differences in shape and size of the bulge were attributed to the non-axisymmetric nature of the tests, which had weak-bonded layers on the parallel vertical planes shown in Fig. 4.8(c). It was assumed that, for anchors with the same diameters and equal D/B ratios, the same volume of material would be displaced at the surface for equal anchor displacements. Thus, if the diameter of the bulge were greater, the height of the bulge would be less. The lower values of surface to anchor displacement ratios illustrated in Fig. 4.18 for the "rotated-box" tests supported this assumption.

Fig. 4.19(b) showed the extensive cracking pattern which occurred on the clay surface at an anchor displacement of 2.6 times that at ultimate uplift resistance in "layered" glyben test no. 8 with D/B = 1.5. It may be noted that the cracking did not extend beyond the boundary of the bulge. The cracking on the surface was due to the regions of high radial tensile stresses at or near the surface, caused by the displacement of the anchor plate as discussed in the previous section. The "starfish" shape of the cracking pattern was typical of tests in both glyben and modified Grangemouth clay. The size of the cracks were related directly to the height of the bulge. In shallow anchor tests, surface cracks appeared soon after the start of the test and well before ultimate uplift resistance was attained. In deep tests, no surface cracks were evident at ultimate uplift resistance.

C. Relationship between Uplift Resistance and Anchor Displacement

In this section the factors which affect the relationship between anchor displacement and the corresponding value of uplift resistance in the uplift resistance tests on samples of "layered" and "non-layered" glyben and modified Grangemouth clay and in the finite element analysis will be discussed. The effect of suction below the anchor plate and creep in the laboratory model samples will also be discussed.

Displacement-controlled model tests without suction and the finite element analysis. Fig. 5.12 depicted curves of the uplift resistance factor $\bar{F}$ corresponding to the anchor displacement ratio d_a/B for finite element runs 1, 2 and 3 at D/B values of 1.5, 3.2 and 5.25 respectively. The figure indicates that the value of ultimate uplift resistance was directly proportional to the D/B ratio of the tests, as proposed by the Shearing Theory (2.2.A), and that the amount of anchor displacement to ultimate uplift resistance was approximately proportional to the D/B ratio of the tests. However, whereas the finite element analysis predicted a general type of failure at all D/B ratios, the laboratory model tests showed that a combination of general and local type failure occurred in the intermediate depth of anchor tests and local type failure occurred in the deep anchor tests. Figs. 4.28 and 4.26 indicated that neither ultimate uplift resistance nor the amount of anchor displacement to ninety percent of ultimate failure respectively were directly proportional to the D/B ratio for other than shallow anchors.

Fig. 6.5 compares the curves of $\bar{F}$ v d_a/B for shallow anchor tests in "layered" and "non-layered" glyben and modified Grangemouth clay and the results from the finite element analysis for a shallow anchor, taken from Figs. 4.21, 4.22, 4.23 and 5.12 respectively.

Considerable differences in the shapes of the curves, the values of ultimate uplift resistance and the amount of anchor displacement to ultimate uplift resistance are indicated. These differences will be discussed by a comparison of the $\bar{F}$ v $d_a/_B$ curves for (a) "layered" and "non-layered" glyben, (b) "non-layered" glyben and modified Grangemouth clay and (c) "non-layered" glyben and the finite element analysis.

(a) "Layered" and "non-layered" glyben. Although the curve for a "rotated-box" sample of glyben is illustrated in Fig. 6.5, the sample is assumed to be "non-layered" for the reasons discussed at the beginning of section 6.3. The slope of the "non-layered" curve is steeper than that of the "layered" curve and a higher value of ultimate uplift resistance is attained at a smaller amount of anchor displacement. As was discussed in section 6.2.A, no significant difference existed between the results of a series of unconfined triaxial compression tests on samples of both "layered" and "non-layered" glyben, whereas a considerable difference existed between the values of tensile strength of the two materials, as was shown in Fig. 4.9. By taking account of these results, a possible explanation of the difference between the $\bar{F}$ v $d_a/_B$ curves of the "layered" and "non-layered" glyben samples can be demonstrated by analogy. Fig. 6.6(a) illustrates a load being applied to a stack of loose cards. Each card represents a separate layer of glyben and the stack of loose cards simulates the "layered" glyben sample, with the assumption that the weak tension bond between the layers is also a weak bond in shear. Fig. 6.6 (b) illustrates the same load being applied to the stack, but in this case the cards are glued together and it is assumed that the resulting block is isotropic and represents the "non-layered" glyben. In the loose stack, the cards can slide over one another when the load is applied

and a large displacement of the load can result. The isotropic card block will have a higher value of structural stiffness than the separate cards and much less movement will take place when the same load is applied. In addition, the sliding of the separate cards will relieve the high radial tensile stress concentrations which may occur in region T in the isotropic block, shown in Fig. 6.6.(b). This explanation accounts for the small amount of cracking in the "layered" shallow anchor glyben samples at ultimate uplift resistance, illustrated in Figs. 4.15 and 4.16, compared with the cracking in the equivalent "non-layered" glyben sample, illustrated in Fig. 4.12.

Referring to Fig. 6.5, when a load which resulted in an $\bar{F}$ value of 3.25 had been applied to the anchor, the $d_{a/B}$ ratio of the "non-layered" test was approximately 0.07. However, in the "layered" sample, the $d_{a/B}$ ratio was greater than 0.4 and it is assumed that ultimate failure took place under this load by the continuous extension in tension of the region X shown in Fig. 6.4(d). However, the "non-layered" sample could continue to sustain an increasing amount of load until a value $\bar{F}_u = 4.3$ was attained, at which stage a tension crack which extended from the surface joined the yielded portion of the sample above the edge of the anchor to form a general failure surface, as illustrated in Fig. 6.4 (c).

(b) <u>"Non-layered" glyben and modified Grangemouth clay</u>. Since it was found by the author that the modified Grangemouth clay did not exhibit "layered" behaviour, it will be compared in this case with "non-layered" glyben. The slopes of the $\bar{F}$ v $d_{a/B}$ curves shown in Fig. 6.5 are significantly different in the two cases. The derivation of the finite element analysis (Appendix E) showed that the structural stiffness of a sample of material in both the

elastic and plastic zones was directly proportional to the value of the elastic modulus of the material. A comparison of the unconfined triaxial compression stress-strain curves in Figs. 4.9 and 4.10 shows that the slope of the glyben curve is considerably steeper than the slope for the curve of modified Grangemouth clay. This indicates that the value of elastic modulus and the resulting structural stiffness in the glyben is considerably higher than for modified Grangemouth clay. Consequently a greater amount of anchor displacement will occur in the modified Grangemouth clay than in the glyben for an equivalent anchor loading. Fig. 4.10 also showed that the stress-strain curve for tension extended to approximately 20% sample strain before failure, compared with approximately 10% sample strain to failure for the "non-layered" glyben, shown in Fig. 4.9. This may account for the lack of cracking exhibited near the surface of the modified Grangemouth clay sample shown in Fig. 4.17.

(c) <u>"Non-layered" glyben and the finite element analysis</u>. Figs. 5.9, 5.10 and 5.11 compared the shapes of the finite element analysis curves for $\bar{F}$ v d_a/B in the shallow, intermediate depth and deep anchor meshes respectively with the results for "non-layered" glyben in equivalent laboratory model tests. As stated previously, the slope of the $\bar{F}$ v d_a/B curve in the finite element analysis was proportional to whatever value of elastic modulus E was used in the analysis. Fig. 5.2 showed the linear elastic non-strain hardening plastic stress-strain curves which were assumed in the finite element analysis, with E = 1200 kN/m^2, E = 430 kN/m^2 and E = 100 kN/m^2. Because of the shape of these stress-strain curves, the relationship between F and d_a/B in the finite element runs was linear when all of the elements in the mesh remained on the elastic portion of the

stress-strain curve, i.e. the relationship was linear until the "critical" element yielded. This is demonstrated in Fig. 5.12 by the linear portions of the $\bar{F}$ v $d_a/_B$ curves from the origin to points Ⓐ, Ⓒ and Ⓔ.

It was pointed out in chapter 5 that the load-displacement relationships produced by the finite element method were only valid at small values of element strain, since the basic element stiffness equations were derived using the assumptions of small strain. The maximum values of strain in the "critical" element at ultimate uplift resistance in Fig. 5.9 for $E = 1200$ kN/m^2, $E = 430$ kN/m^2 and $E = 100$ kN/m^2 were approximately 12%, 33% and 180% respectively. Element strains of greater than the order of 10% were considered to fall outside the category of "small strains" and thus the $\bar{F}$ v $d_a/_B$ curves for $E = 430$ kN/m^2 and $E = 100$ kN/m^2 at all but the lowest values of $d_a/_B$ did not conform to the basic assumptions used to develop the element stiffnesses and are included for illustrative purposes only. This was also true for the higher values of $d_a/_B$ for $E = 430$ kN/m^2 and $E = 100$ kN/m^2 in Figs. 5.10 and 5.11.

. With glyben, stress does not vary linearly with strain and no single assumed value of E in the finite element analysis will produce an $\bar{F}$ v $d_a/_B$ curve of similar shape to the $\bar{F}$ v $d_a/_B$ curve for glyben. Fig. 5.9 illustrates that at very low values of $d_a/_B$, the slope of the glyben curve followed the finite element curve which used the "initial tangent" value of elastic modulus for glyben ($E = 1200$ kN/m^2), i.e. at very small anchor displacements the strain in most of the glyben uplift resistance sample was very small and the material was on the "initial tangent" part of its stress-strain curve which was shown in Fig. 5.2. As the anchor displacement was increased, the strain in the glyben increased also, with the

result that the value of strain and the corresponding stress in the glyben was no longer on the "initial tangent" portion of the stress-strain curve. The shape of the $\bar{F}$ v $d_a/_B$ curve for glyben in Fig. 5.9 reflects the increasing strain in the material.

Fig. 4.26 summarises the values which were shown in Figs. 4.21, 4.22, 4.23 and 6.5 for anchor displacement at 90% of ultimate uplift resistance, together with the results of the remaining laboratory model tests, and illustrates clearly the effect of $D/_B$ on anchor movement. Three distinct curves are depicted which show the values of anchor displacements at 90% of ultimate uplift resistance for samples of "non-layered" and "rotated-box" glyben to be of the order of 60% of the values for "layered" glyben, which in turn were shown to be of the order of 60% of the values for modified Grangemouth clay over the range of $D/_B$ values. Thus the importance of weak tension bonding and the value of elastic modulus which were discussed in parts (a), (b) and (c) of this section are illustrated in their effect on anchor displacement. There is a considerably greater scatter of points on the "layered" glyben curve than on the "non-layered" glyben and modified Grangemouth clay curves, which possibly indicates that the thickness of the layers and the bonding between them was not constant in the "layered" uplift resistance test samples.

Displacement-controlled model tests with suction. Fig. 4.24 showed the $\bar{F}$ v $d_a/_B$ curves for shallow anchor pullout tests in "layered" glyben with and without the suction effect. The effect of the suction in these tests increased the value of $\bar{F}$ by between 60% and 80%. The maximum value of suction was of the order of 27 kN/m^2 compared with the value of 19 kN/m^2 obtained by Ali (1968) from pullout tests conducted from the surface of bentonite and water samples. After the maximum value of uplift resistance pressure had

been attained in the test with suction, subsequent values of uplift resistance pressure fell sharply. An examination of the cavity below the anchor plate after completion of the test showed that the cylindrical walls of the cavity had collapsed inwards at ultimate failure, which partly relieved the suctional effect and caused the marked drop in uplift resistance pressure. It was considered by the author that this form of failure was entirely different from the failure mechanism of the uplift resistance tests without suction and should be considered in a separate investigation.

Load-controlled model tests. Fig. 4.25 illustrated the $\bar{F}$ v d_a/B curves for equivalent load-controlled and displacement-controlled pushout tests in "layered" glyben with $D/B = 4.5$. In the load-controlled test, an additional load was added to the anchor only after displacement of the anchor due to the previous load had ceased. For values of load below about one half of the loading required to cause ultimate failure, the displacement of the anchor ceased shortly after each load had been added, and points A, B and C on the load-controlled test curve in Fig. 4.25 fall very near the displacement-controlled test curve. However, as the total load on the anchor approached the maximum value, anchor displacement continued over a long period of time (the anchor was still displacing slowly twenty four hours after the addition of the penultimate load) and this creep effect is illustrated by the displacements at D, E, F and G in Fig. 4.25.

D. Relationship between the Values of Ultimate Uplift Resistance and the Depth to Breadth Ratio of the Anchor

Fig. 4.27 showed the results of a series of "layered" glyben tests in which $P_u/\gamma_g D$ v D/B was plotted for $c/\gamma_g D$ values of 1.75, 2.5 and 3.7. The results of this series of tests plus the results for all of the other laboratory model tests were then shown in Fig. 4.28. This

figure illustrated the best-fitting curves of $\bar{F}_u$ v D/B for "layered" and "non-layered" glyben and for modified Grangemouth clay.

The mechanism of general failure which was predicted by the finite element analysis for anchors of all depths was discussed in sections 6.3.A and 6.3.C and was shown to be identical to the mechanism of failure predicted by the Shearing Theory (2.2.A). The values of ultimate uplift resistance for the finite element runs with D/B = 1.5, 3.2 and 5.25 were thus the same as those predicted by the Shearing Theory. Fig. 6.7 shows a comparison between the $\bar{F}_u$ v D/B curve plotted from the results of the three finite element runs and the average best-fitting curves from the laboratory model tests shown in Fig. 4.28. Fig. 6.7 demonstrates clearly the difference between the values of ultimate uplift resistance for the general type of failure in deep anchors predicted by the finite element method and the local type of failure for deep anchors shown in the laboratory model tests.

Each of the curves representing the laboratory model tests in Fig. 4.28 can be divided into three portions:

(a) shallow anchor tests: $D/B \leq 2{\cdot}0$: showed an approximately linear relationship between $\bar{F}_u$ and D/B ;

(b) deep anchor tests: $D/B \geq 5{\cdot}0$: showed the value of $\bar{F}_u$ to be practically constant ;

(c) intermediate depth of anchor tests: $D/B > 2{\cdot}0$ and $D/B < 5{\cdot}0$: showed a non-linear relationship between $\bar{F}_u$ and D/B .

(a) <u>Shallow anchor tests ($D/B \leq 2.0$)</u>. Fig. 4.29 illustrated the curves of $\bar{F}_u$ v D/B for the shallow anchor tests. The approximately linear relationship between the ultimate uplift resistance factor $\bar{F}_u$ and D/B accorded with the mode of general failure for shallow anchors proposed by the author in section 6.3.A. It was proposed in that section that ultimate failure was caused by a combination of shear and tension failure in the material directly

above, and in the vicinity of, the edge of the anchor plate. Since a general form of failure was predicted, i.e. one in which a failure surface extended from the anchor plate to the surface, the value of ultimate uplift resistance predicted should be approximately proportional to anchor depth.

A possible explanation of the relative values of ultimate uplift resistance for the "layered" and"non-layered" glyben was proposed by the card analogy in section 6.3.C. Fig. 4.29 illustrates that the values of F_u for shallow tests with $D/B < 0.8$ in modified Grangemouth clay were similar to those for "layered" glyben and for tests in the D/B range 1.0 to 1.8 the values were slightly greater than for "non-layered" glyben.

(b) Deep anchor tests ($D/B \geq 5.0$). Fig. 4.28 shows that the values of ultimate uplift resistance for the deep anchor tests in "non-layered" glyben were of the order of 15% higher than the corresponding values in "layered" glyben. The card analogy proposed in section 6.3.C demonstrated that the "layered" samples had less structural stiffness than the "non-layered" samples. In terms of local failure, this difference in structural stiffness and the corresponding amount of anchor movement to failure appears to have affected the value of ultimate uplift resistance, although to a lesser extent than in the shallow anchor general failure case. There is a considerably greater scatter amongst the results of the deep anchor tests in "layered" glyben than in the "non-layered" glyben, which possibly reflects the variation in thickness of the layers of glyben and the bond between them.

The values of ultimate uplift resistance for the deep anchor tests in modified Grangemouth clay which are shown in Fig. 4.28 were significantly higher than the values for glyben and greater even than the values of ultimate uplift resistance in glyben with suction. It was proposed in section 6.2 that consolidation and a

consequent increase in the strength of the clay in the vicinity of the anchor plate had affected the results of these tests. Thus, when values of ultimate uplift resistance for deep anchors in purely cohesive soils are required, the results of the tests in glyben only will be considered.

(c) Intermediate depth of anchor tests ($2 < D/B < 5$). It was proposed in section 6.3.A that the mechanism of ultimate failure of tests in which the depth of placement of the anchor was in the intermediate range was a combination of general type failure and local type failure. This proposal was supported by the photographic evidence in Fig. 4.13. Fig. 4.28 shows that the values of ultimate uplift resistance of tests in this range fell on a curved portion which linked the portion of the graph which varied linearly with D/B for shallow anchor tests to the horizontal portion of the graph for deep anchor tests.

It is of interest to note the similarity of shape of the curves depicted in Figs. 4.18, 4.26 and 4.28. For shallow anchors, the ratio of the surface displacement to anchor displacement, the anchor displacement ratio to 90% of ultimate uplift resistance, and the value of ultimate uplift resistance varied approximately linearly with D/B, reflecting the mechanism of general type failure which occurred in these tests. For deep anchor tests, these values were approximately constant, reflecting the mechanism of local type failure. The values at intermediate depths fell on curves which linked the shallow and deep anchor linear portions of the plot, and reflected the combination of general and local type failure.

The results illustrated in Figs. 4.18, 4.26 and 4.28 also confirmed that, for tests conducted in "layered" glyben without suction, there was little difference between the results of (i) pullout displacement-controlled tests, (ii) pushout load-controlled tests,

(iii) pushout displacement-controlled tests in which the anchor was initially above the base of the box, and (iv) pushout displacement-controlled tests in which the anchor was initially at the base of the box.

The values of ultimate uplift resistance shown in Fig. 4.28 will be compared in section 6.4 with the values predicted by Vesic's (1963 and 1965) Shallow and Deep Anchor Theories (2.2.D and 2.3.B) and in section 6.5 with the values obtained by Ali (1968), Bhatnagar (1969) and Adams and Hayes (1967) in their model anchor tests.

E. Magnitude, Direction and Distribution of Stresses throughout the Uplift Resistance Sample

In this section, the results of the finite element analysis only will be discussed since values of stresses in the samples were not measured in the model uplift resistance tests.

Order of plastic yielding of the elements in the shallow anchor run no. 1, $D/B = 1.5$. Fig. 5.3 (a) illustrated the order in which the elements yielded plastically in this case. Since the finite element analysis assumed a high tensile strength material in which cracking did not occur at limiting tensile stress, an upper limit of ultimate uplift resistance was produced by the analysis and the mechanism of failure was that predicted by the Shearing Theory (2.2.A), with general failure occurring in the material on a cylindrical slip failure surface above the edge of the anchor plate, extending to the surface of the sample. The elements yielded systematically from the "critical" element at the edge of the anchor plate to the element at the soil surface.

Order of plastic yielding of the elements in the intermediate depth of anchor run no. 2, $D/B = 3.2$. Fig. 5.3(b) illustrated the order in which the elements yielded plastically in this case. As was explained in chapter 5, the finite element program could not predict local failure of the type proposed by Vesic (1963 and 1965) or Meyerhof

and Adams (1968) but continued to increase the loads in specified increments and to re-distribute the resulting excess stresses until a general type of failure occurred. Thus, in the intermediate and deep anchor cases, an upper limit of ultimate uplift resistance value was produced which was considerably higher than the value of ultimate uplift resistance which would have resulted from a local type of failure. The order of yielding shown in Fig. 5.3(b) reflects therefore the order in which plastic yielding would occur under conditions of general failure. It is of interest to note that the elements above the "critical" element yielded systematically, as in run no. 1, up to a height above the anchor of approximately half the depth of the anchor $D/2$. At that stage the elements above the anchor plate started to yield plastically, with the elements above the edge of the anchor plate yielding first. The elements directly above the anchor plate were late to yield, and in fact the element directly above the centre portion of the plate did not yield at all, due to the small values of shear stress in that region, as indicated in Figs. 5.19 and 5.22. The elements to the outside of the "critical cylinder" of elements were slow to yield and only three elements in that region yielded before general failure occurred. This was unlike the case of Vesic's and Meyerhof and Adams's Deep Anchor Theories, in which local plastic failure was predicted in a spherical-type region around the anchor plate.

Order of plastic yielding of the elements in deep anchor run no. 3 with $D/B = 5.25$. Fig. 5.3(c) illustrated the order in which the elements yielded plastically in this case. As was noted in chapter 5, yielding was not shown up to ultimate failure. The order of element yield in the deep test was similar to the order of yield in the intermediate depth of test except that yielding above the "critical" element occurred only up to a distance of $D/3$ above the anchor plate before yielding of the elements above the anchor plate began.

Magnitude and direction of the major principal stresses. Figs. 5.13, 5.14 and 5.15 showed the magnitude and direction of the major principal stresses which were obtained from runs 1, 2 and 3 respectively. The shaded areas in these figures denote regions where the major principal stress was tensile, and the boundaries of these tensile regions are marked with a dotted line.

The following points were noted:

(a) The directions of the major principal stresses in the elastic stages of the analysis shown in parts (a) of Figs. 5.13, 5.14 and 5.15 were similar to the directions of the major principal stresses in the corresponding parts (b) of the figures, in which the directions of the stresses were shown when the material was at or near to ultimate uplift resistance. However, as stated previously, the magnitudes and directions of the major principal stresses shown in parts (b) of Figs. 5.13, 5.14 and 5.15 represented the stresses corresponding to a general type of failure. If the finite element analysis had been capable of predicting a local type of failure, it is considered by the author that the magnitudes and directions of the major principal stresses at or near to ultimate uplift resistance would have been substantially different from those shown in parts (b) of Figs. 5.13, 5.14 and 5.15.

(b) The direction of the major principal stresses in the elements directly above the anchor plate in parts (a) and (b) of Figs. 5.13, 5.14 and 5.15 was approximately vertical, reflecting the direction of the displacement of the anchor. The direction of the major principal stresses in the elements below the anchor plate was generally horizontal, except for those elements immediately below the anchor. Since the largest tensile stresses in the elements were defined as being orthogonal to the direction of the major principal stress, the direction of the largest tensile stresses

below the anchor were approximately vertical and therefore also reflected the direction of the displacement of the anchor.

(c) In parts (a) and (b) of Figs. 5.13, 5.14 and 5.15, the magnitude of the major principal stresses decreased rapidly with increasing distance from the anchor plate.

(d) In parts (a) and (b) of Figs. 5.13, 5.14 and 5.15, the overall pattern of the major principal stresses resembled a vortex with the edge of the anchor plate as its centre. The vortex represented the material above the anchor being pushed upwards and outwards from the anchor and the material below the anchor being pulled upwards and inwards towards the anchor, bearing in mind that the directions of the largest tensile stresses in the shaded regions were orthogonal to the directions of the major principal stresses illustrated.

(e) The directions of the major principal stresses in those elements which had yielded plastically above the "critical" elements in Figs. 5.13, 5.14 and 5.15 were at an angle of $\pi/4$ to the vertical. Since the direction of the maximum shear stress in any element is at $\pi/4$ to the direction of the major and minor principal stresses in the element, the maximum shear stresses in these elements were in the vertical and horizontal directions. As was discussed previously, general ultimate failure was predicted by the finite element analysis on a cylinder above the edge of the anchor plate. Thus the direction of the maximum shear stress in these elements was parallel to the direction of the displacement of this cylinder.

Magnitude and distribution of radial and vertical normal stresses and shear stresses. The magnitude and distribution of stresses in the form of stress fields were presented in Figs. 5.17 to 5.22. The shaded areas in these figures denote regions of tensile stress, the boundaries of which are marked by a dotted line.

It should be noted that in Figs. 5.17 to 5.22, the values of the stress contours were given in terms of the value of the stress at the centre of the "critical" element when it was on the point of yielding. As was discussed in section 5.4 and Appendix E, the values of the normal stresses at the centre of the "critical" element were probably appreciably lower than the maximum values of normal stress which occurred at the edges of the "critical" element. Therefore the values of vertical normal stress shown for the centre of the "critical" element in Figs. 5.17 and 5.20 and the values of radial normal stress shown for the centre of the "critical" element in Figs. 5.18 and 5.21 were probably appreciably lower than the maximum values of these stresses which occurred at the edges of the element. It should be noted also that the magnitude and distribution of the stresses in parts (b) of the figures represented those for a general form of failure and, in the intermediate depth and deep anchor cases, gave considerably greater values of stress than would occur due to local failure.

(a) Vertical normal stress in the shallow anchor run no. 1, $D/B = 1.5$ (Fig. 5.17). The size of the shaded tensile region shown in this figure was considerable, extending in the elastic case (Fig. 5.17(a)) upwards and outwards at an angle of approximately $\pi/4$ to the horizontal from the edge of the anchor plate, and at a steeper angle in the case of ultimate failure (Fig. 5.17(b)). The magnitude of the stresses decreased rapidly with increasing distance from the anchor plate in both parts (a) and (b) of the figure, the values of compressive stress at a distance of B and $3B/2$ above the anchor plate being approximately one half and one quarter respectively of the values of the compressive stress at a distance of $B/2$ above the plate. The patterns of stresses in both the elastic and ultimate failure cases were similar except that, in the latter, a significant concentration of stresses

existed in the elements above the "critical" element.

(b) Radial normal stress in the shallow anchor run no. 1, $D/B = 1.5$. (Fig. 5.18). The patterns of stress distribution in this case were relatively similar to those in the vertical normal stress case discussed above, except that the line between the compressive and the tensile stresses was at a considerably less steep angle to the horizontal. In addition there existed a tensile region which occurred at and near the surface of the sample above the centre of the anchor plate. Directly below the edge of the anchor plate, an area of much reduced tensile stress is shown in both Figs. 5.18 (a) and (b). A corresponding region of low compressive stress does not occur above the anchor plate.

(c) Shear stresses on the $z-r$ and $r-z$ planes in the shallow anchor run no. 1, $D/B = 1.5$ (Fig. 5.19). The pattern of shear stress distribution shown in Fig. 5.19 was quite different from the pattern of distribution for the normal stresses illustrated in Figs. 5.17 and 5.18. Figs. 5.5 and 5.6 illustrated the deformed shapes of the elements which are shown in stages (a) and (b) respectively of Fig. 5.19. Comparison of the shapes of the deformed elements in Figs. 5.5 and 5.6 with the shapes of the elements which depict compressive (positive) and tensile (negative) shear values, illustrated in Fig. E.3 of Appendix E, can account for the pattern of distribution of shear stresses in Fig. 5.19. The vertical contour of 1.0 which extended from the edge of the anchor plate to the sample surface in Fig. 5.19 (b) represents the general slip failure surface at ultimate uplift resistance.

(d) Vertical normal stress in the deep anchor run no. 3, $D/B = 5.25$. (Fig. 5.20). The distribution of vertical normal stress in the deep anchor case was similar to that in the shallow anchor case. However, the high compressive stresses which existed directly above the centre of the anchor plate were completely dissipated before

they reached the surface of the sample in the deep anchor case which resulted in a small area of tensile stress at and near to this surface.

(e) Radial normal stress in the deep anchor run no. 3, $D/B = 5.25$. (Fig. 5.21). The distribution of radial normal stress was similar to that shown in the shallow anchor case except that the area of tensile stress above the centre of the anchor plate extended from the surface to within a height $D/4$ above the anchor plate.

(f) Shear stresses on the $z-r$ and $r-z$ planes in the deep anchor run no. 3, $D/B = 5.25$. (Fig. 5.22). The pattern of stresses shown in Fig. 5.22 was similar to the pattern shown for the shallow anchor case.

6.4. Comparison of Model Test Results obtained by the Author with the Predictions of Vesic's (1963 and 1965) Shallow (2.2.D) and Deep (2.3.B) Anchor Theories

In chapter 2 Vesic's Shallow and Deep Anchor Theories were outlined and discussed. An attempt has been made by the author to quantify the predictions of Vesic's theories in terms of the ultimate uplift resistance factor $\bar{F}_u$ and the depth to breadth ratio of the anchor D/B. Fig. 6.8 shows a comparison between the best-fitting curves of $\bar{F}_u$ v D/B obtained by the author from his model uplift resistance tests, as illustrated in Fig. 4.28 and Vesic's Shallow and Deep Anchor Theories. For a purely cohesive soil, Vesic's Shallow Anchor Theory defined a unique curve of $\bar{F}_u$ v D/B but the value of $\bar{F}_u$ predicted by his Deep Anchor Theory was a function of the rigidity index I_r and the volume change factor Δ of the soil. The values of $\bar{F}_u$ corresponding to $I_r = 500$ and $\Delta = 0.0$, which represented an incompressible clay with very low strain to yield, and $I_r = 20$ and $\Delta = 0.02$, which represented a compressible clay with very high strain to yield, have been calculated by the author for comparative

purposes and are shown in Fig. 6.8. Fig. 6.9 shows these curves for D/B in the shallow anchor range.

A. Shallow Anchor Range

Table 6.2 summarises the differences indicated in Fig. 6.9 between the values of ultimate uplift resistance predicted by Vesic's Shallow Anchor Theory and the values obtained by model tests in glyben and modified Grangemouth clay. These differences reflect the extent to which the failure mechanism proposed by the author and discussed in section 6.3.A reduced the actual value of ultimate uplift resistance for the material from the theoretical upper limit proposed by Vesic's theory.

B. Deep Anchor Range

Fig. 6.8 indicates that the $\bar{F}_u$ values for "non-layered" glyben and "layered" glyben in the deep anchor range were approximately 7.4 and 6.6 respectively. The $\bar{F}_u$ value predicted by Vesic's theory for the non-compressible clay with low strain to yield ($I_r = 500$, $\Delta = 0$) was higher than the values for both types of glyben but the $\bar{F}_u$ value predicted by Vesic's theory for the compressible clay with high strain to yield ($I_r = 20$, $\Delta = 0.02$) was lower than the glyben values. The values of rigidity index (for a Δ value of 0.0) which corresponded to the $\bar{F}_u$ values shown in Fig. 6.8 of "non-layered" and "layered" glyben were calculated by the author from Vesic's deep anchor theory to be $I_r = 90$ and $I_r = 50$ respectively. The average values of rigidity index calculated from the glyben batch no. 3 sample stress-strain curve shown in Fig. 5.2 were $I_r = 7, 30$ and 83 corresponding to values of elastic moduli E of 100 kN/m^2, 430 kN/m^2 and 1200 kN/m^2 respectively, assuming a value of shear strength of 9 kN/m^2 and a value of Poisson's ratio of 0.5. It can be concluded therefore that the values of ultimate uplift resistance which were predicted by Vesic's Deep Anchor Theory corresponded approximately to the values

which were measured from the laboratory model tests in glyben.

As discussed in section 6.2, the values of ultimate uplift resistance from deep anchor tests in modified Grangemouth clay appeared to be affected by consolidation of the clay in the vicinity of the anchor plate. Fig. 6.8 shows that the maximum value of ultimate uplift resistance for modified Grangemouth clay was greater than the value predicted by Vesic for non-compressible clays with a very low strain to yield ($I_r = 500$, $\Delta = 0.0$).

6.5. Comparison of Model Test Results obtained by the Author with Model Test Results obtained by Previous Authors

Fig. 6.10 shows a comparison between the curves of $\bar{F}_u$ v D/B obtained by the author from his model uplift resistance tests, as illustrated in Fig. 4.28, and curves obtained by previous authors from their model uplift resistance tests, as illustrated in Fig. 2.15. Fig. 6.11 shows these curves for D/B ratios in the shallow anchor range. Values predicted by Vesic's Shallow and Deep Anchor Theories are also included in Figs. 6.10 and 6.11.

A. Shallow Anchor Range

For D/B values of less than 1.0, Fig. 6.11 indicates that the values obtained by Ali (1968) for tests in bentonite and water were of the order of 70% greater than those predicted by Vesic from his Shallow Anchor Theory, whereas the values obtained by Bhatnagar (1969) from tests on the same apparatus using a stiff silty clay were less than 50% of those predicted by Vesic for D/B values in this range. Vesic (1969) could offer no explanation for these large differences.

No indication of the tensile strength of bentonite and water was given by Ali but a section through the centre of the anchor plate at ultimate uplift resistance in one of his shallow anchor tests showed that no cracking had taken place in the material. However, this section was the result of the sample being cut open after the test by a wire

saw and, if any cracking pattern had been present in the material, it could well have been obscured by the smearing effect of the wire saw. Stress-strain curves obtained by Ali illustrated that the material had a very low strain to failure of approximately 5%. Even if it were assumed that the bentonite and water was a non-cracking material with high tensile strength, it is difficult to envisage a mechanism of failure in which the value of ultimate uplift resistance would exceed that predicted by Vesic's theory. However, it was noted by the author that the values of shear strength used by Ali to calculate the values of ultimate uplift resistance in his tests were obtained by unconfined triaxial compression strength tests. Values of shear strength for a similar bentonite and water mix obtained by Barksdale (1963) by laboratory vane tests were approximately 60% higher than those obtained by triaxial tests on the same material. If the values of shear strength obtained by the vane tests had been used to calculate values of ultimate uplift resistance in Ali's tests, the resulting values would have agreed well with those predicted by Vesic's theory.

No information about the tensile strength, layering, or cracking patterns of the stiff silty clay was given by Bhatnagar, although it was indicated that the material was compacted in the test box in four-inch layers by hand with steel tampers. Curves of uplift resistance versus anchor displacement given in Bhatnagar's thesis were similar to those obtained by the author for "layered" glyben and modified Grange-mouth clay. The low values of ultimate uplift resistance shown in Fig. 6.11 for the stiff silty clay suggested that the mechanism of failure in the shallow tests was similar to that described for "layered" glyben in sections 6.3.A and 6.3.C, with failure due to continuous extension occurring at a low value of ultimate uplift resistance.

The values of ultimate uplift resistance in the shallow anchor range obtained by Adams and Hayes (1967) from tests in brick clay were

generally similar to those obtained by the author. No information was given by Adams and Hayes about the elastic modulus, tensile strength or cracking patterns of the brick clay and thus no conclusions could be drawn by the author about the mechanism of ultimate failure.

B. Deep Anchor Range

Fig. 6.10 shows that the transition from the approximately linear portion of the shallow anchor curve to the horizontal portion of the deep anchor curve in Ali's tests on bentonite and water took place over a very small range of D/B values, and that deep anchor failure occurred at D/B values of greater than 2.5, indicating that bentonite and water behaved in a somewhat similar manner to the ideal material assumed in Vesic's theory. However, it must be pointed out that bentonite and water, due to its thixotropic properties, resembles some sensitive clays in behaviour, but is generally quite different from the type of remoulded clays which would be used as compacted fill above a high-mast type of anchor footing. The average value of rigidity index for bentonite and water, based on (i) the stress-strain curves in Ali's paper, (ii) an assumed value of Poisson's Ratio of 0.5, and (iii) an assumed value of Δ of 0.0, was approximately 55. This was slightly greater than the value of rigidity index predicted by Vesic's theory for a material with $\Delta = 0.0$ and with the $\bar{F}_u$ value of bentonite and water obtained by Ali adjusted to the $\bar{F}_u$ value corresponding to the laboratory vane shear strength of the material.

As shown in Fig. 6.10, the values of ultimate uplift resistance obtained from Bhatnagar's deep anchor tests on stiff silty clay were slightly greater, at D/B ratios of greater than 7.0, than those obtained by the author from tests in modified Grangemouth clay. It is suggested by the author that, as in modified Grangemouth clay, consolidation of the stiff silty clay used by Bhatnagar, under high

pressure in the deep tests caused an increase in the value of the strength of the clay in the vicinity of the anchor with a consequent increase in the value of ultimate uplift resistance. The silt content of the clay employed by Bhatnagar was appreciably greater than that of the modified Grangemouth clay.

Insufficient information about the properties of brick clay was supplied by Adams and Hayes to enable an average value of rigidity index for the material to be calculated, and thus the values of F_u of brick clay in the deep tests could not be compared with the results obtained by the author or with the results predicted by Vesic's theory.

TABLE 6.1 CATEGORIES OF MEASUREMENTS OBTAINED FROM LABORATORY MODEL TESTS & FINITE ELEMENT ANALYSIS.

CATEGORY	TYPE OF MEASUREMENT
Exclusive to laboratory model tests	Measurement of both surface and internal cracking Effect of creep of the material on uplift resistance results Effect of suction below the anchor plate on uplift resistance results. Relationship between uplift resistance and anchor displacements for large material strains.
Exclusive to finite element analysis	Magnitude, direction and distribution of stresses within the soil mass. Order of yielding of the elements. Detailed displacements of soil within the mass at any stage of uplift resistance (model tests gave an approximate indication only of displacement at the finish of the test)
Obtained from both methods	Relationship between uplift resistance and anchor displacements for small material strains. Values of ultimate uplift resistance. Measurement of surface displacements at small material strains.

TABLE 6.2. VALUES OF ULTIMATE UPLIFT RESISTANCE PREDICTED BY VESIC'S SHALLOW ANCHOR THEORY AND VALUES OBTAINED FROM SHALLOW ANCHOR MODEL TESTS BY THE AUTHOR

Depth to Breadth Ratio	Value of $\bar{F}_u$ from Vesic's Shallow Anchor Theory	'Layered' Glyben		'Non-layered' Glyben		Modified Grangemouth Clay	
		Value of $\bar{F}_u$	$\bar{F}_u$ expressed as a percentage of $\bar{F}_u$ for Vesic's Theory	Value of $\bar{F}_u$	$\bar{F}_u$ expressed as a percentage of $\bar{F}_u$ for Vesic's Theory	Value of $\bar{F}_u$	$\bar{F}_u$ expressed as a percentage of $\bar{F}_u$ for Vesic's Theory
$D/B = 0.6$	2.15	1.10	51 %	1.30	60%	1.10	51 %
$D/B = 1.0$	3.80	2.0	53 %	2.30	61%	2.45	64 %
$D/B = 1.5$	6.15	3.20	52 %	3.85	63 %	4.10	67 %

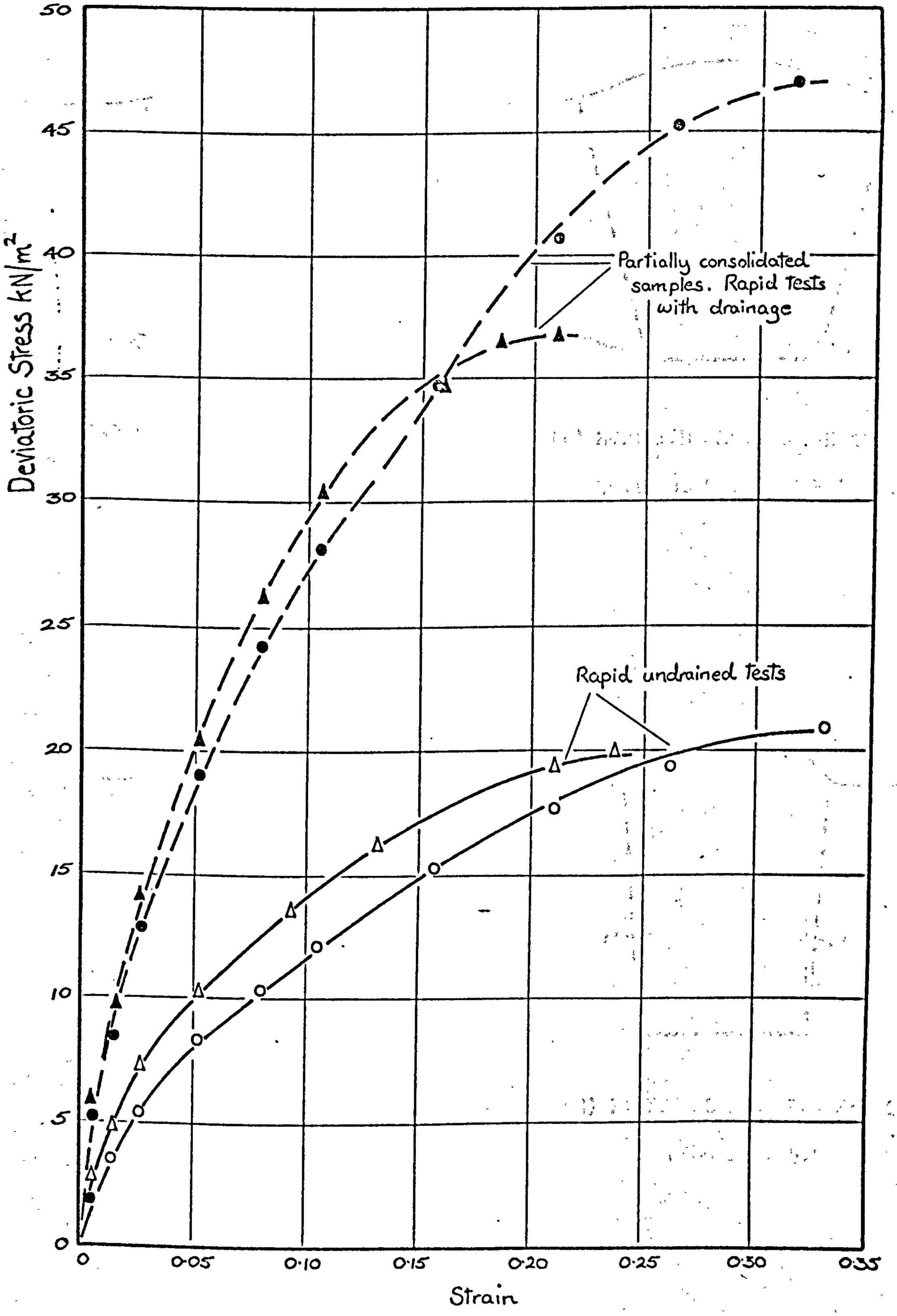

FIG. 6.1. RESULTS OF TRIAXIAL TESTS ON UNDRAINED SAMPLES AND PARTIALLY CONSOLIDATED SAMPLES OF MODIFIED GRANGEMOUTH CLAY

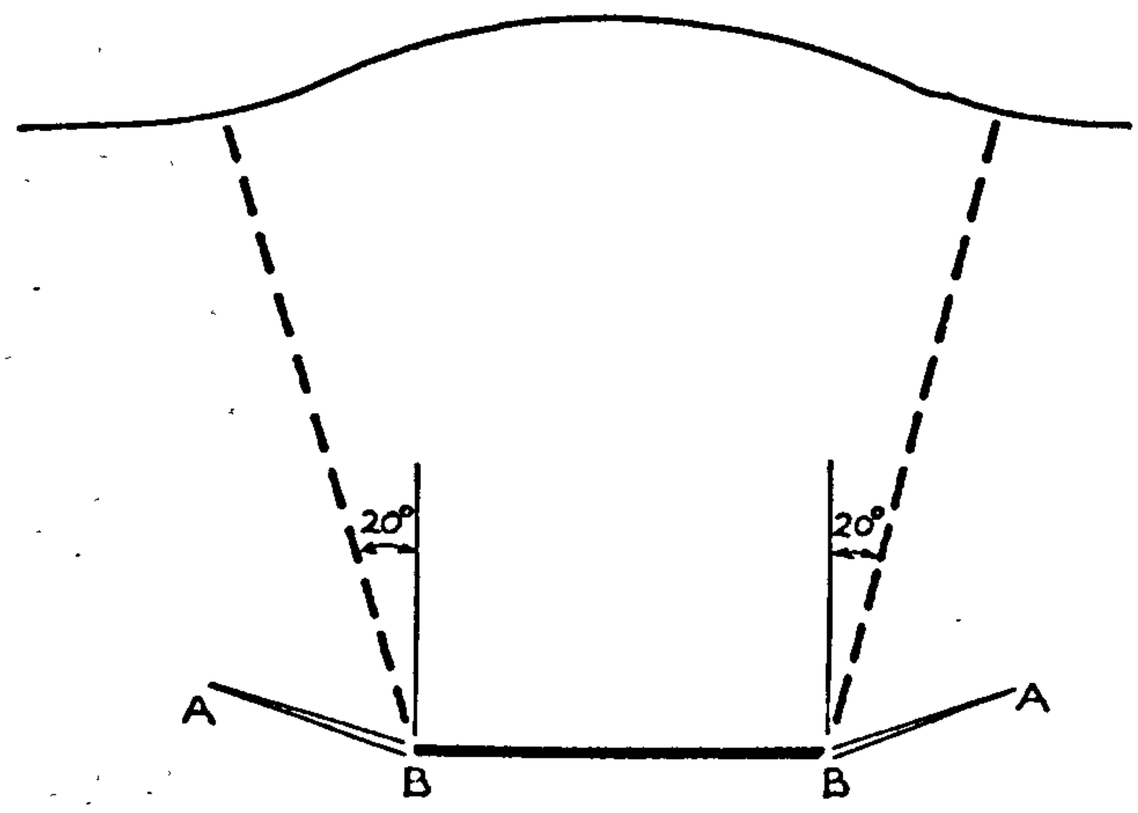

(a) "LAYERED" GLYBEN TEST No. 54

FROM FIG. 4.16

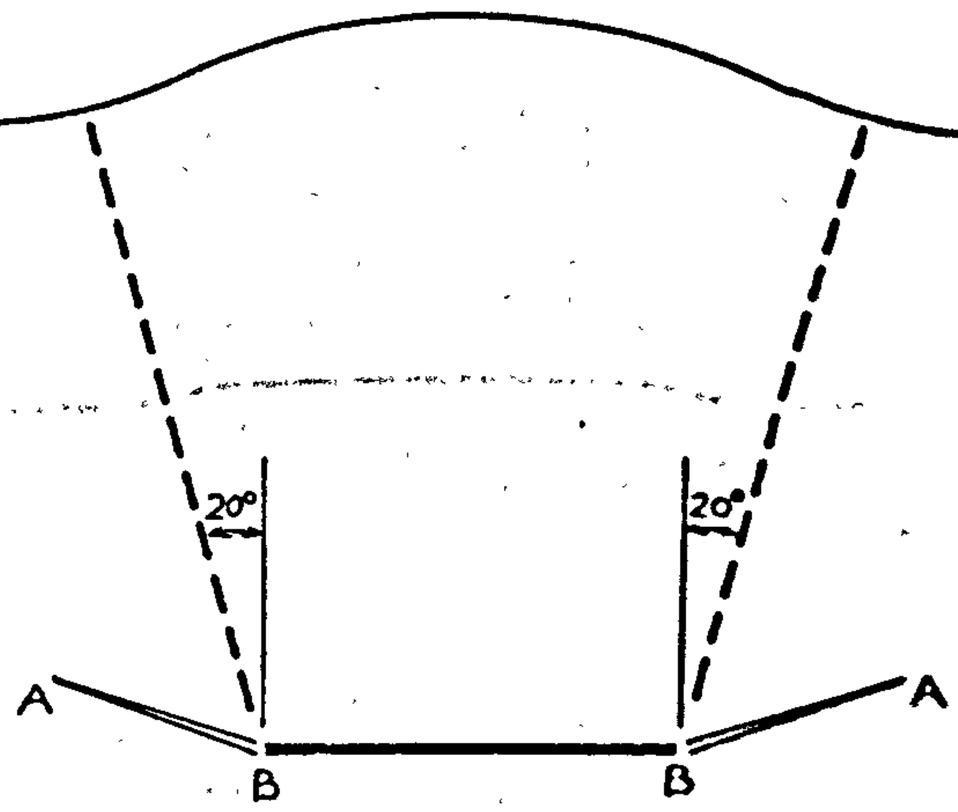

(c) MODIFIED GRANGEMOUTH CLAY

TEST No. 65, FROM FIG. 4.17

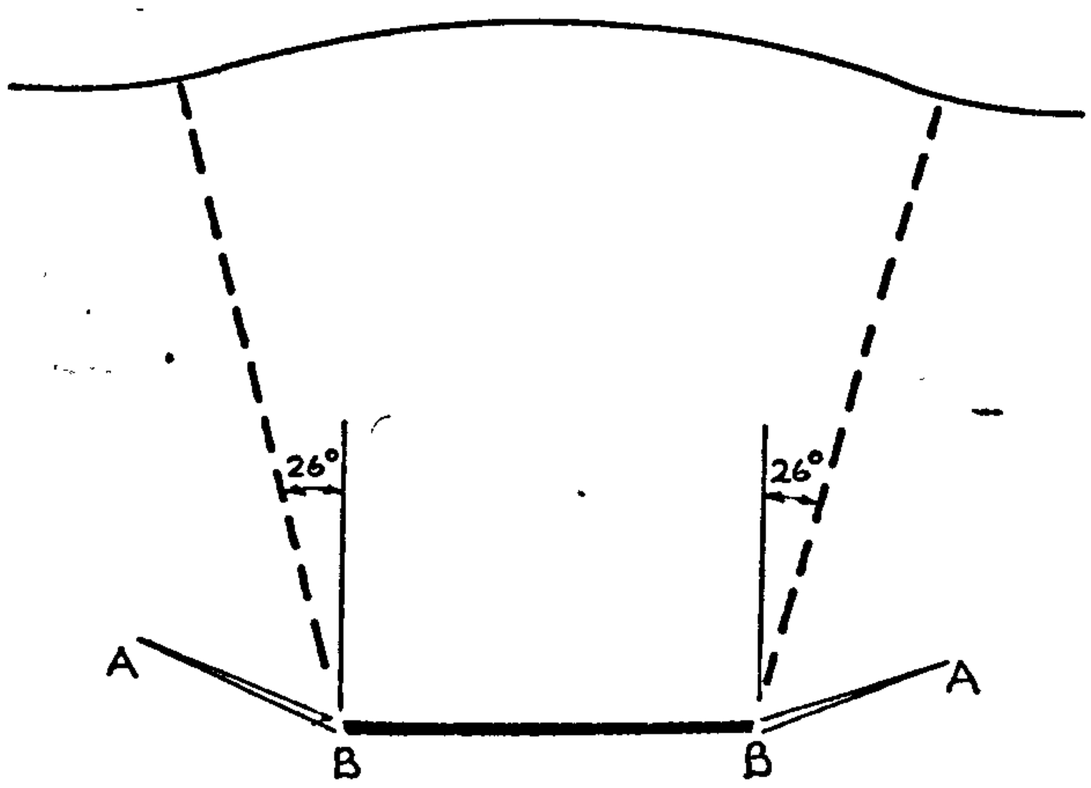

(b) "NON-LAYERED" GLYBEN TEST No. 49

FROM FIG. 4.12

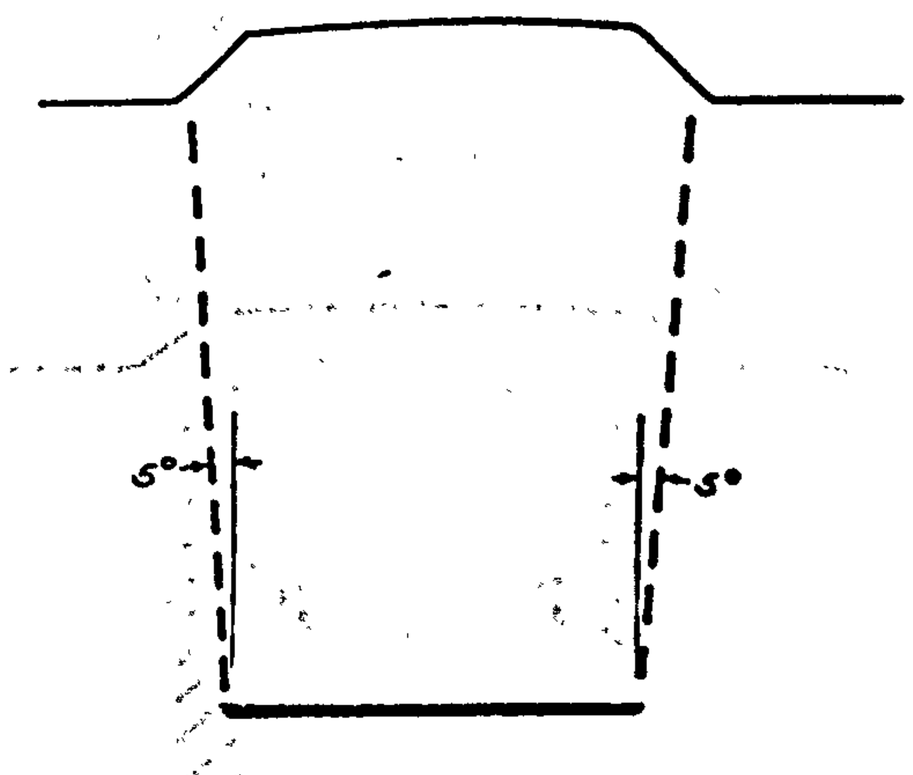

(d) FINITE ELEMENT RUN No. 1

FROM FIG. 5.6

FIG. 6.2. SKETCHES OF CROSS-SECTIONS THROUGH THE CENTRE OF VARIOUS SHALLOW ANCHOR SAMPLES AT ULTIMATE UPLIFT RESISTANCE

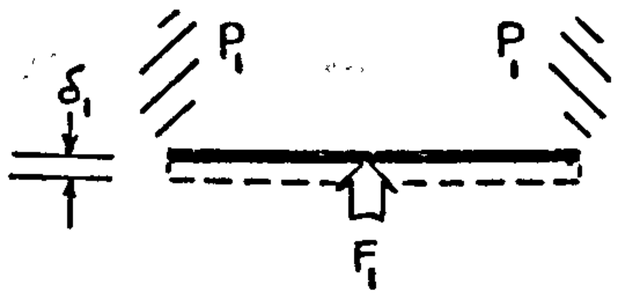

(a)

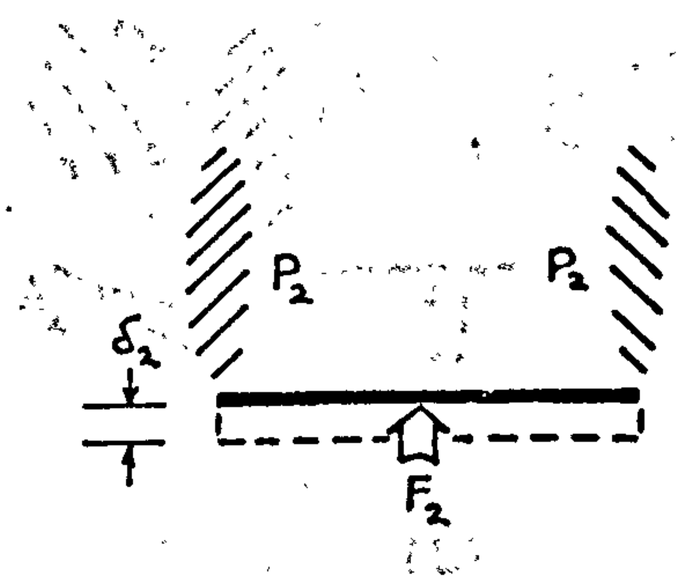

(b)

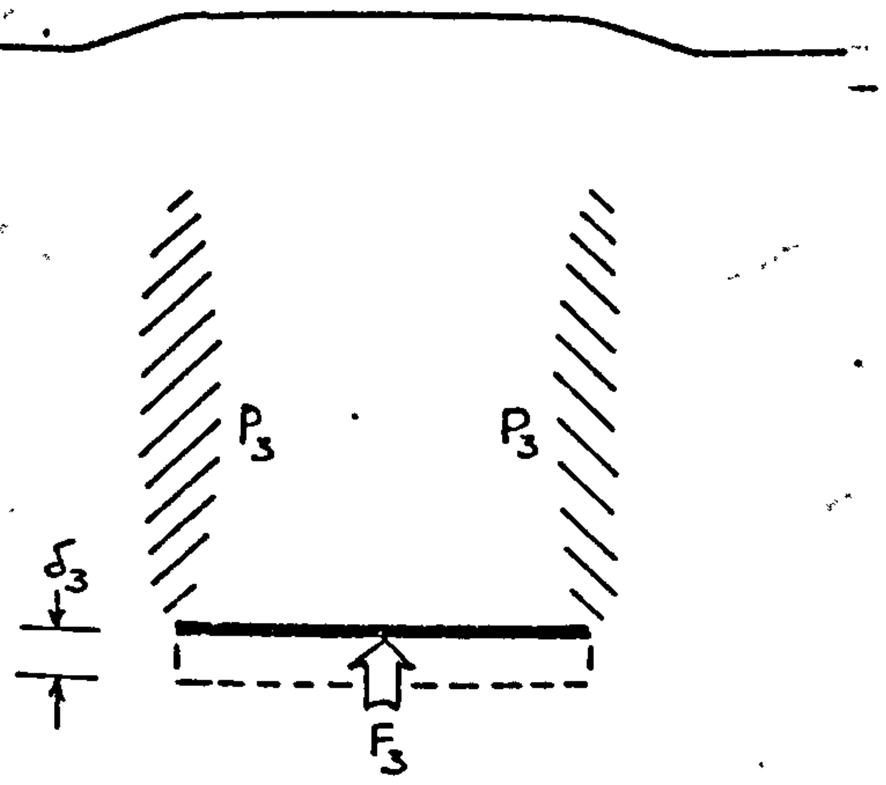

(c)

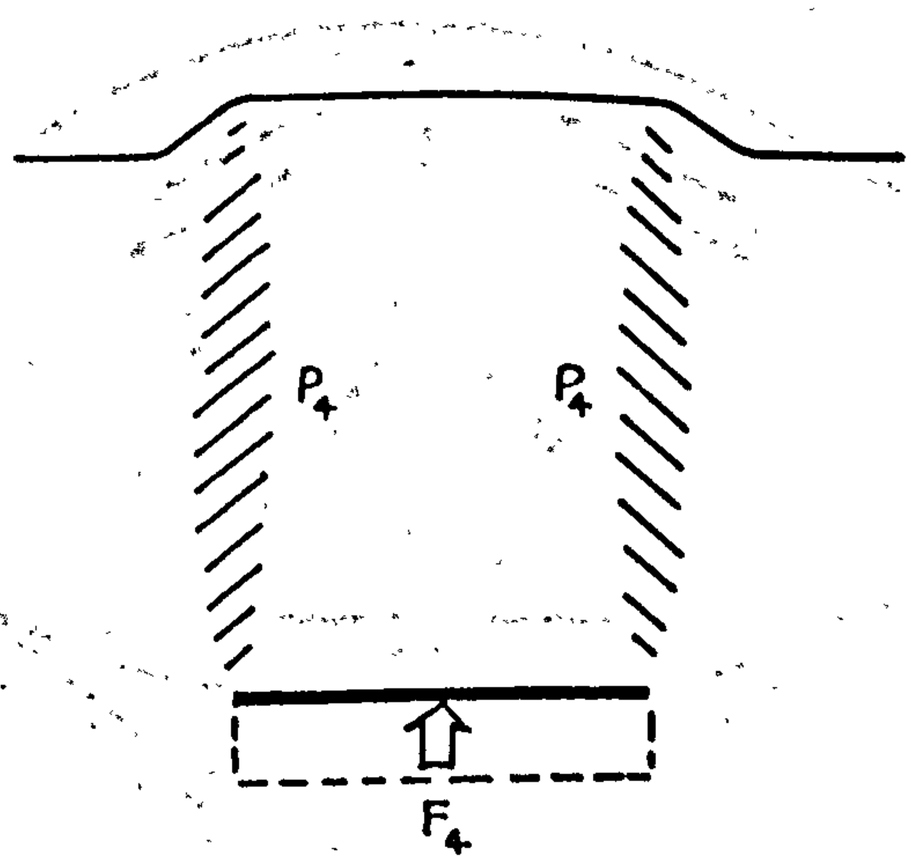

(d)

FIG. 6.3. SHALLOW ANCHOR MODE OF FAILURE PREDICTED BY FINITE ELEMENT METHOD FOR SOILS WITH EQUAL COMPRESSIVE AND TENSILE STRENGTHS IN WHICH NO CRACKING CAN OCCUR

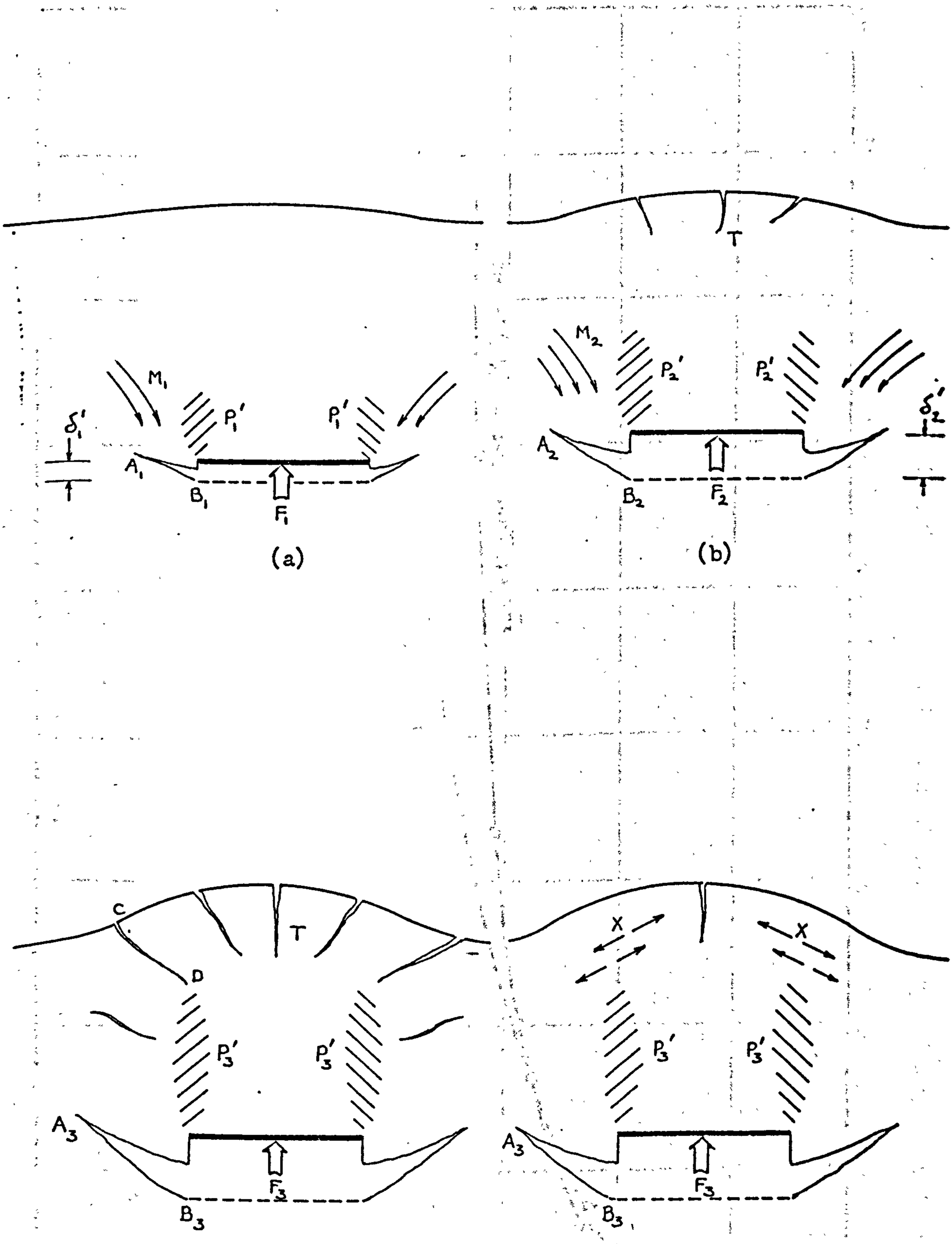

FIG. 6.4. PROPOSED SHALLOW ANCHOR MODE OF FAILURE IN PURELY COHESIVE SOILS WITH RELATIVELY LOW TENSILE STRENGTH IN WHICH CRACKING CAN OCCUR

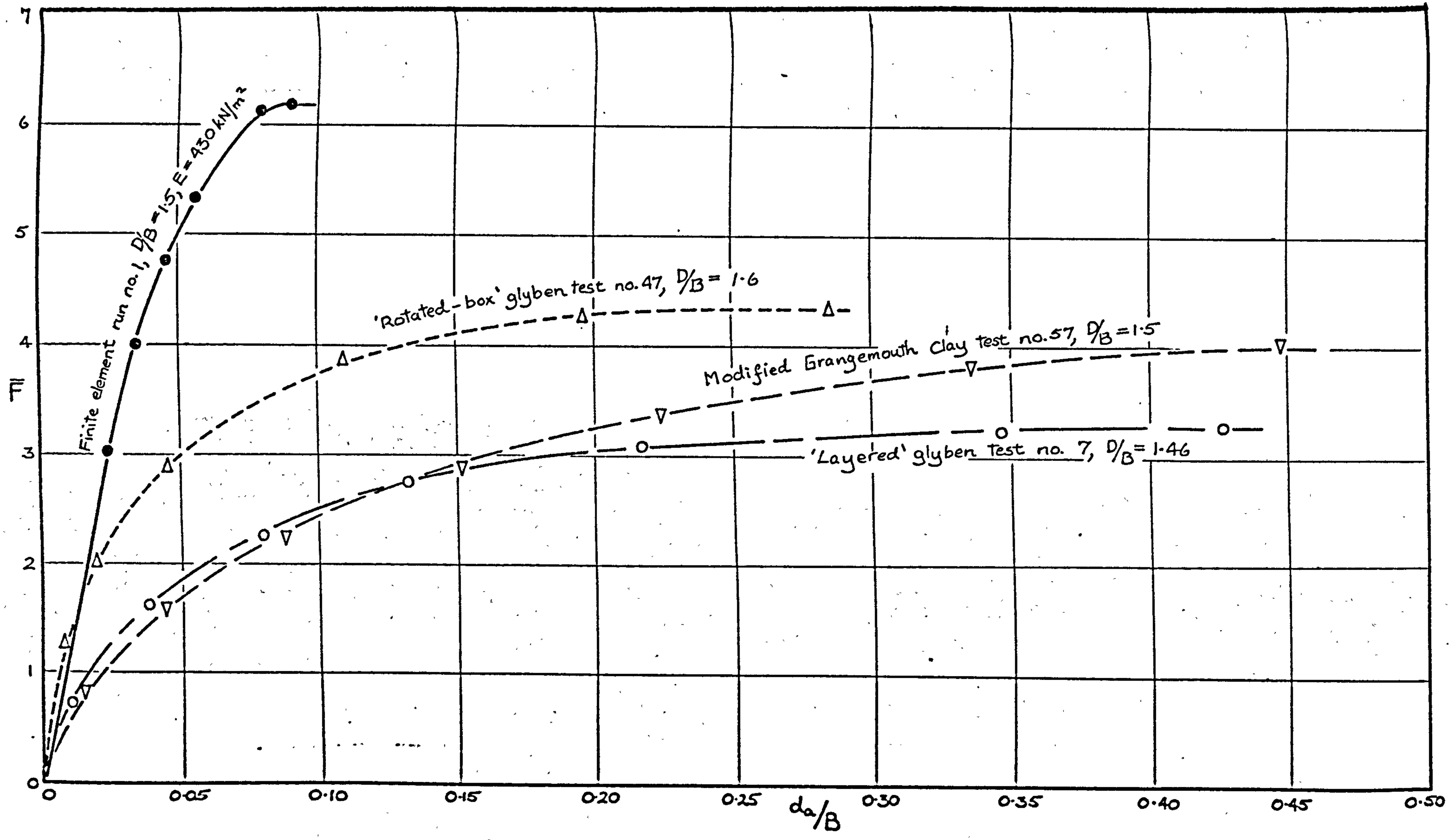

FIG. 6.5. F VERSUS d_a/B FOR SHALLOW ANCHOR MODEL TESTS AND FINITE ELEMENT RUN No. 1

FIG. 6.6. ANALOGY OF LOOSE AND GLUED CARDS TO SIMULATE "LAYERED" AND "NON-LAYERED" GLYBEN RESPECTIVELY

(a) LOOSE CARDS--"LAYERED" GLYBEN

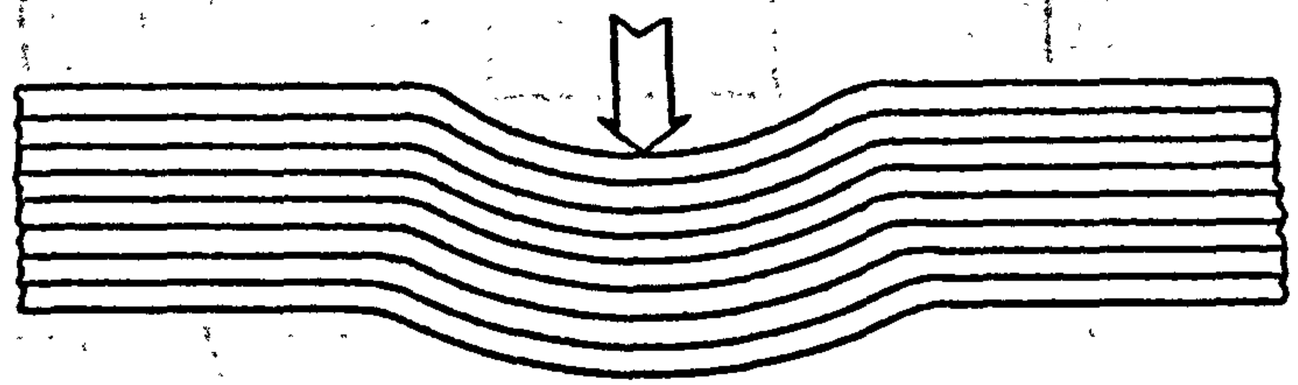

(b) GLUED CARDS--"NON-LAYERED" GLYBEN

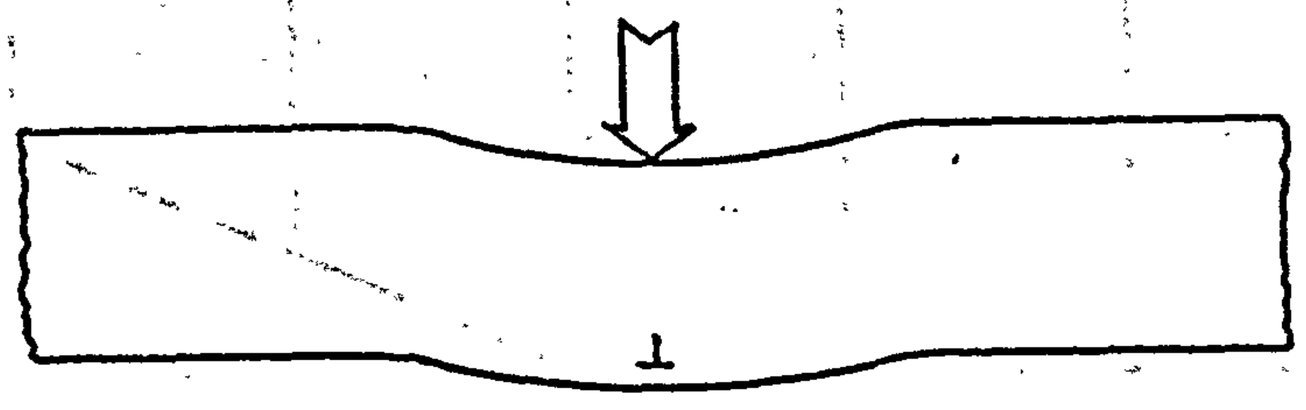

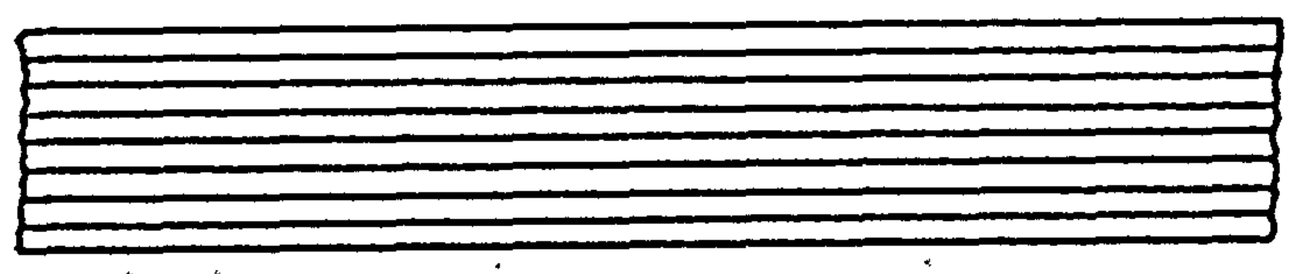

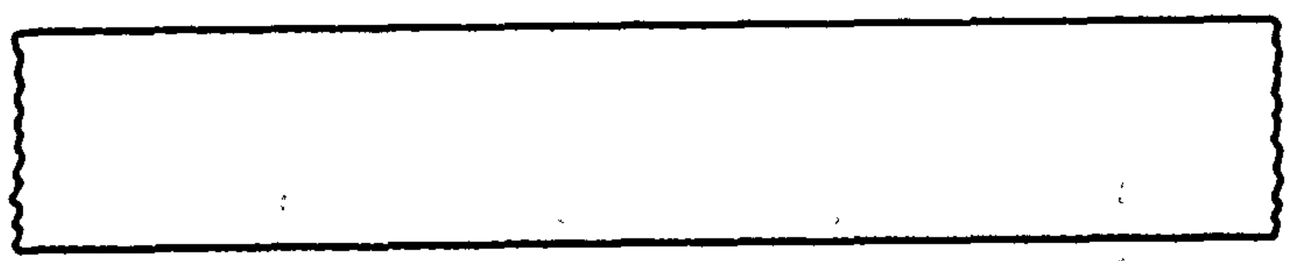

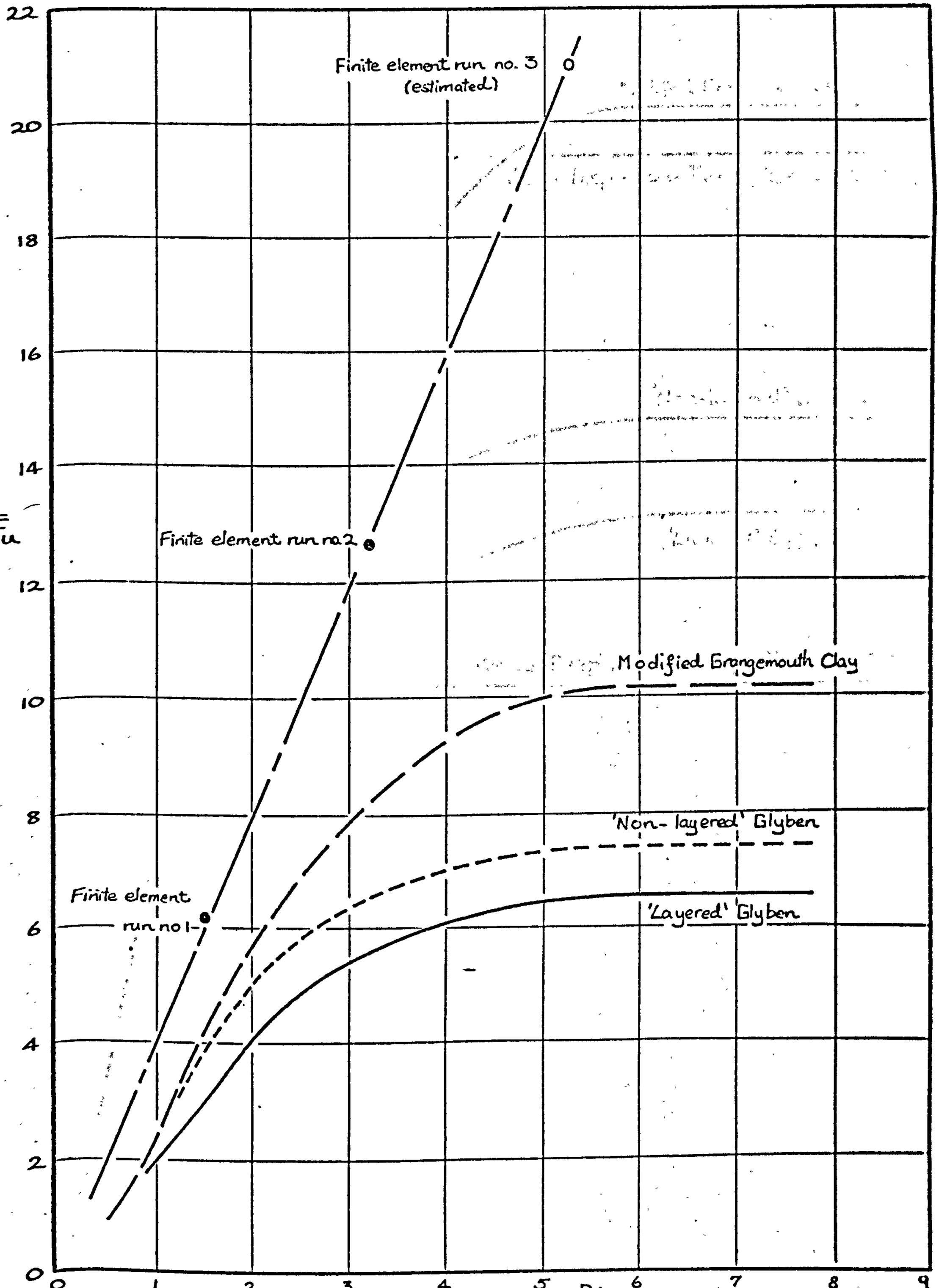

FIG. 6.7. BEST-FITTING CURVES OF $\bar{F}_u$ V D/B FROM RESULTS OF LABORATORY MODEL TESTS AND FINITE ELEMENT ANALYSIS

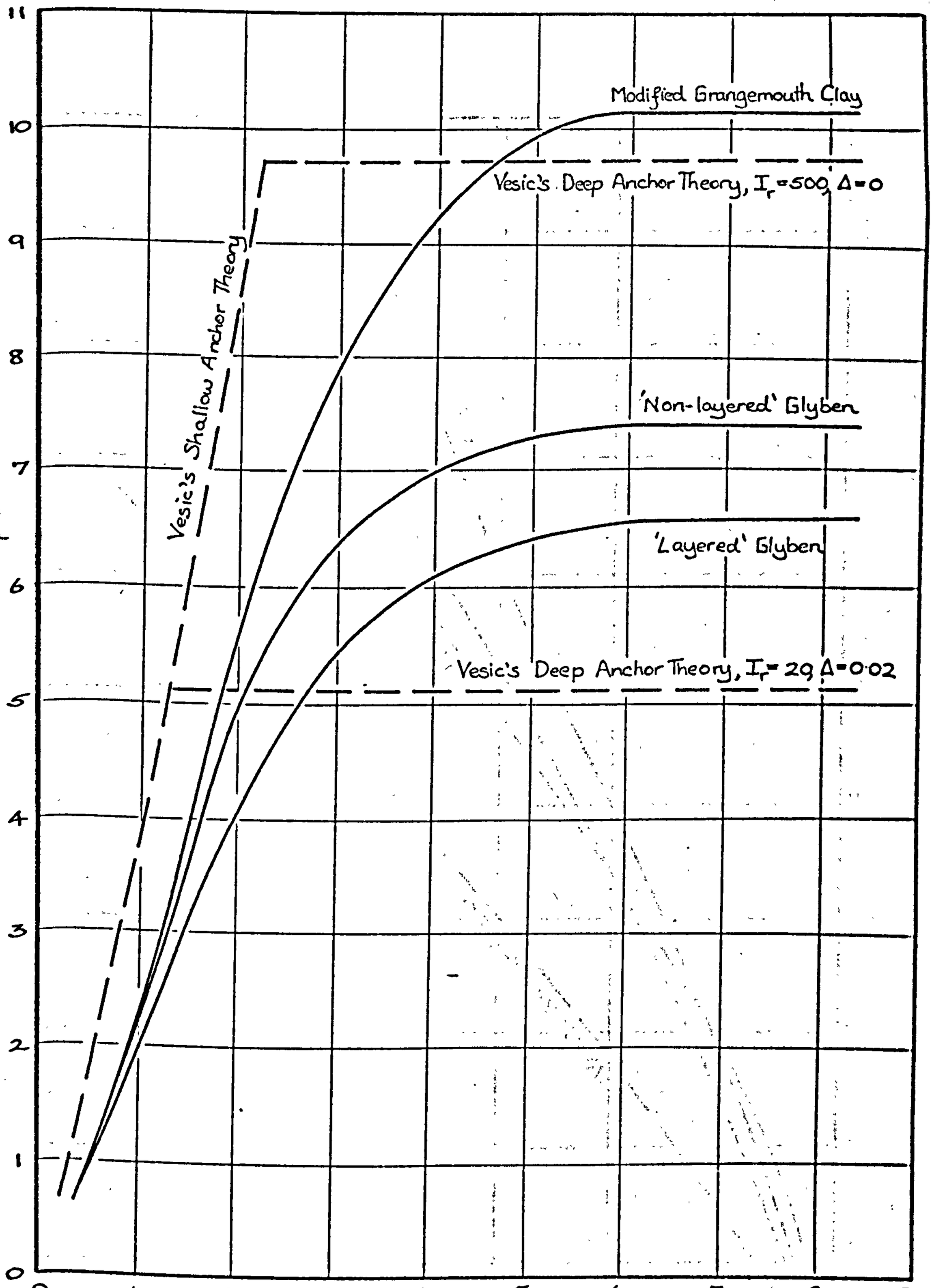

FIG. 6.8. BEST FITTING CURVES OF $\bar{F}_c$ V D/B FROM LABORATORY MODEL TESTS BY THE AUTHOR AND CURVES PREDICTED BY VESIC'S SHALLOW AND DEEP ANCHOR THEORIES

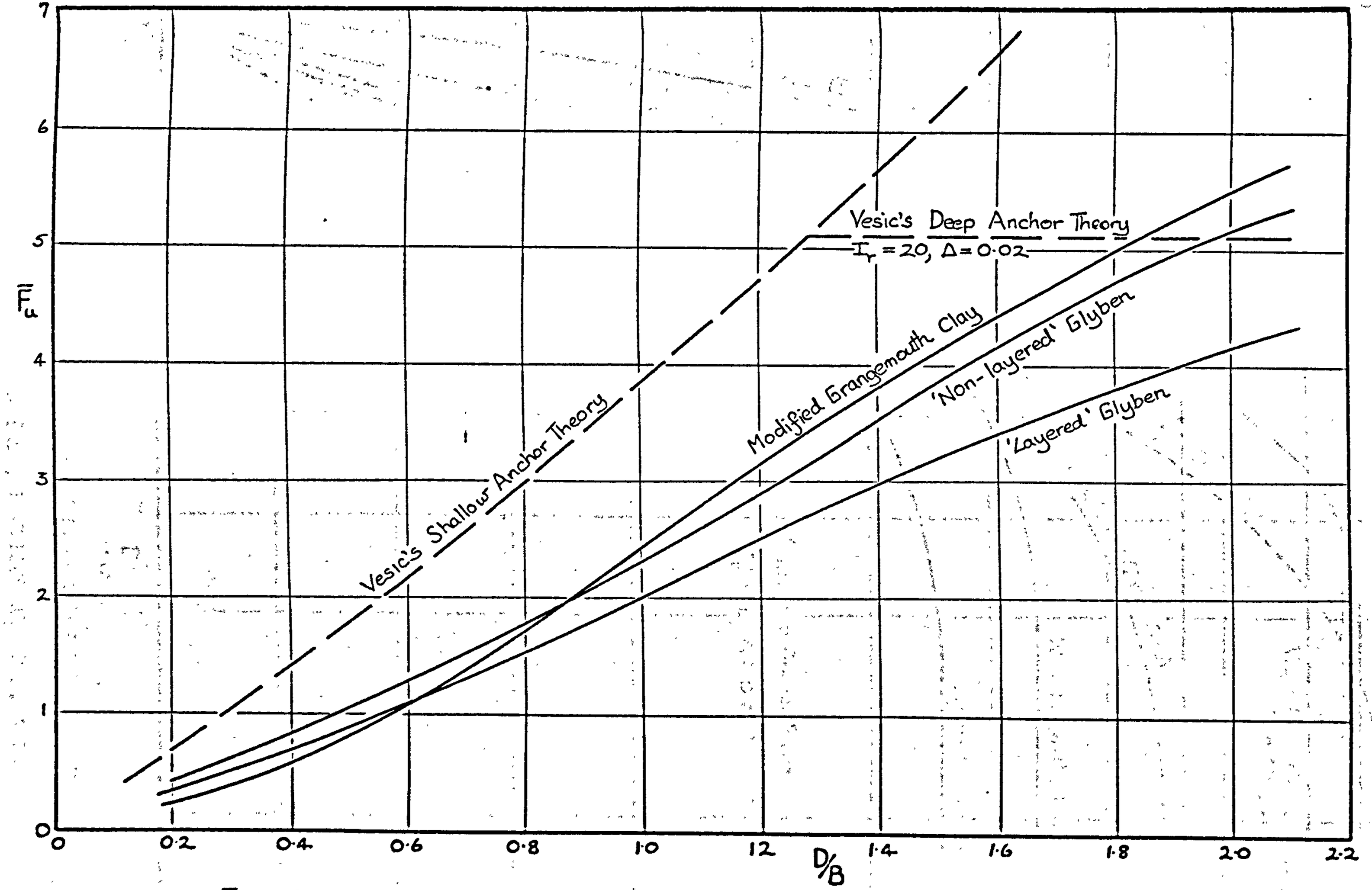

FIG. 6.9. $\bar{F}_u$ V D/B CURVES FROM MODEL TESTS BY AUTHOR AND VESIC'S THEORIES (SHALLOW ANCHOR D/B RANGE)

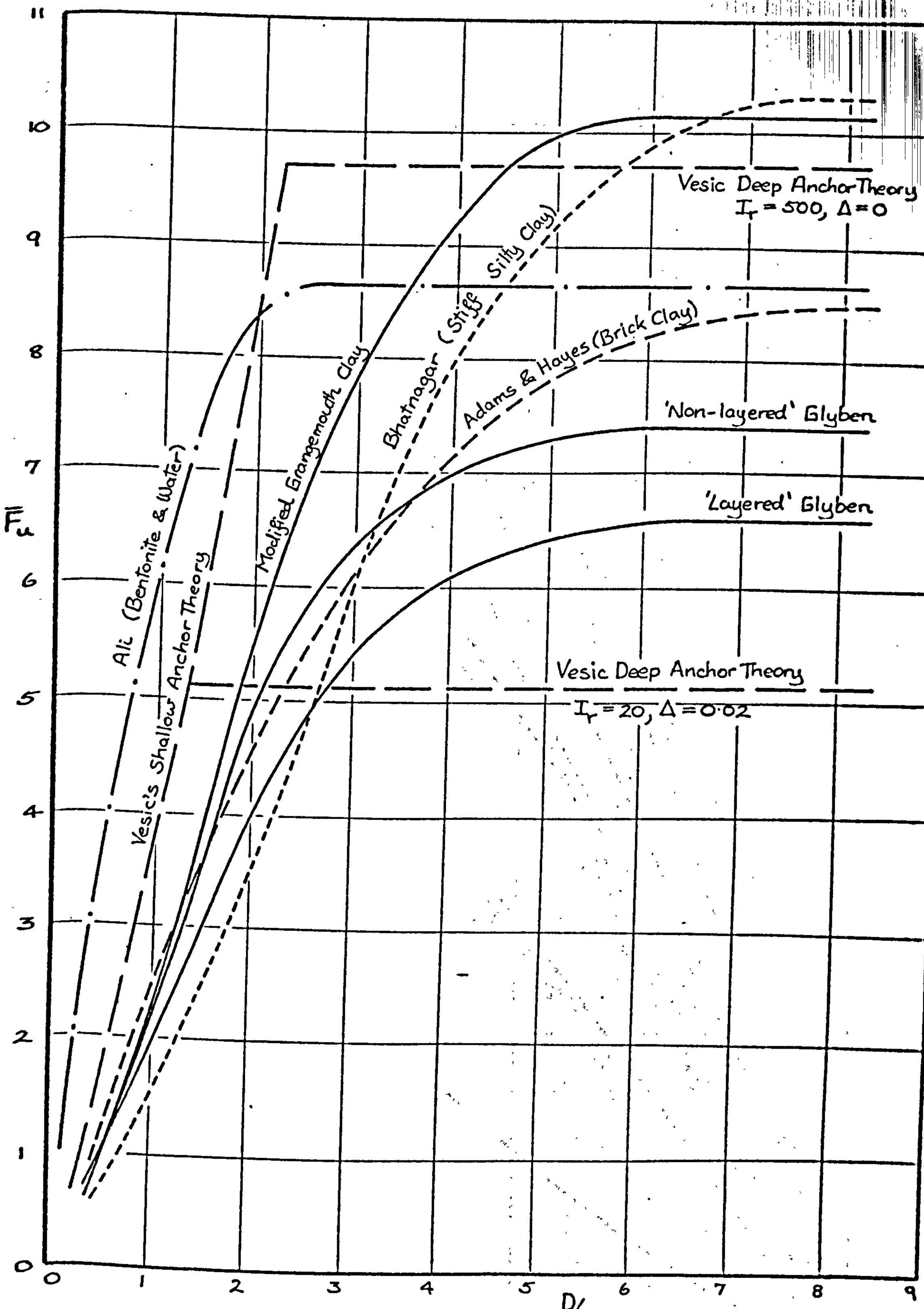

FIG. 6.10. $\bar{F}_u$ V D/B CURVES FROM LABORATORY MODEL TESTS BY THE AUTHOR, PREVIOUS AUTHORS, AND VESIC'S SHALLOW AND DEEP ANCHOR THEORIES

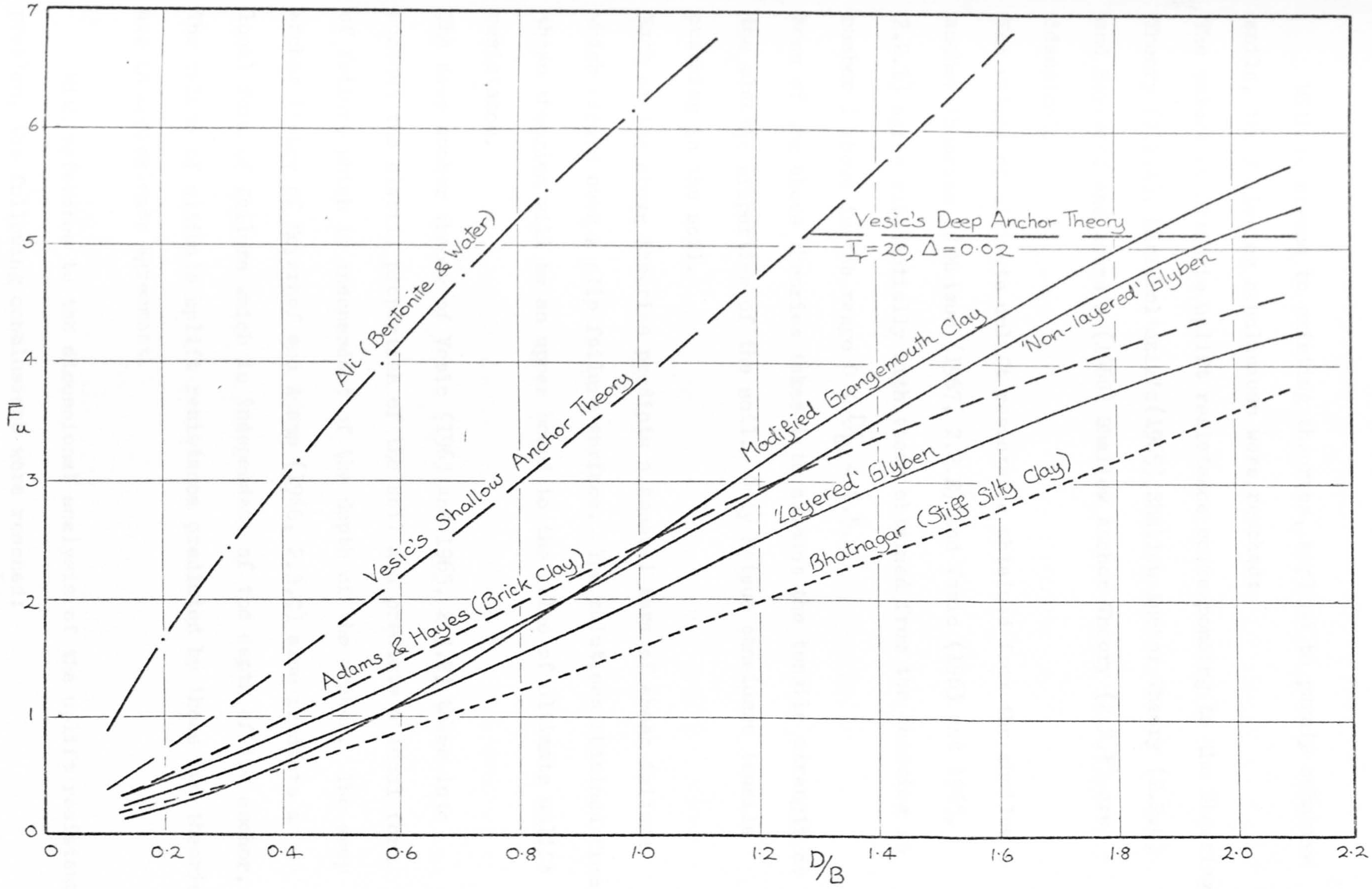

FIG. 6.11. SHALLOW ANCHOR $\bar{F}_u$ V D/B CURVES FROM MODEL TESTS BY AUTHOR, PREVIOUS AUTHORS, AND VESIC'S THEORIES

CHAPTER SEVEN

CONCLUSIONS

With reference to existing theories, applied to purely cohesive soils, the following conclusions were reached:

1. The values of ultimate uplift resistance corresponding to the Shearing Theory (2.2.A), Mariupol'skii's(1965) Shallow Anchor Theory (2.2.C) and Meyerhof and Adams's (1968) Shallow Anchor Theory (2.2.F) are identical.
2. The values of ultimate uplift resistance obtained from the shallow anchor theories of Matsuo (1967, 2.2.E) and Vesic (1963 and 1965, 2.2.D) agree substantially with those obtained from the theories in number 1 above in the range $0 < D/B < 2.5$.
3. None of the above theories takes into account the tensile strength or the elastic properties of the soil. Only Matsuo considers tensile cracking in the soil.
4. Each of the above theories predicts a general form of shear failure which occurs over a slip failure surface. The solutions obtained from these theories will be an upper bound to the value of ultimate uplift resistance.
5. The deep anchor theory of Vesic (1963 and 1965, 2.3.B) takes into account the elastic properties of the soil and predicts a local form of failure which is independent of the depth of the anchor. The deep anchor theory of Meyerhof and Adams (1968, 2.3.C) also predicts a local form of failure which is independent of the depth of the anchor. The values of ultimate uplift resistance predicted by these two theories are in approximate agreement.

With reference to the dimensional analysis of the uplift resistance problem, the following conclusions were reached:

1. The value of the uplift resistance of a purely cohesive soil is depen-

dent primarily upon the elastic properties of the soil, the shear strength of the soil, the tensile strength of the soil, the unit weight of the soil, the plastic volumetric strain of the soil, the adhesion between the soil and the anchor plate, the depth of placement and the diameter of the anchor plate and the diameter of the box (if any) in which the uplift resistance test is performed.

2. The contribution of soil weight to the total value of ultimate uplift resistance is high, according to Vesic's theories, in prototype uplift resistance situations in which:

   (a) a large diameter shallow anchor is employed in soft, purely cohesive soils;

   (b) a very deep anchor is employed in soft, purely cohesive soil.

3. If the prototype anchor described in 2(a) above is modelled using the prototype soil without a centrifuge and if the prototype ultimate uplift resistance pressure is assumed to be the value measured in the model, an underestimation of the prototype ultimate uplift resistance pressure of as much as 50% can occur, according to Vesic's Shallow Anchor Theory. If the prototype anchor described in 2(b) above is modelled using the prototype soil without a centrifuge and the same assumptions are made about the ultimate uplift resistance pressure as for anchor (a), then an underestimation of the prototype ultimate uplift resistance pressure of over 100% can occur, according to Vesic's Deep Anchor Theory.

4. Without the use of a centrifuge, it is impossible to construct uplift resistance models, at normal model scales, which possess dimensional similarity to the prototype for the categories of prototype anchor in which:

   (a) the $c/\gamma_g B$ value of the shallow anchor is less than the order of 0.7;

   (b) the $c/\gamma_g D$ value of the deep anchor is less than the order of 0.28.

With reference to the laboratory model uplift resistance tests conducted in bentonite and glycerine (glyben) and modified Grangemouth clay (clay from the Grangemouth area mixed with Fayles Blue clay), the following conclusions were reached:

1. An apparatus has been designed and constructed in which pullout and pushout model uplift resistance tests can be performed with load-controlled or displacement-controlled loading. The surface displacements of the samples, the anchor displacements, and the anchor loading can be measured electronically at any stage of the test. Coloured strips can be inserted into the sample during preparation and the sample can be split open after the completion of the test.

2. No significant difference exists between the results of pullout and pushout tests in glyben. The results of the load-controlled tests in glyben are similar to the results of equivalent displacement-controlled tests up to approximately one half of the value of ultimate uplift resistance. Beyond this value, the effects of creep become apparent in the load-controlled tests.

3. The initial height of the anchor plate above the base of the box has no significant effect on the results of the tests.

4. In tests in which the suction effect beneath the anchor is not eliminated, a higher value of ultimate uplift resistance is obtained and the mechanism of ultimate failure is different.

5. The results of the tests indicate three distinct categories of anchor depth to breadth (D/B) ratios:

   (a) shallow anchor tests with $0 \leq D/B \leq 2$;

   (b) intermediate depth of anchor tests with $2 < D/B < 5$; and

   (c) deep anchor tests with $D/B \geq 5$.

6. For shallow anchor tests:

   (a) the anchor displacement ratio to ninety percent of ultimate uplift resistance, the value of ultimate uplift resistance, and the ratio of sample surface displacement to anchor displacement are

linearly related to the depth to breadth ratio of the anchor, due to the mechanism of general failure which occurs in the material;

(b) the diameter of the bulge which forms on the surface of the sample due to anchor displacement is of the order of 1.75(for D/B = 0.5) to 2.5 (for D/B = 4.0) times the diameter of the anchor plate;

(c) a mode of ultimate failure is proposed which comprises a combination of yielding above the anchor and in its vicinity due to excess shear and tensile stresses in the material, and tensile cracking of the material;

(d) the amount of anchor displacement to ultimate uplift resistance is a function of the elastic properties of the soil and the bonding between the compacted layers of the soil, as well as a function of the depth to breadth ratio of the anchor;

(e) the values of ultimate uplift resistance of the glyben and the modified Grangemouth clay are between 51 and 67 percent of the values predicted by Vesic's (1963 and 1965) Shallow Anchor Theory, due to the difference between the mechanism of failure predicted by Vesic and the mechanism of failure which occurred in the model tests;

(f) the values of ultimate uplift resistance of the glyben and the modified Grangemouth clay are in good agreement with the results obtained by Adams and Hayes (1967) from model tests in brick clay, but are higher than those obtained by Bhatnagar (1969) from model tests in stiff silty clay and considerably lower than those obtained by Ali (1968) from model tests in bentonite and water.

7. For the deep anchor tests:

(a) the anchor displacement ratio to ninety percent of ultimate uplift resistance and the value of ultimate uplift resistance are approximately constant, due to the mechanism of local failure

which occurs in the material;

(b) the ratio of sample surface displacement to anchor displacement tends to zero with increasing anchor depth;

(c) the amount of anchor displacement to ultimate uplift resistance is a function of the elastic properties of the soil and the bonding between the compacted layers of the soil;

(d) the values of ultimate uplift resistance of the soil predicted by Vesic's (1963 and 1965) Deep Anchor Theory are in reasonable agreement with the results obtained from the deep anchor model tests in glyben.

(e) the values of ultimate uplift resistance of modified Grangemouth clay are higher than the values which were obtained for glyben and higher than the values predicted by Vesic's Deep Anchor Theory. It is proposed that some dissipation of the porewater in the clay occurred during the tests in modified Grangemouth clay and that the resulting consolidation and consequent increase in the strength of the clay in the vicinity of the anchor increased the value of ultimate uplift resistance. The values of ultimate uplift resistance for modified Grangemouth clay are in good agreement with the values obtained by Bhatnagar (1969) from deep anchor model tests in stiff silty clay and it is proposed that some consolidation of the clay in the vicinity of the anchor plate also occurred in Bhatnagar's tests.

8. For tests at an intermediate depth, the anchor displacement ratio to ninety percent of ultimate uplift resistance, the value of ultimate uplift resistance, and the ratio of sample surface displacement to anchor displacement vary in a non-linear manner with the depth to breadth ratio of the anchor. The mechanism of ultimate failure in tests at an intermediate depth is a combination of the general failure mechanism proposed for shallow anchor tests and the local failure mechanism which was found in deep anchor tests.

With reference to the axi-symmetric, iterative, elastic-plastic finite element analysis of the rigid-anchor uplift resistance problem, the following conclusions were reached:

1. The accuracy of the results of the finite element analysis are limited primarily by:
   (a) the assumption of small element strains inherent in the derivation of element stiffnesses;
   (b) the assumption of the original mesh geometry at each successive load increment;
   (c) the assumption of a linear elastic, non-strain hardening plastic material stress-strain curve;
   (d) the assumption of a "non-cracking" material with equal values of tensile and compressive strengths.
2. Within the limitations of the assumptions stated in number 1 above, the finite element analysis can determine:
   (a) the order in which the elements in the mesh yield plastically up to general failure;
   (b) a relationship between the uplift resistance and anchor displacement up to general failure of materials whose values of elastic modulus are high (giving correspondingly low values of element strain);
   (c) the radial and vertical nodal displacements corresponding to any value of anchor displacement at small element strains up to general failure;
   (d) the magnitude and direction of the principal stresses and maximum shear stress in each element corresponding to any value of anchor displacement at small element strains up to general failure;
   (e) the magnitude and distribution of the vertical and radial normal stresses and the shear stresses throughout the mesh corresponding to any value of anchor displacement at small element strains up to general failure.

FUTURE WORK

The following recommendations are made for future work:

1. Model tests by the author have shown that the effect of suction below the anchor plate increases the amount of load to cause ultimate failure of the soil. This suction effect will in general be relevant in the case of high-mast footings in saturated clays although there will be no suction effect in the jacking-out situation. Further model tests in purely cohesive soils could be carried out to examine fully the effect of suction below the anchor plate.

2. The finite element program could be further developed in order to:
   (a) simulate actual stress-ctrain curves for soil in both compression and tension;
   (b) take into account cracking in the soil;
   (c) predict local tyres of failure in the soil.

3. Future finite element programs runs could be used to examine:
   (a) the effect of varying values of Poisson's ratio on the program results;
   (b) the effect of the roughness of the anchor on the program results.

REFERENCES

ADAMS, J.I. and HAYES, D.C. (1967)

"The uplift capacity of shallow foundations"
Ontario Hydro Research Quarterly 19, 1

ALI, M.S. (1968)

"Pullout resistance of anchor plates and anchor piles in soft bentonite clay"
M.S. Thesis, Duke University, Duke Soil Mech. Series no. 17

ASHBEE, R.A. (1969)

"A uni-axial analysis for use in uplift foundation calculations"
Lab.Report no. RD/L/R 1608, CERL, Leatherhead, England

BALLA, A. (1961)

"The resistance to breaking-out of mushroom foundations for pylons"
Proc. 5th Int. Conf. Soil Mech. Found.Engrg., Paris, Vol. 1, pp 569-576

BARKSDALE, R.D. (1963)

"Small-scale cratering tests"
Georgia Inst. of Technology, Atlanta, Georgia

BHATNAGAR, R.S. (1969)

"Pullout resistance of anchors in silty clay"
M.S. Thesis, Duke University, Duke Soil Mech. Series no. 18

BISHOP, A.W. and HENKEL, D.J. (1957)

"The measurement of soil properties in the triaxial test"
Edward Arnold Ltd., London

BISHOP, R.F., HILL, R., and MOTT, N.F. (1945)

"The theory of indentation and hardness tests"
Proc. of Physical Soc. London, 57/3, pp 147-159

BRINCH-HANSEN, J. (1953)

"Earth pressure calculation"
Danish Technical Press, Copenhagen

BURLAND, J.B., and ROSCOE, K.H. (1969)

"Local strains and pore pressures in a normally consolidated clay layer during one-dimensional consolidation"
Geotechnique, Vol. 19, no. 3, pp 335-356.

ESQUIVEL-DIAZ, R.F. (1967)

"Pullout resistance of deeply buried anchors in sand"
M.S. Thesis, Duke University, Duke Soil Mech.Series no. 8

FRASER, R.A. (1971)

"Applications of the finite element method in soil mechanics"
M.Sc. Thesis, University of Manchester

HANNA, T.H., SPARKS, R. and YILMAZ, M. (1972)

"Anchor behaviour in sand"
Journal of Soil Mech. and Found. Div., Proc.ASCE, Vol.98, no. SM 11

IRWIN, M.J. (1968)

"Automatic data-recording for the laboratory consolidation test"
MOT, RRL Report LR 188, Crowthorne, England

KOPAL, I.Z. (1961)

"Numerical Analysis"
Second Ed., Chapman and Hall

MARIUPOL'SKII, L.G. (1965)

"The bearing capacity of anchor foundations"
Soil Mech. and Found. Eng. no. 1, Consultants Bureau, pp 26-32

MATSUO, M. (1967)

"Study on the uplift resistance of footings (1)"
Soil and Foundation, Vol. 7, no. 4

MAYFIELD, B. (1963)

"The performance of a rigid wheel moving in a circular path through clay"
Ph.D. Thesis, University of Nottingham

MEYERHOF, G.G. (1951)

"The ultimate bearing capacity of foundations"
Geotechnique, Vol. 2, pp 301-332

MEYERHOF, G.G. and ADAMS, J.I. (1968)

"The ultimate uplift capacity of foundations"
Canadian Geot. Journal, Vol. 5, no. 4, pp 225-244

SUTHERLAND, H.B. (1965)

"Model studies for shaft raising through cohesionless soils"
Proc. 6th Int. Conf. Soil Mech.Found.Engrg.,Montreal 1965, Vol. 2, pp 410-413

VESIC, A.S. (1963)

"Theoretical studies of cratering mechanisms affecting the stability of cratered slopes"
Georgia Inst. of Technology, Atlanta, Georgia

VESIC, A.S., WILSON, W.E., CLOUGH, G.W. and TAI, TEIN-LIE (1965)

"Theoretical studies of cratering mechanisms affecting the stability of cratered slopes, II"
Georgia Inst. of Technology, Atlanta, Georgia

VESIC, A.S. (1969)

"Breakout resistance of objects embedded in the ocean bottom"
Duke University, Soil Mech. Series no. 20

YAMADA, Y., YOSHIMURA, N. and SAKURAI, T. (1968)

"Plastic stress-strain matrix and its application for the solution of elastic-plastic problems by the finite element method"

Int. Journal Mech.Sci., Vol. 10, pp 343-354

ZIENKIEWICZ, O.C., VALLIAPPAN, S. and KING, I.P. (1969)

"Elasto-plastic solutions of engineering problems, 'initial stress', finite element approach"

Int. Journal Numerical Methods in Engrg., Vol. 1, pp 75-100

APPENDIX A

DERIVATION OF CURVES ILLUSTRATING THE EFFECTS OF SOIL WEIGHT ON THE TOTAL ULTIMATE UPLIFT RESISTANCE PREDICTED BY VESIC'S (1963 and 1965) SHALLOW AND DEEP ANCHOR THEORIES

A.1. Vesic's Shallow Anchor Theory (2.2.D)

The value of $p_u/\gamma_g D$ predicted by Vesic's Shallow Anchor Theory for purely cohesive soils was given in Table 2.1:

$$p_u/\gamma_g D = (c/\gamma_g D) F_c + F_q + B/3D \quad \cdots (A.1)$$

$$= (c/\gamma_g B \cdot B/D) F_c + F_q + B/3D \quad \cdots (A.1A)$$

From the derivation of Vesic's equation, it is known that, in a purely cohesive soil, the factor F_q is a function of the weight of the soil contained within the slip failure surface, excluding the weight of soil contained in the hemisphere of diameter equal to the anchor plate above the anchor plate. $B/3D$ is a function of the weight of soil contained in that hemisphere. The factor F_c is a function of the area of the slip failure surface and consequently a function of D/B .

From Vesic (1965): when $D/B = 0.5$ and $\phi = 0$, then $F_c = 1.76$ and $F_q = 0.33$

Therefore, $p_u/\gamma_g D = \frac{1.76}{0.5} c/\gamma_g B + 0.33 + 0.67$

$$= 3.52\, c/\gamma_g B + 1 \quad \cdots (A.2A)$$

When $D/B = 1.5$ and $\phi = 0$, then $F_c = 6.12$ and $F_q = 0.78$.

Therefore,

$$p_u/\gamma_g D = \frac{6.12}{1.5} c/\gamma_g B + 0.78 + 0.22$$

$$= 4.08\, c/\gamma_g B + 1 \quad \cdots (A.2B)$$

In equations A.2, the value 1 represents the effect of the unit weight of the soil on the value of $h_u/\gamma_g D$ and the terms 3.52 $c/\gamma_g B$ and 4.08 $c/\gamma_g B$ represent the effect of the soil cohesion on the value of $h_u/\gamma_g D$. Thus, in order to calculate the percentage contribution of soil weight to the total ultimate uplift resistance as a function of $c/\gamma_g B$, as shown in Fig.3.1, the following equations were used:

percentage contribution of soil weight to total ultimate uplift resistance ($D/B = 0.5$) = $\frac{100\ \%}{3.52\ c/\gamma_g B + 1}$ ..(A.3A)

percentage contribution of soil weight to total ultimate uplift resistance ($D/B = 1.5$) = $\frac{100\ \%}{4.08\ c/\gamma_g B + 1}$ ..(A.3B)

A.2. Vesic's Deep Anchor Theory (2.3.B)

The value of $h_u/\gamma_g D$ predicted by Vesic's Deep Anchor Theory for purely cohesive soils was given in Table 2.2:

$$h_u/\gamma_g D = c/\gamma_g D\ (\bar{F}_c + 1) + \bar{F}_q \qquad \cdots\cdot(A.4)$$

In a purely cohesive soil, the factor $\bar{F}_q$ is a function of the weight of the soil above the anchor plate. The factor $\bar{F}_c$ is a function of the elastic and cohesive properties of the soil and the value 1 in equation A.4 represents the effect of cohesion on the wedge of soil which the theory predicts will be formed above the anchor plate.

From Vesic (1963 and 1965): when $I_r = 20$, $\Delta = 0.02$ and $\phi = 0$, then $\bar{F}_c = 4.1$ and $\bar{F}_q = 1.0$.

Therefore, $h_u/\gamma_g D = 5.1\ c/\gamma_g D + 1$ $\cdots\cdot(A.5A)$

when $I_r = 500$, $\Delta = 0.0$ and $\phi = 0$, then $\bar{F}_c = 8.7$ and $\bar{F}_q = 1.0$.

Therefore, $h_u/\gamma_g D = 9.7\ c/\gamma_g D + 1$ $\cdots\cdot(A.5B)$

In equations A.5, the value 1 represents the effect of the unit weight of the soil on the value of $h_u/\gamma_g D$ and 5.1 $c/\gamma_g D$ and 9.7 $c/\gamma_g D$ represent the effect of the soil cohesion on the value of $h_u/\gamma_g D$.

Thus, in order to calculate the percentage contribution of soil weight to the total ultimate uplift resistance as a function of $c/\gamma_g D$,

as shown in Fig. 3.2, the following equations were used:

percentage contribution of soil weight to total ultimate uplift resistance

$$\left(\begin{array}{l} I_r = 20, \\ \Delta = 0.02 \end{array}\right) = \frac{100\%}{5.1\,c/\gamma_g D + 1} \quad ..(A.6A)$$

percentage contribution of soil weight to total ultimate uplift resistance

$$\left(\begin{array}{l} I_r = 500 \\ \Delta = 0.0 \end{array}\right) = \frac{100\%}{9.7\,c/\gamma_g D + 1} \quad ..(A.6B)$$

APPENDIX B

DETAILS OF ELECTRICAL AND ELECTRONIC EQUIPMENT AND SUPPLIERS OF SOILS USED IN THE UPLIFT RESISTANCE MODEL TESTS

B.1. Details of Motor, Gearbox and Converter used in the Displacement-Controlled Uplift Resistance Tests

Motor. Hoover Mark IV Motor, single phase, delivering $\frac{1}{4}$ hp at 1425 rpm.
Supplied by Hoover (Electric Motors) Ltd.

Gearbox. Radicon Gearbox, reduction ratio 60:1.
Supplied by David Brown Industries Ltd.

Converter. Produced 1 mm vertical displacement per 15.6 revolutions.
Supplied by Wykeham Farrance Engineering Ltd.

B.2. Details of Transducers and Related Power Supplies

Load Cell. Statham Gold Cell with Load Cell Accessories of 5 lb, 20 lb, 100 lb and 500 lb. Input 5 V, output 16 mV/V, non-linearity and hysteresis less than ± 0.25 per cent of full-scale range.
Supplied by Statham Instruments Inc.

Load Cell Power Supply. APT stabilised d.c. power supply, model SCV 10, supplying 5 V d.c..
Supplied by APT Electronic Industries Ltd.

Displacement Transducers. Linear Variable Displacement Transformers, input 24 V d.c., maximum output dependent on size. Linearity ± 0.5 per cent of full-scale range.

Number: 5 to measure displacements up to 25 mm
3 to measure displacements up to 50 mm
1 to measure displacements up to 125 mm.

Supplied by Electro Mechanisms Ltd.

Displacement Transducer Power Supply. Type PS 24D - 12A.
Twelve channels, output 24 V d.c., converted output from transducers into mV range, maximum 200 mV. Had gain control.
Supplied by Electro Mechanisms Ltd.

This type of power supply and displacement transducer was tested by Irwin (1968) at the Road Research Laboratory and found to be generally satisfactory.

B.3. Details of Data-Logging System

Voltmeter and Data Transfer Unit. The output from the transducers was recorded on a Solartron Digital Voltmeter Model LM 1450 and controlled by a Solartron 20 channel Data Transfer Unit.
Supplied by Solartron Electronic Group Ltd.

Printing and Punching Equipment. Data Dynamics Teletype no. 33 unit, incorporating a typewriter printer and eight-hole puncher unit.
Supplied by Westrex Co. Ltd.

B.4. Details of Suppliers of Soils

Fulbent 150. Supplied by:
Fullers' Earth Union Ltd.,
Patteson Court,
Redhill, Surrey.

Fayles Blue Clay. Supplied by:
Pike Bros. Fayle and Co. Ltd.,
Wareham,
Dorset.

APPENDIX C

DETAILS OF MEASUREMENT OF STRENGTH TESTS

C.1. Laboratory Vane Test

The vane testing machine was manufactured by Wykeham Farrance Engineering Ltd. The vane employed was $\frac{1}{2}$ inch (12.7 mm) high by $\frac{1}{2}$ inch (12.7 mm) in diameter, and had four separate vanes. The machine was powered by a small electric motor which rotated the torque spring attached to the vane at approximately 0.06 rpm. By using a vane with an extended shaft, it was possible to perform vane tests on samples in the uplift resistance boxes at any depth and in any position in the box. On average, between six and eight vane tests were conducted in each box prior to testing. Table 4.2 showed the average values of vane shear strength for each batch of clay. The coefficient of variation of the strengths of the six to eight tests per box was in general between 2.5 and 5 percent.

C.2. Triaxial Compression Tests

All of the triaxial tests were conducted on a standard triaxial testing machine manufactured by Wykeham Farrance Engineering Ltd. Each of the samples tested was $1\frac{1}{2}$ inches (38.1 mm) in diameter and 3 inches (76.2 mm) long. To minimise friction between the piston and the bush on the top of the cell, a standard rotating bush was employed. Because of the very low values of strength being measured, a five pound or twenty pound Statham Load Cell was used instead of a proving ring to obtain greater accuracy. It was found that the weight of the piston and attachments could account for a considerable proportion of the total load at failure in the weakest samples, and consequently a universal joint was developed to join the top end of the piston to the load cell in order to prevent the piston resting on the sample before the test commenced. In all of the tests, the rate of strain in the sample being tested was 0.060 mm/mm per minute.

A. Tests in Glyben

Series of triaxial test samples were prepared after approximately every five uplift resistance tests. This resulted in one series of tests on batch no. 1 glyben, three series of tests on batch no. 2 glyben, four series of tests on batch no. 3 glyben and two series of tests on batch no. 4 glyben. Each series of tests consisted of the order of six samples. Table 4.2 showed the average values of undrained shear strength for each batch of glyben. The coefficient of variation of the strengths of the samples in the various series of tests ranged from 7.5 to 15 percent. The "layered" sample blocks were made up in 6 inch (152.4 mm) concrete cube moulds. For batches 2, 3 and 4, the samples were trimmed from the blocks and for batch no. 1 the samples were extruded from thin-walled tubes which had been inserted into the blocks. The "non-layered" sample blocks were prepared in the same manner as the "non-layered" core for the uplift resistance tests. The majority of the triaxial tests were on "layered" samples since the majority of the uplift resistance tests were on "layered" samples.

A separate series of undrained tests in batch no. 2 glyben were also conducted to confirm Mayfield's (1963) findings that glyben was a $\phi = 0$ material under varying values of cell pressure in the undrained condition. The results of this series of tests showed clearly that this was the case. All of the subsequent tests were undrained and conducted at zero cell pressure and without rubber membranes.

B. Tests in Modified Grangemouth Clay

The blocks of modified Grangemouth clay for triaxial tests were prepared by the same method as the "layered" glyben blocks and the samples were trimmed from these blocks. An initial series of undrained tests were conducted to ascertain that the material possessed no internal friction in the undrained condition. The tests were conducted on six samples, two at zero cell pressure, two at a cell pressure of approximately 100 kN/m^2 and two at a cell pressure of approximately

200 kN/m^2. No difference in the strength or manner of yielding of these samples was found.

Two series of undrained tests with six samples in each series were subsequently performed at zero cell pressure and without rubber membranes. Table 4.2 showed the resulting average values of undrained shear strength of the modified Grangemouth clay. The coefficient of variation of the strengths of the samples in both series of tests were of the order of 10%.

C.3. Tension Tests

The tension apparatus developed by the author was simple in concept and was designed to provide values of the unconfined strength of undrained samples of clays in tension. A photograph of the apparatus is shown in Fig. C.1. The samples were tested on a standard Wykeham Farrance triaxial frame at a rate of 0.060 mm/mm per minute, using a five pound Statham Load Cell to measure the load on the samples. A view of a typical sample and its attachments is shown in Fig. C.2. The sample had an average length of 4 inches (101.6 mm) with end diameters of $2\frac{1}{2}$ inches (63.5 mm) and a narrowed central portion of diameter $1\frac{1}{2}$ inches (38.1 mm). Of the 76.2 mm length, the end portions were each 25.4 mm long and the central portion was also 25.4 mm long. The remainder of the length was used in transitions between the differing diameters. The samples were trimmed carefully with a fine wire saw and straight edge on a soil lathe which had been constructed to produce the appropriate shape of sample. Care was taken not to deform the sample during trimming and to ensure that the transitional faces between the wide top and bottom sections and the narrow central section of the sample were well rounded at their top and bottom corners to prevent unnecessary stress concentration. The top end portion of the sample fitted neatly into a thin-walled aluminium cylinder with one closed end, which was attached by a universal joint to a rod connected to the load cell. The base end portion of the

sample fitted into a similar aluminium cylinder which was attached to the base plate of the testing frame. The sample was firmly held inside these aluminium cylinders by split sections of curved aluminium, moulded to the shape of the transitional portions and clamped to the aluminium cylinders by Jubilee Clips, as shown in Fig. C.2. Great care was taken to ensure that the sample was centralised in the loading frame to prevent the creation of bending moments in the sample.

Two samples of batch no. 4 "layered" glyben, two samples of batch no. 4 "non-layered" glyben and two samples of modified Grangemouth clay were tested in the apparatus. Each pair of samples gave consistent results and the values of tensile strength for each type of clay were shown in Table 4.2. The failure planes were always approximately horizontal and always occurred either just above the bottom or just below the top of the narrow portion of the sample, which suggested that some stress concentrations existed in these areas despite attempts to eliminate them by rounding the transition edges. A plan view of the failed cross-sections are shown in photographs in Fig. C.3 and are discussed in chapter 6.

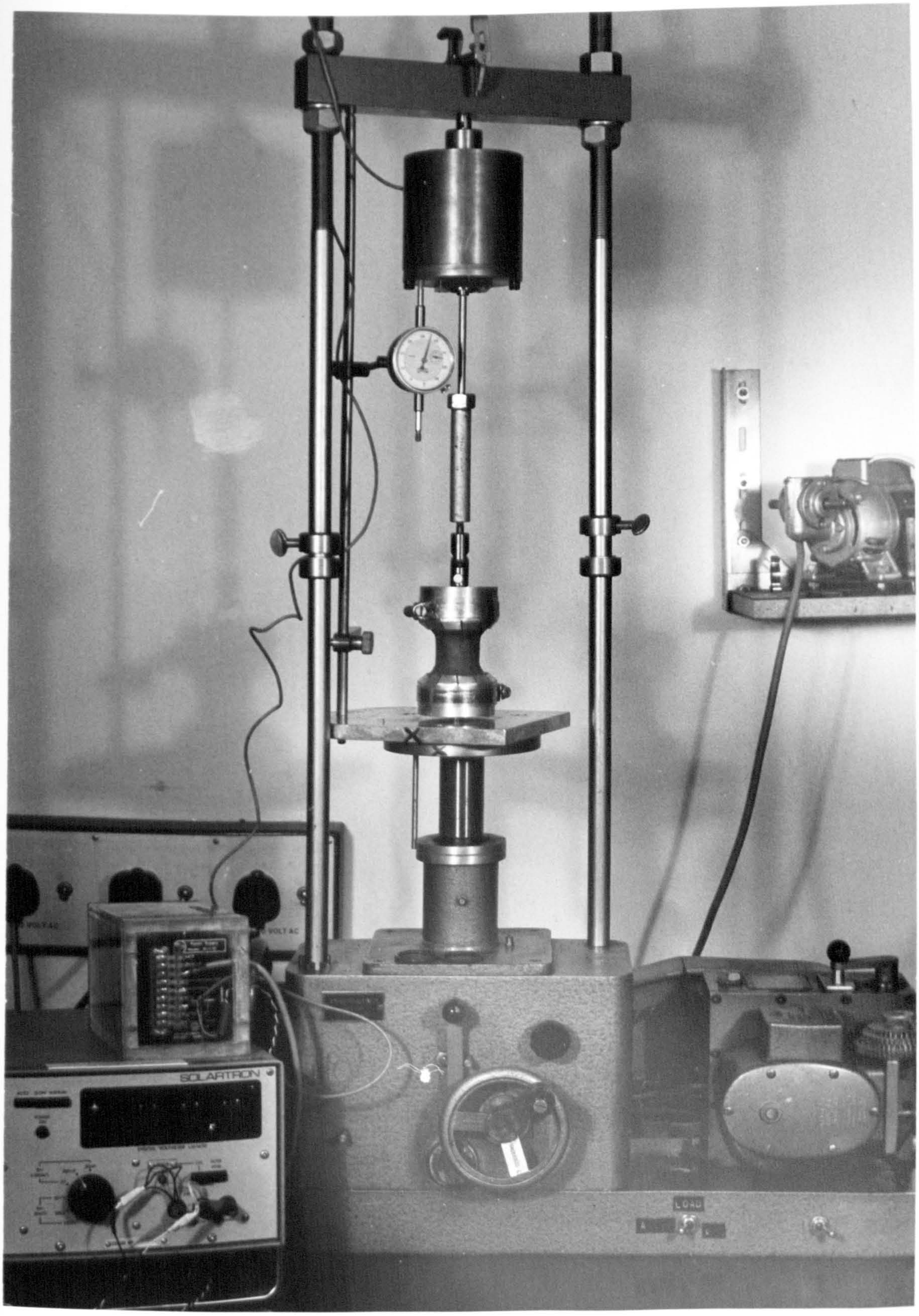

FIG. C.1. TENSION TESTING APPARATUS

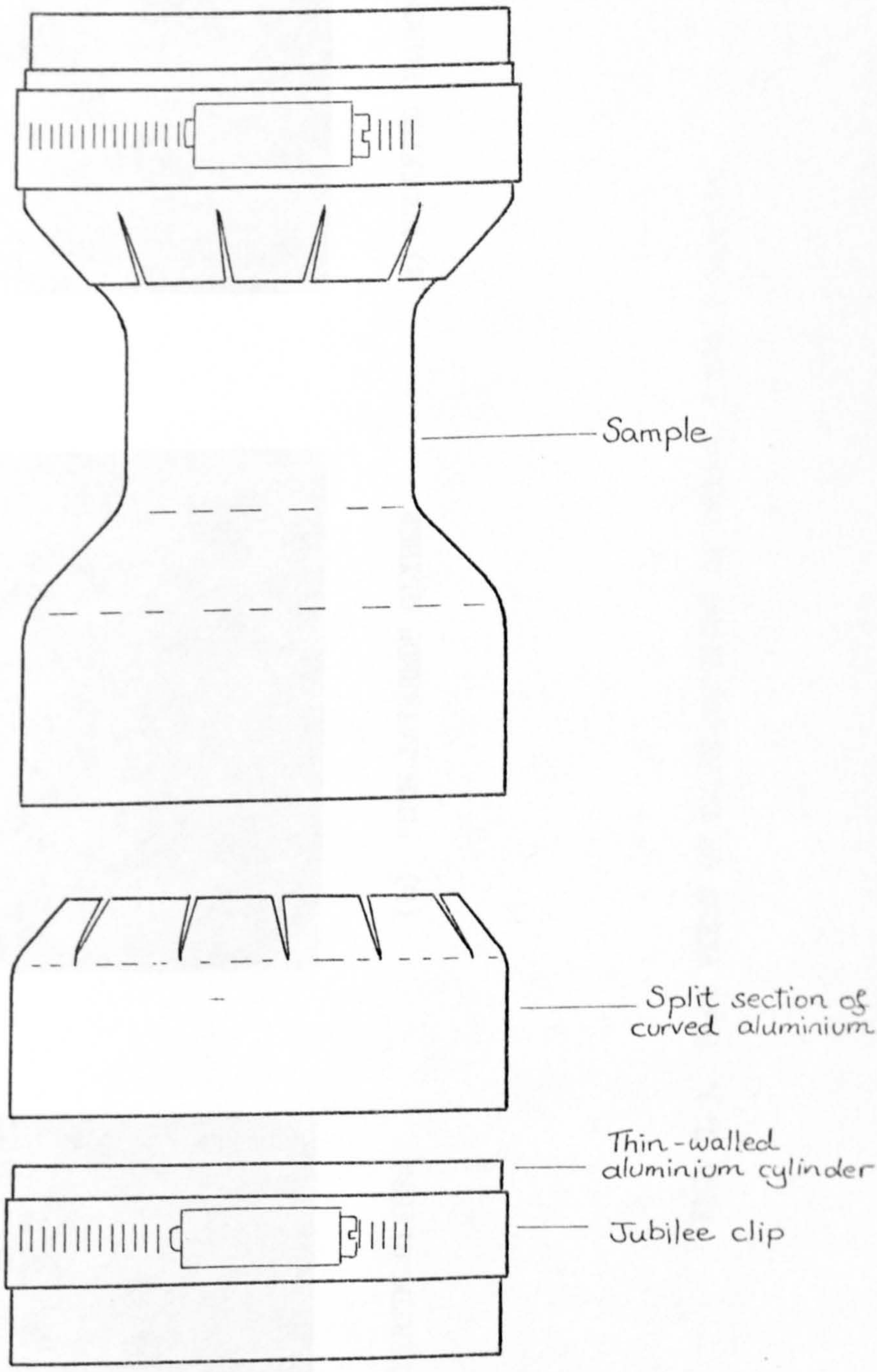

FIG. C.2. VIEW OF TENSILE SAMPLE WITH ATTACHMENTS (TO SCALE)

(a) "LAYERED" GLYBEN

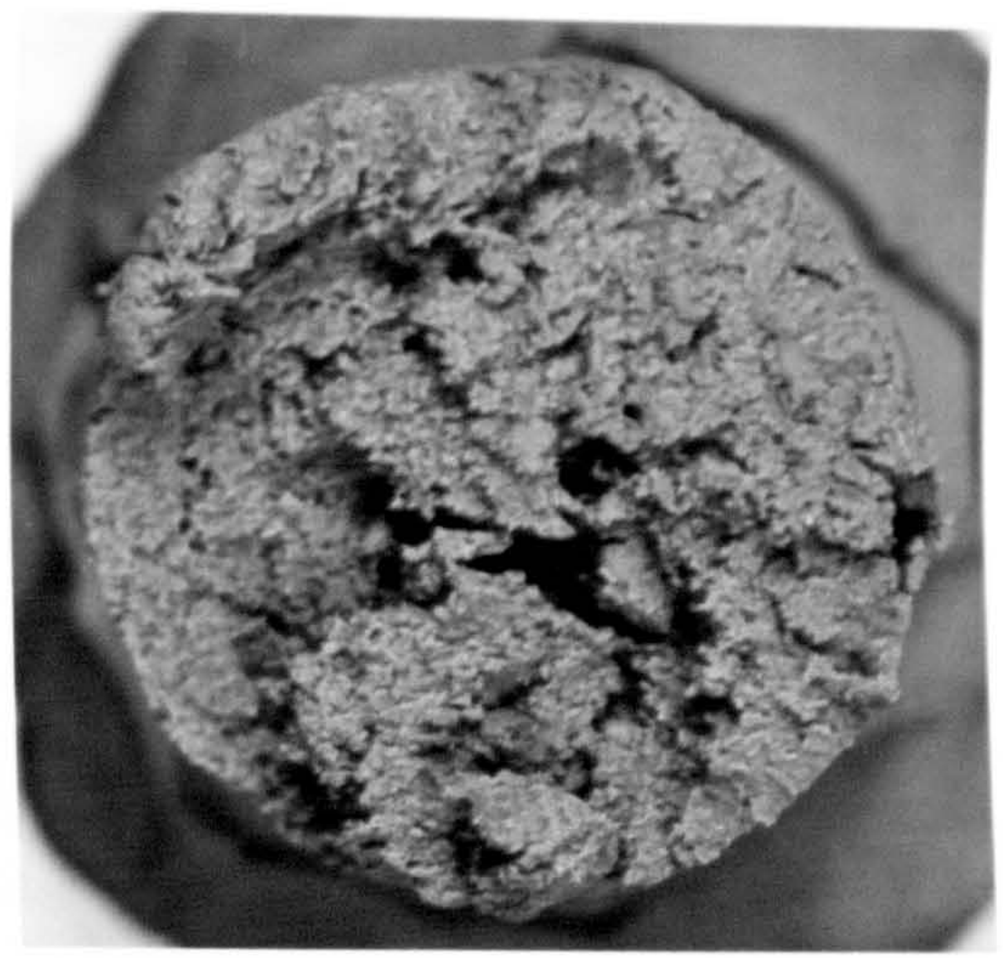

(b) "NON-LAYERED" GLYBEN

(c) MODIFIED GRANGEMOUTH CLAY

FIG. C.3. PLAN VIEWS OF CROSS-SECTIONS OF FAILED TENSILE SAMPLES

APPENDIX D

DETAILS OF VOLUME CHANGE TESTS

The volume change apparatus involved a standard triaxial testing frame, perspex cell, and volume change indicator of the single burette type, manufactured by Wykeham Farrance Engineering Ltd. The method used is described by Bishop and Henkel (1957). The volume change indicator read to an accuracy of 0.1 cc which allowed volume changes of approximately 0.006 per cent of the volume of the 4 inch (101.6 mm) diameter by 8 inch (203.2 mm) long samples to be measured. The cell pressures which were applied to the samples ranged from 7 kN/m^2 to 55 kN/m^2. The rate of testing to find the volume change due to deviatoric stress was 0.060 mm/mm per minute. The perspex cell which was used in the tests was calibrated for various cell pressures before the samples were inserted. It was found that, because of the construction of the cell, it was impossible to remove the air bubbles which were not displaced from the very top portion of the cell when the cell was being filled with de-aired water. Care was therefore taken to ensure that the volume of air in the cell during the actual volume change tests was similar to that in the cell during calibration.

One sample of batch no. 3 "layered" glyben and one sample of modified Grangemouth clay were tested. The 101.6 mm x 203.2 mm sample of glyben was trimmed from a block of glyben which was compacted in the uplift resistance box of base 300 mm square. The 101.6 mm x 203.2 mm sample of modified Grangemouth clay was compacted in two six-inch concrete cube moulds which were clamped one on top of the other. Fig. 4.11 showed the volume change in the samples due to variations of cell pressure. Negligible volume change occurred in the samples when the deviatoric stress was applied.

APPENDIX E

DESCRIPTION OF FINITE ELEMENT PROGRAM

The elastic-plastic finite element program which was developed originally by Dr. I.M. Smith was a plane stress program. Dr. Smith, with the assistance of the author, adapted this program to the axi-symmetric case. The program had then to be further adapted by the author for use in the uplift resistance problem as follows:

(a) large values of stiffness were added to the structural stiffness vector and equivalent values were added to the force vector to simulate displacement of the rigid anchor plate, as described in section E.6;

(b) a procedure which calculated the residual loads was added (section E.7);

(c) a procedure which calculated material self-weight stresses was added (section E.10);

(d) a procedure which calculated the load adjustment factor R was added (section E.12);

(e) procedures which calculated the anchor loads were added (section E.15);

(f) a procedure which calculated the magnitudes and directions of the principal stresses in each element was added (section E.16).

In addition, the procedure which generated the co-ordinates and degree of freedom numbers for each element was substantially modified to take account of the meshes employing varying element dimensions and to take account of the separate anchor plate nodes.

In this appendix, a description of the main features of the finite element program which was used in the uplift resistance analysis is given. The order in which the features are described corresponds to the order in which they appear in the flow chart which is included inside the back cover of this thesis. In general, the various functions and

relationships which were used in the program will be outlined but not proved.

E.1. Elastic Stress-Strain Matrix [D]

The elasticity matrix [D] which relates the elastic strains $\{\epsilon\}$ to the elastic stresses $\{\sigma\}$ in the axially symmetric case is:

$$\begin{Bmatrix} \sigma_r \\ \sigma_z \\ \tau_{rz} \\ \sigma_\theta \end{Bmatrix} = [D] \begin{Bmatrix} \epsilon_r \\ \epsilon_z \\ \gamma_{rz} \\ \epsilon_\theta \end{Bmatrix} \qquad \ldots\ldots(E.1)$$

where

$$[D] = \frac{E(1-\nu)}{(1+\nu)(1-2\nu)} \begin{bmatrix} 1 & \frac{\nu}{1-\nu} & 0 & \frac{\nu}{1-\nu} \\ & 1 & 0 & \frac{\nu}{1-\nu} \\ \text{symmetric} & & \frac{1-2\nu}{2(1-\nu)} & 0 \\ & & & 1 \end{bmatrix} \qquad \ldots(E.2)$$

Equations E.1 and E.2 show that the values of elastic stresses which correspond to given values of elastic strains are directly proportional to the value of elastic modulus E and dependent on, but not directly proportional to, the value of Poisson's ratio ν .

E.2. Derivation of the Isoparametric Quadrilateral Element

In the investigation, isoparametric quadrilateral elements were chosen. Although the elements are termed quadrilateral, it must be remembered that, in the axi-symmetric case, the elements are in fact toroidal solids of revolution which are quadrilateral in section.

Each of the four nodes possessed two degrees of freedom at each node, i.e. radial freedom (u) and vertical freedom (v) as shown in Fig. E.1. The displacements δ of each node had therefore two components:

$$\{\delta_i\} = \begin{Bmatrix} u_i \\ v_i \end{Bmatrix} \qquad \ldots\ldots(E.3)$$

where i equals the number of the node of the element.

If the quadrilateral illustrated in Fig. E.1 is considered to be a rectangle and if each component of displacement varies in a linear manner along each side of the element, then continuity of displacement of all points on the element sides common to adjacent elements will be ensured. However, when a quadrilateral element is substituted for the rectangle, the displacement of the points on the sides of the quadrilateral element will not in general vary linearly with the general co-ordinates r and z. If the general system of co-ordinates is replaced by a local co-ordinate system in terms of r' and z' as shown in Fig. E.1, continuity and linear variation of displacements along the sides of the quadrilateral element will be maintained.

The shape function $[N]$ relates the position of any point (r, z) within the element to the positions of the nodal points of the element. The shape function used in the program can be expressed as:

$$r = N_i r_i + N_j r_j + N_k r_k + N_\ell r_\ell \qquad \ldots\ldots (E.4)$$

$$z = N_i z_i + N_j z_j + N_k z_k + N_\ell z_\ell$$

where

$$N_i = \tfrac{1}{4}(1 - r')(1 - z')$$

$$N_j = \tfrac{1}{4}(1 - r')(1 + z')$$

$$N_k = \tfrac{1}{4}(1 + r')(1 + z')$$

$$N_\ell = \tfrac{1}{4}(1 + r')(1 - z')$$

This is a linear co-ordinate transformation.

The displacement function relates the displacement of any point (u, v) within the elements to the displacement of the nodal points of the element. The linear quadrilateral element displacement function used in the program can be defined as:

$$u = N_i u_i + N_j u_j + N_k u_k + N_\ell u_\ell \qquad \ldots (E.5)$$

$$v = N_i v_i + N_j v_j + N_k v_k + N_\ell v_\ell$$

Where the displacement functions and the shape functions are the same,

the element is termed isoparametric. Although the elements which were derived in the program were quadrilateral elements, the elements of the meshes used for the uplift resistance problem were rectangular elements, i.e. a simplified form of the general quadrilateral element.

E.3. Strain-Displacement Matrix [B]

The matrix $[B]$, which relates the strains $\{\epsilon\}$ at any point within the element to the displacements $\{\delta\}$ at any point within the element, is expressed in the axi-symmetric case as:

$$\begin{Bmatrix} \epsilon_r \\ \epsilon_z \\ \gamma_{rz} \\ \epsilon_\theta \end{Bmatrix} = [B] \begin{Bmatrix} u_i \\ v_i \\ u_j \\ v_j \\ u_k \\ v_k \\ u_\ell \\ v_\ell \end{Bmatrix} \qquad \cdots\cdots (E.6)$$

$$[B] = \begin{bmatrix} \frac{\partial N_i}{\partial r} & 0 & \frac{\partial N_j}{\partial r} & 0 & \frac{\partial N_k}{\partial r} & 0 & \frac{\partial N_\ell}{\partial r} & 0 \\ 0 & \frac{\partial N_i}{\partial z} & 0 & \frac{\partial N_j}{\partial z} & 0 & \frac{\partial N_k}{\partial z} & 0 & \frac{\partial N_\ell}{\partial z} \\ \frac{\partial N_i}{\partial z} & \frac{\partial N_i}{\partial r} & \frac{\partial N_j}{\partial z} & \frac{\partial N_j}{\partial r} & \frac{\partial N_k}{\partial z} & \frac{\partial N_k}{\partial r} & \frac{\partial N_\ell}{\partial z} & \frac{\partial N_\ell}{\partial r} \\ \frac{N_i}{r} & 0 & \frac{N_j}{r} & 0 & \frac{N_k}{r} & 0 & \frac{N_\ell}{r} & 0 \end{bmatrix} \qquad \cdots (E.7)$$

This relationship will only hold good if the displacements are small. Since u has been defined as a function of $[N]$ in terms of the local co-ordinates (r', z'), in order to obtain $[B]$ in terms of the general co-ordinates (r, z), the Jacobian transformation matrix must be used:

$$\begin{Bmatrix} \frac{\partial}{\partial r'} \\ \frac{\partial}{\partial z'} \end{Bmatrix} = \begin{bmatrix} \frac{\partial r}{\partial r'} & \frac{\partial z}{\partial r'} \\ \frac{\partial r}{\partial z'} & \frac{\partial z}{\partial z'} \end{bmatrix} \begin{Bmatrix} \frac{\partial}{\partial r} \\ \frac{\partial}{\partial z} \end{Bmatrix} = [J] \begin{Bmatrix} \frac{\partial}{\partial r} \\ \frac{\partial}{\partial z} \end{Bmatrix} \qquad \cdots (E.8)$$

thus $$\begin{Bmatrix} \frac{\partial}{\partial r} \\ \frac{\partial}{\partial z} \end{Bmatrix} = [J]^{-1} \begin{Bmatrix} \frac{\partial}{\partial r'} \\ \frac{\partial}{\partial z'} \end{Bmatrix}$$

E.4. Element Stiffness Matrix [KM]

The total stiffness of the element is given by the integral:

$$[KM] = \int_{\text{element vol.}} [B]^T [D][B] \, d(\text{el. vol.})$$

$$= 2\pi \int_{\text{el. vol.}} [B]^T [D][B] \, r \, dr \, dz \qquad \cdots (E.9)$$

in the axi-symmetric case. Since the exact integration of a quadrilateral is time-consuming and subject to programming errors, a numerical integration using the Gaussian quadrature formulae was employed. A detailed description of these formulae can be found by reference to Kopal (1961). In the numerical integration, the stiffness of each quadrilateral element is evaluated at each of the nine points shown in Fig. E.2 and the results from these nine points are added together to obtain the overall element stiffness. Since each quadrilateral element has eight degrees of freedom, the element stiffness matrix will be an 8 x 8 matrix.

E.5. Structural Stiffness Vector {BK}

After the element stiffnesses for all of the elements in the mesh have been calculated, they are combined together in the structural stiffness vector $\{BK\}$. The structural stiffness vector is normally in the form of a matrix. Since this matrix is always symmetrical and banded, the upper triangle only is stored as a $[N \times (\omega+1)]$ matrix, where N is the total number of degrees of freedom in the mesh and ω is the half-band width of the matrix. However, for ease of storage in this program, this matrix is converted into a vector in which there are $N \times (\omega+1)$ terms.

E.6. Nodal Loads and Displacements

From consideration of minimum potential energy concepts, the relationship between the radial and vertical forces F which are applied to the nodes of the mesh, and the resulting displacements can be expressed as:

$$\begin{Bmatrix} F_1 \\ F_2 \\ \cdot \\ \cdot \\ \cdot \\ F_N \end{Bmatrix} = \{BK\} \begin{Bmatrix} \delta_1 \\ \delta_2 \\ \cdot \\ \cdot \\ \cdot \\ \delta_N \end{Bmatrix} \quad \cdots\cdots (E.10)$$

where N equals the total number of degrees of freedom in the mesh.

Loads are added to specified nodal degrees of freedom, and to calculate the corresponding displacements at these degrees of freedom, N simultaneous equations must be solved. In this program, the Gaussian elimination technique is employed to solve these equations.

In the uplift resistance problem, the anchor plate was considered to be rigid, which required that all vertical displacements of the nodes which represented the anchor plate were required to be identical. To achieve this, very large values of stiffness, of the order of 10^5 to 10^7 times the stiffness for the soil, were incorporated in the leading diagonal of the structural stiffness matrix (vector), in positions which corresponded to the vertical degrees of freedom of the anchor plate nodes. The corresponding terms in the force vector were given the same large values, multiplied by the required displacement of the anchor plate. This ensured that the vertical displacements of the anchor nodes were always those prescribed, whilst equilibrium at the nodes and complete compatibility overall were maintained.

E.7. Residuals

In order to check that the Gaussian elimination procedure was working correctly and that the structure represented by the mesh and the resulting simultaneous equations were well-conditioned, a procedure to calculate the residual loads was incorporated in the program. These residual loads indicated any errors in the Gaussian elimination procedure or any ill-conditioning of the structure and were calculated

by substituting the nodal displacements obtained from equation E.10 back into equation E.10 to obtain the values of the terms in the force vector. These values were subtracted from the original values in the force vector and the remaining values in the force vector which should theoretically have been zero, were termed residual loads. In the uplift resistance program, the values of the residuals obtained were of the order of 10^{-11} to 10^{-13}. These very small values indicated that no errors were present in the Gaussian elimination procedure and that the structure was well-conditioned. Residual loads were calculated for the first increment of load only.

Calculation of the residual loads involved storage of the structural stiffness vector $\{BK\}$ in both its original form and in the form suitable for use in the Gaussian elimination procedure. In order to obtain enough storage space in the computer, the $\{BK\}$ vector in its original form had to be stored on disc since there was insufficient storage space in the core store of the KDF9 computer.

E.8. Values of Element Strain

Equations E.6 and E.7 expressed the relationship between strain at any point in the element and the nodal displacements of the element. In the uplift resistance program, the strains at the centre only of each element were calculated.

E.9. Values of Element Stress

Equation E.1 expressed the relationship between the elastic strains and the corresponding elastic stresses at any point in the element. Since the strains in each element were calculated for a point at the centre only of the element, the corresponding stresses were also calculated at the centre only of the element.

Sign Convention. Fig. E.3 illustrates the sign convention adopted in the program. Positive signs indicated compressive stresses and strains and negative signs indicated tensile stresses and strains.

E.10. Stresses due to Material Self-Weight

The self-weight of the material is taken into account by including in the stress vector the stresses at the centre of each element due to the material self-weight. Although there are stresses in the material due to self-weight, the corresponding strains and nodal displacements due to self-weight are not included in the program since the co-ordinates of each element used in the program are assumed to represent the position of the material after it has reached equilibrium under its own weight. The stresses due to material self-weight in each element are:

$$\sigma_z = \gamma_g d$$
$$\sigma_r = \sigma_\theta = K_o \sigma_z \qquad \cdots\cdots (E.11)$$
$$\tau_{rz} = 0$$

where d = the depth from the top surface of the mesh to the centre of the element

K_o = the coefficient of earth pressure at rest.

E.11. Von Mises Yield Stress Criterion

The Von Mises Yield Criterion for the axi-symmetric case can be expressed in the form:

$$\bar{\sigma}_y = \sqrt{0.5\left[(\sigma_r-\sigma_\theta)^2 + (\sigma_\theta-\sigma_z)^2 + (\sigma_z-\sigma_r)^2 + 6\tau_{rz}^2\right]} \qquad \cdots (E.12)$$

where $\bar{\sigma}_y$ is the uniaxial stress at yield. The value of the yield stress in shear in this criterion is greater by a factor of 1.155 than the yield stress in shear given by the Tresca Yield Criterion.

E.12. Calculation of Factor R by which the Initial Increment of Load is adjusted so that the "Critical" Element is on the Point of Yield

As long as the stresses and strains in all of the elements in the mesh are on the elastic portion of the material stress-strain curve, then the nodal displacements and element stresses and strains will be directly proportional to the magnitude of the nodal loads (forces). Therefore, in an incremental loading elastic-plastic analysis, it is desirable that only the first load increment produces stresses and

strains in all of the elements on the elastic portion of the stress-strain curve. It is also desirable that this load increment be large enough to bring the "critical" element to the point of yield. This increment will then be the largest load which can be applied to the mesh in order that all of the elements remain elastic, and any further increment of load, no matter how small, will cause the "critical" element to yield.

In the uplift resistance program, an arbitrary vertical displacement was applied initially to the element nodes which represented the anchor. The values of the Von Mises Stress $\bar{\sigma}$ in each element, corresponding to the arbitrary anchor displacement, were then calculated. For a material which was assumed to be weightless, the factor R by which the arbitrary anchor displacement was multiplied to bring the "critical" element to the point of yield was:

$$R = \frac{\bar{\sigma}_y}{\bar{\sigma}_{max}} \qquad \cdots\cdots(E.13)$$

where $\bar{\sigma}_y$ = the specified value of Von Mises Yield Stress

$\bar{\sigma}_{max}$ = the value of Von Mises Stress in the "critical" element due to the arbitrary displacement.

For a material which possessed self-weight, the factor R had to be found by the solution of a quadratic equation, since, although the stresses in the elements due to the applied loading were proportional to that loading, the stresses due to self-weight in each element were constant and independent of the magnitude of the applied loading.

E.13. Elastic-Plastic Stress-Strain Matrix [DPL]

In Section E.1, the elasticity matrix [D] which related the elastic strains to the elastic stresses in the material was presented. Yamada et.al.(1968) derived explicitly the equivalent plastic stress-strain matrix [DPL] for a Von Mises material in the general three-dimensional case. This equation was adapted by the author for the axi-symmetric case in a linear elastic, non-strain hardening plastic

material, of the type illustrated in Fig. E.4. Hence:

$$\begin{Bmatrix} \sigma_r \\ \sigma_z \\ \tau_{rz} \\ \sigma_\theta \end{Bmatrix} = [DPL] \begin{Bmatrix} \epsilon_r \\ \epsilon_z \\ \gamma_{rz} \\ \epsilon_\theta \end{Bmatrix} \qquad \cdots\cdots (E.14)$$

where

$$[DPL] = [D] - FAC\,[PL]$$

$$[PL] = \frac{3E}{2\bar{\sigma}_y^{\,2}(1+\nu)} \begin{bmatrix} \sigma_r'^{\,2} & \sigma_r'\sigma_z' & \sigma_r'\tau_{rz} & \sigma_r'\sigma_\theta' \\ & \sigma_z'^{\,2} & \sigma_z'\tau_{rz} & \sigma_z'\sigma_\theta' \\ \text{symmetric} & & \tau_{rz}^{\,2} & \sigma_\theta'\tau_{rz} \\ & & & \sigma_\theta'^{\,2} \end{bmatrix} \qquad \cdots (E.15)$$

in which the dashes stand for deviatoric stresses, i.e.:

$$\sigma_r' = \sigma_r - \frac{(\sigma_r + \sigma_z + \sigma_\theta)}{3} \qquad \text{etc.}$$

The coefficient FAC is a factor which reduces the effect of the plasticity part [PL] of the [DPL] matrix if the load increment brings the value of Von Mises Stress $\bar{\sigma}$ in an element on to the plastic portion of the stress-strain curve from a point on the elastic portion of the curve, i.e. the relationship between the stresses and strains which are on the elastic portion of the stress-strain curve is governed solely by the elasticity matrix [D] and only when the stress in the element has reached a value of $\bar{\sigma}_y$ is the relationship governed by [DPL]. If the stresses in the element were on the plastic portion of the stress-strain curve before the load increment occurred, then the value of FAC would be unity.

E.14. "Initial Stress" Process for Redistributing Out-of-Balance Stresses

A complete description of this process which was developed by Zienkiewicz, Valliappan and King (1969) is given by Fraser (1971). The process is illustrated in Fig. E.4 and described briefly in the

follcwing paragraphs.

Equation E.14 can be expressed in the incremental form:

$$\{d\sigma\} = [DPL]\{d\epsilon\} \qquad \cdots\cdot (E.14A)$$

The "initial stress" process is based on the calculation of an "initial stress" vector $\{d\sigma''\}$ such that the incremental form of equation E.1:

$$\{d\sigma\} = [D]\{d\epsilon\} + \{d\sigma''\} \qquad \cdots (E.1A)$$

gives equivalent values of $\{d\sigma\}$ to those in equation E.14.A.

An example of the way in which this method was employed in the uplift resistance program follows. The stresses in the "critical" element, after the first load increment (adjusted by factor R) has been added, are considered. The Von Mises Stress in the element at this stage can be considered to be $\bar{\sigma}_y$, at point A in Fig. E.4. This stress is termed σ_o . The second load increment $\{dF\}$ is now added. The elastic strains due to this increment are calculated from:

$$\{d\epsilon_1\} = [B]\{d\delta_1\} \qquad \cdots\cdot (E.6A)$$

and from this, the elastic stress increment $\{d\sigma_1'\}$ is calculated:

$$\{d\sigma_1'\} = [D]\{d\epsilon_1\} \qquad \cdots (E.1A\ bis)$$

However, the actual stress increments which should have occurred, since the stresses must lie on the plastic portion of the stress-strain curve, are given by:

$$\{d\sigma_1\} = [DPL]\{d\epsilon_1\} \qquad \cdots (E.14A)$$

The $[DPL]$ matrix is given by equation E.15 and involves values of σ_r , σ_z , σ_θ and τ_{rz} . In the uplift resistance program, these stresses were taken as the stresses which existed in the element before the current load increment was applied.

The "initial stress" is the difference between the elastic and total stress increments in the element:

$$\{d\sigma_1''\} = \{d\sigma_1'\} - \{d\sigma_1\} \qquad \cdots\cdot (E.16)$$

The "initial stresses" which exist within the element must be balanced by a set of nodal forces $\{P\}$. From a consideration of the equality

of internal and external work on the element, the relationship between the "initial stresses" and the resulting balancing nodal loads can be expressed as:

$$\{P\} = \int_{\text{element vol.}} [B]^T \{d\sigma''\}\, d(\text{el. vol.}) \qquad \cdots\cdots (E.17)$$

After this procedure has been repeated for all of the elements which have yielded, the resulting load vector $\{P\}$ is added to the external load vector and the process to find the elastic, total and "initial stresses" and the balancing loads is repeated in a second iteration. After n iterations, the values of $\{dF_n\}$, $\{d\delta_n\}$, $\{d\sigma'_n\}$ and $\{d\sigma''_n\}$ become constant, which indicates that the excess stresses in the yielded elements have been re-distributed to the non-yielded elements.

In programs where external load increments are added to the specified nodes, structural failure is indicated by non-convergence of the terms $\{dF_n\}$, $\{d\delta_n\}$, $\{d\sigma'_n\}$ and $\{d\sigma_n''\}$ after a large number of iterations. The non-convergence indicates that no more re-distribution of excess stresses is possible in the structure. In the uplift resistance program, external displacements were applied to the anchor nodes. Although convergence continued to occur at structural failure in this case, no increase in the values of stresses and strains in the elements and in the values of the total resulting external loads on the nodes occurred when continued increments of anchor displacements were applied.

E.15. Method of obtaining Anchor Loads

Since specified displacements, as opposed to loads, were applied to the anchor nodes, the resulting loads on the nodes had to be calculated. For the first anchor displacement, when all of the elements were on the elastic portion of the stress-strain curve, the loads on the nodes, corresponding to the nodal displacements, could be calculated in the manner used to calculate the residual loads:

$$\{F\} = \{BK\}\{\delta\} \qquad \ldots \text{(E.10 bis)}$$

except that in this case, the large values of stiffnesses which had been added to prescribed terms in the leading diagonal of the structural stiffness matrix, as explained in section E.6, were removed. However, when some elements had yielded plastically, equation E.10 could no longer be used to obtain nodal loads, since the loads obtained would be the "elastic" loads corresponding to $\{\delta\}$.

In order to obtain the nodal loads corresponding to nodal displacements when elements had yielded plastically, the author developed a procedure which employed a form of equation E.17 to relate the total nodal forces to the stresses in the elements:

$$\{F_{NODE}\} = \int_{\text{element vol.}} [B]^T \{\sigma\} \, d(\text{vol.}) \qquad \ldots\ldots \text{(E.17A)}$$

The forces on the anchor node, due to the first (elastic) anchor displacement were obtained by the two methods described above, i.e. by (i) equation E.10 and by (ii) equation E.17.A, and were compared. The forces on all of the anchor nodes, except that which represented the edge of the anchor plate, agreed well in the two methods. However, the force on the edge node obtained from method (ii) was only of the order of half of that obtained from method (i) in each of runs 1, 2 and 3. This can be explained as follows. The element which supplies the major part of the edge nodal force is the "critical" element. In section E.9 it was stated that the stress in any element was taken to be the stress which occurred at the centre of the element. In the majority of elements in the mesh, the stress at the centre of the element will be representative of the stresses in other parts of the element, provided the elements are small. However, in the "critical" element, large values of compressive and tensile normal stresses and shearing stresses will occur at varying points in the element and the stress at the centre of the element will therefore not be representative of the stresses throughout the element.

In order to obtain a more accurate estimate of the nodal loads on the edge node of the anchor plate up to ultimate failure, the values of the edge nodal loads obtained from method (ii) were multiplied by the ratio of the edge node loads due to the first anchor displacement obtained by method (i) to those due to the first anchor displacement obtained by method (ii). This is termed method (iii), and it assumed that the relationship between the stresses at various points in the "critical" element and the stresses at the centre of the element remained constant up to ultimate failure.

Since the finite element analysis predicted a general form of ultimate failure of the type proposed in the Shearing Theory (2.2.A), the theoretical value of ultimate uplift resistance was available and could be compared with that obtained by method (iii) described in the previous paragraph. These are shown in Table E.1.

TABLE E.1. THEORETICAL AND FINITE ELEMENT VALUES OF $\bar{F}_u$

Run Number	D/B	Theoretical value of $\bar{F}_u$	Adjusted finite element value of $\bar{F}_u$ by method (iii)
1	1.5	6.0	6.19
2	3.2	12.8	12.65
3	5.25	21.0	not continued to ultimate failure

The values shown in Table E.1 suggest that the curves of $\bar{F}$ v d_a/B for runs 1, 2 and 3 obtained by method (iii) and shown in Figs. 5.9, 5.10, 5.11 and 5.12 depict with reasonable accuracy the $\bar{F}$ v d_a/B relationship which would have been calculated by the finite element program if an accurate estimate of the nodal loads at the edge of the anchor plate could have been obtained from equation E.17.A.

E.16. Principal Stresses

Due to the symmetry of the axi-symmetric case, the circumferential normal stress is a principal stress. All of the remaining stresses can be represented on any r - z cross-section through the axis of symmetry of the mesh.

The values of the major principal stresses used were:

$$\left.\begin{matrix}\sigma_{maj.}\\ \sigma_{min.}\end{matrix}\right\} = \frac{\sigma_z + \sigma_r}{2} \pm \sqrt{\left(\frac{\sigma_z - \sigma_r}{2}\right)^2 + \tau_{rz}^{\,2}} \qquad \ldots (E.18)$$

The maximum value of shear stress was:

$$\tau_{max} = \frac{\sigma_{maj} - \sigma_{min.}}{2} \qquad \ldots (E.19)$$

and the angle which the major principal stress made with the horizontal was:

$$\theta = \tfrac{1}{2} \tan^{-1}\left(\frac{2\tau_{rz}}{\sigma_z - \sigma_r}\right) \qquad \ldots (E.20)$$

Care had to be taken with the sign of θ in order that the correct angle was computed.

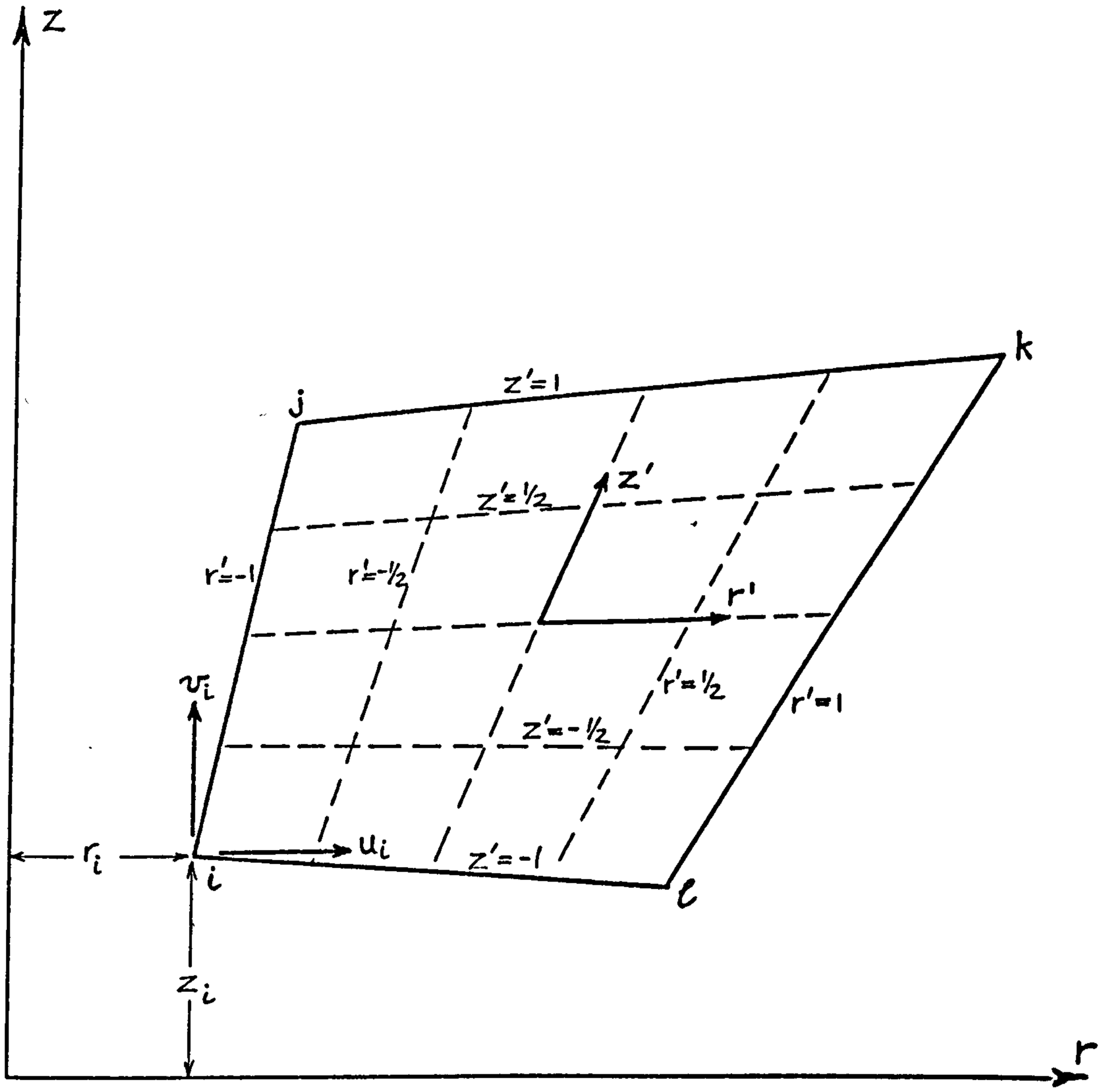

FIG. E.1. GENERAL (r,z) AND LOCAL (r',z') CO-ORDINATE SYSTEMS FOR QUADRILATERAL ELEMENT

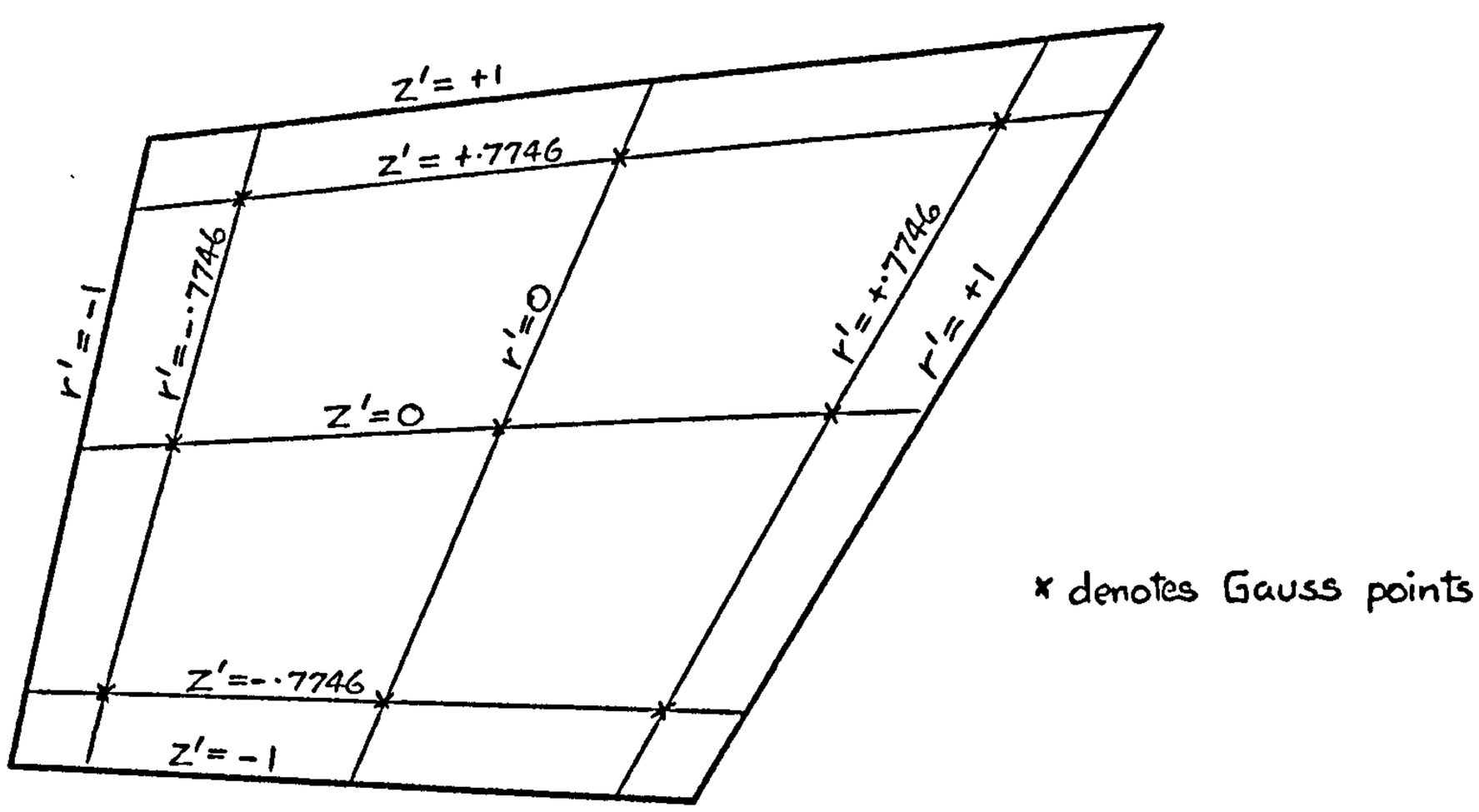

FIG. E.2. POSITIONS IN QUADRILATERAL ELEMENT OF THE NINE SAMPLING POINTS USED IN THE 3x3 GAUSSIAN QUADRATURE FORMULAE

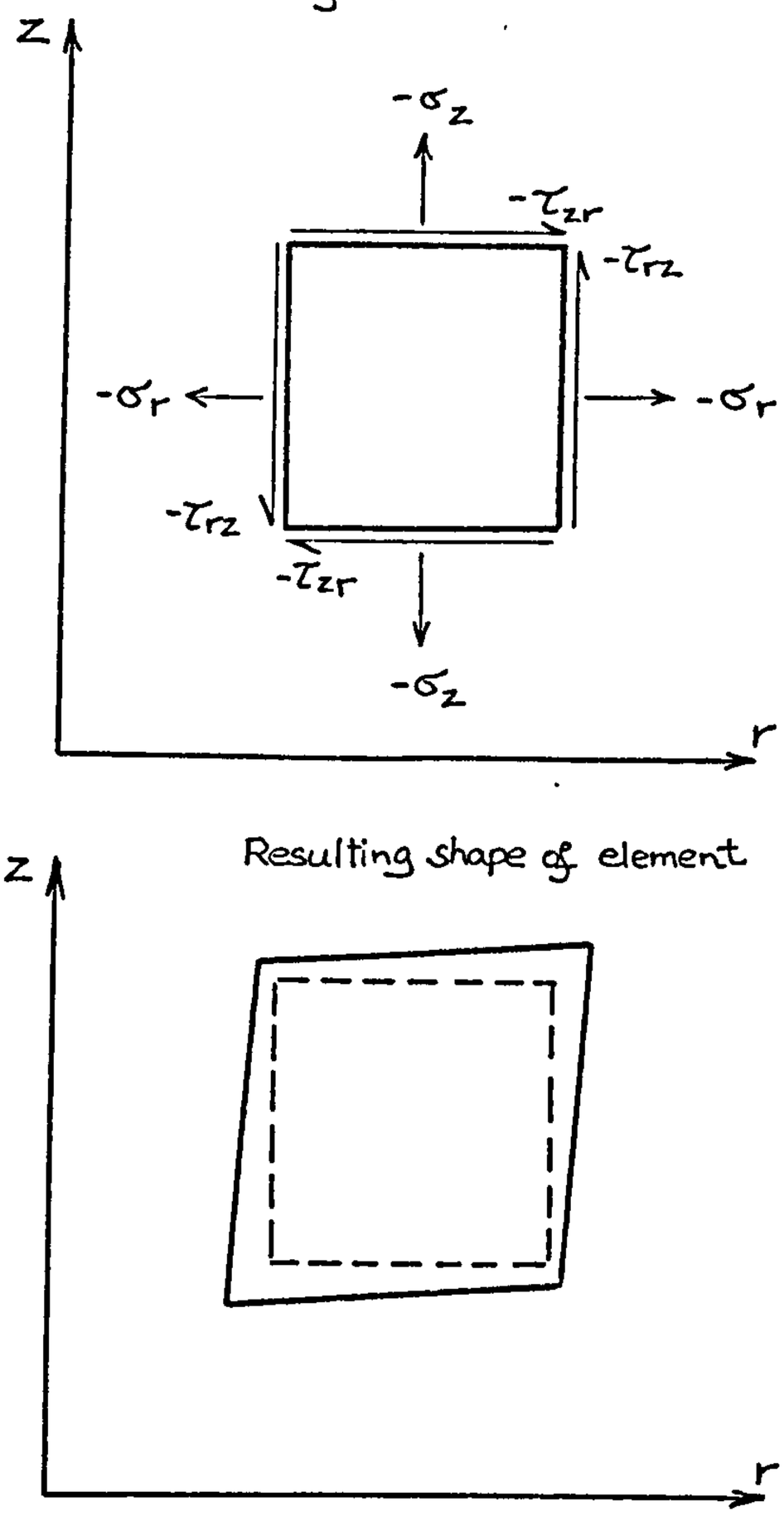

(a) TENSILE STRESSES

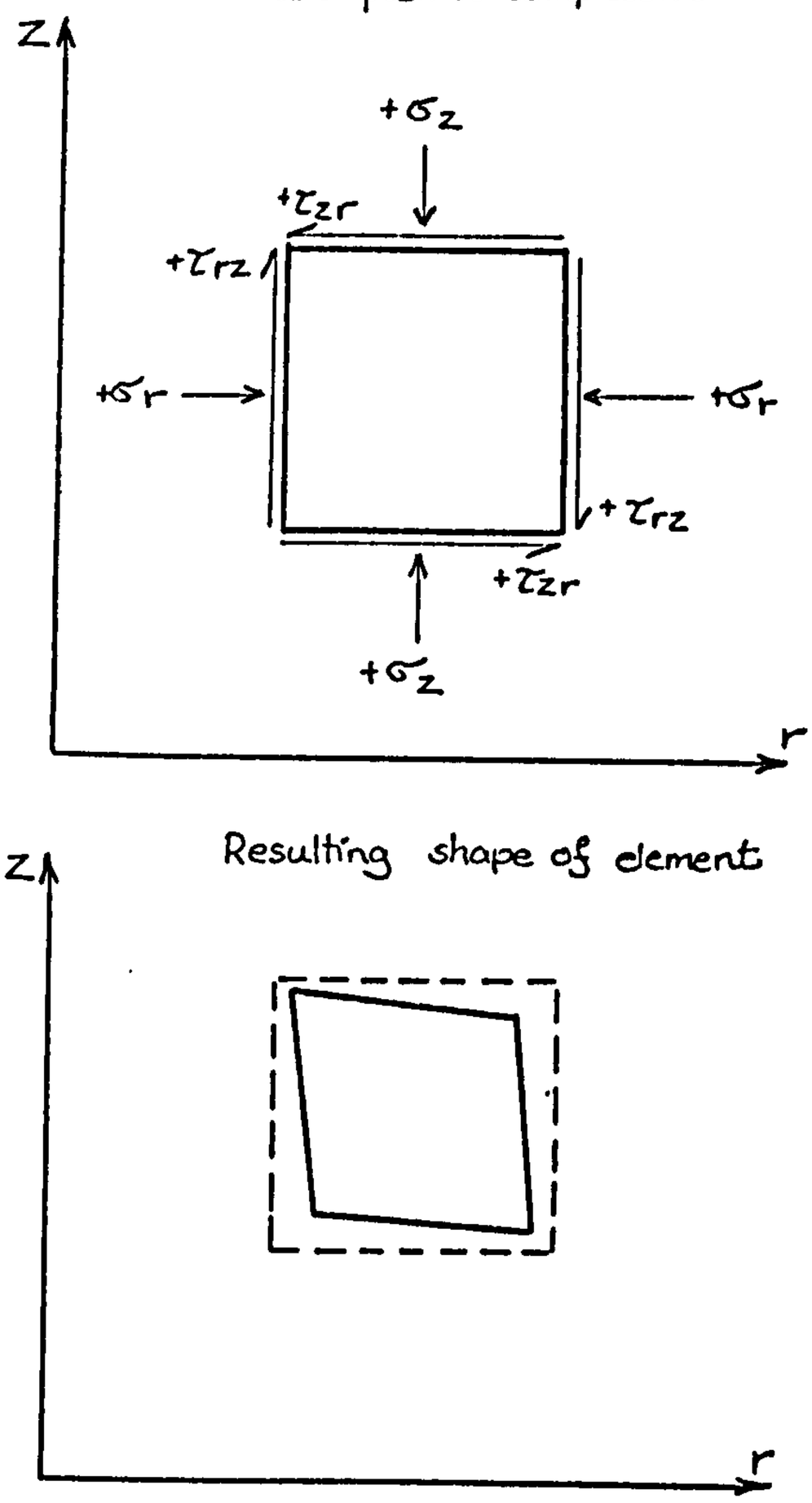

(b) COMPRESSIVE STRESSES

FIG. E.3. DETAILS OF THE SIGN CONVENTION ADOPTED IN THE FINITE ELEMENT PROGRAM

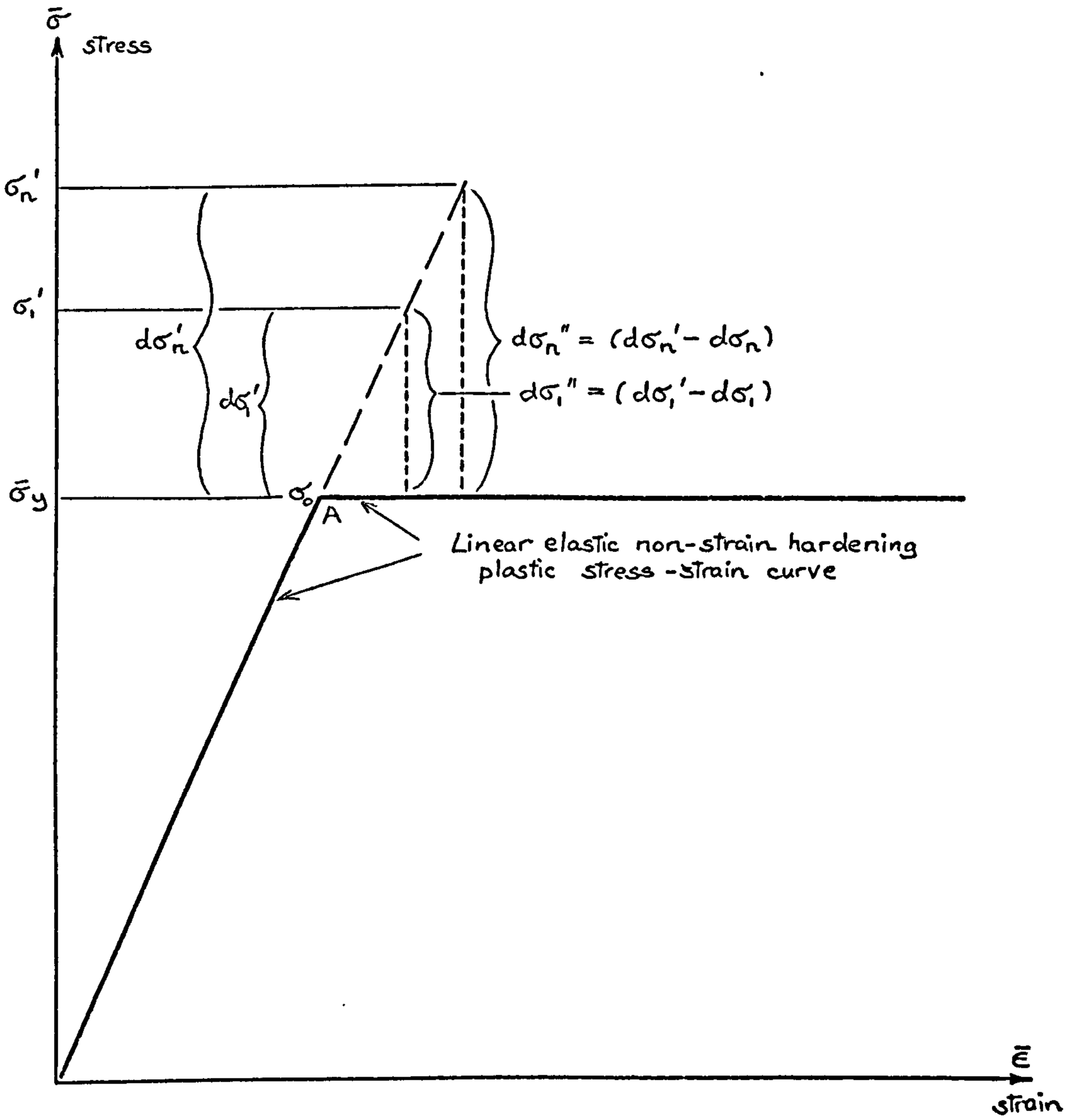

FIG. E.4. ILLUSTRATION OF THE "INITIAL STRESS" PROCEDURE

BEGIN

READ IN : NO. OF ELEMENTS, NO OF NODES, NO. OF DEGREES OF FREEDOM, NO. OF RESTRAINED NODES, NO. OF LOADED NODES, HALF-BAND WIDTH SIZE, TYPE & SIZE OF ELEMENT INFORMATION, MESH INFORMATION, SELF-WEIGHT INFORMATION, VALUES OF E, ν & $\bar{\sigma}_y$, NO. OF INCREMENTS & ITERATIONS

PRINT OUT : ALL VALUES READ IN ABOVE

CALCULATE [D] MATRIX FROM E & ν

CYCLE NO. OF FINITE ELEMENTS

READ IN : RESTRAINED NODE NOS. & PARTICULARS OF RESTRAINTS

PRINT OUT : RESTRAINED NODE NOS. & PARTICULARS

FORM NODAL FREEDOM ARRAY
CALCULATE CO-ORDINATES OF ELEMENTS
FORM [B] MATRIX FROM ELEMENT CO-ORDINATES
FORM ELEMENT STIFFNESS MATRIX $[KM] = \int_{el.vol.} [B]^T [D][B]\, d(VOL)$
FORM STRUCTURAL STIFFNESS MATRIX AND STORE AS VECTOR $\{BK\}$

PRINT OUT : CO-ORDINATES & STIFFNESSES OF ELEMENT

READ IN : LOADED NODE NOS. & CORRESPONDING LARGE SPRING STIFFNESSES

PRINT OUT : LOADED NODE NOS. & CORRESPONDING LARGE SPRING STIFFNESSES

INSERT LOADED NODE SPRING STIFFNESSES INTO VECTOR $\{BK\}$

REDUCE $\{BK\}$ TO AN APPROPRIATE FORM FOR GAUSSIAN ELIMINATION

CYCLE NO. OF LOAD INCREMENTS

FORM APPROPRIATE LOAD VECTOR $\{F\}$

CYCLE NO. OF ITERATIONS

CALCULATE NODAL DISPLACEMENTS $\{\delta\}$ FROM: $\{F\} = \{BK\}\{\delta\}$, SOLVING EQUATIONS BY GAUSSIAN ELIMINATION PROCEDURE

PRINT OUT : NODAL DISPLACEMENTS, INCREMENT AND ITERATION NO.

TEST : IS THIS THE FIRST INCREMENT AND ITERATION ?

YES

NO

CALCULATE RESIDUAL LOADS AND NODAL LOADS

PRINT OUT : RESIDUAL LOADS AND NODAL LOADS

CYCLE NO. OF FINITE ELEMENTS

FORM [B] MATRIX
CALCULATE INCREMENTS OF ELASTIC STRAIN IN THE ELEMENT : $\{d\varepsilon\} = [B]\{\delta\}$
CALCULATE CORRESPONDING STRESS INCREMENTS IN THE ELEMENT : $\{d\sigma'\} = [D]\{d\varepsilon\}$

TEST : IS THIS THE FIRST INCREMENT?

YES

NO

CALCULATE SELF-WEIGHT STRESSES & ADD TO $\{d\sigma'\}$

TEST : IS THIS THE FIRST ITERATION ?

NO

YES

CALCULATE FACTOR R

PRINT OUT : VALUE OF R

CALCULATE VALUE OF $d\bar{\sigma}$, VON MISES STRESS FUNCTION FOR ELEMENT STRESS INCREMENTS

ADD INCREMENTS OF STRESS $d\sigma'$ IN ELEMENT TO STRESSES σ_0 IN ELEMENT BEFORE LAST INCREMENT

CALCULATE VALUE OF $\bar{\sigma}_0$, VON MISES STRESS FUNCTION FOR STRESSES IN ELEMENT BEFORE LAST INCREMENT

CALCULATE VALUE OF $\bar{\sigma}$, VON MISES STRESS FUNCTION FOR TOTAL STRESSES IN ELEMENT AT THIS STAGE

TEST : IS $\bar{\sigma} \geq \bar{\sigma}_y$?

NO

YES

TEST : IS THIS THE LAST INCREMENT ?

NO

YES

TEST : IS $\bar{\sigma}_0 \geq \bar{\sigma}_y$?

NO

YES

CALCULATE FACTOR FAC

TEST : IS $\bar{\sigma} \geq \bar{\sigma}_y$?

NO

YES

TEST : IS THIS THE LAST INCREMENT ?

NO

YES

TEST : IS $\bar{\sigma}_o \geq \bar{\sigma}_y$?

NO

YES

CALCULATE FACTOR FAC

FAC = 1·0

FORM [DPL] MATRIX FROM $\{\sigma_o\}$ STRESSES

CALCULATE STRESS INCREMENTS $\{d\sigma\}$ FROM [DPL] MATRIX :
$\{d\sigma\} = [DPL]\{d\varepsilon\}$
CALCULATE "INITIAL STRESS" VALUES : $\{d\sigma^*\} = \{d\sigma'\} - \{d\sigma\}$

CALCULATE OUT-OF-BALANCE LOADS $\{P\}$ IN EACH DIRECTION AT EACH NODE.
$\{P\} = \int_{el.vol.} [B]^T \{d\sigma^*\} d(VOL)$.
ACCUMULATE THESE VALUES OF $\{P\}$, LOAD VECTOR $\{F\} = \{F\} + \{P\}$

TEST: IS THIS THE LAST ITERATION ?

NO

YES

TEST : IS THIS THE LAST ELEMENT ?

NO

YES

TEST: HAS $\bar{\sigma}$ BEEN LESS THAN $\bar{\sigma}_y$ FOR ALL ELEMENTS?

NO

YES

CALCULATE STRESSES IN ELEMENT : $\{\sigma\} = \{\sigma_o\} + \{d\sigma\}$
CALCULATE STRAINS IN ELEMENT : $\{\epsilon\} = \{\epsilon_o\} + \{d\varepsilon\}$

CALCULATE VALUE OF $\bar{\sigma}$, VON MISES STRESS FUNCTION FOR TOTAL STRESSES IN ELEMENT AT THIS STAGE. CALCULATE CORRESPONDING VALUE OF $\bar{\epsilon}$

PRINT OUT : CURRENT VALUE OF $d\bar{\sigma}$, $\bar{\sigma}$, $\bar{\epsilon}$ FOR THE ELEMENT, AND THE INCREMENT NO.

TEST : DOES THE ELEMENT CONTAIN A LOADED NODE ?

NO

YES

TEST : IS THIS THE LAST ELEMENT ?

NO

YES

CALCULATE FORCES AT ELEMENT NODES : $\{F_{NODE}\} = \int_{el.vol.} [B]^T \{\sigma\} d(VOL)$
ACCUMULATE VALUES OF $\{F_{NODE}\}$

TEST : IS THIS THE LAST ELEMENT ?

NO

YES

PRINT OUT : FOR ALL ELEMENTS :- $\{\sigma\}$, $\{\epsilon\}$, $\{F_{NODE}\}$ AND INCREMENT NO.

CYCLE NO. OF FINITE ELEMENTS

PRINT OUT : VALUES OF PRINCIPAL STRESSES, MAXIMUM SHEAR STRESS & DIRECTIONS OF MAJOR PRINCIPAL STRESS IN EACH ELEMENT, AND INCREMENT NO.

CALCULATE VALUES OF PRINCIPAL STRESSES, MAXIMUM SHEAR STRESS & DIRECTION OF MAJOR PRINCIPAL STRESS IN EACH ELEMENT

END

FLOW CHART OF FINITE ELEMENT ANALYSIS UPLIFT RESISTANCE PROGRAM

J.R. DAVIE JULY 1973